Oceanologia

Official Journal of the Polish Academy of Sciences: Institute of Oceanology and Committee on Maritime Research

This journal is supported by the Ministry of Science and Higher Education, Warsaw, Poland

Indexed in: ISI Journal Master List, Science Citation Index Expanded, Scopus, Current Contents, Zoological Record, Thomson Scientific SSCI, Aquatic Sciences and Fisheries Abstracts, DOAJ

IMPACT FACTOR ANNOUNCED FOR 2017 IN THE 'JOURNAL CITATION REPORTS' IS 1.614; 5-year IF is 1.585

Publisher
Elsevier Sp. z o.o.
22, Jana Pawła II Avenue
00-133 Warsaw, Poland

Associate Publisher
Chen Lin
c.lin@elsevier.com
+86-10-8520 8768

ISSN 0078-3234

Oceanologia (2019) 61, 291—299

Available online at www.sciencedirect.com

ScienceDirect

journal homepage: www.journals.elsevier.com/oceanologia/

ORIGINAL RESEARCH ARTICLE

Effect of drag coefficient formula choice on wind stress climatology in the North Atlantic and the European Arctic

Iwona Wróbel-Niedźwiecka *, **Violetta Drozdowska, Jacek Piskozub**

Institute of Oceanology, Polish Academy of Sciences, Sopot, Poland

Received 13 December 2018; accepted 26 February 2019
Available online 9 March 2019

KEYWORDS
Drag coefficient;
European Arctic;
North Atlantic;
Parameterizations

Summary Interactions between the atmosphere and the ocean determine boundary conditions for physical and biogeochemical processes in adjacent boundary layers, and the ocean surface is a complex interface where all air-sea fluxes take place and is a crucial valuable for ocean circulation and the ecosystem. We have chosen to study the differences between the relevant or most commonly used parameterizations for drag coefficient (C_D) for the momentum transfer values, especially in the North Atlantic (NA) and the European Arctic (EA), using them together with realistic wind field. We studied monthly mean values of air-sea momentum flux resulting from the choice of different drag coefficient parameterizations, adapted them to momentum flux (wind stress) calculations using wind fields, sea-ice masks, as well as integrating procedures. We compared the resulting spreads in momentum flux to global values and values in the tropics, an area of prevailing low winds. We found that the spread of results stemming from the choice of drag coefficient parameterization was 14% in the Arctic, the NA and globally, but it was higher (19%) in the tropics. On monthly time scales, the differences were larger at up to 29% in the NA and 36% in the EA (in months of low winds) and even 50% locally (the area west of Spitsbergen). Comparing the values of drag coefficient from chosen parameterizations, it showed that momentum fluxes were largest for all months, in both regions with low and high winds, when the C_D values increased linearly with wind speed.

* Corresponding author at: Institute of Oceanology, Polish Academy of Sciences, ul. Powstańców Warszawy 55, 81-712 Sopot, Poland. Tel.: +48 587311801; fax: (+48 58) 551 21 30.
E-mail address: iwrobel@iopan.gda.pl (I. Wróbel-Niedźwiecka).
Peer review under the responsibility of Institute of Oceanology of the Polish Academy of Sciences.

Production and hosting by Elsevier

https://doi.org/10.1016/j.oceano.2019.02.002

1. Introduction

The surface of the ocean is a complex boundary layer through which all air-sea fluxes of mass, momentum and energy take place. Determining the nature and consequences of exchanges between the atmosphere and the ocean is one of the greatest challenges in climate and sea studies, as well as ocean modelling and prediction. In this article we focus mainly on the surface momentum flux by which the atmospheric winds drive oceanic currents (so that the ocean acts as a sink for atmospheric momentum), which determine current system and sea state conditions and are most commonly parameterized using bulk aerodynamic formulae. Our goal is to evaluate how much the average monthly and annual momentum transfer values depend on the choice of non-dimensional drag coefficient (C_D), using the actual wind field from the North Atlantic (NA) and the European Arctic (EA), and demonstrate existing differences as a result of the formula used.

The ocean surface mixed layer is a region where kinematic forcing affects the exchange of horizontal momentum and controls transport from the surface to depths (Bigdeli et al., 2017; Gerbi et al., 2008). Any attempt to properly model the momentum flux from one fluid to another as the drag force per unit area at the sea surface (surface shear stress, τ) takes into account other physical processes responsible for generating turbulence such as boundary stress, boundary buoyancy flux, and wave breaking (Rieder et al., 1994; Toba et al., 2001). Fluxes across the sea surface usually depend nonlinearly on the relevant atmospheric or oceanic parameters. Over the past fifty years, as the collection of flux data has increased, many empirical formulas have been developed to express the ocean surface momentum flux as a relationship between C_D, wind speed (U_{10}), and surface roughness (z_0) (Andreas et al., 2012; Bunker, 1976; Donelan et al., 1997; Garratt, 1977; Kukulka et al., 2007; Large and Pond, 1981; Trenberth et al., 1989; Wu, 1969, 1982; Yelland and Taylor, 1996). These formulas can be divided into two groups. One group of theories gives the C_D at level z in terms of wind speed and possibly one or more sea-state parameters (for example, Enriquez and Friehe, 1997; Geernaert et al., 1987; Yelland and Taylor, 1996), while the second group provides formulas for roughness length z_0 in terms of atmospheric and sea-state parameters (for example, Andreas et al., 2012 (further referred to as A12), Donelan et al., 1997; Wu, 1969).

As the exchange of air-sea momentum is difficult to measure directly over the ocean, meteorologist and oceanographers often rely on bulk formulas first parameterized by Taylor (1916), that relate the fluxes to averaged wind speed through transfer coefficients:

$$\tau = \rho C_{Dz} U_z^2, \tag{1}$$

where τ is the momentum flux of surface stress, ρ is air density, C_{Dz} is the non-dimensional drag coefficient appropriate for z height, and U_z is the average wind speed at some reference height z above the sea. C_{Dz} is commonly identified as C_{DN10} or C_{D10} which is neutral-stability, 10-m drag coefficient (Toba et al., 2001), defined as:

$$C_{DN10} = \frac{\tau}{\rho U_{10}^2} = \left(\frac{u_*}{U_{10}}\right)^2, \tag{2}$$

where u_* is friction velocity. Alternatively, the neutrally stratified momentum flux can be determined from the logarithmic profile, thus Eq. (1) can be expressed as:

$$C_{DN10} = \left[\frac{\kappa}{\ln(10/z_0)}\right]^2, \tag{3}$$

where z_0 [m] is the aerodynamic roughness length, which is the height, above the surface to define the measure of drag at which wind speed extrapolates to 0 on the logarithmic wind profile (Andreas et al., 2012), and κ is von Kármán constant ($\kappa = 0.4$).

At the same time, we can define the value of friction velocity by the following equation:

$$\tau = \rho u_*^2. \tag{4}$$

Comparison with bulk formula (1) leads to the equation:

$$u_*^2 = C_{D10} U_{10}^2. \tag{5}$$

Some of the first studies (Garratt, 1977; Wu, 1969, 1982) focused on the relationship between wind stress and sea surface roughness, as proposed by Charnock (1955), and they formulated (for winds below 15 m s^{-1}) the logarithmic dependence of the stress coefficient on wind velocity (measured at a certain height) and the von Kármán constant. Currently common parameterizations of the drag coefficient are a linear function of 10 m wind speed (U_{10}), and the parameters in the equation are determined empirically by fitting observational data to a curve. The general form is expressed as (Guan and Xie, 2004):

$$C_D 10^3 = (a + bU_{10}). \tag{6}$$

In this work our focus is on the average flux values using seven different drag coefficient parameterizations (Table 1), chosen for their importance for the history of the field out of many published within the last half century (Bryant and Akbar, 2016).

All of the parameterizations are generated from the vertical wind profile, but they differ in the formulas used. Two of the parameterizations which we chosen are formulated as power-law of the relationship between C_D and U_{10} (Eq. (7) and (13) in Table 1), three are formulated as linear-law (Eqs. (8)–(10) and (12) in Table 1), and one as constant value of the relationship (Eq. (11) in Table 1). All the above studies propose different parameterizations (see Fig. 1) for the drag coefficient and the function of wind speed, which reflects the difficulties in simultaneously measuring at high sea stress (or friction velocity) and wind speed.

Wu (1969) compiled data from 12 laboratory studies and 30 oceanic observations, formulated power-law (for breezes and light winds) and linear-law (for strong winds) relationships between the wind-stress coefficient (C_z) and wind velocity (U_{10}) at a certain height z at various sea states. In his study, he used roughness Reynolds numbers to characterize the boundary layer flow conditions, and he assumed that the sea surface is aerodynamically smooth in the range of $U_{10} < 3$ m s^{-1}, transient at wind speed 3 m s^{-1} $< U_{10} <$ 7 m s^{-1}, and aerodynamically rough at strong winds $U_{10} > 7$ m s^{-1}. He also showed that the wind-stress coefficient and surface roughness increase with wind speed at light winds ($U_{10} < 15$ m s^{-1}) and is constant at high winds ($U_{10} > 15$ m s^{-1}) with aerodynamically rough flow.

Table 1 Neutral drag coefficient values over the ocean taken from the recent literature for a reference height of 10 m: C_{D10} is the drag coefficient dependent on surface roughness, C_{DN10} is the expression of neutral-stability (10-m drag coefficient), U_{10} is the mean wind speed measured at 10 m above the mean sea surface, U_{10N} is the 10-m neutral-stability wind speed, and a and b are proportionality constant.

Eq. no.	Source	Wind speed range [m s^{-1}]	$C_{DN(10)}$ ($\times 10^3$)
7	Wu (1969)	1–15	$0.5U_{10}^{0.5}$
8	Garratt (1977)	4–21	$0.75 + 0.067U_{10}$
9	Wu (1982)	>1	$0.8 + 0.065U_{10}$
10	Yelland and Taylor (1996)	3–6	$0.29 + \frac{3.1}{U} + \frac{7.7}{U_{10N}^2}$
		6–26	$0.60 + 0.070U_{10N}$
11	NCEP/NCAR	Everywhere	1.3
12	Large and Yeager (2004)	Everywhere	$\frac{2.7}{U_{10N}} + 0.142 + 0.076U_{10N}$
13	Andreas et al. (2012)	Everywhere	$\left(\frac{u_*}{U_{10N}}\right)^2 = a^2\left(1 + \frac{b}{a}U_{10N}\right)^2$ $a = 0.0583$, $b = -0.243$

Garratt (1977), who assessed the 10 m neutral drag coefficient (C_{DN10}) based on 17 publications, confirmed the previous relationship and simultaneously suggested a linear form of this relationship for light wind. Wu (1980) proposed the linear-law formula for all wind velocities and later (Wu, 1982) extended this even to hurricane wind speeds. Yelland and Taylor (1996) presented results obtained from three cruises using the inertial dissipation method in the Southern Ocean and indicate that using the linear-law relationship between the drag coefficient and wind speed (for $U_{10} > 6$ m s^{-1}) is better than using u_* with U_{10}. The NCEP/NCAR reanalysis (Kalnay et al., 1996) uses a constant drag coefficient of 1.3×10^{-3} while, for example, the Community Climate System Model version 3 (Collins et al., 2006) uses a single mathematical formula proposed by Large and Yeager (2004) for all wind speeds. Andreas et al. (2012) based on available datasets, friction velocity coefficient versus neutral-stability wind speed at 10 m, and sea surface roughness tested the approach proposed by Foreman and Emeis (2010) for friction velocity in order to find the best fit for parameters $a = 0.0583$ and $b = -0.243$. They justify their choice by demonstrating that u_* vs. U_{10N} has smaller experimental uncertainty than C_{DN10}, and that one expression of C_{DN10} for all wind speeds overstates and overestimates results in low and high winds (Figs. 7 and 8 in A12).

In this paper we investigate how the relevant or most commonly used parameterizations for drag coefficient (C_D) affect value of momentum transfer values, especially in the North Atlantic and the European Arctic. Our task was to demonstrate how big differences can be as a result of the

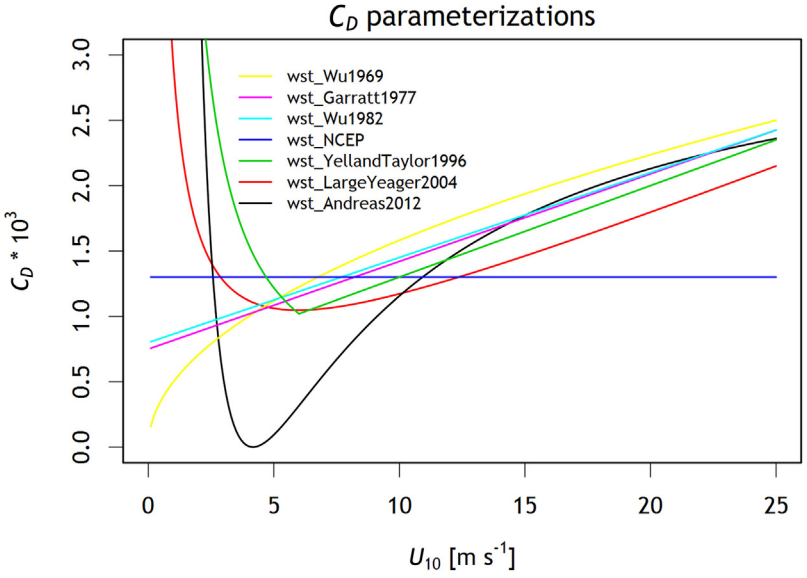

Figure 1 The drag coefficient parameterization used in the study (Eqs. (7)–(13) in Table 1) as a function of wind speed U_{10} [m s^{-1}].

formula used. As is widely known, the exact equation that describes the connection between the drag coefficient and wind speed depends on the author (Geernaert, 1990). Our intention here is not to re-invent or formulate a new drag parameterization for the NA or the EA, but to revisit the existing definition of drag parameterization, and, using satellite data, to investigate how existing formulas represent the environment in the North Atlantic Ocean. We concentrated on wind speed parameterizations, because wind speed is a parameter that is available in every atmospheric circulation model. Therefore, it is used in all air-sea flux parameterizations, and presently it is used even when sea state provides a closer physical coupling to the drag coefficient (for review see Geernaert et al., 1986).

2. Material and methods

We calculated monthly and annual mean momentum fluxes using a set of software processing tools called the FluxEngine (Shutler et al., 2016), which was created as part of the OceanFlux Greenhouse Gases project funded by the European Space Agency (ESA). Since the toolbox, for now, is designed to calculate only air-sea gas fluxes but it does contain the necessary datasets for other fluxes, we made minor changes in the source code by adding parameterizations for the air-sea drag relationship. For the calculations, we used Earth Observation (EO) U_{10} for 1992–2010 from the GlobWave project (http://globwave.ifremer.fr/). GlobWave produced a 20-year time series of global coverage multi-sensor cross-calibrated wave and wind data, which are publicly available via the Ifremer/CERSAT cloud. Satellite scatterometer derived wind fields are at present believed to be at least equally as good as wind products from reanalyses (see, for example, Dukhovskoy et al., 2017) for the area of our interest in the present study. The scatterometer derived wind values are calibrated to the U_{10N}, and, therefore, are fit for use with the neutral-stability drag coefficient (Chelton and Freilich, 2005). All data came in netCDF-4 format. The output data is a compilation file that contains data layers, and process indicator layers. The data layers within each output file, which are part of the FluxEngine, include statistics of the input datasets (e.g., variance of wind speed, percentage of ice cover), while the process indicator layers include fixed masks as land, open ocean, coastal classification, and ice.

All analyses using the global data contained in the FluxEngine software create a gridded ($1^\circ \times 1^\circ$) product. The NA was defined as all sea areas in the Atlantic sector north of 30°N, and the EA subset was those sea areas north of 64°N (Fig. 2). We also defined the subset of the EA east of Svalbard ("West Svalbard" between 76° and 80°N and 10° to 16°E), because it is a region that is studied intensively by multiple, annual oceanographic ship deployments (including that of the r/v *Oceania*, the ship of the institution the authors are affiliated with). FluxEngine treats areas with sea-ice presence in a way that is compatible with Lüpkes et al. (2012) multiplying the water drag coefficient by the ice-free fraction of each grid element. We also define "tropical ocean" as all areas within the Tropics (23°S to 23°N) in order to test the hypothesis that the new A12 parameterization will produce significantly lower wind stress values in the region.

3. Results and discussion

Some of the parameterizations used were limited to a restricted wind speed domain. We used them for all the global wind speed data to avoid data gaps for winds that

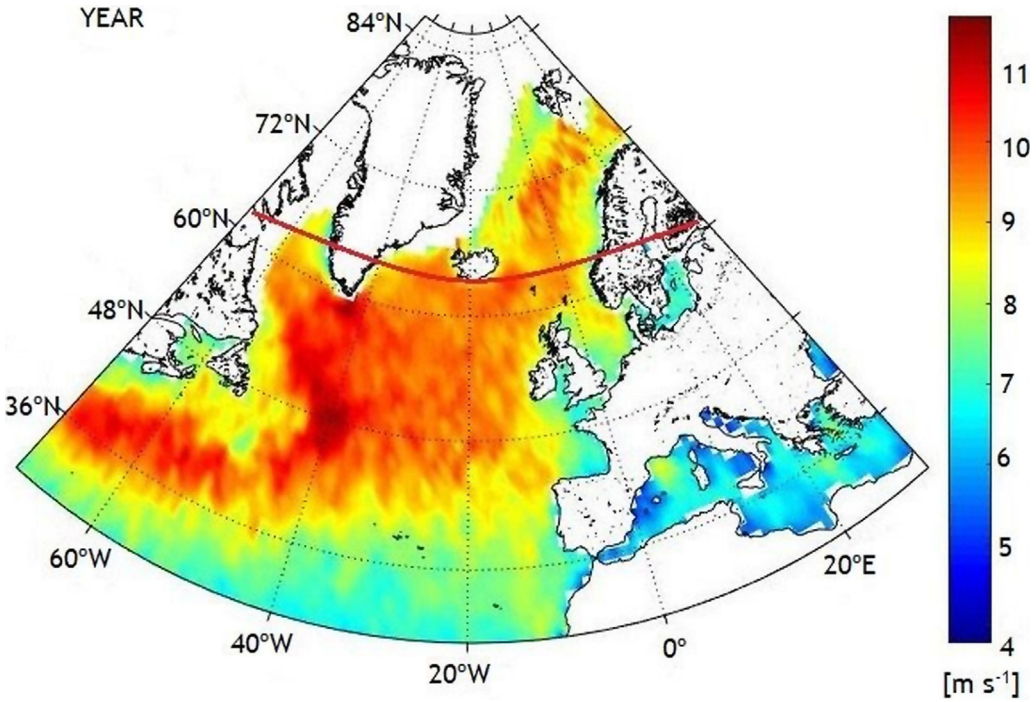

Figure 2 Annual mean wind speed U_{10} [m s^{-1}] in the study area — the North Atlantic and the European Arctic (north of the red line). (For interpretation of the references to color in this figure legend, the reader is referred to the web version of this article.)

were too high or too low for a given parameterization (Fig. 1). Results from those calculation are available online under the link in Ocean Science Discussion https://www.ocean-sci-discuss.net/os-2018-61/.

Since wind velocity was used to estimate C_D, Fig. 1 shows a wide range of empirical formulas and Fig. 2 shows annual mean wind speed U_{10} [m s^{-1}] in the NA and the EA. The differences between the parameterizations are distinct (Fig. 1). The C_D values from the parameterizations 7–9 (Table 1) increased linearly with wind speed while the results from the parameterizations 10, 12, 13 (Table 1) decreased at low winds speed (for $U_{10} < 10$ m s^{-1}). Despite many measurements, the drag coefficient still has wide variability at low and moderate wind speeds. Our results showed that at lower wind values (<10 m s^{-1}) the differences between the drag coefficient parameterizations are greater than at higher speeds (>10 m s^{-1}) and the most outlier results are those obtained from the power law parameterization of A12. The lower the wind speed, the higher the uncertainty are, and at low winds it is uncertainty by a factor of 0.5–1.5 depending on the formula used, while at moderate winds it is uncertainty by a factor of 1.5–2.0 (Fig. 1). At a wind value of about 15 m s^{-1}, the results from Eqs. (8), (9) and (13) (Table 1) overlapped providing the same values for the drag coefficient parameterizations. Additionally, we compared directly the results of the two parameterizations for the drag air-sea relation that uses different dependencies (Fig. 1). For this estimation we chose the two most-recent parameterizations (Eqs. (12) and (13) in Table 1) that showed the lowest values and change seasonally depending on the area used. As a result, these months with weak winds have significantly lower momentum flux values, which could be the effect of statistically weaker wind in ocean areas having stable winds with waves travelling in the same direction as the wind at similar speeds. Comparison showed that the A12 parameterization demonstrates almost zero sea surface drag for winds in the range of 3–5 m s^{-1}, which is compensated for by a certain surplus value for strong winds. The small drag coefficient values facilitate what Grachev and Fairall (2001) describe as the transfer of momentum from the ocean to the atmosphere at wind speeds of 2–4 m s^{-1}, which correspond to the negative drag coefficient value. Such events require specific meteorologist conditions, but this strongly suggests that the average C_D value for similar wind speeds could be close to zero. The annual mean wind speed in the NA is 10 m s^{-1}, and in the EA it is 8.5 m s^{-1} (Fig. 2).

Fig. 3 presents maps of the mean boreal winter DJF and summer JJA momentum fluxes for the chosen C_D parameterizations (Wu, 1969 and A12 – the ones with the largest and smallest C_D values). The supplementary materials contain complete maps of annual and seasonal means for all the parameterizations. The zones of the strongest winds are in the extra-tropics in the winter hemisphere (southern for JJA and northern for DJF). The older Wu (1969) parameterization produces higher wind stress values than A12 in both regions with high and low winds and C_D values are consistently higher for all wind speeds except the lowest ones (which, after multiplying by U^2, produced negligible differences in wind

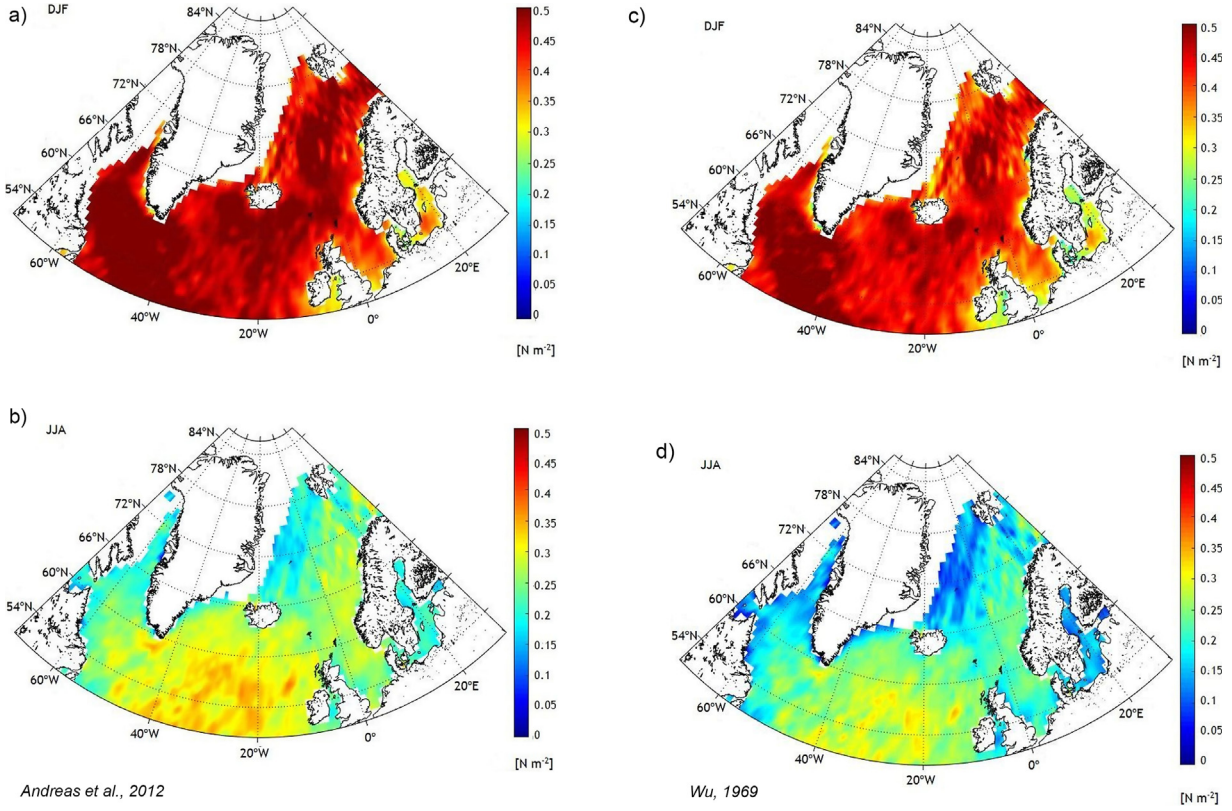

Figure 3 Maps of momentum flux [N m^{-2}] across the sea surface (wind stress) for boreal winters (a and c) and summers (b and d) for Wu (1969) and A12 drag coefficient parameterizations (the two parameterizations with the highest and lowest average values, respectively).

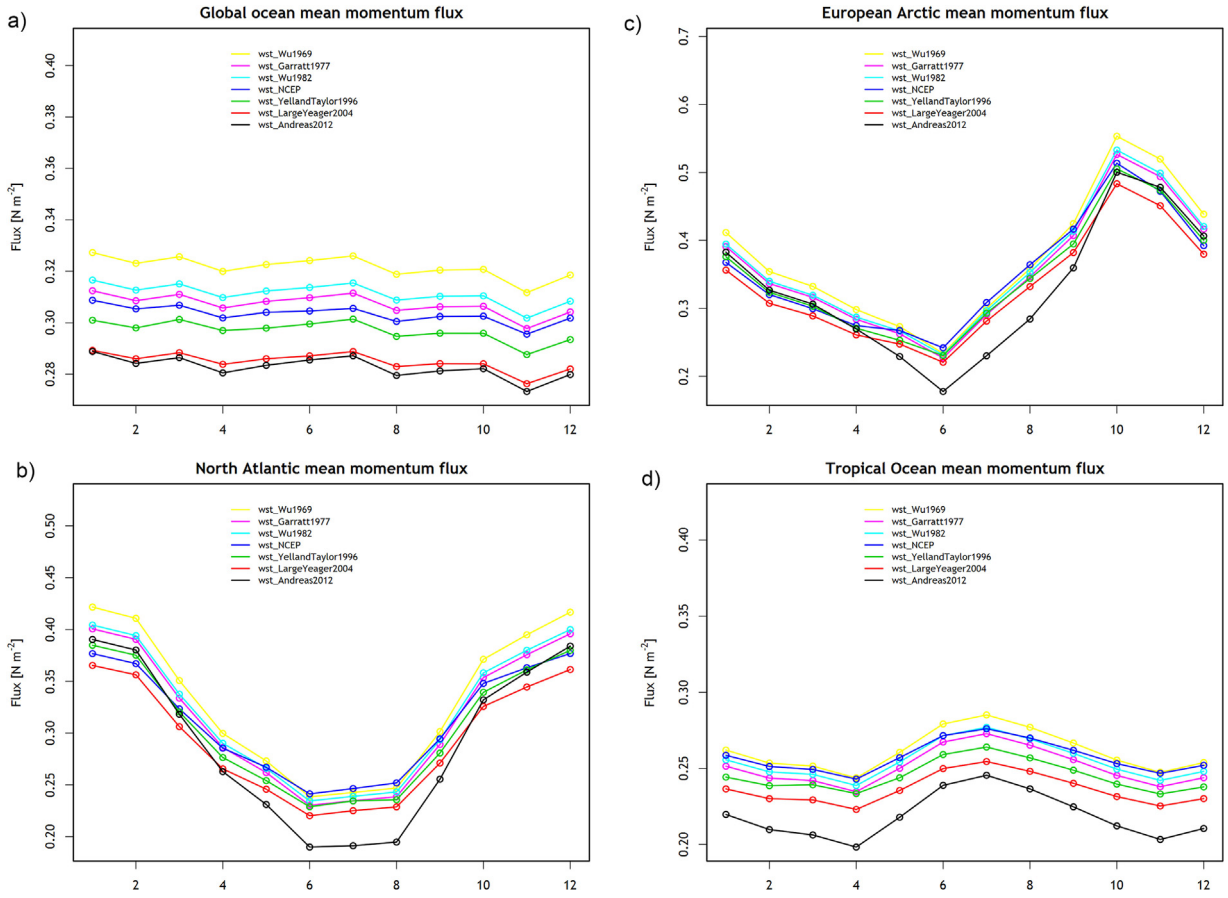

Figure 4 Monthly average momentum flux values [N m^{-2}] for (a) global ocean, (b) North Atlantic, (c) European Arctic, and (d) tropical ocean. The regions are defined in the text.

stress for the lowest winds). The average monthly values for each of the studied areas are shown in Fig. 4. For global data (Fig. 4a), not much seasonal change is noted, because the strongest winds are in fall and winter, but these seasons are the opposite in the northern and southern hemispheres. The parameterization with the largest momentum flux values for all months is that of Wu (1969), the linear one, while the two parameterizations with the lowest values are the sinusoidal

Table 2 Area average annual mean values of momentum flux (wind stress) [N m^{-2}] for all the studied regions and parameterizations. In each column the percentage values are normalized to A12, the parameterization that produced the smallest average flux values.

	Global	North Atlantic	Arctic	W. Spitsbergen	Tropics
Wu (1969)	0.322 (114%)	0.330 (114%)	0.375 (114%)	0.360 (114%)	0.261 (119%)
Garratt (1977)	0.307 (109%)	0.316 (109%)	0.358 (109%)	0.344 (110%)	0.251 (115%)
Wu (1982)	0.311 (110%)	0.320 (110%)	0.363 (110%)	0.349 (111%)	0.255 (117%)
NCEP/NCAR	0.303 (107%)	0.312 (107%)	0.353 (107%)	0.341 (108%)	0.258 (118%)
Yelland and Taylor (1996)	0.297 (105%)	0.306 (105%)	0.348 (106%)	0.335 (107%)	0.245 (112%)
Large and Yeager (2004)	0.285 (101%)	0.293 (101%)	0.333 (101%)	0.320 (102%)	0.236 (108%)
Andreas et al. (2012)	0.283 (100%)	0.290 (100%)	0.329 (100%)	0.314 (100%)	0.219 (100%)

ones (A12; Large and Yeager, 2004). For the NA (Fig. 4b), much more pronounced seasonal wind changes, the situation is more complicated. With high winter winds, the A12 parameterization is no longer the one that produces the smallest wind stress (it is actually in the middle of the seven). However, for low summer winds, it is the lowermost outlier. Actually, in summer, the constant C_D value used by the NCEP/NCAR reanalysis produces the highest wind stress values in the NA. The situation is similar for the EA (a subset of the NA), the wind stress values of which are shown in Fig. 4c, and for the WS area (not shown). In the Arctic summer, A12 produces the least wind stresses, while all the other parameterizations look very similar qualitatively (even more so in the Arctic than in the whole NA). Because the A12 parameterization behaves so distinctly differently with low winds, we also show seasonal results for the tropical ocean (Fig. 4d). The seasonal changes are subdued for the whole tropical ocean with the slight domination of the Southern Hemisphere (the strongest winds are during the boreal summer) with generally lower momentum transfer values (monthly averages in the range of 0.2—0.3 N m^{-2} compared to 0.2—0.4 N m^{-2} for the NA and 0.2—0.5 N m^{-2} for the Arctic). The sequence of values for the parameterization is similar to that of the global ocean, but there are differences. Here the NCEP/NCAR constant

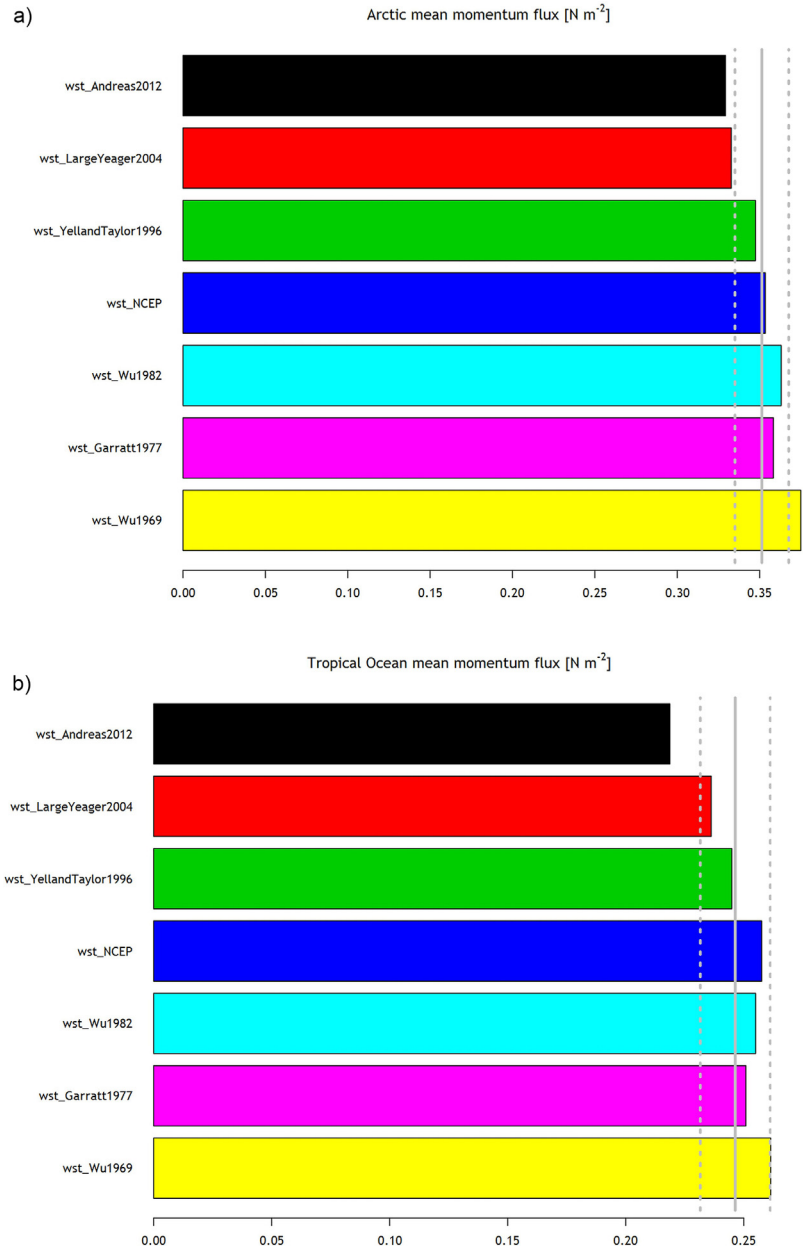

Figure 5 Area annual average momentum flux values for (a) European Arctic and (b) Tropical ocean. The vertical solid line is the average of all seven parameterization and the dashed lines are standard deviations for the presented values. Global and the North Atlantic results are not shown because the relative values for different parameterizations are very similar (see Table 2), scaling almost identically between the basins.

parameterization is the second highest (instead of Wu, 1982 for the global ocean) while, unlike in the case of the global ocean, A12 produces visibly lower values than does the Large and Yeager (2004) parameterization.

Table 2 and Fig. 5 present the annual average air-sea momentum flux values (in N m^{-2}) for all the regions studied and all the parameterizations. The results show that the annual North Atlantic momentum fluxes, depending on the formula used, varies from −0.290 N m^{-2} for A12 to 0.333 N m^{-2} for Wu (1969). In the case of global annual average, the values are −0.283 and 0.322, respectively. Table 2 shows also the same data "normalized" to the A12 data (presented as percentages of A12, which produced the lowest values for each region), which allows us to visualize the relative differences. A surprising result is the annual ratios of the parameterizations values for the global, the NA, and the Arctic regions (Fig. 4 shows that this is not true on monthly scales). The spread of the momentum flux results is 14% in all three regions, and even flux values themselves are larger in the NA than globally and larger in the Arctic than in the whole of the NA basin. In the NA region with winds stronger than average for world ocean, the formula giving highest momentum transfer results are the ones with highest values for strong winds, with exception of Andreas et al. (2012) which is lower due to its low values for lower winds speeds. The smaller WS region, with winds that are, on average, weaker than those of the whole Arctic (but stronger than those of the whole NA), had slightly different ratios of the resultant fluxes. For the tropical ocean, which is included for comparison because of its weaker winds, the spread in momentum flux values on an annual scale is 19%. The spreads are even larger on monthly scales (not shown). The difference between A12 and Wu (1969) and NCEP/NCAR (the two parameterizations producing the largest fluxes on monthly scales) are 27% and 29% for the NA (in July), 31% and 36% for the Arctic (in June), 42% and 51% for the WS region (in July), and 23% and 22% for the tropical ocean (in April), respectively. Seasonality in the tropics is weak, therefore, the smallest monthly difference of 16% (July) is larger than the difference for the global data in any month (the global differences between the parameterizations have practically no seasonality). On the other hand, the smallest monthly differences between the parameterizations in the NA, the Arctic, and the WS regions are all 7%, in the month of the strongest winds (January).

Because the value of momentum flux is important for ocean circulation, its correct calculation in coupled models is very important, especially in the Arctic, where cold halocline stratification depends on the amount of mixing (Fer, 2009). We show that with the parameterization used in modelling, such as the NCEP/NCAR constant parameterization and Large and Yeager (2004), production stress results differ by about 5%, on average (both in the Arctic and globally), and the whole range of parameterizations leads to results that differ, on average, by 14% (more in low wind areas) and much more on monthly scales. One aspect that needs more research is the fact that the newest parameterization, A12, produces less momentum flux than all the previous ones, especially in lower winds (which, by the way, continues the trend of decreasing values throughout the history of the formulas discussed). The A12 parameterization is based on the largest set of measurements of friction velocity as a function of wind speed and utilizes the recently discovered fact that b in equation (6) is not negligible. It also fits the observations that developed swell at low wind velocity has celerity which leads to zero or even negative momentum transfer (Grachev and Fairall, 2001). Therefore, the significantly lower A12 results for the tropical ocean (the trade wind region) and months of low winds elsewhere could mean that most momentum transfer calculations are overestimated. This matter needs further study, preferably with new empirical datasets. Based on our results, we still do not know which one of the parameterizations can be recommended as the most suitable for the NA and the EU study. Further investigation of the differences in the parameterization of the exchange coefficient in the various algorithm would help in resolving this problem.

4. Conclusions

In the present work, we assessed how the choice of parameterization affects the momentum fluxes when calculated on an ocean. This allows constraining of the uncertainty caused by the parameterization choice.

Despite many measurements, the drag coefficient still has wide variability at low and moderate wind speeds. The lower the wind speed, the higher the uncertainty are, and at low winds it is uncertainty by a factor of 0.5–1.5 depending on the formula used, while at moderate winds it is uncertainty by a factor of 1.5–2.0 (Fig. 1). The annual mean wind speed in the NA is 10 m s^{-1}, and in the EU it is 8.5 m s^{-1}.

We showed that the choice of drag coefficient parameterization can lead to significant differences in resultant momentum flux (or wind stress) values. Comparing the values of momentum flux across the sea surface from the power law parameterization, it showed that in both regions with low and high winds, the parameterizations specified for all wind speeds (Eq. (13) in Table 1) has lower values of wind stress than the parameterizations specified for light winds (Eq. (7) in Table 1). In the Arctic, the NA, and globally the differences between the wind stress, depending on formula used, are 14% and they are higher in low winds areas and can be much larger on monthly scales, up to 29% in the NA and 36% in the EA (in months of low winds), and even 50% locally in the area west of Spitsbergen. For months that have the highest average winds, the percentage differences are smaller (about 7% everywhere), but because the absolute value of the flux are largest for high winds, this 7% discrepancy is also important for air-sea momentum flux values.

Acknowledgements

We would like to express our gratitude to Ed Andreas for inspiring us. His untimely departure is an irreplaceable loss to the air-sea exchange community.We would also like to thank the entire OceanFlux team. This publication was financed with funds from the Centre for Polar Studies for the period 2014-2018, KNOW-Leading National Research Centre, Sosnowiec, Poland and from OceanFlux Greenhouse Gases Evolution, a project funded by the European Space Agency, ESRIN Contract No. 4000112091/14/I-LG with the help from National Science Centre funds, contract no. UMO-2016/21/N/ST10/00387.

Appendix A. Supplementary data

Supplementary data associated with this article can be found, in the online version, at doi:10.1016/j.oceano.2019.02.002.

References

Andreas, E.L., Mahrt, L., Vickers, D., 2012. A new drag relation for aerodynamically rough flow over the Ocean. J. Atmos. Sci. 69 (8), 2520–2539, http://dx.doi.org/10.1175/JAS-D-11-0312.1.

Bigdeli, A., Loose, B., Nquyen, A.T., Cole, S.T., 2017. Numerical investigation of the Arctic ice-ocean boundary layer and implications for air-sea gas fluxes. Ocean Sci. 13 (1), 61–75, http://dx.doi.org/10.5194/os-13-61-2017.

Bryant, K.M., Akbar, M., 2016. An exploration of wind stress calculation techniques in hurricane storm surge modeling. J. Mar. Sci. Eng. 4 (3), 58–83, http://dx.doi.org/10.3390/jmse4030058.

Bunker, A.F., 1976. Computations of surface energy flux and annual air-sea interaction cycles of the North Atlantic. Ocean Mon. Weather Rev. 104 (9), 1122–1140, http://dx.doi.org/10.1175/1520-0493(1976)104<1122:COSEFA>2.0.CO;2.

Charnock, H., 1955. Wind stress on a water surface. Q. J. Roy. Meteorol. Soc. 81, 639–640, http://dx.doi.org/10.1002/qj.49708135027.

Chelton, D.B., Freilich, M.H., 2005. Scatterometer-based assessment of 10-m wind analyses from the operational ECMWF and NCEP numerical weather prediction models. MWR Mon. Weather Rev. 133, 409–429.

Collins, W.D., Bitz, C.M., Blackmon, M.L., Bonan, G.B., Bretherton, S.C., Carton, A.J., Chang, P., Doney, S.C., Hack, J., Henderson, T. B., Kiehl, J.T., Large, W.G., McKenna, D.S., Santer, B.D., Smith, R.D., 2006. The Community Climate System Model version 3 (CCSM3). J. Climate 19 (11), 2122–2143, http://dx.doi.org/10.1175/JCLI3761.1.

Donelan, M.A., Drennan, W.M., Katsaros, K.B., 1997. The air-sea momentum flux in conditions of wind sea and swell. J. Phys. Oceanogr. 27 (10), 2087–2099, http://dx.doi.org/10.1175/1520-0485(1997)027<2087:TASMFI>2.0.CO;2.

Dukhovskoy, D.S., Bourassa, M.A., Peterson, G.N., Steffen, J., 2017. Comparison of the surface vector winds from atmospheric reanalysis and scatterometer-based wind products over the Nordic Seas and the northern North Atlantic and their application for ocean modeling. J. Geophys. Res. - Oceans 122, 1943–1973, http://dx.doi.org/10.1002/2016JC012453.

Enriquez, A.G., Friehe, C.A., 1997. Bulk parameterization of momentum, heat, and moisture fluxes over a coastal upwelling area. J. Geophys. Res. - Oceans 102 (C3), 5781–5798, http://dx.doi.org/10.1029/96JC02952.

Fer, I., 2009. Weak vertical diffusion allows maintenance of cold halocline in the central Arctic. Atmos. Oceanic Sci. Lett. 2 (3), 148–152, http://dx.doi.org/10.1080/16742834.2009.11446789.

Foreman, R.J., Emeis, S., 2010. Revisiting the definition of the drag coefficient in the marine atmospheric boundary layer. J. Phys. Oceanogr. 40, http://dx.doi.org/10.1175/2010JPO4420.1.

Garratt, J.R., 1977. Review of drag coefficients over oceans and continents. Mon. Weather Rev. 105 (7), 915–929, http://dx.doi.org/10.1175/1520-0493(1977)105<0915:RODCOO>2.0.CO;2.

Geernaert, G.L., 1990. Bulk parameterizations for the wind stress and heat flux. In: Geernaert, G.L., Plant, W.L. (Eds.), Surface Waves and Fluxes, vol. I. Kluwer, 91–172.

Geernaert, G.L., Katsoros, K.B., Richter, K., 1986. Variation of the drag coefficient and its dependence on sea state. J. Geophys. Res. 91 (C6), 7667–7679, http://dx.doi.org/10.1029/JC091iC06p07667.

Geernaert, G.L., Larsen, S.E., Hansen, F., 1987. Measurements of the wind stress, heat flux, and turbulence intensity during storm conditions over the North Sea. J. Geophys. Res. - Oceans 92 (C13), 13127–13139, http://dx.doi.org/10.1029/JC092iC12p13127.

Gerbi, G.P., Trowbridge, J.H., Edson, J.B., Plueddemann, A.J., Terray, E.A., Fredericks, J.J., 2008. Measurements of momentum and heat transfer across the air-sea interface. J. Phys. Oceanogr. 38 (5), 1054–1072, http://dx.doi.org/10.1175/2007JPO3739.1.

Grachev, A.A., Fairall, C.W., 2001. Upward momentum transfer in the marine boundary layer. J. Phys. Oceanogr. 31 (7), 1698–1711.

Guan, C., Xie, L., 2004. On the linear parameterization of drag coefficient over sea surface. J. Phys. Oceanogr. 34 (12), 2847–2851, http://dx.doi.org/10.1175/JPO2664.1.

Kalnay, E., Kanamitsu, M., Kistler, R., Collins, W., Daeven, D., Gandin, L., Iredell, M., Saha, S., White, G., Woollen, J., Zhu, Y., Chelliah, M., Ebisuzaki, W., Higgins, W., Janowiak, J., Mo, K. C., Ropelewski, C., Wang, J., Leetmaa, A., Reynolds, R., Jenne, R., Joseph, D., 1996. The NCEP/NCAR 40-year reanalysis project. Bull. Am. Meteor Soc. 77 (3), 437–471.

Kukulka, T., Hara, T., Belcher, S.E., 2007. A model of the air-sea momentum flux and breaking-wave distribution for strongly forced wind waves. J. Phys. Oceanogr. 37 (7), 1811–1828, http://dx.doi.org/10.1175/JPO3084.1.

Large, W.G., Pond, S., 1981. Open ocean momentum flux measurements in moderate to strong winds. J. Phys. Oceanogr. 11 (3), 324–336, http://dx.doi.org/10.1174/1520-0485(1981)011<0324:OOMFMI>2.0.CO;2.

Large, W.G., Yeager, S.G., 2004. Diurnal to decadal global forcing for ocean and sea-ice models: the data sets and flux climatologies. Technical Note NCAR/TN-460+STR. NCAR, Boulder, CO.

Lüpkes, C., Gryanik, V.M., Hartmann, J., Andreas, E.L., 2012. A parameterization, based on sea-ice morphology, of the neutral atmospheric drag coefficients for weather prediction and climate models. J. Geophys. Res. - Atmos. 117 (D13), http://dx.doi.org/10.1029/2012JD01763.

Rieder, K.F., Smith, J.K., Weller, R.A., 1994. Observed directional characteristics of the wind, wind stress, and surface waves on the open ocean. J. Geophys. Res. - Oceans 99 (C11), 589–596, http://dx.doi.org/10.1029/94JC02215.

Shutler, J.D., Piolle, J.-F., Land, P.E., Woolf, D.K., Goddijn-Murphy, L., Paul, F., Girard-Ardhuin, F., Chapron, B., Donlon, C.J., 2016. FluxEngine: a flexible processing system for calculating air-sea carbon dioxide gas fluxes and climatologies. J. Atmos. Ocean. Technol. 33 (4), 741–756, http://dx.doi.org/10.1175/JTECH-D-14-00204.1.

Taylor, G.I., 1916. Skin friction of the wind on the Earth's surface. Proc. Roy. Soc. London A92, 196–199.

Toba, Y., Smith, S.D., Ebuchi, N., 2001. Historical drag expressions. In: Jones, I.S.F., Toba, Y. (Eds.), Wind Stress Over the Ocean. Cambridge Univ. Press, New York, 35–53.

Trenberth, K.E., Large, W.G., Olson, J.G., 1989. The effective drag coefficient for evaluating wind stress over the Oceans. J. Climate 2 (12), 1507–1516, https://www.jstor.org/stable/26196243.

Wu, J., 1969. Wind stress and surface roughness at air-sea interface. J. Geophys. Res. 74 (2), 444–455, http://dx.doi.org/10.1029/JB074i002p00444.

Wu, J., 1980. Wind stress coefficients over the sea surface near neutral conditions — a revisit. J. Phys. Oceanogr. 10 (5), 727–740, http://dx.doi.org/10.1175/1520-0485(1980)010<0727:WSCOSS>2.0.CO;2.

Wu, J., 1982. Wind-stress coefficients over sea surface from breeze to hurricane. J. Geophys. Res. 87 (C12), 9704–9706, http://dx.doi.org/10.1029/JC087iC12p09704.

Yelland, M., Taylor, P.K., 1996. Wind stress measurements from the open ocean. J. Phys. Oceanogr. 26 (4), 541–558, http://dx.doi.org/10.1175/1520-0485(1996)026<0541:WSMFTO>2.0.CO;2.

Oceanologia (2019) 61, 300—307

Available online at www.sciencedirect.com

ScienceDirect

journal homepage: www.journals.elsevier.com/oceanologia/

ORIGINAL RESEARCH ARTICLE

"Noise" in climatologically driven ocean models with different grid resolution

Shengquan Tang [a,b], Hans von Storch [b,a,*], Xueen Chen [a], Meng Zhang [b]

[a] College of Oceanic and Atmospheric Sciences, Ocean University of China, Qingdao, China
[b] Institute of Coastal Research, Helmholtz-Zentrum Geesthacht, Geesthacht, Germany

Received 26 July 2018; accepted 11 January 2019
Available online 28 January 2019

KEYWORDS
"Noise";
Internal variability;
South China Sea;
Eddies;
Model resolution

Summary The internally generated variability in the climate system, which is unrelated to any external factors, can be conceptualized as "noise". This noise is a constitutive element of high-dimensional nonlinear models of such systems. In a three-layer nested simulation, which is forced by climatological (periodic) atmospheric forcing and includes an (almost) global model, a West-Pacific model, and South China Sea (SCS) model, we demonstrate that such "noise" builds also ocean models. They generate variability by themselves without an external forcing. The "noise" generation intensifies with higher resolution, which favors macroturbulence.

1. Introduction

The climate system is a high-dimensional macroturbulent system, which features many nonlinear processes. Based on the concept of the "stochastic climate model" (Hasselmann, 1976) the trajectory of the climate system can be described as that of an inert system subject to internally generated variations, which may be conceptualized as "noise". Here, we use the term "noise" to refer to variability which cannot be traced back to external "drivers". Instead, the variability is generated internally.

The net-effect of very many degrees of freedom interacting through many non-linearities is the creation of variability, which is well described by the mathematical construct of random processes. If this variability is really stochastic, or, in other words: if God is really rolling a dice, is irrelevant, as we cannot disentangle the high-dimensional dynamics, but we find that the description as stochastic noise is doing the job.

Since macro-turbulence is an inherent part of the dynamics of the climate system then such "noise" should be present also in such models. Without such "noise", the climate system will be incompletely described and may lack

* Corresponding author at: Institute of Coastal Research, Helmholtz Zentrum Geesthacht, Geesthacht, 21502, Germany.
Tel.: +49 40 4192 4472; fax: +49 (0)41 52 87-1403.
E-mail address: hvonstorch@web.de (H. von Storch).
Peer review under the responsibility of Institute of Oceanology of the Polish Academy of Sciences.

Production and hosting by Elsevier

https://doi.org/10.1016/j.oceano.2019.01.001

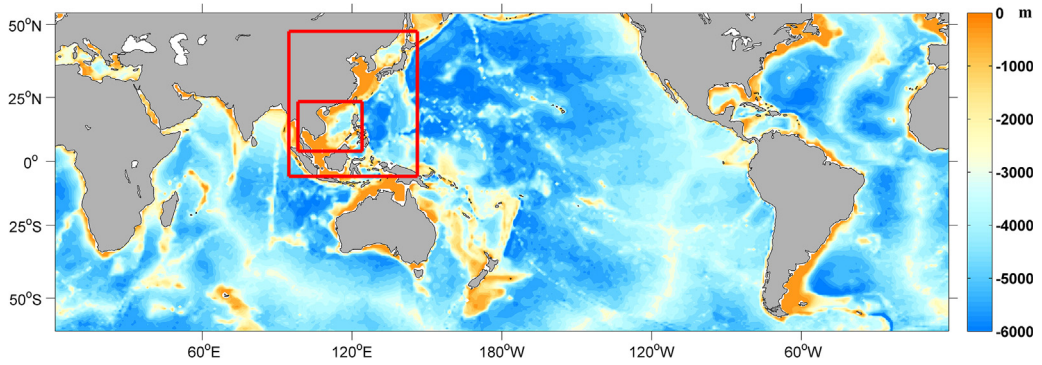

Figure 1 The regions of the three-layer nested simulation, which includes an (almost) global model, a West-Pacific model, and a South China Sea (SCS) model.

significant features. Therefore, the recognition of the "noise" is helpful for scientists to explore the climate dynamics and modeling.

"Noise" represents for certain issues a nuisance (hiding real effects, as for instance when deriving eddy statistics from satellite data) but is also constitutive for the dynamical properties of the climate system (von Storch et al., 2001). "Noise", i.e., unprovoked, internal variability, has significant implications for issues like "detection and attribution of climate change" (Hasselmann, 1993) and for numerical experimentation with climate models (Chervin and Schneider, 1976; Weisse et al., 2000).

Since the nonlinear high-dimensional ocean system is part of the climate system, we suggest that the ocean system should also generate significant "noise", which is unrelated to any external factors (atmospheric forcing, lateral boundary conditions, and so on). Moreover, since "noise" takes place in climate models describing macro-turbulence, we suggest that the formation of "noise" in the ocean model may intensify with ocean model resolution increasing.

Some may find our suggestion about noise in ocean models almost trivial; indeed, in the framework of the stochastic climate model, it is mostly so. However, most climate modelers hardly know about the stochastic climate model, and it seems that many climate scientists are not aware of this unprovoked variability. There seem to be quarter in the climate science community, where efforts are made to find "explanations" for whatever what appears as not normal, but which may be simply the effect of this internal variability.

In the present study, we use a three-layer nested numerical simulation, which is subject to climatological atmospheric forcing, to test our hypothesis. The concerned region in this study is the South China Sea (SCS). The existing and intensity of "noise" in the SCS will be discussed in the framework of this three-layer nested simulation. The model resolutions change from coarse to fine, so the "noise" generation is conditioned by different model resolution.

The present paper is organized as follows. A brief introduction the simulation setup is given in Section 2. The results of the simulation and "noise" in the simulation are presented in Section 3. Conclusions are summarized in Section 4.

The subject of this paper is not finding out how well the simulations of the dynamics of the SCS are reproducing observed features. Such studies have been plentiful (e.g., Wang et al., 2006; Zhang and von Storch, 2016), but the issue dealt with here is merely the conceptual issue of "noise" generation.

Table 1 Spatial averages of the daily BS variances and SSH variances in the SCS simulated by the three models.

	BS variance [Sv^2]			SSH variance [m^2]		
Model	Global	WP	SCS	Global	WP	SCS
Spring	0.5539	0.6141	1.1015	0.0004	0.0004	0.0005
Summer	1.0083	1.3374	2.2178	0.0010	0.0010	0.0012
Autumn	0.4382	0.6262	1.1739	0.0004	0.0004	0.0005
Winter	1.1281	1.3245	1.6055	0.0010	0.0009	0.0011

2. Simulation setup

The ocean model used in this study is the Hybrid Coordinate Ocean Model (HYCOM). The HYCOM used in this study is a primitive equation ocean general circulation model. Its vertical coordinates are isopycnic in the open, stratified ocean, but smoothly change to z coordinates in the weakly stratified upper-ocean mixed layer, and change to terrain-following sigma coordinate in shallow water regions, and back to z-level coordinates in very shallow water (Bleck, 2002). The vertical mixing schemes chosen in this paper is the K-Profile Parameterization (KPP) scheme (Large et al., 1994). The KPP scheme provides mixing throughout the water column with an abrupt but smooth transition between the vigorous mixing in the surface boundary and the relatively weak diapycnal mixing in the ocean interior.

A three-layer nested numerical simulation in HYCOM is performed, with an almost global model (60°S–54°N, 180°W–180°E) with 1° grid resolution, an embedded West-Pacific (WP) model (6°S–48°N, 95°E–146°E) with 0.2° grid resolution, an embedded South China Sea (SCS) model (4°N–24°N, 98.4°E–124.4°E) with 0.04° grid resolution. The different integration regions are shown in Fig. 1.

The global model starts from the state of zero velocity and is run 50 model years. After 25 model years, the global model reaches a (cyclo) stationary state. The fields of last 25 model years in the global model are taken as the boundary forcing

fields for the WP model. The fields in the 26th year of the global model are taken as the initial state of the WP model, which is run for 25 years. After 2 model years, the WP model trajectory becomes stationary. The fields of last 23 model years in the WP model are taken as the boundary forcing fields for the SCS model. The fields in the 3rd year of the WP model are taken as the initial state of the SCS model, and the SCS model is run 23 model years. After 2 model years, the SCS model reaches stationary.

The nested simulation is exposed to periodic climatological atmospheric forcing, with a fixed annual cycle, and without weather variability. The atmospheric forcing, including the net shortwave longwave radiation, precipitation, air relative humidity, air temperature, sea surface temperature, and wind speed, are all from the monthly Comprehensive Ocean-Atmosphere Data Set (COADS) climatology with 1 grid resolution.

The daily average data of the last 21 year in these three models are used to study the "noise". The barotropic stream-

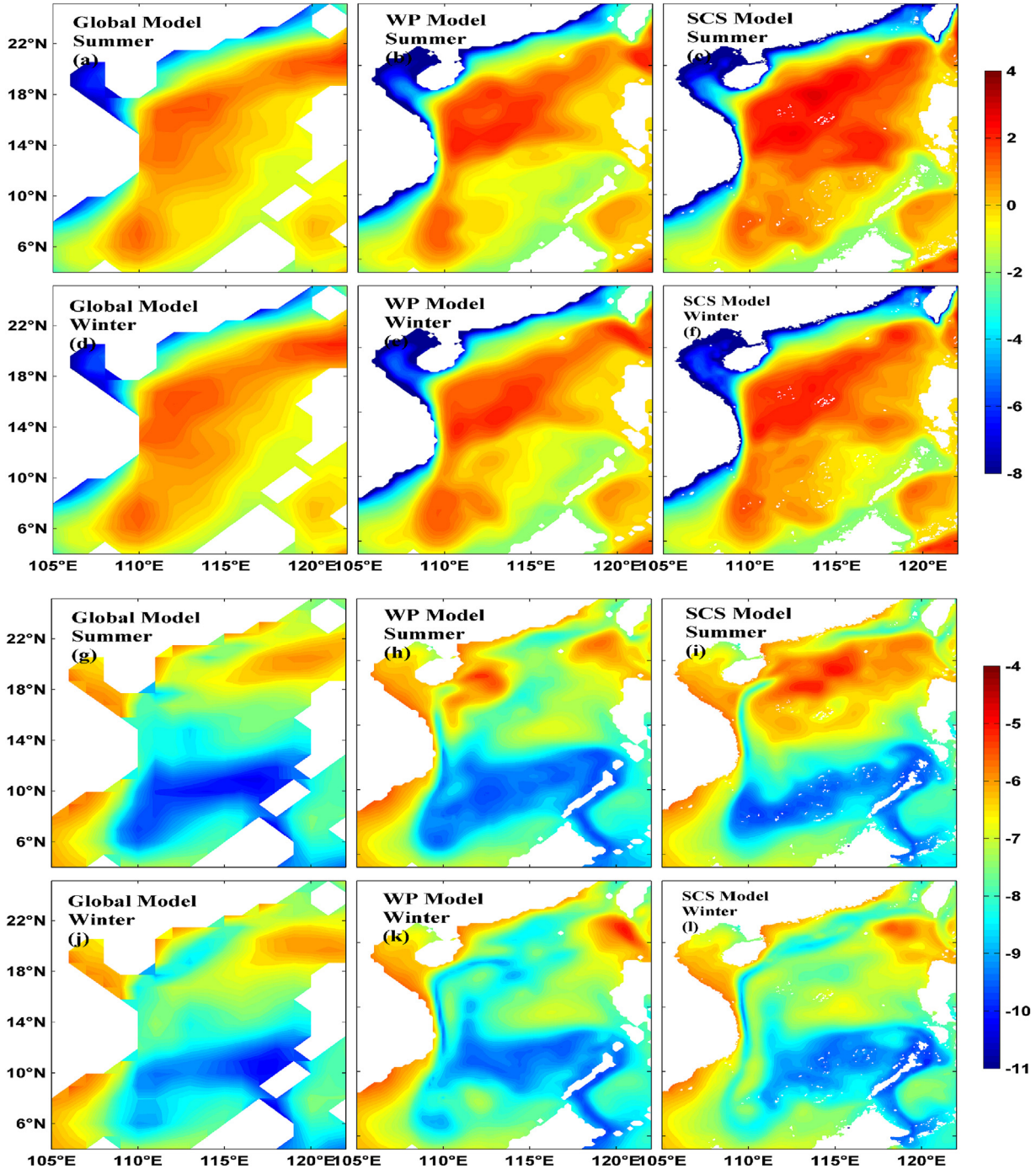

Figure 2 The spatial distributions of logarithm of daily variances of BS (top) and SSH (bottom) in the SCS simulated for summer and winter by the global model (a, d; g, j), the WP model (b, e; h, k) and the SCS model (c, f; i, l).

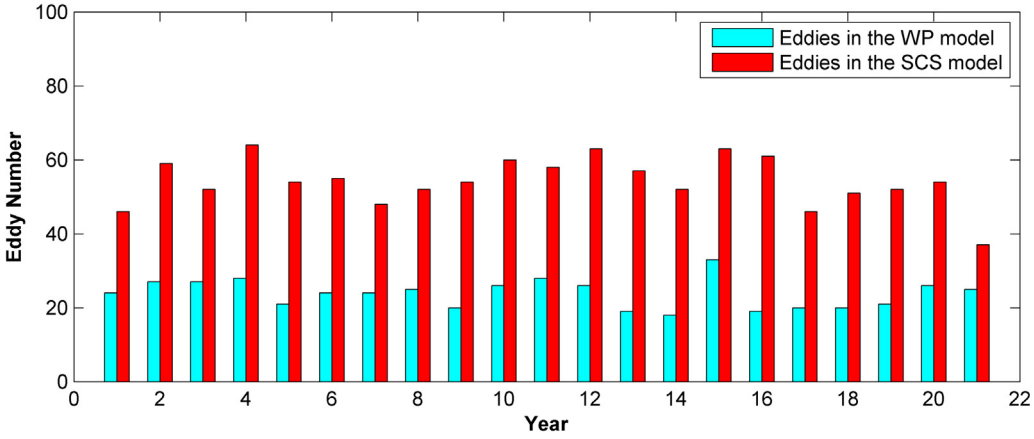

Figure 3 The annual number of eddy tracks in the WP simulation (blue bar) and in the SCS simulation (red bar).

function (BS) and sea surface height (SSH) simulated by these three models are discussed in this study.

3. Results

3.1. The amount of variability of BS and SSH in these three models

We measure the amount of variability by the variances of daily values at each grid point. The variance is calculated by subtracting the annual and semi-annual cycle. The annual and semi-annual cycle are fitted from the full-time series by harmonic analysis.

Table 1 lists variances of daily BS and SSH averaged across the SCS. The BS variances in the WP model are increased compared to the global model, and even larger variances can be found in the SCS model. The SSH variances in the WP model are approximately equal to that in the global model, and slightly larger variances are found in the SCS model.

The maps in Fig. 2 show the spatial distributions of the logarithm of BS variances and SSH variances in the SCS in two seasons (summer and winter monsoon) simulated by these three models (global, WP, and SCS). From the global model to the SCS model, with the model resolution increasing, the BS variances in the whole SCS strongly increase. In terms of SSH the changes are regionally different: While in the northern SCS, an increase from the global model to the SCS model is emerging, in the southern SCS, the differences are small. We suggest that the higher resolution model generates more or more intense eddies, which leads to intensified variability on all time scales (Hasselmann, 1976).

For comparing the eddies in the WP model and SCS model, we employed an eddy detection and tracking algorithm to search all eddies in the SCS. In order to compare, the SSH of the SCS model is interpolated from 0.04° resolution to 0.2° resolution. This algorithm only relies on the discrete SSHA (Zhang and von Storch, 2018). The potential eddy points are determined by the SSHA extrema in a moving 5×5 grid box according to the suggestion of Faghmous et al. (2015), with a relative intensity ≥ 5 mm. The relative intensity (RI) is defined by the absolute SSHA difference of the extrema and the mean SSHA of the other 24 neighbors in the box. The eddy centers at the consecutive time steps that are

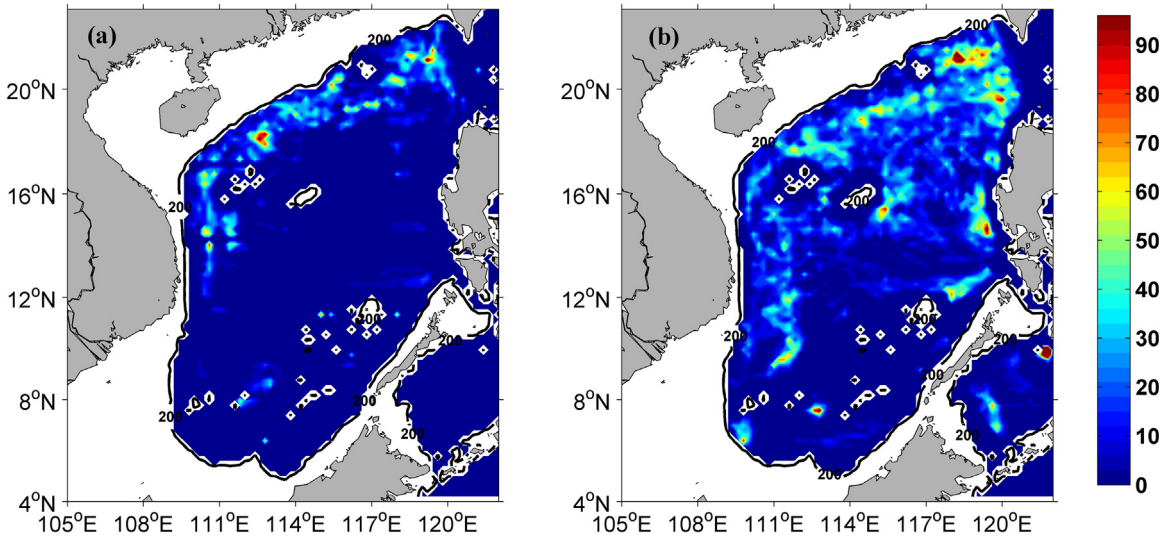

Figure 4 The total number of eddy occurrence for the 21 model years in the WP model (a) and SCS model (b). The units are the numbers of the eddy. The black lines indicate the 200 m isobaths.

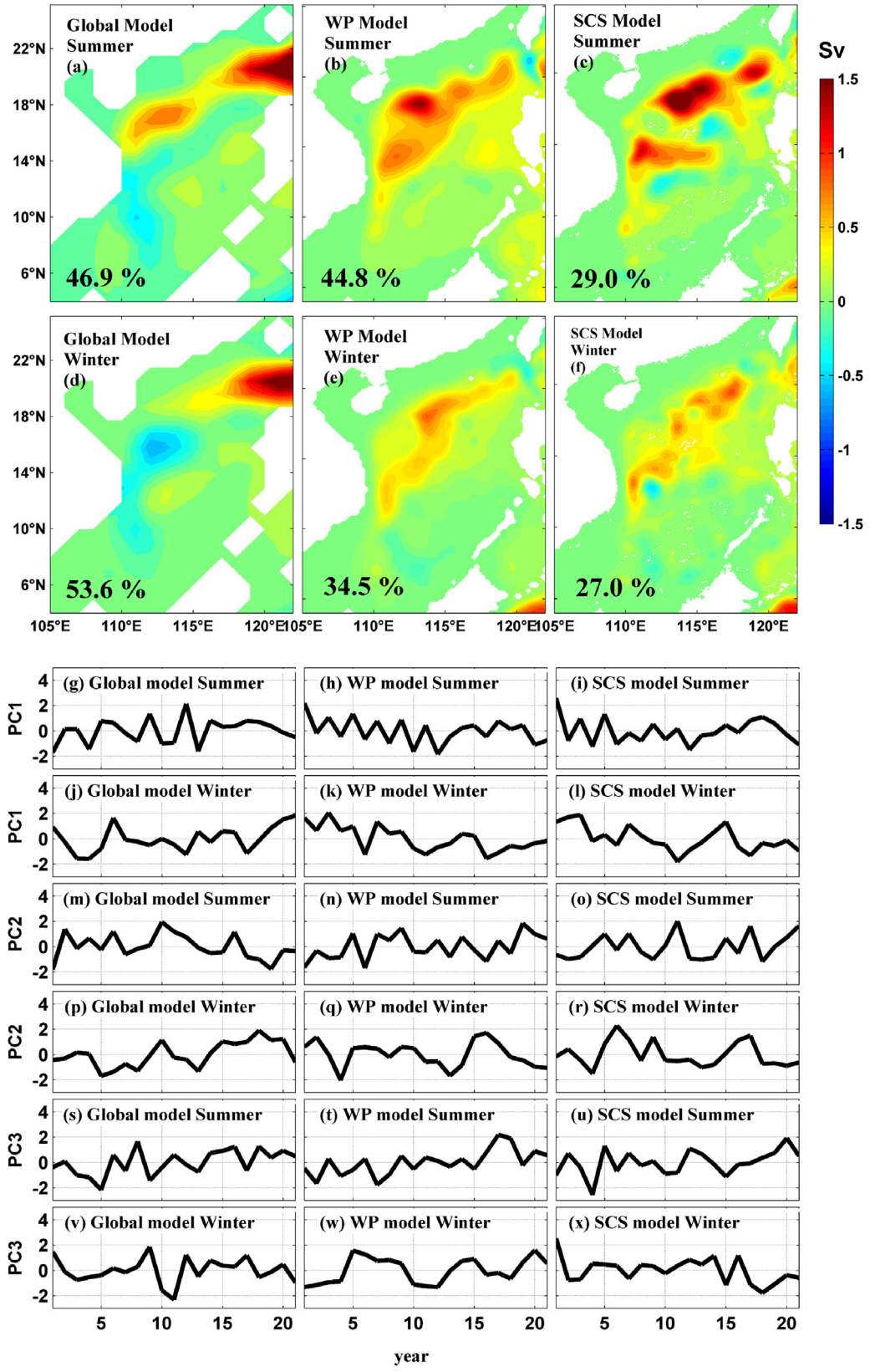

Figure 5 The first leading EOF patterns (in Sv) (a–f) and associated standardized principal component (PC1) (g–l) of the summer and of winter mean BS in the SCS. The PC2 (m–r) and PC3 (s–x) of BS in the SCS in summer and winter are from the three-layer nested simulation. The numbers in the bottom left corner of (a–f) indicate the percentages of variance described by the first leading EOF.

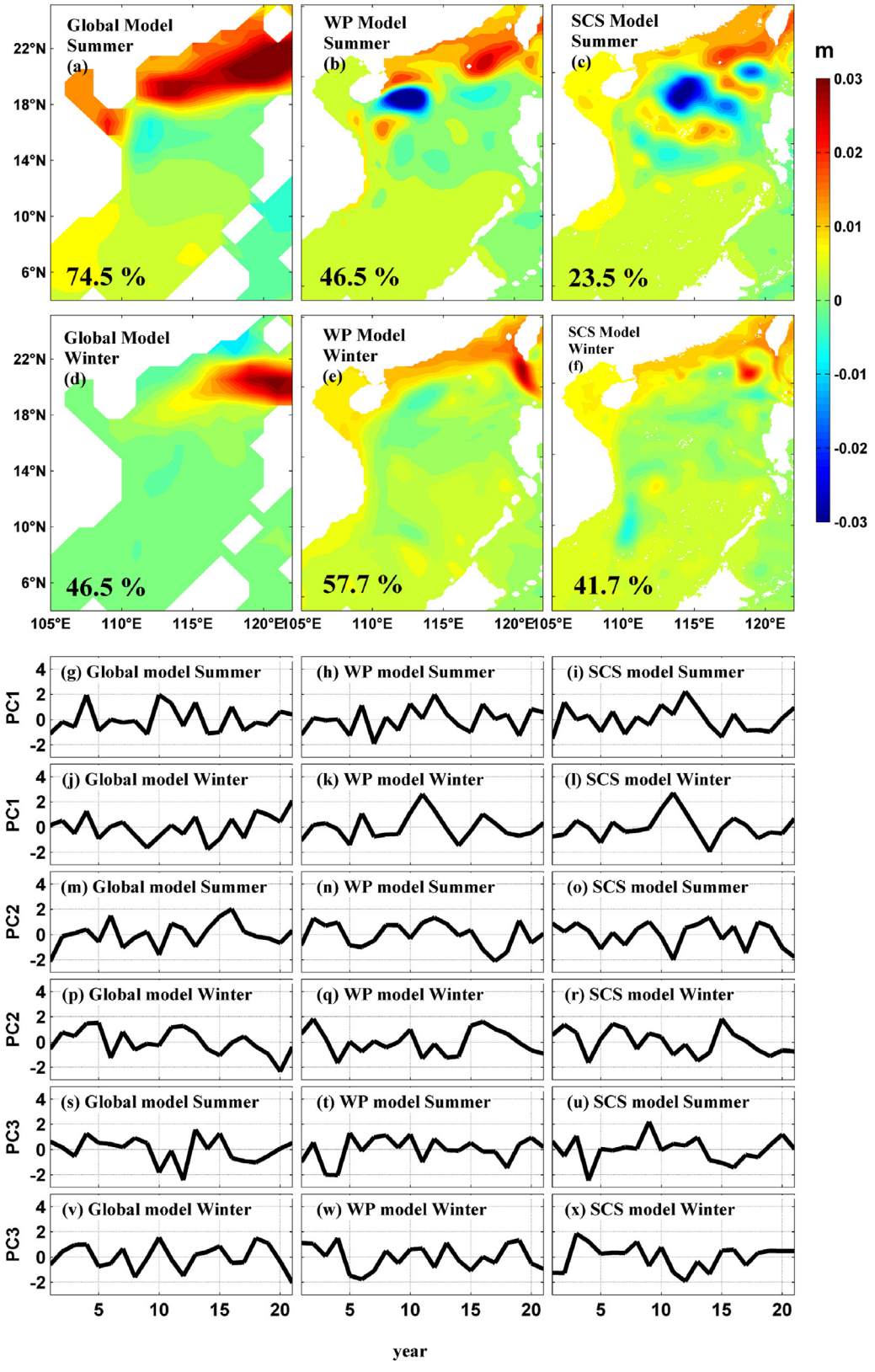

Figure 6 The first leading EOF patterns of SSH (in m) (a–f) and associated standardized principal component (PC1) (g–l) of SSH in the SCS in summer and winter from the three-layer nested simulation. The PC2 (m–r) and PC3 (s–x) of SSH in the SCS in summer and winter are from the three-layer nested simulation. The numbers in the bottom left corner of (a–f) indicate the percentages of variance described by the first leading EOF.

Table 2 Cumulative percentages of variance described by the first three EOFs of BS (left) and SSH (right) in the SCS.

	BS			SSH		
	Global model	WP model	SCS model	Global model	WP model	SCS model
Spring	84.5	81.3	56.6	85.7	80.9	57.8
Summer	74.3	75.3	53.3	90.5	67.7	52.8
Autumn	82.2	64.7	54.1	90.8	68.2	67.0
Winter	76.5	72.1	48.9	80.8	77.8	63.2

connected if their distance is $\leq$ 25 km (considering the eddy traveling speed $\leq$ 25 km per day) and the RI difference is $\leq$ 1.5 times of the RI in the previous time step. For the eddy tracks, the eddy should be tracked over at least 30 days.

Fig. 3 shows that the annual eddy track numbers generated by the WP model are in all years smaller than those found in the SCS model. The eddy tracks numbers are comparable to those found by Chen et al. (2011) in satellite data.

Fig. 4 shows the distribution of eddy occurrence for the 21 model years in the WP model and the SCS model, according to which the SCS model generates more eddies in the SCS, especially in the northern SCS.

We conclude that, since the atmosphere forcing of these three models is the same without any weather or interannual-variability, this increased variability in higher resolution models is internally generated by models.

3.2. Dominant modes of BS and SSH in these three models

Empirical Orthogonal Functions (EOF) decompose the time series of fields. A few orthogonal modes capture the main variability (Lorenz, 1956; von Storch and Zwiers, 1999). We apply the EOF decomposition to the BS and SSH fields in the South China Sea. The EOFs have been normalized so that the standard deviation of the time coefficients (principal component, PC) is 1 — so that the different intensity of the EOFs is given by the patterns.

Figs. 5 and 6 show the first leading EOF patterns and associated standardized principal component (PC) for BS and SSH, respectively. All the PCs of BS and SSH in these three models appear stationary. The variability is not due to trends, which may be indicative for equilibrating from an initial state. Since the forcing in these three models is periodic and "without weather", these variations must be caused by internal dynamics, likely in the spirit of the "stochastic climate model".

Table 2 lists the sum of percentages of variance described by the first three EOFs for BS and SSH, respectively. We find that the leading EOFs of BS in the global model represent a higher percentage of cumulative variance than that in the WP model, and the leading EOFs of BS in the WP model explain the higher percentage of cumulative variance than that in the SCS model. From the global model to the SCS model, with model resolution increasing, the percentages of the sum of variances represented by the first three EOFs for BS decrease (except for summer).

The situations with of SSH are similar to that of BS, except for winter: The first leading EOF of SSH in the global model explains a lower percentage of variance than that in the WP model (Fig. 6). We speculate that, because the resolution in the global model is too coarse, the Kuroshio invasion path in the global model is farther west and much broader than that in reality and in the WP and SCS simulations — which is reflected by a very strong first leading EOF (Fig. 6). Therefore, the variability in the northern SCS in the global model is exaggerated compared to both the WP and SCS model.

We conclude that higher resolution models generate more "noise" so that a smaller percentage of the overall variability is represented by the dominant EOFs in the higher resolution models.

4. Conclusion

Basing on a three-layer nested simulation, which is forced by periodic climatological atmospheric forcing, featuring a global model, a West-Pacific model and South China Sea model, we find that high-dimensional nonlinear-systems like ocean dynamics generate variability by itself without an external forcing, and that "noise" generations are stronger in models with higher resolution, which favors the building of macro-turbulence. Here "noise" is meant as variability which emerges in an "unprovoked" manner, i.e., which is unrelated to external drivers, and is not deterministically related to initial conditions.

It is important to note that we are not referring to low-dimensional non-linear systems which may generate beautiful attractors and other phenomena, but high-dimensional systems, whose variability maybe described by stochastic processes.

Ocean models can generate "noise" by internal nonlinear or stochastic dynamics, in the spirit of the "stochastic climate model". From the global model to the SCS model, with model resolution increasing, the "noise" generation increase. The higher resolution models can internally generate variability, which is absent in the lower resolution models. Because that higher resolution models generate more "noise", a smaller percentage of the overall variability is represented by dominant EOFs in the higher resolution models. The higher resolution models generate more "noise", which can motivate the generation of eddies in the ocean. This is important for scientists who study eddies in ocean models.

"Noise" may in some cases be a nuisance, but in dynamical simulations, it is a constitutive element of the dynamics of the system, which makes the dynamics richer, but creates the need of statistical efforts for determining if a change is beyond the range of internal variations. This becomes a significant issue when studying the effects of climate change or numerical experiments on the effect of formulating processes in models.

So far, this practice is not widely recognized in ocean sciences (but, see for instance Leroux et al., 2018), even if this mechanism is an almost trivial consequence of the concept of the stochastic climate model. In atmospheric sciences this is well-known, which may be related to the fact that atmospheric eddies have been part of the dynamics in most quasi-realistic atmospheric models, while global ocean models have for long operated with coarse resolution, without eddies but strong numerical viscosity and diffusion so that the late Ernst Maier—Reimer joked that older ocean models would be filled with mustard and not with water.

Another factor, which may limit the role of such internal variability in coastal seas, is the presence of tides, which acts as a kind of viscosity, erasing quickly and efficiently the emergence of non-forced long-living anomalies.

Acknowledgments

This work is supported by the Project "Oceanic Instruments Standardization Sea Trials (OISST)", (2016YFC1401300) of National Key Research and Development Plan, and Taishan scholars Program. Thanks should be given to China National Super Computing Center in Jinan for providing the computing resources and Ms. Liu Xin for computing technology support.

References

Bleck, R., 2002. An oceanic general circulation model framed in hybrid isopycnic-Cartesian coordinates. Ocean Model. 4, 55—88, http://dx.doi.org/10.1016/S1463-5003(01)00012-9.

Chen, G., Hou, Y., Chu, X., 2011. Mesoscale eddies in the South China Sea: Mean properties, spatiotemporal variability, and impact on thermohaline structure. J. Geophys. Res. 116, C06018, http://dx.doi.org/10.1029/2010JC006716.

Chervin, R.M., Schneider, S.H., 1976. On determining the statistical significance of climate experiments with general circulation models. J. Atmos. Sci. 33 (3), 405—412, http://dx.doi.org/10.1175/1520-0469(1976)033<0405:ODTSSO>2.0.CO;2.

Faghmous, J.H., Frenger, I., Yao, Warmka, R., Lindell, A., Kumar, V., 2015. A daily global mesoscale ocean eddy dataset from satellite altimetry. Sci. Data 2, 150028, http://dx.doi.org/10.1038/sdata.2015.28.

Hasselmann, K., 1976. Stochastic climate models Part I. Theory. Tellus 28 (6), 473—485, http://dx.doi.org/10.1111/j.2153-3490.1976.tb00696.x.

Hasselmann, K., 1993. Optimal fingerprints for the detection of time-dependent climate change. J. Climate 6 (10), 1957—1971, http://dx.doi.org/10.1175/1520-0442(1993)006<1957:OFFTDO>2.0.CO;2.

Large, W.G., McWilliams, J.C., Doney, S.C., 1994. Oceanic vertical mixing: a review and a model with a nonlocal boundary layer parameterization. Rev. Geophys. 32 (4), 363—403, http://dx.doi.org/10.1029/94RG01872.

Leroux, S., Penduff, T., Bessières, L., Molines, J., Brankart, J., Sérazin, G., Barnier, B., Terray, L., 2018. Intrinsic and atmospherically forced variability of the AMOC: insights from a large-ensemble ocean hindcast. J. Climate 31 (3), 1183—1203, http://dx.doi.org/10.1175/JCLI-D-17-0168.1.

Lorenz, E.N., 1956. Empirical orthogonal functions and statistical weather prediction. Sci. Rep. No. 1, Statistical Forecasting Project. M.I.T., Cambridge, MA, 48 pp.

von Storch, H., Zwiers, F.W., 1999. Statistical Analysis in Climate Research. Cambridge Univ. Press, Cambridge, 293—305.

von Storch, H., von Storch, J.-S., Müller, P., 2001. Noise in the climate system — ubiquitous, constitutive and concealing. In: Engquist, B., Schmid, W. (Eds.), Mathematics Unlimited — 2001 and Beyond. Part II. Springer Verlag, Berlin, Heidelberg, 1179—1194, http://dx.doi.org/10.1007/978-3-642-56478-9_62.

Wang, Y., Fang, G., Wei, Z., Qiao, F., Chen, H., 2006. Interannual variation of the South China Sea circulation and its relation to El Niño, as seen from a variable grid global ocean model. J. Geophys. Res. 111, C11S14, http://dx.doi.org/10.1029/2005JC003269.

Weisse, R., Heyen, H., von Storch, H., 2000. Sensitivity of a regional atmospheric model to a sea state-dependent roughness and the need for ensemble calculations. Mon. Weather Rev. 128 (10), 3631—3642, http://dx.doi.org/10.1175/1520-0493(2000)128<3631:SOARAM>2.0.CO;2.

Zhang, M., von Storch, H., 2016. Towards downscaling oceanic hydrodynamics - Suitability of a high-resolution OGCM for describing regional ocean variability in the South China Sea. Oceanologia 59 (2), 166—176, http://dx.doi.org/10.1016/j.oceano.2017.01.001.

Zhang, M., von Storch, H., 2018. Distribution features of travelling eddies in the South China Sea. Research Activities in Atmospheric and Oceanic Modelling. 2018 Blue Book, vol. 2. 2—31.

Oceanologia (2019) 61, 308—320

Available online at www.sciencedirect.com

ScienceDirect

journal homepage: www.journals.elsevier.com/oceanologia/

ORIGINAL RESEARCH ARTICLE

Seasonal patterns and environmental drivers of *nir*S- and *nir*K-encoding denitrifiers in sediments of Daya Bay, China

Rongjun Shi [a,1], **Shumin Xu** [a,b,1], **Zhanhui Qi** [a,*], **Honghui Huang** [a,*], **Qingyang Liang** [a]

[a] *Guangdong Provincial Key Laboratory of Fishery Ecology and Environment and Key Laboratory of Open-Sea Fishery Development, Ministry of Agriculture, South China Sea Fisheries Research Institute, Chinese Academy of Fishery Science, Guangzhou, China*
[b] *College of Marine Science of Shanghai Ocean University, Shanghai, China*

Received 19 September 2018; accepted 12 January 2019
Available online 28 January 2019

KEYWORDS
Abundance;
Community structure;
*nir*S-encoding denitrifiers;
*nir*K-encoding denitrifiers;
Sediment;
Daya Bay

Summary The seasonal patterns of the denitrifiers (denitrifying bacteria) in the sediment of Daya Bay, southern China, were examined using quantitative PCR and high-throughput MiSeq sequencing methods in spring, summer and winter. The abundance and diversity of *nir*S-encoding denitrifiers were much higher than that of *nir*K-encoding denitrifiers, indicating that the former probably dominated the denitrification processes in sediments of Daya Bay. The average abundance and diversity of *nir*S-encoding denitrifiers were much higher in spring than that in summer and winter, on the other hand, the abundance of *nir*K-encoding denitrifiers showed the opposite pattern. The species composition of *nir*S-encoding denitrifiers community in spring differed significantly from that in summer and winter, whereas, no significant difference existed between summer and winter. The dominant environmental drivers for the diversity of community species were NO_2^-, NO_3^- and DO concentrations. The abundances of dominant genera of *nir*S-encoding denitrifiers, *Accumulibacter* sp. and *Cuprizvidus* sp., were significantly higher in

* Corresponding authors at: South China Sea Fisheries Research Institute, 231 West Xingang Road, Guangzhou 510300, Guangdong Province, China. Tel.: +86 02084457660; fax: +8602084451442
E-mail addresses: qizhanhui@scsfri.ac.cn (Z. Qi), huanghh@scsfri.ac.cn (H. Huang).
[1] Contributed equally to this work.
Peer review under the responsibility of Institute of Oceanology of the Polish Academy of Sciences.

ELSEVIER Production and hosting by Elsevier

https://doi.org/10.1016/j.oceano.2019.01.002

summer and winter than that in spring, and were negatively correlated with NO_2^-, NO_3^-, and DO concentrations ($p < 0.05$). In contrast, the abundances of *Azoarcus* sp. and *Halomonas* sp., were highest in spring, and were positively correlated with NO_3^- and NO_2^- content ($p < 0.05$). For *nir*K-encoding denitrifiers, a significant difference in community composition was observed between spring and winter. No obvious correlation was found between community composition of *nir*K-encoding denitrifiers and environmental parameters.

1. Introduction

Agricultural and other anthropogenic activities, e.g., mariculture, result in increasing nitrogen load to freshwater and marine systems, causing eutrophication problems. Therefore, denitrification that removed "excess" N from the water bodies plays an important role in alleviating eutrophication (Abell et al., 2013; Bowen et al., 2014). Based on the consequences of denitrification reactions, the nitrate was consequently catalyzed by four kinds of enzymes, i.e., nitrate reductase which was encoded by *nap*A or *nar*G genes, nitrite reductase encoded by *nir*S or *nir*K genes, nitric oxide reductase encoded by *nor*B or *nor*Z genes, and nitrous oxide reductase encoded by *nos*Z gene (Shrewsbury et al., 2016). Among of them, the nitrite reductase which catalyzing the reaction that leads to the formation of gaseous nitrogen (nitric oxide) through nitrite, is the rate-limiting enzyme for the denitrification processes (Baker et al., 2015; Chen et al., 2013).

Nitrite reductase encoded either by *nir*K or *nir*S are evolutionarily distinct but functionally equivalent (Glockner et al., 1993; Shrewsbury et al., 2016). Therefore, the bacteria which have either *nir*S or *nir*K gene are often considered to be denitrifying bacteria and are found in a variety of environments, including marine, estuarine, wetland and bay (Braker et al., 2000; Gao et al., 2016; Lee and Francis, 2016; Li et al., 2017a). Previous studies reported that the abundance and distribution of denitrifying bacteria in sediments could be affected by various environmental factors, including temperature, dissolved oxygen (DO), dissolved inorganic nitrogen (DIN, e.g., NO_3^-, NO_2^- and NH_4^+) and organic matter content in sediments (Gao et al., 2016; Huang et al., 2011; Li et al., 2017a; Reyna et al., 2010). Reasonably, there were markedly spatial and temporal variations in denitrifiers community profiles, e.g., the species diversity and abundance (Gao et al., 2016; Yang et al., 2015a).

Daya Bay, located in the northwestern part of the South China Sea, is a typical subtropical bay with an area of approximately 600 km^2. Approximately 60% of the water in the Bay is less than 10 m deep, and most of its water originates from the South China Sea and three small rivers (Ni et al., 2015; Wang et al., 2006). The rapid expanding of coastal aquaculture and industries increased nitrogen loading to the bay, which contributed to various environmental issues in Daya Bay, such as eutrophication, annual algal blooms, and hypoxia (Song et al., 2009). In recent years, many studies have been carried out to address the ecological and anthropogenic factors contributing to these effects (Jiang et al., 2016; Ma et al., 2014; Wu et al., 2016, 2017a). Microorganisms associated with nitrogen cycle play important role in the cycling and removal of nitrogen from coastal waters. However, information on the distribution profiles of *nir*K- and *nir*S-encoding denitrifiers, and the major environmental drivers are still very limited.

In this study, quantitative polymerase chain reaction (qPCR) and high-throughput MiSeq sequencing were used to examine the seasonal patterns and environmental drivers of denitrifying bacteria in sediments from Daya Bay. The objectives were: (1) to investigate the seasonal patterns of the *nir*S- and *nir*K-denitrifying bacteria inhabiting the sediment of Daya Bay, and (2) to examine the key environmental factors which determine the spatial-temporal heterogeneities of *nir*S- and *nir*K-denitrifying bacterial community in Daya Bay. We hope to provide useful information to further understand the responses of denitrifying bacteria communities to environmental factors.

2. Material and methods

2.1. Study area and sample collection

Surface sediments were collected using an Ekman-Birge type bottom sampler in winter (December 2015), spring (March 2016), and summer (August 2016) from four stations, i.e., D1, D2, D3 and D4, in Daya Bay, Southern China (Fig. 1). Sediment samples were gently placed on a white enamel tray (30 cm × 60 cm), the top 2 cm sediment was collected using a stainless steel ruler. For each sampling station, triplicate samples of surface sediment were collected, mixed and homogenized. Each sediment sample was further divided into two parts: one was stored at −80°C for DNA extraction and another one was stored at −20°C for sedimentary chemical parameters analyses.

2.2. Physiological and chemical parameters analyses

At each sampling station, temperature, pH, salinity and DO of overlying water were measured with a multiprobe sonde (Yellow Springs Instrument Co., Dayton, OH, USA). Moisture content (MC), total nitrogen (TN), sulfide, total organic carbon (TOC), nitrate (NO_3^-), nitrite (NO_2^-) and ammonia (NH_4^+) of sediment were measured in laboratory. Sediment samples (about 2 g) were weighed and then reweighed after

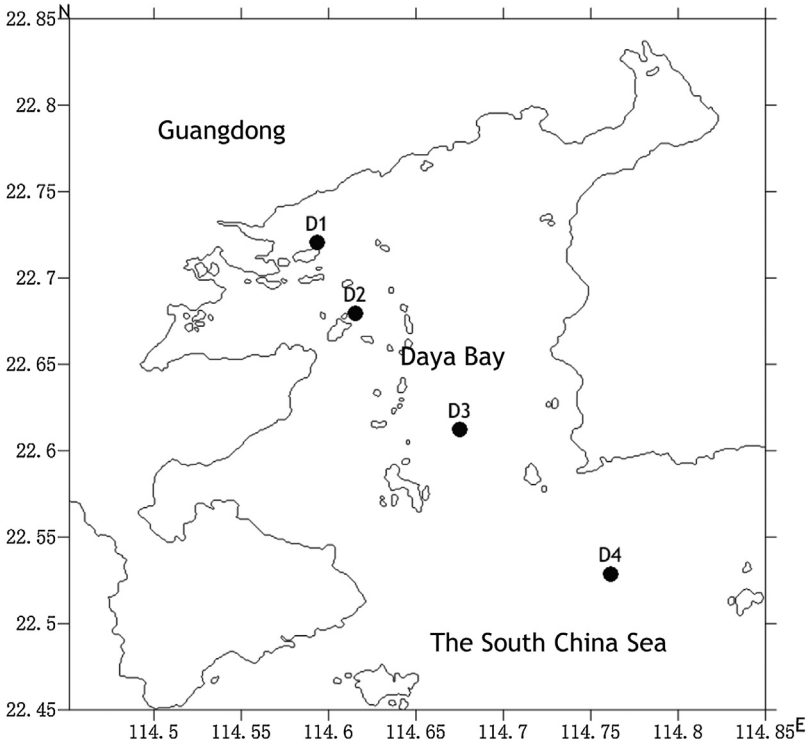

Figure 1 Sediment sampling stations in Daya Bay, Southern China.

dried at 60°C to a constant weight. The differences in weights were defined as moisture content. In addition, TOC were detected according to the method described in Yang et al. (2015b). TN was measured using potassium persulfate oxidation method. Sediment samples (about 0.1 g) that had already been dried at 60°C were dissolved in 25 ml oxidant solutions (NaOH:$K_2S_2O_8$ = 0.15 M:0.15 M) after homogenizing and grounding to fine powder. Aliquots of the samples were then heated for 1 h at 124°C and centrifuged at 3000 × *g* for 10 min. 2 ml of the separated supernatants were diluted with ultrapure water to 25 ml to manually determine TN with a spectrophotometer (Shanghai Precision Science Instrument Co. Ltd., Shanghai, China) according to marine monitoring specifications (GB/T 12763.4-2007, 2007).

Sediment samples (10 g) mixed with KCl solution (2 M, 40 ml) were shaken with an oscillator for 1 h (200–300 rpm) (Keeney and Nelson, 1982; Shrewsbury et al., 2016). Aliquots of the samples were centrifuged at 3000 × *g* for 10 min and then the supernatants obtained were diluted with KCl solution to 75 ml to determine NO_3^-, NO_2^- and NH_4^+ concentrations according to marine monitoring specifications (GB/T 12763.4-2007, 2007).

2.3. DNA extraction and high-throughput MiSeq sequencing

The samples were centrifuged at 1000 × *g* for 30 s to ensure consistency of sampling quantity. The centrifuged samples (approximately 0.25 g) were then used for DNA extraction with the ZymoBiomics DNA mini kit (Zymo Research Co., Irvine, CA, USA) following the manufacturer's instructions. Purity and concentrations of the extracted DNA were examined using a spectrophotometer (NanoDrop Technologies Inc., Wilmington, DE, USA) and were visualized with agarose gel electrophoresis. The resultant DNA was then amplified through PCR (the primers are listed in Table 1) and sequenced using Solexa MiSeq Genome Analyzer (Illumina Inc., San Diego, CA, USA). All the sequences used in this study are publicly available at the NCBI Sequence Read Archive (http://www.ncbi.nlm.nih.gov/Traces/sra) under gene accession no. SRP125795.

2.4. Fluorescence quantitative PCR (qPCR)

The primers listed in Table 1 targeting the *nir*S and *nir*K genes were applied to determine the abundance of denitrifying

Table 1 Oligonucleotide sequences of primers used for PCR and qPCR assays.

Target gene	Primer	Sequence [5′→3′]	References
*nir*K	*FlaCu*	ATCATGGTSCTGCCGCG	Hallin and Lindgren (1999), Yi et al. (2015)
	R3Cu	GCCTCGATCAGRTTRTGGTT	
*nir*S	*cd3aF*	GTSAACGTSAAGGARACSGG	Throbäck et al. (2004), Zheng et al. (2015)
	R3cdR	GASTTCGGRTGSGTCTTGA	

bacteria by qPCR according to Yi et al. (2015). Linearized plasmids containing *nir*S and *nir*K were used to generate standard curves. All standard and sample reactions were performed in triplicate, and all the standard curves showed excellent correlations between the DNA template concentration and the crossing point with high coefficients of determination ($R^2 > 0.99$). The results indicated that the qPCR efficiency values for *nir*S and *nir*K were 0.924 and 1.006, respectively. Finally, the abundance of *nir*S and *nir*K genes was calculated based on the constructed standard curve, and then converted into copies per gram of sediment.

2.5. Data analysis

Raw tags were quality-filtered by Trimmomatic (Bolger et al., 2014) and merged by FLASH (Magoc and Salzberg, 2011) to obtain the effective tags. After quality filtration, sequence analysis of effective tags was performed using Uparse software (Uparse v7.0.1001, http://drive5.com/uparse/), and sequences with ≥97% similarity were assigned to the same OTUs according to Wu et al. (2017b). A representative sequence of each OTU was aligned with sequences downloaded from the FunGene database (Fish et al., 2013). Statistical analyses were performed using R version 3.3.3 (R Core Team, Vienna, Austria). Alpha diversity indices (Chao1, Pielou's evenness, Shannon–Wiener, and Simpson indices), Correspondence analysis (CA) plots, heat maps and Mantel tests were calculated and generated using R. Besides, Bray–Curtis distance was used for the genera of *nir*S and OTUs of *nir*K distance metric, and euclidian distances were used to describe the underlying structure of our environmental variables in mantel tests (Hollister et al., 2010; Yang et al., 2015b).

Extended error bar plots were created using STAMP (Parks et al., 2014). Phylogenetic tree was created by mega 7 program with the maximum likelihood method and the reliability of the tree topologies was estimated by performing 1000 bootstrapping replicates.

3. Results

3.1. Physiological and chemical characteristics of sediment

The spatial and temporal patterns of salinity, pH, temperature, DO, MC, TOC, NO_2^-, NO_3^-, NH_4^+, and TN at each sampling station are shown in Table 2. Temperature was higher in summer than that in spring and winter. Salinity in D1 was lower than the other stations in all seasons. Water DO and NO_2^- concentrations in all stations were highest in spring, followed by winter and summer. TOC at D1 and D2 stations were higher than that at D3 and D4 stations. No obvious spatial and temporal pattern of the other environmental parameters was observed.

3.2. Abundance of *nir*S-encoding and *nir*K-encoding denitrifiers

The abundance of *nir*S-encoding denitrifiers was 6.48–20.34 × 10^{10} copies g^{-1} sediment in spring, which was about 10 times higher than the abundance in summer and winter (1.44–66.76 × 10^8 copies g^{-1} sediment) ($p < 0.05$) (Fig. 2A, B). However, no significant differences were observed among the three seasons, although the abundances of *nir*K-encoding denitrifiers in summer and winter were higher than that in spring (Fig. 2C, D). In addition, the abundance of *nir*S was higher than that of *nir*K in all the three seasons. In particular, *nir*S abundance in spring was higher than abundance of *nir*K in all seasons ($p < 0.05$). Generally, the abundance of *nir*S-encoding and *nir*K-encoding denitrifiers at stations D2 and D3 was higher than that at stations D1 and D4.

Table 2 Water and sediment selected properties at experimental sites in Daya Bay.

Season	Station	Salinity	pH	T[a]	DO[b]	MC[c]	TOC[d]	NO_2^-[e]	NO_3^-[e]	NH_4^+[e]	TN[f]
				[°C]	[mg L^{-1}]	[%]	[%]	[nmol g^{-1} dry weight]			[μmol g^{-1} dry weight]
Spring	D1	31.05	8.04	19.9	13.08	64.02	1.4	17.42	19.60	0.13	26.99
	D2	31.84	8.14	18.8	11.82	69.49	1.43	19.26	24.77	6.80	9.55
	D3	32.77	8.2	19.1	9.98	49.69	0.85	13.46	13.72	3.09	59.61
	D4	33.22	8.3	17.4	8.27	53.34	0.75	14.31	30.75	7.38	69.1
Summer	D1	30.40	8.44	30.8	5.7	56.01	1.66	7.19	2.18	4.33	28.26
	D2	31.95	8.45	30.0	6.47	63.95	1.42	8.25	9.03	0.01	21.59
	D3	32.01	8.05	30.8	6.68	60.78	1.31	8.22	7.94	0.01	60.21
	D4	31.85	8.16	30.9	7.45	39.71	0.74	3.67	4.21	0.005	32.11
Winter	D1	33.34	8.16	19.34	8.32	72.97	1.98	15.11	25.97	2.19	26.19
	D2	33.59	8.15	19.68	8.31	71.66	1.83	12.58	18.98	34.73	31.02
	D3	34.47	8.13	18.16	8.01	44.63	0.64	6.42	13.61	18.03	6.37

[a] T, water temperature.
[b] DO, water dissolved oxygen.
[c] MC, the moisture content of sediment.
[d] TOC, total organic carbon content of sediment.
[e] NO_2^-, NO_3^- and NH_4^+ concentrations of sediment.
[f] TN, total nitrogen content of sediment.

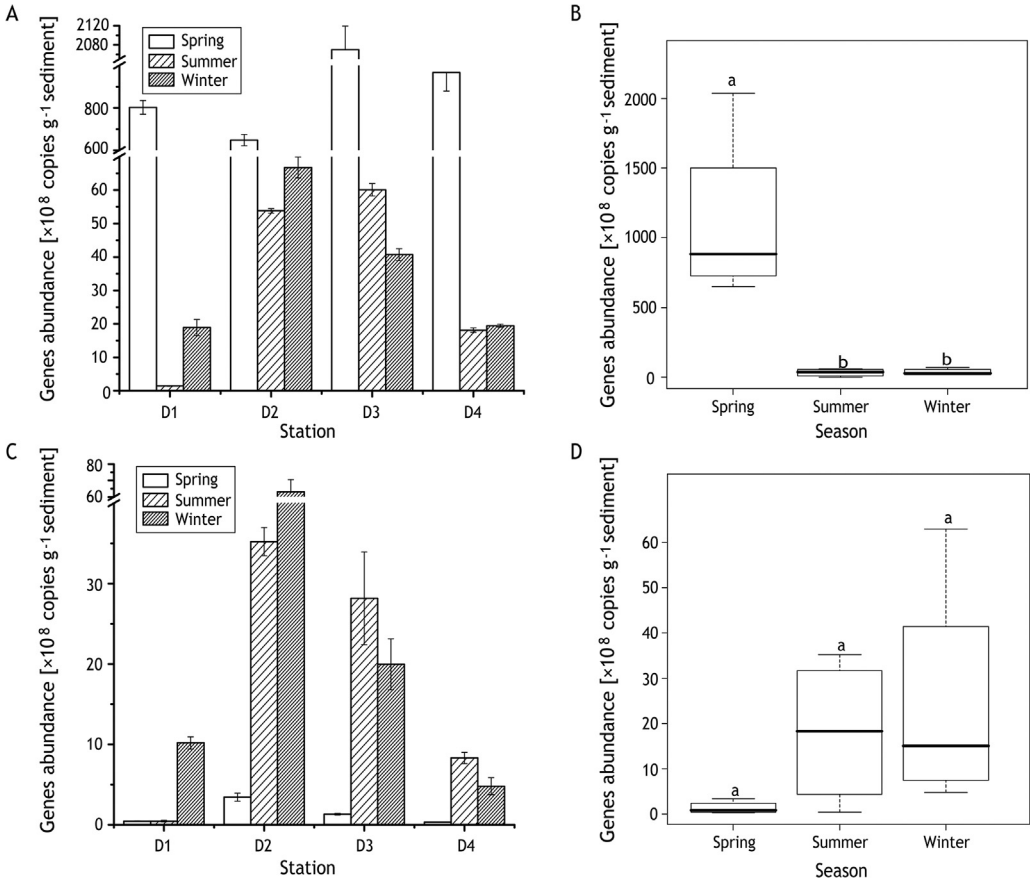

Figure 2 Abundances of *nir*S (A, B) and *nir*K (C, D) genes in the sediment of Daya Bay, China. (A) and (C) error bars represent the standard error of triplicate samples. (B) and (D) different lowercase letters represent statistically significant differences between seasons ($p < 0.05$).

3.3. Community diversity of *nir*S- and *nir*K-encoding denitrifiers

Totally 533,461 effective tags of *nir*S were obtained from sediment samples. These tags were clustered into 4296 OTUs with a similarity cut-off of 97%. The Shannon–Wiener indices of *nir*S-encoding denitrifiers were 0.68–0.71 in spring, which was significantly higher than that in summer and winter (0.53–0.58) ($p < 0.05$) (Table 3). In addition, Pielou's evenness and Simpson (1/*D*) indices exhibited similar patterns as the Shannon–Wiener index. No significant difference in the species richness index (Chao1) was observed among the three seasons ($p > 0.05$).

Similarly, 571,199 *nir*K tags were obtained and clustered into 1123 OTUs with a similarity cut-off of 97%. The Chao1, Shannon–Wiener, and Simpson (1/*D*) indices of *nir*K-encoding denitrifiers were lower than that of *nir*S-encoding denitrifiers, particularly in spring, although no significant difference among the three seasons for any of the indices was observed ($p > 0.05$).

3.4. Spatial and temporal distribution profiles of *nir*S- and *nir*K-encoding bacterial communities

Spatial and temporal distributions of denitrifier communities were compared using CA based on all OTUs (Fig. 3). The distribution of *nir*S-encoding denitrifiers did not differ between summer and winter. However, the distribution was significantly different between spring and the other seasons (Fig. 3A). An obvious difference in *nir*K-encoding denitrifier communities was detected between spring and winter (Fig. 3B). In spring, the community structures of *nir*S- and *nir*K-encoding denitrifiers in station D1 were significantly different from other stations.

3.5. Composition of *nir*S- and *nir*K-encoding denitrifiers

The OTUs of *nir*S-encoding denitrifiers were assigned to 191 genera representing 20 different phyla. The dominant phyla were Proteobacteria (42.43–64.89% of the total OTUs at all stations) and Actinobacteria (0.09–3.75%, Fig. 4A). Further analysis indicated that the identified members of Proteobacteria belonged to four classes, i.e., Alphaproteobacteria, Betaproteobacteria, Gammaproteobacteria and Deltaproteobacteria, of which Betaproteobacteria and Gammaproteobacteria were the dominant classes.

The relative abundance of Betaproteobacteria in spring (14.06–27.64% of the total OTUs) was slightly lower than that in summer and winter (26.95–33.0%, Fig. 4A). However, all genera abundance of Betaproteobacteria (except *Vogesella* sp.) was significantly different between spring and the other

Table 3 Richness and diversity estimates of *nir*S- and *nir*K-encoding bacteria in the Daya Bay sediment.

Gene	Season	Station	OTUs	Chao1	Pielou's evenness index	Shannon–Wiener index [*H*]	Simpson index [1/*D*]
*nir*S	Spring	D1	830	951.63	0.71	4.76	35.90
		D2	868	961.51	0.68	4.60	33.13
		D3	730	872.08	0.71	4.67	42.63
		D4	746	866.23	0.68	4.50	30.58
	Summer	D2	953	953.19	0.53	3.61	12.32
		D3	1108	1118.66	0.57	4.02	16.02
		D4	980	965.81	0.58	3.99	14.56
	Winter	D2	1136	1175.42	0.58	4.12	17.52
		D3	709	722.28	0.54	3.57	12.60
		D4	1168	1211.16	0.56	3.94	15.07
*nir*K	Spring	D1	619	688.00	0.68	4.38	24.05
		D2	631	645.53	0.67	4.33	14.58
		D3	602	653.07	0.63	4.02	8.46
		D4	528	578.83	0.50	3.16	5.05
	Summer	D2	665	724.70	0.57	3.68	8.16
		D3	672	711.28	0.61	4.00	8.38
		D4	616	658.02	0.59	3.80	7.15
	Winter	D2	666	740.45	0.50	3.23	5.70
		D3	613	662.08	0.57	3.68	8.07
		D4	589	641.64	0.64	4.10	16.70

seasons ($p < 0.05$, Fig. 4B). *Azoarcus* sp. and *Polymorphum* sp. were the dominant genera in spring, whereas *Accumulibacter* sp. and *Cuprizvidus* sp. were the dominant genera in summer and winter. The relative abundance of Gammaproteobacteria was significantly higher in spring (24.56–29.23%) than in summer and winter (9.37–12.36%). *Halomonas* sp. and *Pseudomonas* sp. were highest in spring compared to that in summer and winter ($p < 0.05$).

Compared with Betaproteobacteria and Gammaproteobacteria, the abundance of Alphaproteobacteria and Deltaproteobacteria was found to be lower. The dominant genera of the Alphaproteobacteria were *Azospirillum* sp. and *Polymorphum* sp. in spring and *Magnetospirillum* sp. and *Bradyrhizobium* sp. in summer and winter, and the dominant genus of Deltaproteobacteria was *Myxococcus* sp. in summer and winter. The abundance of *Polymorphum* sp., *Bradyrhizobium* sp., and *Myxococcus* sp. differed significantly between spring and the other seasons ($p < 0.05$, Fig. 4B). In addition, the relative abundance of Actinobacteria, whose dominant genus was *Kocuria* sp., was highest in spring ($p < 0.05$). There was no significant difference in the abundance of *nir*S-encoding denitrifiers between summer and winter.

Phylogenetic analysis indicated that a large proportion of unique OTUs matched uncultured environmental *nir*K assemblages. It was also observed that the majority of OTUs closely matched to sequences retrieved from GenBank belonged to samples isolated from estuaries (e.g., San Francisco Bay and Yellow River Estuary), marine habitats (e.g., Arabian Sea and

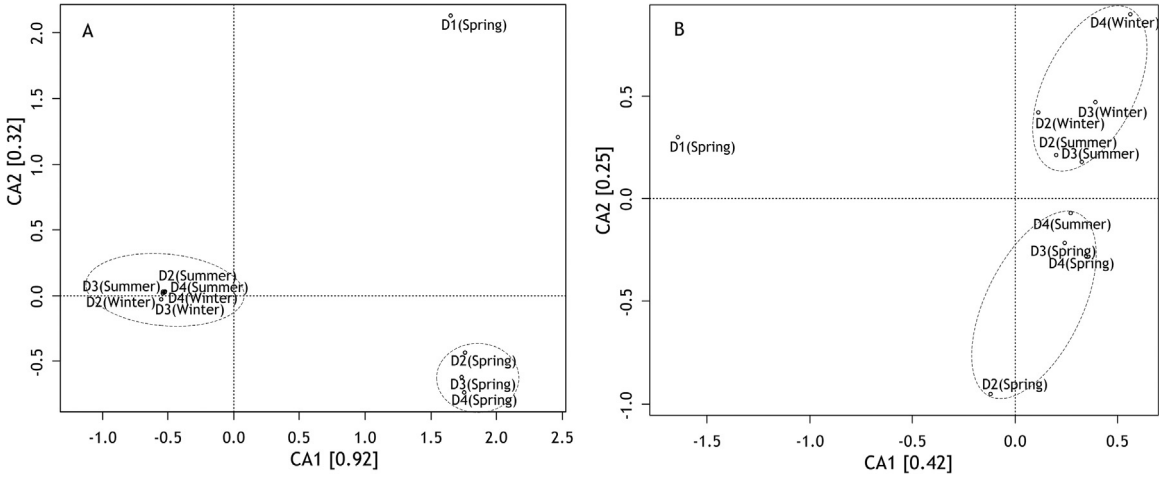

Figure 3 Community structures of *nir*S- (A) and *nir*K-encoding bacteria (B). Ordination plots from correspondence analysis (CA) were generated based on OTUs of denitrifying bacteria in sediment of Daya Bay, China.

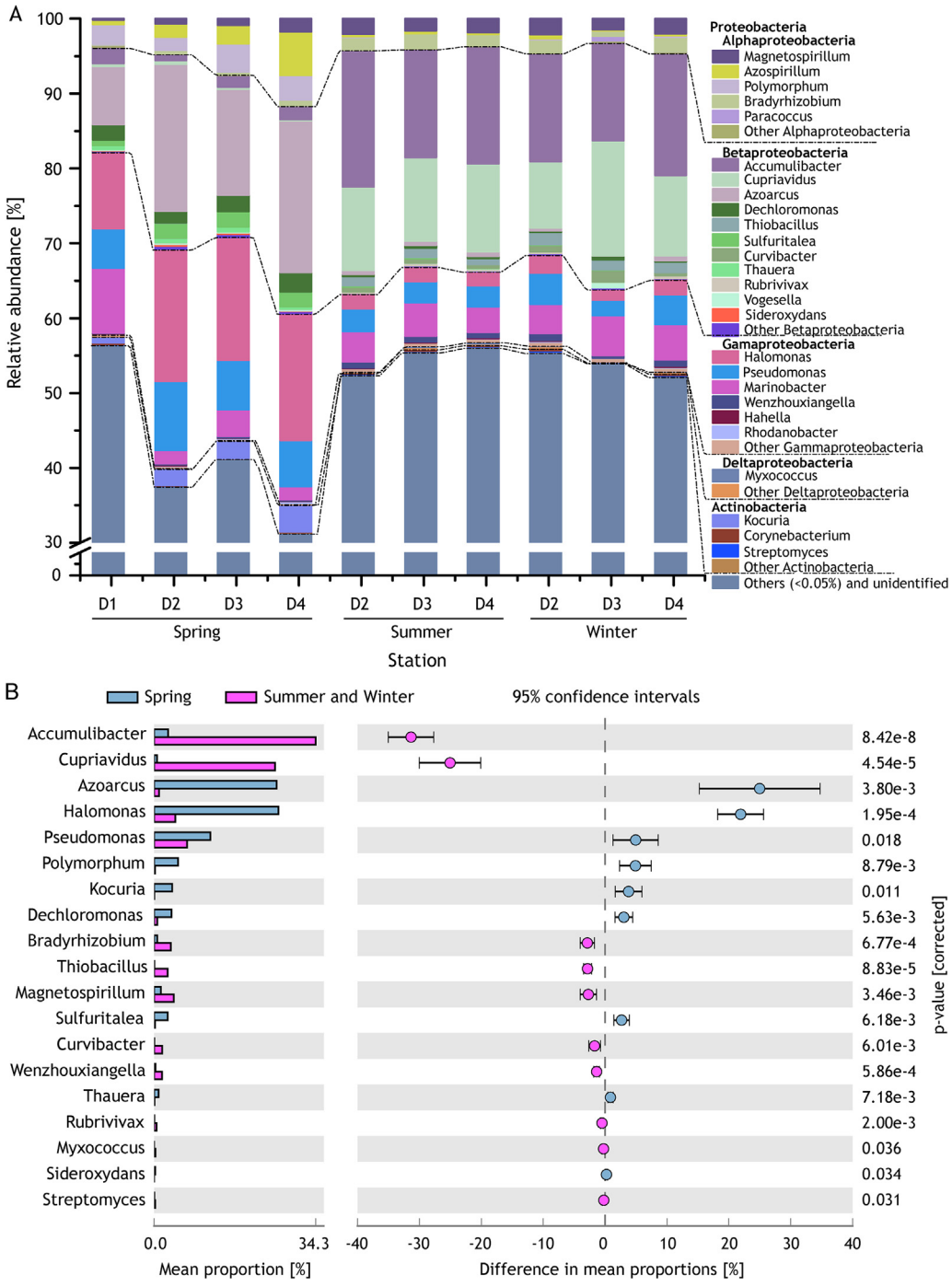

Figure 4 Taxonomic classification (A) and extended error bar plot (B) of *nir*S-encoding denitrifiers. Genera with low proportions (<0.05%) at all stations were grouped with corresponding phyla, classes, or others to increase readability.

East China Sea), wetland restoration sites, and landfill cover soils (Fig. 5). Furthermore, database alignment indicated that only 4.73% of *nir*K OTUs could be assigned to Proteobacteria because of limited available databases. Therefore, further analysis of the *nir*K gene was restricted to the most abundant 50 OTUs, which were assigned to clusters A–D based on phylogenetic analysis (Fig. 5). The dominant cluster at all sampling stations was cluster B (26.66–67.49% of the total OTUs at all stations), followed by cluster A (5.23–44.13%), cluster D (6.44–13.0%), and cluster C (0.53–4.46%, Fig. 6A).

The results indicated that the relative abundance of cluster A, which was phylogenetically similar to Proteobacteria, was highest in winter (25.80–44.13%), followed by summer (10.43–28.76%), and spring (5.23–23.96%, Fig. 6A). A decreasing trend in the relative abundance of cluster A was observed from stations D2, D3 to D4 in all seasons. Whereas, the relative abundance of cluster B was

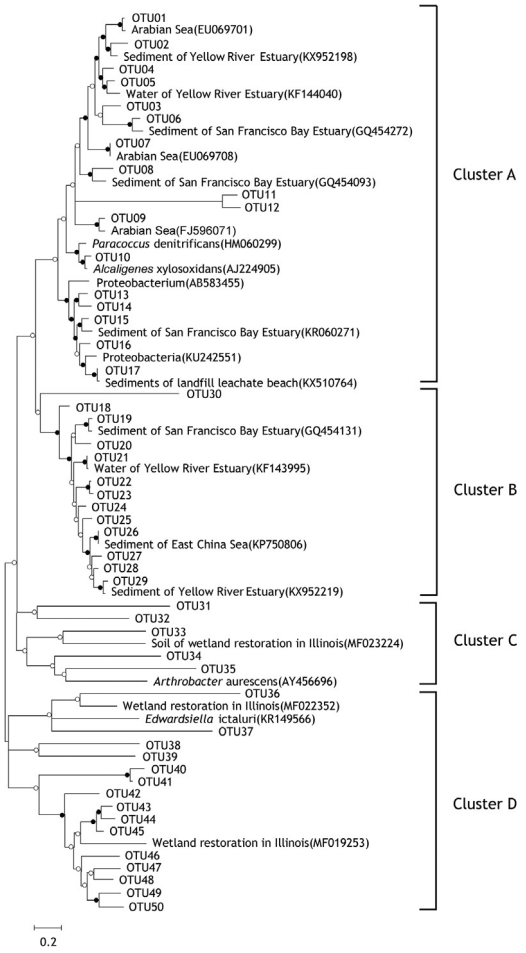

Figure 5 Maximum likelihood phylogenetic tree of *nir*K sequences isolated from Daya Bay, China. Bootstrap values greater than 50% ($n = 1000$) are shown with solid circles and those less than 50% are shown with open circles on the corresponding nodes.

highest in spring (30.15–67.49%), followed by summer (34.35–47.74%), and winter (26.66–36.86%) and an increasing trend was observed from stations D2, D3 to D4 in all seasons. Compared with clusters A and B, the relative abundance of clusters C and D was relatively low and evenly distributed across all stations and seasons. In addition, the abundance of OTU15, OTU23, and OTU37 was significantly higher in summer compared with spring ($p < 0.05$, Fig. 6B). However, the distribution of OTU24 and OTU31 was significantly higher in spring than in winter ($p < 0.05$). The distribution of OTU26, OTU44, and OTU49 was significantly higher in summer than in winter ($p < 0.05$).

3.6. Relationships between denitrifying bacteria and environmental factors

Mantel test indicated that DO, NO_2^- and NO_3^- contents were the most key factors significantly shaping *nir*S-encoding denitrifier communities (Table 4, $p < 0.05$). Thus, *nir*S-encoding denitrifiers, whose proportions were higher than 0.05% in all sampling sites, were divided into three groups based on the correlation between their abundance and environmental factors (Fig. 7A). The representative genera of the first group were *Marinobacter* sp., *Myxococcus* sp., *Bradyrhizobium* sp., *Cuprizvidus* sp., *Magnetospirillum* sp., and *Accumulibacter* sp. Their abundances were negatively correlated with NO_2^-, NO_3^- and DO content, however, positively correlated with temperature. In contrast, for the second group, the representative genera were *Azospirillum* sp., *Azoarcus* sp., *Halomonas* sp., *Polymorphum* sp., and *Kocuria* sp. Their abundances were positively correlated with NO_2, NO_3^- and DO content, however, negatively correlated with temperature. For the third group, the representative genera were *Paracoccus* sp., *Pseudomonas* sp., and *Corynebacterium* sp., abundance was correlated with salinity and TOC.

No significant correlationship between environmental factors and *nir*K-encoding denitrifier communities was observed (Table 4, $p > 0.05$). However, for those *nir*K-encoding denitrifiers whose mean relative abundance of OTUs $> 0.5\%$ still can be divided into four groups (Fig. 7B). The abundance of representative OTU of OTU15 in the first group was significantly negatively correlated with NO_2^-, NO_3^- and DO content ($p < 0.05$), but positively correlated with temperature. For the second group, the abundances of OTU22 and OTU36 were positively correlated with TN content, but negatively correlated with TOC ($p < 0.05$). For the third group, the abundances of OTUs of OTU25, OTU33, OTU39, OTU41 and OTU47 were positively correlated with DO. For the fourth group, the abundances of OTU11 and OTU12 were positively correlated with TOC, MC and NH_4^+.

4. Discussion

In the present study, both *nir*K- and *nir*S-encoding denitrifiers, which had been reported to be widespread in various sediments, were detected in the sediment of Daya Bay, China (Alcántara-Hernández et al., 2014; Chen et al., 2017; Li et al., 2017a; Tang et al., 2016), and the abundance and community diversity of *nir*K-encoding denitrifiers were much lower than *nir*S-encoding denitrifiers. This was probably due to their different ecological strategies or niches, such as the requirement for different enzyme substrates (Huang et al., 2011). Our results were consistent with previous studies which reported that *nir*S-encoding denitrifiers were more widespread than *nir*K-encoding denitrifiers in sediments of the Yellow River Estuary (Li et al., 2017a), San Francisco Bay (Lee and Francis, 2016) and the Elkhorn Slough Estuary (Smith et al., 2015). Since the proportion of *nir* gene determines the potential denitrification rate, the denitrifying potential of *nir*S-encoding bacteria is significantly greater than that of *nir*K-encoding bacteria (Graham et al., 2010). In addition, the higher community diversity of *nir*S-encoding denitrifiers indicated that they had stronger environmental adaptiveness than *nir*K-encoding denitrifiers.

It is reasonable that higher variations in environmental factor, e.g., temperature variation between summer and winter, may lead to significant changes in biological communities. However, in the present study, the abundance and composition of *nir*S-encoding denitrifiers did not differ significantly between summer and winter. A similar finding was reported by Gao et al. (2016), they found that the

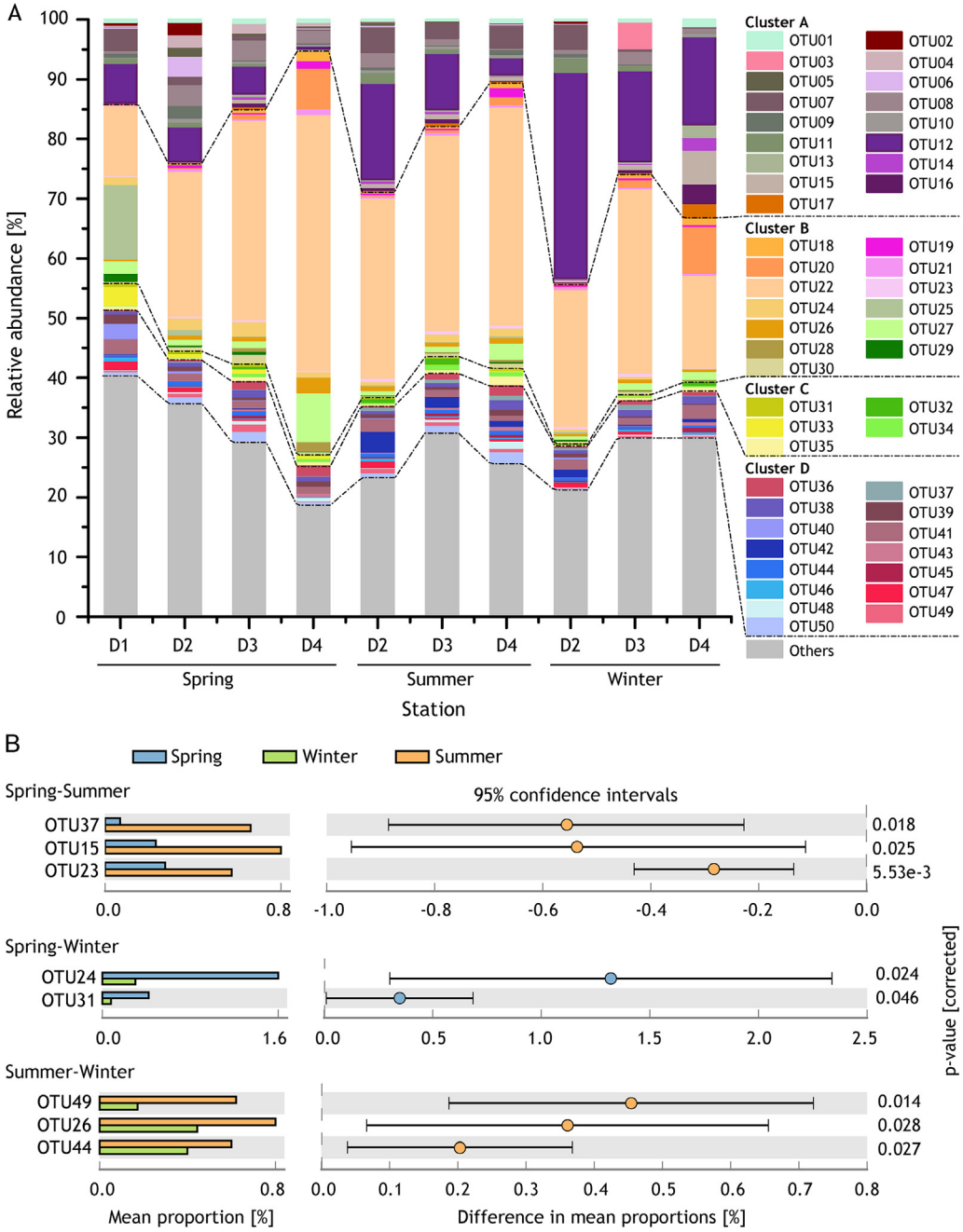

Figure 6 Taxonomic classification (A) and extended error bar plot (B) of *nir*K-encoding denitrifiers. The analysis was based on the most abundant 50 OTUs from different sampling station.

distribution and composition of *nir*S-encoding denitrifiers had a significant latitudinal differentiation, but without a seasonal shift between summer and winter. Nevertheless, greater differences were found between spring and the other seasons. For example, significant differences in abundance and composition of *nir*S-encoding denitrifiers were detected between spring and the other seasons, with NO_2^- and DO concentrations as the dominant environmental drivers (Figs. 7 and 8). Similarly, significant community differences in *nir*K-encoding denitrifiers were also detected between spring and winter. The abundance of *nir*S-encoding denitrifiers was highest in spring ($p < 0.05$), however, the abundance of *nir*K-encoding denitrifiers was lowest in spring.

The significant community differences between spring and the other seasons may be due to the different requirements of bacteria on DO, $NO_2^-$and NO_3^-, which tended to be higher in spring than in summer or winter in Daya Bay, located at a subtropical zone. In spring, the light intensity and water temperature could promote the growth of phytoplankton, which might result in high levels of DO in the overlying water. High levels of DO promote ammonia-oxidizing process at the surface of sediment, providing the substrates (e.g., NO_2^- and NO_3^-) for denitrifying bacteria (Abell et al., 2013; Smith et al., 2015). Consistently, in the present study, the evenness and diversity of *nir*S-encoding denitrifiers were positively correlated with DO, NO_2^- and NO_3^- concentrations

Table 4 Relationships between environmental factors and community composition of *nir*S genera or *nir*K OTUs based on Spearman's rank correlation of Mantel test.

	*nir*S		*nir*K	
	Mantel statistic (r)	Significance (p)	Mantel statistic (r)	Significance (p)
Salinity	0.18	0.13	0.29	0.10
pH	−0.10	0.67	−0.05	0.54
Temperature	0.13	0.19	−0.18	0.83
DO[a]	**0.44**	**0.024**	0.29	0.13
MC[b]	−0.13	0.77	−0.003	0.50
TOC[c]	−0.12	0.77	0.16	0.19
NO_2^-	**0.61**	**0.004**	0.16	0.19
NO_3^-	**0.35**	**0.025**	0.23	0.16
NH_4^+	0.03	0.41	0.12	0.29
TN[d]	−0.03	0.52	0.07	0.33

[a] DO, dissolved oxygen; [b] MC, moisture content; [c] TOC, total organic carbon; [d] TN, total nitrogen.
Bold-faced entries indicate significance values in which $p < 0.05$.

(Fig. 8). In addition, the bacterial growth can be promoted by the dissolved organic matters from phytoplankton metabolism (Li et al., 2017b). On the other hand, the competition between *nir*S-encoding and *nir*K-encoding denitrifiers could be a possible reason for the lower abundance of *nir*K-encoding denitrifiers in spring. Furthermore, the abundance and distribution of *nir*S- and *nir*K-encoding denitrifiers at station D1 were significantly different from that at the other stations. This could be due to D1 located near the Dan'ao River estuary in Daya Bay. This river lead to higher nutrients (e.g., nitrogen and phosphate) input to the bay (Ke et al., 2017). This may also influence the amount of phytoplankton and other environmental factors related to the denitrification processes.

In accordance with previous studies (Braker et al., 2000; Kim et al., 2016), the compositions of *nir*S-encoding and *nir*K-encoding denitrifiers were typical of sediment environments, with Proteobacteria being the dominant phylum. This phylum exhibits relatively high phylogenetic and phenotypic diversities, which may explain its ability to colonize a large range of aquatic environments (He and Zhang, 2016; Liu et al., 2015). Within the Proteobacteria community, Betaproteobacteria and Gammaproteobacteria were the two dominant classes of *nir*S-encoding denitrifiers in the Daya Bay. In particular, Betaproteobacteria, which has a strong ability to decompose organic matter (Fahy et al., 2006; Patel et al., 2014), was the most abundant denitrifier in the present study. In addition, a minority of *nir*S-encoding

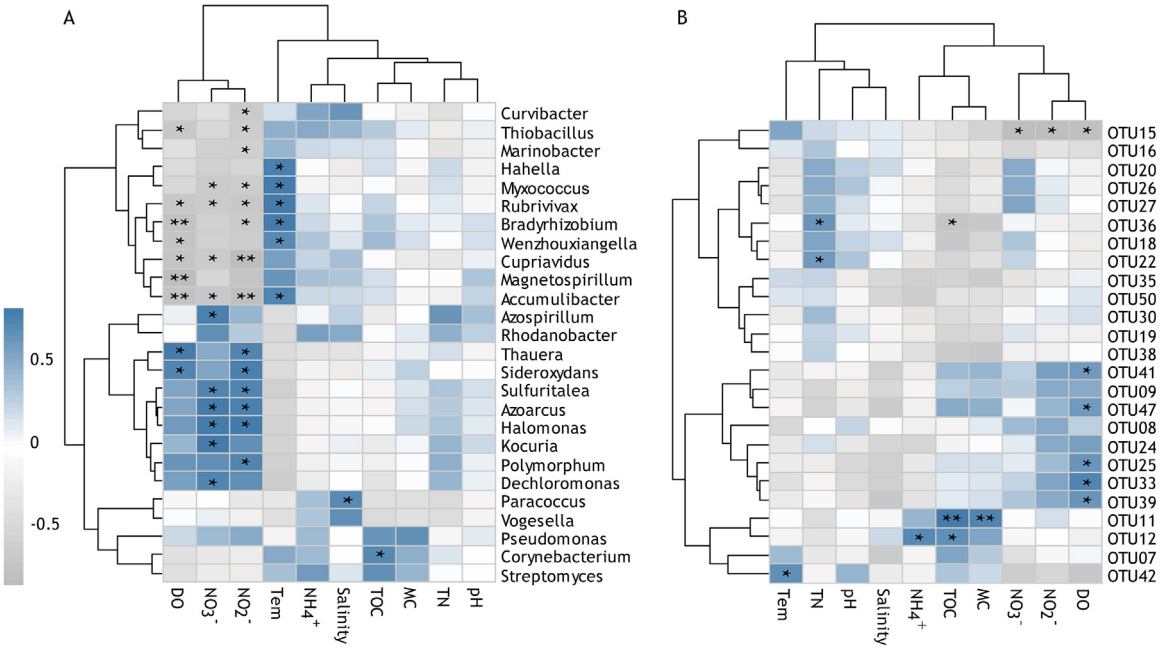

Figure 7 Correlation coefficients between environmental factors and abundance of *nir*S- (A) and *nir*K-encoding denitrifiers (B). Genera (A) and OTUs (B) with low proportions (<0.05% and 0.5%, respectively) at all sites were removed to increase readability. * and ** represent the significant correlation ($p < 0.05$) and extremely significant correlation ($p < 0.01$), respectively.

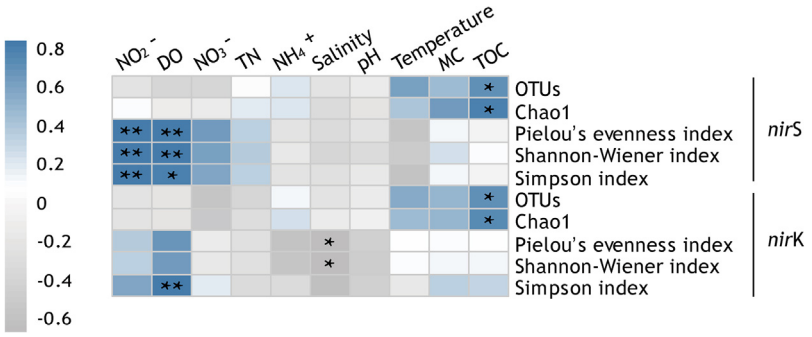

Figure 8 Correlation coefficient between richness and diversity of *nir*S- and *nir*K-encoding denitrifiers and environmental factors. * and ** represent the significant correlation ($p < 0.05$) and extremely significant correlation ($p < 0.01$), respectively.

denitrifier was assigned to the Actinobacteria phylum. Reasonably, the dominant clusters of *nir*K-encoding denitrifiers at all stations were B and A clusters, which were phylogenetically similar to Proteobacteria.

Overlying water quality and sediment characteristics such as salinity, temperature, TOC, MC, NO_2^-, and NH_4^+ concentration have been demonstrated to be associated with sediment denitrification in aquatic ecosystems (Gao et al., 2016; Giles et al., 2017; Liu et al., 2018; Long et al., 2017; Wang et al., 2013). The present study indicated that NO_2^-, NO_3^- and DO were the most important factors influencing *nir*S-encoding denitrifier communities in Daya Bay. It had been reported that denitrification occurred predominantly in suboxic and anoxic environments (Huang et al., 2011; Gao et al., 2016; Yang et al., 2015a), however, serious hypoxic condition could inhibit the growth of denitrifying bacteria due to the lack of NO_2^- and NO_3^-, since they were produced from ammonia-oxidizing reactions which need enough oxygen in the sediment (Testa et al., 2015). The deficiency of reaction substrates resulted in the dominance of *Accumulibacter* sp., *Cuprizvidus* sp., *Bradyrhizobium* sp., *Magnetospirillum* sp., and *Myxococcus* sp. in *nir*S-encoding denitrifiers communities in summer and winter, with the abundance of *Accumulibacter* sp. and *Cuprizvidus* sp. significantly higher than that in spring ($p < 0.05$). The community structure of *nir*S-encoding denitrifiers changed in spring due to the higher levels of NO_3, NO_2^- and DO. Accordingly, the genera *Azoarcus* sp., *Polymorphum* sp., *Halomonas* sp., *Pseudomonas* sp., *Azospirillum* sp., *Polymorphum* sp., and *Kocuria* sp. became the dominant denitrifying bacteria in spring. The abundances of *Azoarcus* sp. and *Halomonas* sp. were highest in spring and were positively correlated with NO_3^-, and NO_2^- concentrations ($p < 0.05$, Fig. 7A). On the other hand, correlations between the OTUs of *nir*K-encoding denitrifiers and environmental factors were relatively weak. The possible reasons for this could be due to *nir*K-encoding denitrifiers were not so sensitive to environmental variation as *nir*S-encoding denitrifiers and/or in this study the correlation coefficients were calculated based on a relatively small taxon of OTUs.

It has been reported that almost all denitrifying bacteria are heterotrophic and the spatial distribution of them is probably impacted by TOC, which is the primary electron donor for respiration by denitrifiers (Burgin and Hamilton, 2007; Huang et al., 2011; Ibekwe et al., 2016; Wu et al., 2017b). In the present study, positive relationships between the sediment TOC content and richness of denitrifying bacteria were detected ($p < 0.05$, Fig. 8), this was in agreement with previous studies (Bruesewitz et al., 2011; Small et al., 2016). In addition to the amount of organic matter, the diversity of *nir*S- and *nir*K-encoding denitrifiers may also be regulated by the quality of organic matter such as organic composition and size spectra (Liu et al., 2018; Stelzer et al., 2014). Further studies are needed to test the influences of seasonal variations in organic matter quality in sediment on denitrifiers community in Daya Bay.

Acknowledgments

The authors thank the valuable comments and suggestions from anonymous reviewers and editor. This worked was supported by the National Key Research and Development Program of China (2018YFD0900704, 2018YFD0900703), Major State Basic Research Development Program of China (973 Program, 2015CB452904), Fund of Key Laboratory of Open-Sea Fishery Development, Ministry of Agriculture, P. R. China (LOF 2018-03). Central Public-interest Scientific Institution Basal Research Fund, South China Sea Fisheries Research Institute, CAFS (2015TS25, 2017YB06), Science and Technology Planning Project of Guangdong Province (2017B030314042), Financial Fund of the Ministry of Agriculture, China (NFZX2018).

References

Abell, G.C.J., Ross, D.J., Keane, J.P., Oakes, J.M., Eyre, B.D., Robert, S.S., Volkman, J.K., 2013. Nitrifying and denitrifying microbial communities and their relationship to nutrient fluxes and sediment geochemistry in the Derwent Estuary, Tasmania. Aquat. Microb. Ecol. 70 (1), 63–75, http://dx.doi.org/10.3354/ame01642.

Alcántara-Hernández, R.J., Centeno, C.M., Ponce-Mendoza, A., Batista, S., Merino-Ibarra, M., Campo, J., Falcón, L.I., 2014. Characterization and comparison of potential denitrifiers in microbial mats from King George Island, Maritime Antarctica. Polar Biol. 37 (3), 403–416.

Baker, H.B., Kröger, B., Brooks, P.J., Smith, R.K., Czarnecki, J.M., 2015. Investigation of denitrifying microbial communities within an agricultural drainage system fitted with low-grade weirs. Water Res. 87, 193–201, http://dx.doi.org/10.1016/j.watres.2015.09.028.

Bolger, A.M., Lohse, M., Usadel, B., 2014. Trimmomatic: a flexible trimmer for illumina sequence data. Bioinformatics 30 (15), 2114–2120, http://dx.doi.org/10.1093/bioinformatics/btu170.

Bowen, J.L., Babbin, A.R., Kearns, P.J., Ward, B.B., 2014. Connecting the dots: linking nitrogen cycle gene expression to nitrogen fluxes in marine sediment mesocosms. Front. Microbiol. 5, 429, http://dx.doi.org/10.3389/fmicb.2014.00429.

Braker, G., Zhou, J., Wu, L., Devol, A.H., Tiedje, J.M., 2000. Nitrite reductase genes (*nir*K and *nir*S) as functional markers to investigate diversity of denitrifying bacteria in Pacific Northwest marine sediment communities. Appl. Environ. Microb. 66 (5), 2096–2104, http://dx.doi.org/10.1128/AEM.66.5.2096-2104.2000.

Bruesewitz, D.A., Hamilton, D.P., Schipper, L.A., 2011. Denitrification potential in lake sediment increases across a gradient of catchment agriculture. Ecosystems 14 (3), 341–352, http://dx.doi.org/10.1007/s10021-011-9413-2.

Burgin, A.J., Hamilton, S.K., 2007. Have we overemphasized the role of denitrification in aquatic ecosystems? A review of nitrate removal pathways. Front. Ecol. Environ. 5 (2), 89–96, https://www.jstor.org/stable/20440584.

Chen, X., Peltier, E., Sturm, B.S., Young, C.B., 2013. Nitrogen removal and nitrifying and denitrifying bacteria quantification in a stormwater bioretention system. Water Res. 47 (4), 1691–1700, http://dx.doi.org/10.1016/j.watres.2012.12.033.

Chen, J., Ying, G., Liu, Y., Wei, X., Liu, S., He, L., Yang, Y., Chen, F., 2017. Nitrogen removal and its relationship with the nitrogen-cycle genes and microorganisms in the horizontal subsurface flow constructed wetlands with different design parameters. J. Environ. Sci. Heal. 52 (8), 804–818, http://dx.doi.org/10.1080/10934529.2017.1305181.

Fahy, A., McGenity, T.J., Timmis, K.N., Ball, A.S., 2006. Heterogeneous aerobic benzene-degrading communities in oxygen-depleted groundwaters. FEMS Microbiol. Ecol. 58 (2), 260–270, http://dx.doi.org/10.1111/j.1574-6941.2006.00162.x.

Fish, J.A., Chai, B., Wang, Q., Sun, Y., Brown, C.T., Tiedje, J.M., Cole, J.R., 2013. FunGene: the functional gene pipeline and repository. Front Microbiol. 4, 291, http://dx.doi.org/10.3389/fmicb.2013.00291.

Gao, J., Hou, L., Zheng, Y., Liu, M., Yin, G., Li, X., Lin, X., Yu, C., Wang, R., Jiang, X., Sun, X., 2016. *nir*S-Encoding denitrifier community composition, distribution, and abundance along the coastal wetlands of China. Appl. Microbiol. Biotechnol. 100 (19), 8573–8582, http://dx.doi.org/10.1007/s00253-016-7659-5.

GB/T 12763.4-2007, 2007. Specifications for oceanographic survey – Part 4: Survey of chemical parameters in sea water. Standards Press of China, Beijing, 17–22, (in Chinese).

Giles, E.M., Daniell, J.T., Baggs, M.E., 2017. Compound driven differences in N_2 and N_2O emission from soil; the role of substrate use efficiency and the microbial community. Soil Biol. Biochem. 106, 90–98, http://dx.doi.org/10.1016/j.soilbio.2016.11.028.

Glockner, A.B., Jüngst, A., Zumft, W.G., 1993. Copper-containing nitrite reductase from Pseudomonas aureofaciens is functional in a mutationally cytochrome cd1-free background (NirS-) of *Pseudomonas stutzeri*. Arch. Microbiol. 160 (1), 18, http://dx.doi.org/10.1007/BF00258141.

Graham, D., Trippett, C., Dodds, W., O'Brien, J., Banner, E., Head, I., Smith, M., Yang, R., Knapp, C., 2010. Correlations between in situ denitrification activity and nir-gene abundances in pristine and impacted prairie streams. Environ. Pollut. 158 (10), 3225–3229, http://dx.doi.org/10.1016/j.envpol.2010.07.010.

Hallin, S., Lindgren, P.E., 1999. PCR detection of genes encoding nitrite reductase in denitrifing bacteria. Appl. Environ. Microbiol. 65 (4), 1652–1657.

He, T., Zhang, X., 2016. Characterization of bacterial communities in deep-sea hydrothermal vents from three oceanic regions. Mar. Biotechnol. 18 (2), 232–241, http://dx.doi.org/10.1007/s10126-015-9683-3.

Hollister, E.B., Engledow, A.S., Hammett, A.J.M., Provin, T.L., Wilkinson, H.H., Gentry, T.J., 2010. Shifts in microbial community structure along an ecological gradient of hypersaline soils and sediments. ISME J. 4, 829–838, http://dx.doi.org/10.1038/ismej.2010.3.

Huang, S., Chen, C., Wu, Y., Wu, Q., Zhang, R., 2011. Characterization of depth-related bacterial communities and their relationships with the environmental factors in the river sediments. World J. Microbiol. Biotechnol. 27 (11), 2655–2664, http://dx.doi.org/10.1007/s11274-011-0739-x.

Ibekwe, A.M., Ma, J., Murinda, S., Reddy, G.B., 2016. Bacterial community dynamics in surface flow constructed wetlands for the treatment of swine waste. Sci. Total Environ. 544 (15), 68–76, http://dx.doi.org/10.1016/j.scitotenv.2015.11.139.

Jiang, T., Chen, F., Yu, Z., Lu, L., Wang, Z., 2016. Size-dependent depletion and community disturbance of phytoplankton under intensive oyster mariculture based on HPLC pigment analysis in Daya Bay, South China Sea. Environ. Pollut. 219, 804–814, http://dx.doi.org/10.1016/j.envpol.2016.07.058.

Ke, Z., Tan, Y., Huang, L., Zhao, C., Jiang, X., 2017. Spatial distributions of $\delta^{13}C$, $\delta^{15}N$ and C/N ratios in suspended particulate organic matter of a bay under serious anthropogenic influences: Daya Bay, China. Mar. Pollut. Bull. 114 (1), 183–191, http://dx.doi.org/10.1016/j.marpolbul.2016.08.078.

Keeney, D.R., Nelson, D.W., 1982. Inorganic forms of nitrogen. In: Page, A.L. (Ed.), Methods of Soil Analysis. Part 2. Chemical and Microbiological Properties. American Society of Agronomy, Inc., Soil Science Society of America, Inc., Madison, 643–698.

Kim, H., Bae, H., Reddy, K.R., Ogram, A., 2016. Distributions, abundance and activities of microbes associated with the nitrogen cycle in riparian and stream sediments of a river tributary. Water Res. 106, 51–61, http://dx.doi.org/10.1016/j.watres.2016.09.048.

Lee, J.A., Francis, C.A., 2016. Spatiotemporal characterization of San Francisco Bay denitrifying communities: a comparison of *nir*K and *nir*S diversity and abundance. Microb. Ecol. 73 (2), 271–284, http://dx.doi.org/10.1007/s00248-016-0865-y.

Li, F., Li, M., Shi, W., 2017a. Distinct distribution patterns of proteobacterial *nir*K- and *nir*S-type denitrifiers in the Yellow River estuary, China. Can. J. Microbiol. 63 (8), 708–718, http://dx.doi.org/10.1139/cjm-2017-0053.

Li, J., Jiang, X., Jing, Z., Li, G., Chen, Z., Zhou, L., Zhao, C., Liu, J., Tan, Y., 2017b. Spatial and seasonal distributions of bacterioplankton in the Pearl River Estuary: The combined effects of riverine inputs, temperature, and phytoplankton. Mar. Pollut. Bull. 125 (1–2), 199–207, http://dx.doi.org/10.1016/j.scitotenv.2017.02.208.

Liu, X., Hu, H., Liu, Y., Xiao, K., Cheng, F., Li, J., Xiao, T., 2015. Bacterial composition and spatiotemporal variation in sediments of Jiaozhou Bay, China. J. Soil. Sediment 15 (3), 732–744, http://dx.doi.org/10.1007/s11368-014-1045-7.

Liu, W., Yao, L., Jiang, X., Guo, L., Cheng, X., Liu, G., 2018. Sediment denitrification in Yangtze lakes is mainly influenced by environmental conditions but not biological communities. Sci. Total Environ. 616–617, 978–987, http://dx.doi.org/10.1016/j.scitotenv.2017.10.221.

Long, X.E., Shen, J.P., Wang, J.T., Zhang, L.M., Di, H., He, J.Z., 2017. Contrasting response of two grassland soils to N addition and moisture levels: N_2O emission and functional gene abundance. J. Soil. Sediment 17 (2), 384–392, http://dx.doi.org/10.1007/s11368-016-1559-2.

Ma, Y., Ke, Z., Huang, L., Tan, Y., 2014. Identification of human-induced perturbations in Daya Bay, China: Evidence from plankton size structure. Cont. Shelf Res. 72, 10–20, http://dx.doi.org/10.1016/j.csr.2013.10.012.

Magoc, T., Salzberg, S.L., 2011. FLASH: Fast length adjustment of short reads to improve genome assemblies. Bioinformatics 27 (21), 2957–2963, http://dx.doi.org/10.1093/bioinformatics/btr507.

Ni, Z., Huang, X., Zhang, X., 2015. Picoplankton and virioplankton abundance and community structure in Pearl River Estuary and

Daya Bay, South China. J. Environ. Sci.-China 32, 146–154, http://dx.doi.org/10.1016/j.jes.2014.12.019.

Parks, D.H., Tyson, G.W., Hugenholtz, P., Beiko, R.G., 2014. STAMP: Statistical analysis of taxonomic and functional profiles. Bioinformatics 30 (21), 3123–3124, http://dx.doi.org/10.1093/bioinformatics/btu494.

Patel, V., Munot, H., Shouche, Y.S., Madamwar, D., 2014. Response of bacterial community structure to seasonal fluctuation and anthropogenic pollution on coastal water of Alang-Sosiya ship breaking yard, Bhavnagar, India. Bioresource Technol. 161, 362–370, http://dx.doi.org/10.1016/j.biortech.2014.03.033.

Reyna, L., Wunderlin, D.A., Genti-Raimondi, S., 2010. Identification and quantification of a novel nitrate-reducing community in sediments of Suquía River basin along a nitrate gradient. Environ. Pollut. 158 (5), 1608–1614, http://dx.doi.org/10.1016/j.envpol.2009.12.014.

Shrewsbury, L.H., Smith, J.L., Huggins, D.R., Carpenter-Boggs, L., Reardon, C.L., 2016. Denitrifier abundance has a greater influence on denitrification rates at larger landscape scales but is a lesser driver than environmental variables. Soil Biol. Biochem. 103, 221–231, http://dx.doi.org/10.1016/j.soilbio.2016.08.016.

Small, G.E., Finlay, J.C., Mckay, R.M.L., Rozmarynowycz, M.J., Brovold, S., Bullerjahn, G.S., Spokas, K., Sterner, R.W., 2016. Large differences in potential denitrification and sediment microbial communities across the Laurentian great lakes. Biogeochemistry 128 (3), 353–368, http://dx.doi.org/10.1007/s10533-016-0212-x.

Smith, J.M., Mosier, A.C., Francis, C.A., 2015. Spatiotemporal relationships between the abundance, distribution, and potential activities of ammonia-oxidizing and denitrifying microorganisms in intertidal sediment. Microb. Ecol. 69 (1), 13–24, http://dx.doi.org/10.1007/s00248-014-0450-1.

Song, X., Huang, L., Zhang, J., Huang, H., Li, T., Su, Q., 2009. Harmful algal blooms (HABs) in Daya Bay, China: an in situ study of primary production and environmental impacts. Mar. Pollut. Bull. 58 (9), 1310–1318, http://dx.doi.org/10.1016/j.marpolbul.2009.04.030.

Stelzer, R.S., Scott, J.T., Bartsch, L.A., Parr, T.B., 2014. Particulate organic matter quality influences nitrate retention and denitrification in stream sediments: evidence from a carbon burial experiment. Biogeochemistry 119, 387–402, http://dx.doi.org/10.1007/s10533-014-9975-0.

Tang, Y., Zhang, X., Li, D., Wang, H., Chen, F., Fu, X., Fang, X., Sun, X., Yu, G., 2016. Impacts of nitrogen and phosphorus additions on the abundance and community structure of ammonia oxidizers and denitrifying bacteria in Chinese fir plantations. Soil Biol. Biochem. 103, 284–293, http://dx.doi.org/10.1016/j.soilbio.2016.09.001.

Testa, J.M., Brady, D.C., Cornwell, J.C., Owens, M.S., Sanford, L.P., Newell, C.R., Suttles, S.E., Newell, R.I.E., 2015. Modeling the impact of floating oyster (*Crassostrea virginica*) aquaculture on sediment-water nutrient and oxygen fluxes. Aquacult. Environ. Interact. 7, 205–222, http://dx.doi.org/10.3354/aei00151.

Throbäck, I.N., Enwall, K., Jarvis, Å., Hallin, S., 2004. Reassessing PCR primers targeting *nir*S, *nir*K and *nos*Z genes for community surveys of denitrifying bacteria with DGGE. FEMS Microbiol. Ecol. 49 (3), 401–417, http://dx.doi.org/10.1016/j.femsec.2004.04.011.

Wang, Y.S., Lou, Z.P., Sun, C.C., Wu, M.L., Han, S.H., 2006. Multivariate statistical analysis of water quality and phytoplankton characteristics in Daya Bay, China, from 1999 to 2002. Oceanologia 48 (2), 193–211.

Wang, C., Zhu, G., Wang, Y., Wang, S., Yin, C., 2013. Nitrous oxide reductase gene (*nos*Z) and N_2O reduction along the littoral gradient of a eutrophic freshwater lake. J. Environ. Sci. 25, 44–52, http://dx.doi.org/10.1016/S1001-0742(12)60005-9.

Wu, F., Huang, J., Dai, M., Liu, H., Huang, H., 2016. Using ciliates to monitor different aquatic environments in Daya Bay, South China Sea. Can. J. Zool. 94 (4), 265–273.

Wu, M., Wang, Y., Wang, Y., Yin, J., Dong, J., Jiang, Z., Sun, F., 2017a. Scenarios of nutrient alterations and responses of phytoplankton in a changing Daya Bay, South China Sea. J. Marine Syst. 165, 1–12, http://dx.doi.org/10.1016/j.jmarsys.2016.09.004.

Wu, H., Wang, X., He, X., Zhang, S., Liang, R., Shen, J., 2017b. Effects of root exudates on denitrifier gene abundance, community structure and activity in a micro-polluted constructed wetland. Sci. Total Environ. 598, 697–703, http://dx.doi.org/10.1016/j.scitotenv.2017.04.150.

Yang, A., Zhang, X., Agogué, H., Dupuy, C., Gong, J., 2015a. Contrasting spatiotemporal patterns and environmental drivers of diversity and community structure of ammonia oxidizers, denitrifiers, and anammox bacteria in sediments of estuarine tidal flats. Ann. Microbiol. 65 (2), 879–890, http://ir.yic.ac.cn/handle/133337/7357.

Yang, J., Ma, L., Jiang, H., Wu, G., Dong, H., 2015b. Salinity shapes microbial diversity and community structure in surface sediments of the Qinghai-Tibetan Lakes. Sci. Rep. 6, 25078, http://dx.doi.org/10.1038/srep25078.

Yi, N., Gao, Y., Zhang, Z., Wang, Y., Liu, X., Zhang, L., 2015. Response of spatial patterns of denitrifying bacteria communities to water properties in the stream inlets at Dianchi Lake, China. Int. J. Genomics 9, 1–11, http://dx.doi.org/10.1155/2015/572121.

Zheng, Y., Hou, L., Liu, M., Gao, J., Yin, G., Li, X., Deng, F., Lin, X., Jiang, X., Chen, F., Zong, H., Zhou, J., 2015. Diversity, abundance, and distribution of *nir*S-harboring denitrifiers in intertidal sediments of the Yangtze estuary. Microb. Ecol. 70 (1), 30–40, http://dx.doi.org/10.1007/s00248-015-0567-x.

Oceanologia (2019) 61, 321—330

Available online at www.sciencedirect.com

ScienceDirect

journal homepage: www.journals.elsevier.com/oceanologia/

ORIGINAL RESEARCH ARTICLE

Linking sea level dynamic and exceptional events to large-scale atmospheric circulation variability: A case of the Seine Bay, France

Imen Turki*, **Nicolas Massei**, **Benoit Laignel**

Continental and Coastal Morphodynamic Laboratory, Normandy University, Rouen, France

Received 16 September 2018; accepted 15 January 2019
Available online 1 February 2019

KEYWORDS
Sea level dynamic;
Envelope approach;
Demodulated surges;
Storm events;
Climate patterns

Summary In this study, the multi-time-scale variability of the South English Channel (case of the Seine Bay, North France) sea level and its exceptional events have been investigated in relation with the global climate patterns by the use of wavelet multi-resolution decomposition techniques. The analysis has been focused on surges demodulating by an envelope approach. The low-frequency components of the interannual (2.1-yr, 4-yr, 7.8-yr) and the interdecadal (15.6-yr and 21.2-yr) time-scales, extracted from 46-years demodulated surges, have been correlated to 36 exceptional stormy events according to their intensity. Results have revealed five categories of storms function on their correlation with the interannual and the interdecadal demodulated surges: events with high energy are manifested at the full scales while moderate events are only observed at the interannual scales. The succession of storms is mainly carried by the last positive oscillations of the interannual and the interdecadal scales. A statistical downscaling approach integrating the discrete wavelet multi-resolution analysis for each time-scale has been used to investigate the connection between the local dynamic of surges and the global atmospheric circulation from SLP composites. This relation illustrates dipolar patterns of high-low pressures suggesting positive anomalies at the interdecadal scales of 15.6-yr and 21.3-yr and the interannual scales of 4-yr while negative anomalies at 7.8-yr should be related to a series of physical mechanisms linked to the North-Atlantic and ocean/atmospheric circulation oscillating at the same time-scales. The increasing storm frequency is probably related to the Gulf Stream variation and its weakening trend in the last years.

* Corresponding author at: Continental and Coastal Morphodynamic Laboratory, Normandy University, Rouen 76821, France. Tel. +0033 235146952; fax: +0033 235140019.
E-mail addresses: imen.turki@univ-rouen.fr (I. Turki), nicolas.massei@univ-rouen.fr (N. Massei), benoit.laignel@univ-rouen.fr (B. Laignel).
Peer review under the responsibility of Institute of Oceanology of the Polish Academy of Sciences.

Production and hosting by Elsevier

https://doi.org/10.1016/j.oceano.2019.01.003

1. Introduction

During the last decades and in relation with the global evolution induced by climate change, the oceanographic scientific community have devoted their efforts to improve our understanding of the impacts of climate fluctuations on coastal hydrodynamic variability, in particular during stormy events. Several approaches have been extensively employed to investigate the extreme physical dynamic of the sea level and simulate the impact of the global climate oscillations for providing different coastal projections. For this reason, determining how and to what extent the large-scale climate oscillations can be identified in the oceanographic parameters and storm surges is required.

In the present context of global changes, the combined effects of the sea level rise and the land loss are commonly mentioned as a consequence of climate variability (e.g., Devoy, 2008; Nicholls et al., 2010). In the same context, the land loss itself is often a result of an increasing storminess responsible for coastal erosion (Stive et al., 2002) or flooding areas whose repeated restoration might be inefficient and the land is abandoned.

The acceleration of the sea level rise along the coastal mid-Atlantic in recent decades, where the climate is strongly influenced by the Gulf Stream (GS), is possibly caused by the Atlantic Meridional Overturning Circulation (AMOC) and its upper branch, the GS. Consequently, coastal communities have observed a significant increase in flooding frequency in the last years (Mitchell et al., 2013).

By the hypothesis that the variation in the GS location and strength is responsible on changes in the sea surface height gradient across the GS and, consequently, the sea level variability on both sides of the stream, the elevation of the sea surface gradient is proportional to the surface velocity of the GS. Then, the weakening of the GS strength will raise the sea level northwest of the GS; which is suggested by several recent studies (e.g., Ezer and Corlett, 2012; Ezer et al., 2013; Levermann et al., 2005; Sallenger et al., 2012). The impact of the GS variation on coastal sea level has been demonstrated by many observations (Sweet et al., 2009) and circulations models (Ezer, 2001) of the Atlantic Oceans and, also, by Global Climate models (Yin et al., 2009).

The effects of continuous changes in atmospheric patterns on sea level dynamic and stormy events have been investigated through a series of probabilistic approaches based on of climate indices by the use of nonstationary analyses of extremes (e.g. Minguez et al., 2012). Marcos et al. (2012) have related changes in the median and the higher-order percentiles of observed water levels in the Mediterranean Sea by the large-scale atmospheric circulation of winter North Atlantic Oscillation (NAO). Moreover, Menendez and Woodworth (2010) have demonstrated that changes in extreme events are due to changes in mean sea levels; they have reported the important role of the NAO and the Arctic Oscillation (AO) indices on the extreme sea level variability along the European coasts. Then, Masina et al. (2015) have shown a similar behavior between the regional and global scales at Venice and Porto Corsini (Adriatic Sea) from a detailed analysis of the annual mean sea level evolution. They have evidenced a relation between increasing extreme water levels since the 1990s and changes in wind regime, in particular, the intensification of Bora and Sirocco winds events whose intensity and frequency have been increased after the second half of the 20th century.

One of the challenges in investigating the sea level dynamic with global patterns related to Climate circulation is how to identify the multi-scale variability associated with the different physical processes involved.

In the framework of the further altimetry mission of Surface Water and Ocean Topography (SWOT), planned for launch in 2021, Turki et al. (2015) have investigated the low-frequencies of the sea level variability in the eastern English Channel (NW France) at annual and inter-monthly scales. Such changes result from the combining effect of meteorological and oceanography forces with an important contribution of the hydrological signal coming from the Seine river; the climate signature of the NAO circulation is also observed at the annual scales. Massei et al. (2017) have focused on the relation of the local Seine hydrological variability with the global climate patterns, and the time-scale dependence of this connection by developing a downscaling modeling basing on an empirical statistical approach. Their works have shown that the multi-scale links between the sea level pressure (SLP) and the regional hydrological variations are statistically significant for frequencies greater than 2 years (3.2-yr, 7.2-yr and 19.3-yr); they should be caused by coupling effects of North-Atlantic oceanic paths and atmospheric circulation.

In this context, the present research has been carried out to investigate the multi-time-scale variability of the sea level in the Seine Bay (South English Channel) and its exceptional events in relation with the global climate patterns by the use of high-resolution spectral techniques. A special focus is devoted to the connection of stormy events and their occurrence with the atmospheric circulation. The paper is organized as follow. After the introduction, the second section presents the data and the methodological approach used. Section 3 provides all results and discussions of the multi-scale sea level variability in relation to the exceptional events and the teleconnections of the atmospheric circulation. Finally, some concluding remarks and further researches are presented in Section 4.

2. Data and methodological approach

2.1. Sea level and climatological data set

Hourly sea level measurements, extracted from Le Havre tide gauge between 1964 and 2010, have been provided by the National Navy Hydrographic Service (http://refmar.shom.fr/en/home); see Fig. 1. Climatological data in the North Atlantic zone have been extracted from the National Center for Environmental Prediction and National Center for Atmospheric Research-1 (NCEP/NCAR-1) reanalysis (Kalnay et al., 1996) with a time resolution of a month. This dataset represents the North Atlantic atmospheric dynamics over the North Atlantic region (75°W–35°E and 15°E–75°N) with a horizontal spatial resolution of 2.5*2.5 (i.e., 1125 grid-points). As suggested by previous researches, SLP field is considered as a good indicator for the local hydro-climatic conditions (e.g., Massei et al., 2017; Ruigar and Golian, 2015); it has been used in the present analysis and will be

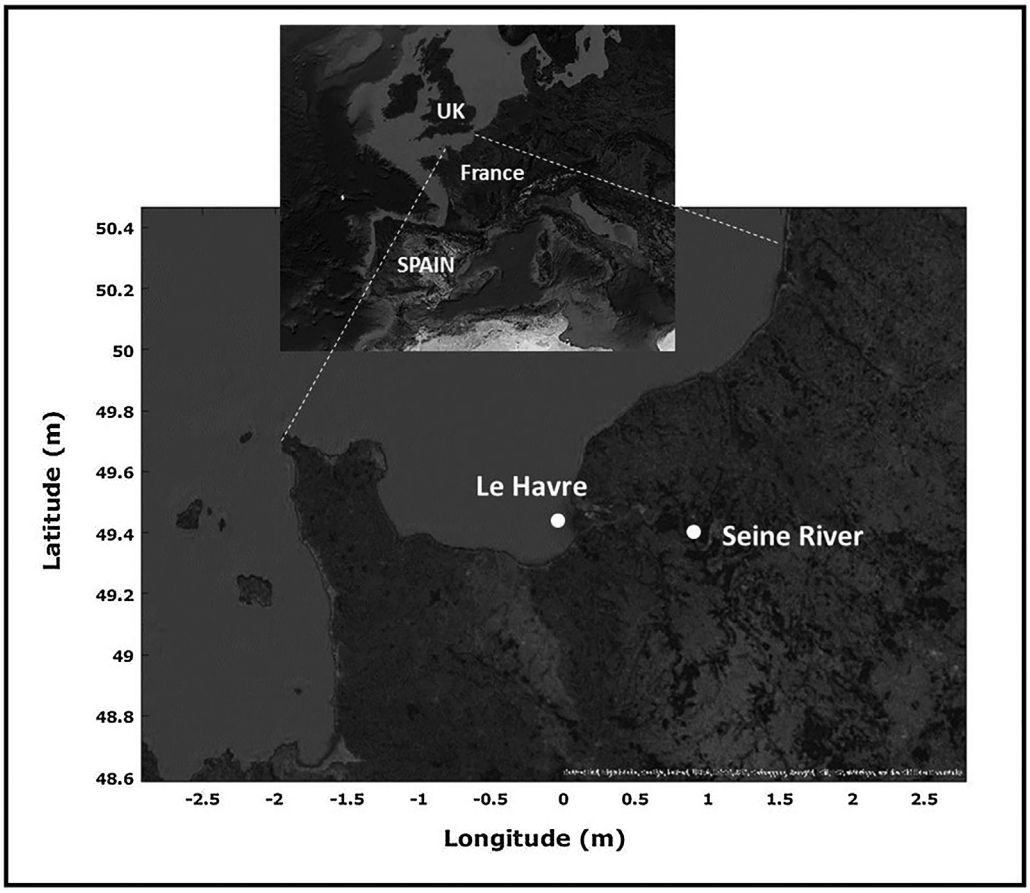

Figure 1 Study area: the Seine Bay located in the south-eastern English Channel (NW France).

referred to "large scale" in the subsequent parts of the analysis while local scale" refers to the sea level.

2.2. Tidal modulation and residual sea level

The total sea level height, resulting from the astronomical and the meteorological processes, exhibits a temporal non-stationarity explained by the combining effects of the long-term trend in the mean sea level, the modulation by the deterministic tidal component and the stochastic signal of surges, and the interactions between tides and surges. The occurrence of extreme sea levels is controlled by periods of high astronomically generated tides, in particular at inter-annual scales when two phenomena of precession cause systematic variation of high tides. The modulation of tides contributes to the enhanced risk of coastal flooding.

The separation between tidal and non-tidal signals is an important task in any analysis of sea level timeseries. The stochastic component associated with the non-tidal variation in the Seine Bay, extracted from Le Havre tide gauge, is mainly explained by the meteorological and the hydrological effects of the Seine river reaching the bay during flood events. By the hypothesis of independence between the astronomical and the stochastic effects, the non-linear relationship between both components is not considered to separate the tidal modulation from the total sea level.

Using the classical harmonic analysis, the tidal component has been modeled as the sum of a finite set of sinusoids at specific frequencies to determine the determinist phase/amplitude of each sinusoid and predict the astronomical component of tides. In order to obtain a quantitative assessment of the non-tidal contribution in storminess changes, technical methods basing on MATLAB t-tide package have been used to estimate year-by-tear tidal constituents. The sea level measurements present strong tidal modulations which have long been recognized by their significant effects on long-term changes (e.g., Gratiot et al., 2008); in particular, those produced at inter-annual scales. These processes result from 18.61-year lunar nodal cycle and the 8.85-year cycle of lunar perigee and influence the sea level as a quasi 4.4-year cycle (Menendez and Woodworth, 2010; Wood, 2001; Woodworth and Blackman, 2004).

A year-by-year tidal simulation (Shaw and Tsimplis, 2010) has been applied to the sea level timeseries to determine the amplitude and the phase of tidal modulations using harmonic analysis fitted to 18.61, 9.305, 8.85, and 4.425-year sinusoidal signals (Pugh, 1987).

2.3. Demodulated surges by the use of envelope technique

Once the annual sea level trend and the tidal components have been removed, the residual signal has been used as 'surges' to be demodulated by an envelope approach, a preliminary step before the frequency decomposition by the multi-resolution wavelet.

Determining envelopes of a statistical signal is generally used for detecting the amplitude modulation. In the present research, the objective is to detect if any (and what) underlying low- frequency component controls the variations of the sea level signal amplitude. The most known envelope is the analytic one based on the Hilbert transform. However and in practice, calculating envelopes of real signals in environmental contexts is different from analytic ones, although these uniquely define envelopes (Yang, 2017). The most methods for envelope identification depend on extrema detection followed by a low-pass filter. The envelopes of real signals are obtained using a spline interpolation from extrema sequences, as used for instance in the empirical mode decomposition (EMD) (Massei and Fournier, 2012; Massei et al., 2017). Here, the present work is more particularly interested in high surges with extreme values from considering only the upper envelope of a real-valued surge signal by identifying all the local maxima and interpolating between them using a cubic spline.

2.4. Atmospheric composite maps

The relationship between the local sea level variability and the global atmospheric patterns has been investigated to identify the physical links at different time-scales by the use of the Sea Level Pressure (SLP) field. The procedure for investigating this global/local scale connection consists in decomposing both the SLP field and the surge signal across the different time-scales into a series of wavelet details (WD) using a multiresolution analysis.

Then, for each wavelet time-scale, an associated SLP composite map is constructed by: (1) calculating the point-wise (i.e. at each grid-point) positive temporal mean of the SLP field WD at this scale for high values of the corresponding surge WD, (2) similarly, calculate the point-wise negative temporal mean of SLP field WD for low values of surge WD, (3) computing the difference positive mean-negative mean SLP value at each grid point (Massei et al., 2017). Here, "high" and "low" values of sea level WD have been chosen such as they exceed +0.5 or fall below −0.5 standard deviation (SD). Statistically significant regions have been estimated for each wavelet scale from the highest to the lowest frequencies; the degrees of freedom has been adjusted according to the wavelet scale and the "effective" sample size N from the actual sample size N has been calculated according to the first order autocorrelation coefficient AR[1] of each of the two positive and negative mean SLP WD (Mitchell et al., 1966).

3. Results and discussions

3.1. Sea level dynamic and exceptional events in the Seine Bay

The sea level variability in the Seine Bay has been investigated from the 46-year record. Once the tidal components and the regressive trend of the sea level rise were removed, the signal of surges has been demodulated by an envelope approach; then, the upper envelope has been calculated by joining local extrema and using a spline function (Fig. 2a).

Taking the Fourier transform of the original and the demodulated surges, the spectrums S_S and S_{SM} have been simulated in Fig. 2b with the aim to illustrate the different frequency components characterizing each signal. Compar-

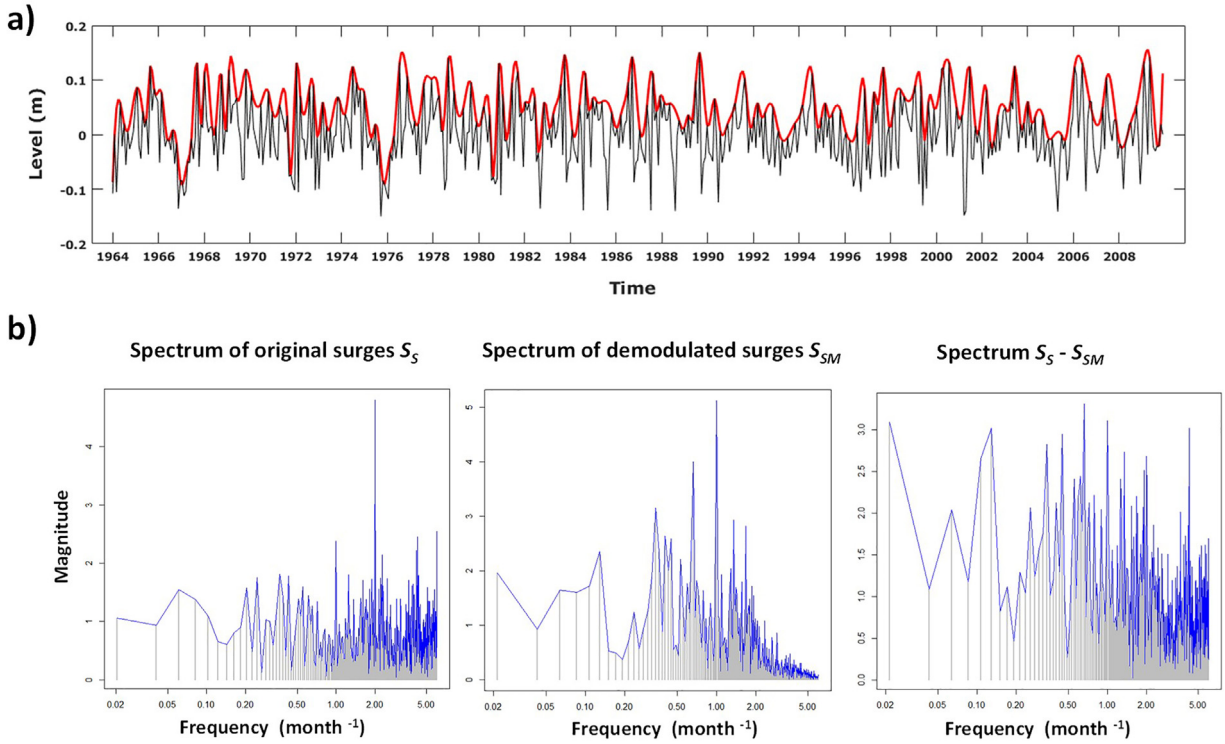

Figure 2 (a) The maxima envelope (thick line) of the mean monthly surges (thin line) between 1961 and 2010; (b) spectrum of the original S_S, demodulated S_{SM} surges, and the difference $S_S - S_{SM}$.

ing both spectrums shows that the interpolative envelope contains the message signal of the original surges: similarities of the main components with the most vibration of the high-frequency components in the original signal vs a clear illustration of low-frequency components in the demodulated signal. Hence, the simulated upper envelope can be used to modulate the main information of nonstationary surges.

The interpolative envelope, used for demodulating nonstationary surges, contains the lower chirp signal component with the fault characteristic frequency and its harmonic interferences. The demodulated surges cover a series of frequencies with different time-periods able to reconstruct the most variability of the original signal. This result confirms the last investigations reported by Yang (2017); they have concluded that the envelopes of real-valued stationary and nonstationary signals contain some low-frequency components of the original signal and some new components generated by the new-Nyquist extrema sampling.

Fig. 3 displays the continuous wavelet spectrum of the total sea level (a), surges (b) and the demodulated surges (c). The first spectrum (Fig. 3a) shows that most of the energy is homogenously located around 1-yr with more than 90% of the total variance. By removing the astronomical components, the signal of surges reveals the existence of frequencies lower than 1-yr, differently distributed at 2-yr and 4-yr scales; it illustrates a non-homogenous repartition during the period 1964–2010 (Fig. 3b) with two peaks of energy in both periods 1970–1980 and 2000–2001. The 2-yr and 4-yr frequencies are even more pronounced in the spectrum of the demodulated surges where the interannual and the interdecadal frequencies of 8-yr and 15-yr, respectively, are clearly structured with a high concentration of energy (Fig. 3c).

A multiresolution analysis has been applied to the demodulated surges with the aim to extract the different components explaining the total variability of the envelope. The process has resulted in the separation of 9 components, the so-called wavelet details numbered from D1 to D9.

The different wavelet details have been associated to the following time-scales: intermonthly (D1, D2 and D3), annual (D4), interannual (D5, D6 and D7) and interdecadal (D8 and D9) scales. The most part of these frequencies has been illustrated as peaks of energy in the continuous wavelet spectrum (Fig. 3c).

The focus of the present research is to investigate the key role of the low-frequency components (higher than 2-yr) with a mean explaining variance of 82.7% from the total demodulated signal (Table 1): ∼2.1-yr, ∼4-yr, ∼7.8-yr, ∼15.6-yr and ∼21.3-yr. This distribution of variance between 2-yr and 21-yr implies the importance of the large-scale variability in surges of the Seine Bay.

Similar scales, reported by Massei et al. (2017) from Seine watershed precipitations, have only presented a mean explained variance of 30% showing a low contribution of the large-scales in the total energy of the signal and highlighting the eventual weak dependence between high and low frequencies. In the case of high discrepancies between the different frequencies composing some statistical signals and with the aim to extract their low-frequency components, demodulating their evolution by the use of the envelope technique should be a useful way to investigate more deeply their large-scale behavior.

A total of 36 exceptional stormy events (from E_1 to E_{36}) produced in the Seine bay during the period 1964–2010 and with surges higher than 2-yr return period level has been extracted from REFMAR data base (Table 2). The different storms have been reported to the low-frequency components of the demodulated surges by vertical color bars (Fig. 4).

Five categories have been defined and attributed to the different storms according to their surge return period (Re): "A" with Re = 2-yr, "B" 2-yr <Re<5-yr, "C" with 5-yr <Re<10-yr, "D" with 10-yr <Re<20-yr and "E" with Re > 20-y using gray, yellow, red, purple and dark purple colors, respectively. The closing events succeeding in time within a given period (days to months) are represented in Fig. 4 by only one vertical bar whose color is attributed to the higher category of storms produced during this period.

The first two categories of storms with a moderate surge return period are related to higher frequencies and can be observed at scales smaller than ∼4-yr. For example, stormy events E_8, E_{16} and $E_{17\text{-}19}$ of the category "A" (gray box in Fig. 4) are mainly manifested at 2.1-yr and seem to be not expressed at higher scales. $E_{3\text{-}7}$, $E_{9\text{-}10}$ and $E_{32\text{-}34}$ of the category "B" (yellow box in Fig. 4) are well observed at the interannual scales 2.1-yr and 4-yr. The events E1, E_{11}, $E_{20\text{-}21}$, E_{35} and E_{36} of the category "C" (red box in Fig. 4) are manifested at the three scales 2.1-yr, 4-yr and 7.8-yr. The category "E", E_{13}, $E_{28\text{-}29}$ and $E_{30\text{-}31}$ (dark purple box in Fig. 4),

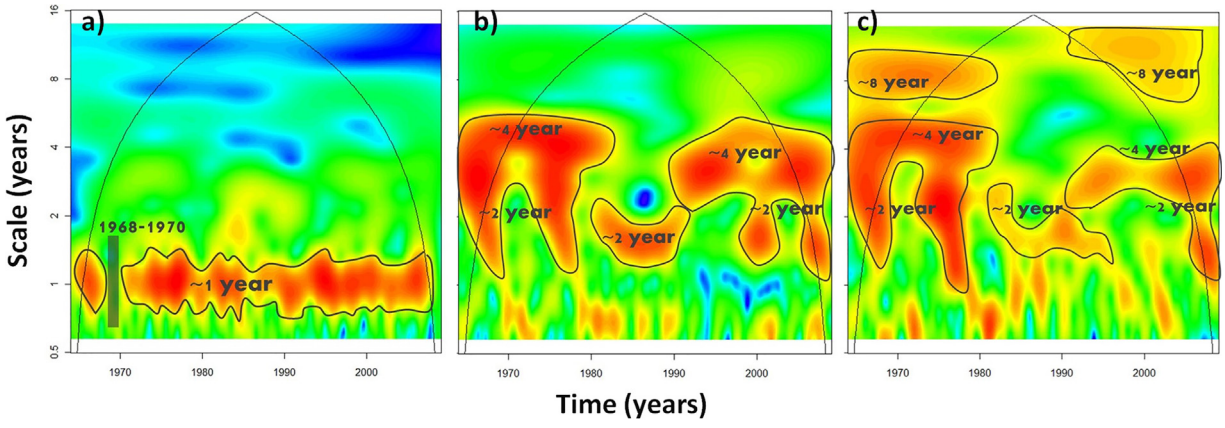

Figure 3 Continuous wavelet diagram of the monthly mean sea level: (a) the total sea level, (b) the surges and (c) the demodulated surges (maxima envelope) between 1964 and 2010.

Table 1 Equivalent Fourier period, standard deviation and energy, expressed as the percentage of total standard deviation of the maxima envelope, associated with each component (i.e. wavelet details and smooth) of Seine surges between 1964 and 2010.

Surges	D1–D4	D5	D6	D7	D8	D9	Total
Fourier period (yr)	$\leq\sim1$	~2.1	~4	~7.8	~15.6	~21.3	–
Standard deviation (m)	0.01	0.009	0.005	0.0035	0.003	0.005	–
Energy (%)	17.3	32	26	11	8	5.7	100

is fully manifested at the different time-scales while E_2, $E_{14\text{-}15}$ and $E_{23\text{-}27}$ of the category "D" (purple box in Fig. 4) pass away the lowest frequency of 21.1-yr.

According to this analysis, 36 high stormy events (Re > 2-yr) have been identified during a period of 46 years; they are of different categories depending on the surge return period and the time-scale associated with the spectral period: 19 events of category "A" with 2.1-yr, 6 events of category "B" with 4-yr, 5 events of category "C" with 7.8-yr, 3 events of each category "D" and "E" with 15.6-yr and 21.3-yr, respectively.

The distribution of storms is not homogeneous in time and their occurrence according to the different categories takes a nonstationary behavior since the number of events in a window of one-year changes in time. Results have shown that 24 among 46 years do not display any significant event (Re > 2-yr) emphasizing alternating phases of moderate energy and storminess. Moderate phases with non-significant

Table 2 List of stormy events produced between 1964 and 2010; only storms with surge return period (Re) higher than 2 years.

Number of event	Date of event	Return period of surges (Re)	Tidal cycle
E_1	20 January 1965	5–10 years	Spring tide (coefficient 102)
E_2	27 November 1965	10–20 years	Neap tide (coefficient 68)
E_3	11 March 1967	2 years	Neap tide (coefficient 86)
E_4	04 October 1967	2–5 years	Spring tide (coefficient 113)
E_5	13 November 1967	2 years	Neap tide (coefficient 63)
E_6	02 November 1967	2–5 years	Spring tide (coefficient 111)
E_7	07 January 1968	2 years	Neap tide (coefficient 50)
E_8	06 July 1969	2 years	Neap tide (coefficient 67)
E_9	06 February 1974	2 years	Spring tide (coefficient)
E_{10}	09 February 1974	2–5 years	Spring tide (coefficient 112)
E_{11}	25 December 1976	2–5 years	Neap tide (coefficient 70)
E_{12}	15 December 1979	2 years	Neap tide (coefficient 66)
E_{13}	13 December 1981	>20 years	Spring tide (coefficient 104)
E_{14}	25 October 1984	2 years	Spring tide (coefficient 100)
E_{15}	22 November 1984	10–20 years	Spring tide (coefficient 102)
E_{16}	15 October 1987	2 years	Neap tide (coefficient 28)
E_{17}	20 December 1989	2 years	Neap tide (coefficient 90)
E_{18}	03 January 1990	2 years	Spring tide (coefficient 103)
E_{19}	26 February 1990	2 years	Spring tide (coefficient 106)
E_{20}	20 January 1994	2–5 years	Neap tide (coefficient 50)
E_{21}	15 April 1994	5–10 years	Spring tide (coefficient 100)
E_{22}	19 February 1996	2 years	Spring tide (coefficient 113)
E_{23}	25 December 1999	10–20 years	Spring tide (coefficient 104)
E_{24}	22 January 2000	5–10 years	Spring tide (coefficient 106)
E_{25}	08 February 2000	2 years	Neap tide (coefficient 88)
E_{26}	04 April 2000	2 years	Spring tide (coefficient 98)
E_{27}	02 September 2000	2 years	Spring tide (coefficient 94)
E_{28}	10 October 2000	>20 years	Spring tide (coefficient 101)
E_{29}	29 October 2000	2 years	Spring tide (coefficient 95)
E_{30}	17 September 2001	>20 years	Spring tide (coefficient 115)
E_{31}	28 December 2001	2 years	Neap tide (coefficient 74)
E_{32}	08 February 2004	2 years	Spring tide (coefficient 90)
E_{33}	10 December 2004	2 years	Neap tide (coefficient 79)
E_{34}	08 April 2005	2–5 years	Spring tide (coefficient 104)
E_{35}	11 March 2008	5–10 years	Spring tide (coefficient 106)
E_{36}	09 January 2009	5–10 years	Spring tide (coefficient 108)

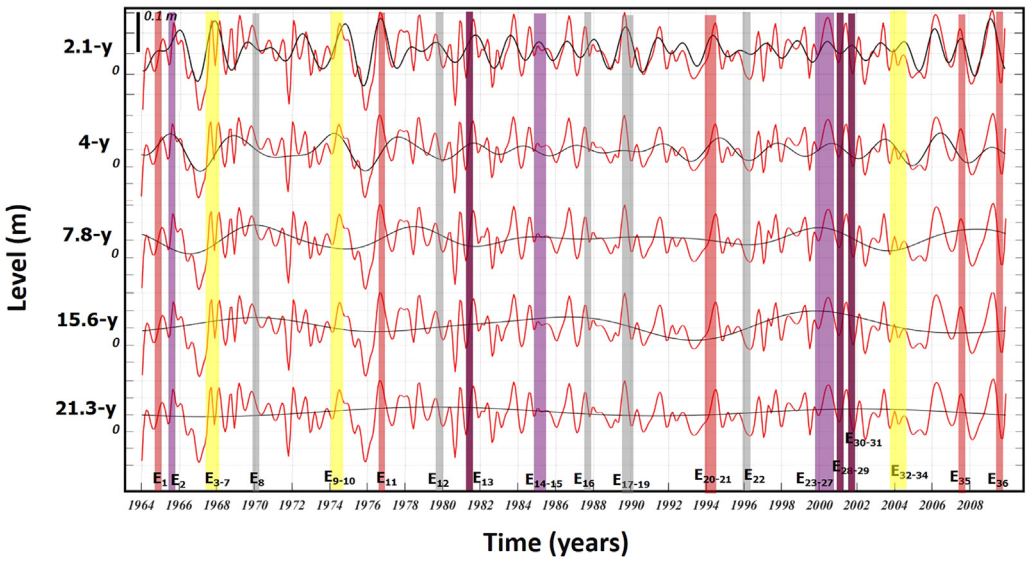

Figure 4 Multiresolution decomposition of the monthly surges, using the so-called, redundant, maximum-overlap discrete wavelet transform. Wavelet detail at scales higher than 1 year: 2.1-yr, 4-yr, 7.8-yr, 15.6-yr and 21.3-yr. The 36 exceptional stormy events with different categories function of their return period (Re), occurred during the period 1964–2010, are illustrated by colored boxes: "A" (gray line) Re = 2-yr, "B" (yellow line) 2-yr $<$ Re $<$ 5-yr, "C" (red line) 5-yr $<$ Re $<$ 10-yr, "D" (purple line) 10-yr $<$ Re $<$ 20-yr and "E" (dark purple line) $>$ 20-yr.

storms are longer with 3–4 successive years during the first 35 years (1964–2000) and decrease to 2 years in the beginning of the last decade when the succession of events seems to be more important. Stormy phases display different categories of events mainly distributed between November and February with only 11% of storms observed in October. Some events for each of September (2000, 2001), April (1994 and 2000) and March (1967 and 2008), July (1967) have been associated with the category "A".

This connection between the low-frequency components and the historical record of the exceptional events suggests that storms would occur differently according to a series of physical processes oscillating at multi-time-scales; these processes control their frequency and their intensity.

The seasonal dependence between stormy events and the extreme sea levels, already observed in previous works (e.g., Tsimplis and Woodworth, 1994), is mainly caused by astronomical forces of spring tides and meteorological conditions of seasonal storms. This dependence explains the distribution of storms and their organization in time; which is strongly related to the large-scale variability of surges. For example, the four storms of 1967 (E_3 to E_6) and the five storms of 2000 (E_{25} to E_{29}) show a seasonal dependence in their succession, tidal phase and intensity (return period).

The combining effect of local driven forces with meteorological, oceanographic and hydrological origins explains the most significant of the stochastic signal of surges in the Seine Bay where the fluvial activity plays an important role in changes of water elevations. This activity is largely observed during flooding periods; an example is produced in December 2001 (e.g., Massei and Fournier, 2012) when E_{31} of the category A has occurred.

The origin of physical processes responsible for storm surges exhibits a temporal nonstationary behavior due to a combination between the seasonal, the interannual and the interdecadal variability, and a non-linear interaction between the different time-scales. The assessment of the nonstationary effect on the estimation of extreme surges should be largely considered in the methods of extreme analysis by the use of the nonstationary models. For example, a time-dependent Generalized Extreme Value (GEV) distribution has been used by Masina and Lamberti (2013) to model the nonstationary features contained in the sea level time series by introducing the seasonality effect of GEV parameters (location, scale and shape) in order to improve the fitting of extreme values and reduce the uncertainty on the estimation of the return levels.

3.2. Relationship between storm surge dynamics and the atmospheric patterns

This section is focused on the connection between the local large-scale variability of surges and the global climate changes induced by the atmospheric circulation.

The climate patterns, extensively studied over the last two decades, have been mainly described by the NAO mechanisms (e.g. Hurrell et al., 2003). The SLP fields covering the English Channel, between 1964 and 2010, have been used with their different structures to characterize the climate patterns from the wavelet multiresolution decomposition into different time-scales.

Five composite maps have been calculated from the SLP field and the large-scale components of demodulated surges (Fig. 5). Provided maps are focused only on low frequencies ranging between 2.1-yr (D5) and 21.3-yr (D9) whose fluctuations correspond to oscillations periods less than half the length of the time series, and with the high-energy contribution on the variance of the total signal. As suggested by these

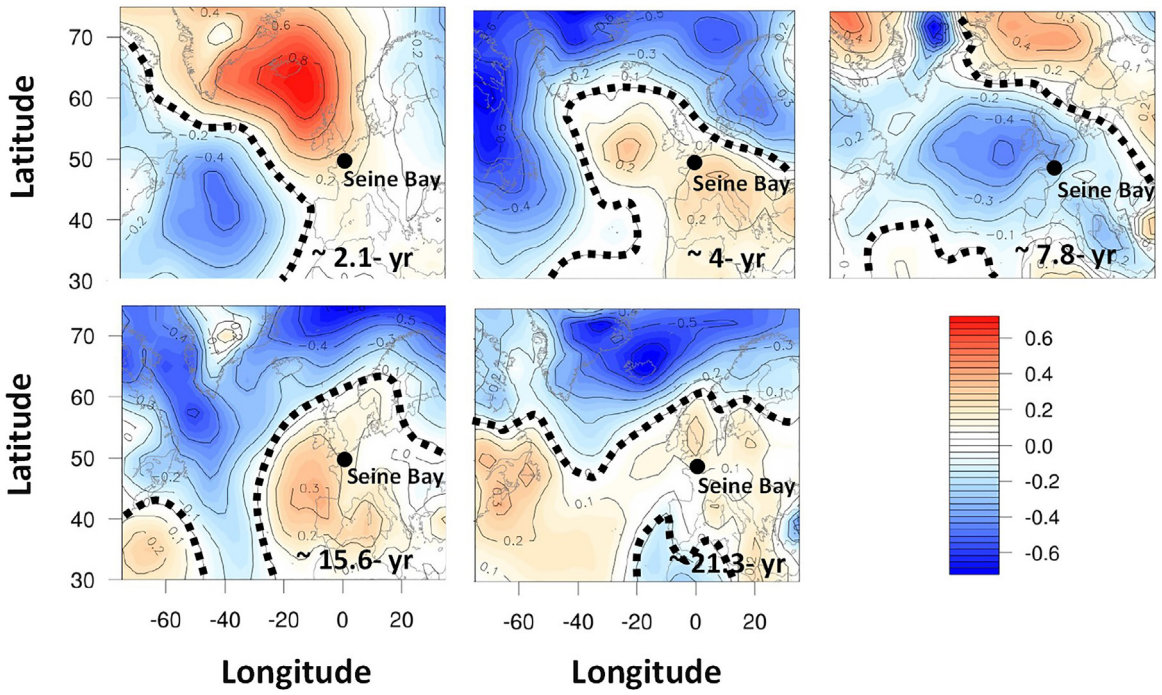

Figure 5 Composite maps of SLP generated for each scale based on surge variability. Black dashed lines indicate statistically significant regions (Student *t*-test with a 95% confidence limit).

composite maps, the relationship between the demodulated surges and the SLP fields is statistically significant and varies spatially in magnitude and phase. The spatial extent and the location of high-low pressure regions displayed by the atmospheric patterns are organized differently according to the time-scales of variability. Both 2.1-yr and 7.8-yr time-scales have shown dipolar structures with high-pressure anomalies located over the northern North Atlantic/sub-Arctic regions and low-pressure anomalies across the Atlantic (2.1-yr time-scale) and developing toward the English Channel and the North Sea (7.8-yr time-scale). Such dipolar structures can be associated with the typical western circulation, reminiscent of the negative NAO regime, more particularly for the 7.8-yr time-scale. This distribution should be attributed to the cyclonic circulation over northwestern Europe (50°N) with an alternating increase and decrease of West moisture fluxes from the Atlantic Ocean to the southern side of the English Channel and the Seine Bay.

On the contrary, 4-yr (D6), 15.6-yr (D8) and 21.3-yr (D9) time-scales have pointed North-South structures that could not be related to western circulation. Trough-shaped SLP anomalies in the center of the North-Atlantic basin would suggest weakened western circulation dynamics that would not be preeminent at these time-scales. In their analysis of multi-time-scale hydroclimate dynamics over the Seine river watersheds in Northern France, Massei et al. (2017) have found similar pattern shapes of SLP composites calculated from the Seine rainfall at the same time-scales.

Similar low-frequency oscillations have also been outlined by Feliks et al., 2011 in relation with NAO patterns of the simulated marine atmospheric boundary layer (MABL) forced with SST from a simple Ocean Data Analysis. Such relations to NAO index have been also observed by Turki et al. (2015) from the sea level fluctuations for scales between 1-yr and 3-yr, while the origin of higher frequencies, smaller than 1-yr, is related to the seasonal cycle of alternating high-low energy and changes in river discharges and temperature.

The different time-scales of the local variability of surges is not linearly related to the atmospheric circulation processes since their spatial extent, highlighted by the wavelet-based composite analysis, seems to be not fully similar according to the different scales of the hydro-climatic variability; each time-scale is associated with a determined physical mechanism explaining the oscillation period of changes.

The “switch on” and “off” of the influence of climate patterns on the variability of surges have an important application for many predictability issues. In this way, if SLP structures and surges anomalies are of similar patterns, the use of surges for predicting its variability from the SLP patterns at different time-scales could increase the accuracy of statistical predictions. At these scales, the atmospheric teleconnections explained by a series of physical mechanisms show a nonstationary behavior with a focus in the stochastic variability of surges.

This behavior is still under debate (Martin-Rey et al., 2012; Polo et al., 2008; Rodriguez-Fonseca et al., 2009).

According to their works related to the nonstationarities of the Atlantic influence on the Pacific in the 20th century, Lopez-parages et al. (2013) have shown that the statistical predictability of the rainfall variability can be improved by selecting the most suitable predictors depending on the period on which the prediction is carried out. They have also suggested that the nonstationary link between rainfall and SST takes place when the dipolar patterns of rainfall is

reinforced and coincides with negative phases of the AMO (Atlantic Multidecadal Oscillation) index along the 20th century.

Hence, the results obtained here point out a nonstationary behavior of the teleconnections between the local surges and the global SLP field, in particular for the interannual oscillations modulated by the interdecadal scales. The physical coherent modulation at a multi-scale variability is mainly related to the atmospheric circulation influenced generally by ocean currents and the Gulf Stream (GS). Several questions behind the reasons for this nonstationary teleconnections remain open, as the origin of the modulating factors.

In fact, the sea level pressure (SLP) and the baroclinic instability of wind stress are related to the GS path as given by NCEP reanalysis. In fact, the dominant signal is a northward (southward) displacement of the GS after the NAO reaches positive (negative) extrema (Frankignoul et al., 2001).

In the present context of global changes, the underlying issue of rising sea levels is combined to more stormy events and extremes. The increasing trend of stormy events in the Seine Bay, probably induced by the sea level rise scenarios of the English Channel, should be highly correlated with large variations in the GS transport (Ezer et al., 2013). The hypothesis of the GS transport reduction resulting in slower surface geostrophic currents, smaller gradients across the GS, and higher variations in the coastal sea level in the north GS has been supported by global climate models and satellite observations. Ezer et al. (2013) have demonstrated a strong relation between the coastal sea level changes and the GS variations on time-scales ranging from a few months to many decades with an increasing explained variance. The shift of the GS from 6—8 year oscillation cycle to a continuous weakening trend since the beginning the last century; which corresponds to the period of changes in storm organization and an increase in their frequency in time.

4. Conclusions

This research is focused on investigating the nonstationary dynamic of surges in the Seine Bay (southern side of the English Channel, NW France) and its nonlinear relationship with the global atmospheric circulation basing on a spectral approach of wavelet multi-resolution decomposition. By the use a new technique of envelope for demodulating surges, the large-scale variability has been quantified during 46 years (1964—2010). A total of 36 exceptional stormy events has been reported to the interannual (2.1-yr, 4-yr and 7.8-yr) and interdecadal (15.6-yr and 21.3-yr) time-scales of surges. Results have suggested a strong connection between the categories of storms, their intensity (return period 'Re') and their organization in time with the large-scale variability of surges. In fact, the interannual scales of 15.6-yr and 21.3-yr have been linked to stormy events with Re higher than 10 years; storms with Re of 2 years are only manifested at 2.1-yr scales, while events with Re between 2 and 10 years have been reported to 4-yr and 7.8-yr scales. Dipolar patterns of high-low pressures have been detected at 2.1-yr and 7.8-yr scales and should be related to the western circulation having an impact on the sea surge maxima, while the variability of 4-yr, 15.6-yr and 21.3-yr should obey to different mechanisms related to the pronounced North-South circulation processes and NAO, as interpreted from the distribution of SLP anomalies.

The present investigation brings some interesting results about the nonstationary behavior the teleconnections between the local surges and the global climate circulation at large-time scales. By simulating the low-frequency components of demodulated surges and SLP fields, results have highlighted the important role of the interdecadal frequencies in the modulation of interannual variability. Deeper investigations related to the physical mechanisms responsible for this nonstationary dynamic are required in order to improve our understanding of the system climate-ocean changes.

The conclusion of this research suggests that wind—stress variations driven by energetic currents such as the GS may play a key role in coastal sea level changes. Establishing a strong connection between large-scale sea level changes with flooding risks and the GS gradients could improve our understanding of the relation between the global climate patterns and the local sea level changes; also allow us to infer the future projections of sea level change and extreme events.

This finding can represent a step forward in the understanding of the role of the sea level surges and should be useful to improve the downscaling models of sea surges, therefore allowing a better assessment of flood risks. Further works will be focused on developing the large-scale/local-scale nonstationary models by the use of different large-scale variables related to the atmospheric circulation. This may allow proposing the improved statistical downscaling models and exploring the capabilities of such models to produce forecasts of the probability of extreme sea level trends by considering the interannual and the interdecadal variability of global climate patterns.

Acknowledgments

The authors are grateful to ANR funded project “RICCOCHET” of French national program as well as the international project COTEST funded by CNES-TOSCA and related to the future mission of Surface Water and Ocean Topography (SWOT). Authors thank also National Navy Hydrographic Service and National Center for Environmental Prediction for providing sea level and atmospheric data. Also, the authors greatly thank the reviewers and the editors of the journal Oceanologia for their useful suggestions to improve the manuscript.

References

Devoy, R.J.N., 2008. Coastal vulnerability and the implications of sea level rise for Ireland. J. Coast. Res. 24 (2), 325—341, http://dx.doi.org/10.2112/07A-0007.1.

Ezer, T., 2001. Can long-term variability in the Gulf Stream transport be inferred from sea level? Geophys. Res. Lett. 28 (6), 1031—1034, http://dx.doi.org/10.1029/2000GL011640.

Ezer, T., Atkinson, L.P., Corlett, W.B., Blanco, J.L., 2013. Gulf Stream's induced sea level rise and variability along the U.S. mid-Atlantic coast. J. Geophys. Res. 118, 685—697, http://dx.doi.org/10.1002/jgrc.20091.

Ezer, T., Corlett, W.B., 2012. Analysis of relative sea level variations and trends in the Chesapeake Bay: is there evidence for acceler-

ation in sea level rise? In: Proc Oceans'12 MTS/IEEE, October 14–19, IEEE Xplore, http://dx.doi.org/10.1109/OCEANS.2012.6404794.

Feliks, Y., Ghil, M., Robertson, A.W., 2011. The atmospheric circulation over the North Atlantic as induced by the SST field. J. Clim. 24 (2), 522–542, http://dx.doi.org/10.1175/2010JCLI3859.1.

Frankignoul, C., Coëtlogon, G., Joyce, T.M., Dong, S., 2001. Gulf Stream variability and ocean–atmosphere interactions. J. Phys. Oceanogr. 31 (12), 3516–3529, http://dx.doi.org/10.1175/1520-0485(2002)031<3516:GSVAOA>2.0.CO;2.

Gratiot, N., Anthony, E.J., Gardel, A., Gaucherel, C., Proisy, C., Wells, J.T., 2008. Significant contribution of the 18.6 year tidal cycle to regional coastal changes. Nat. Geosci. 1 (3), 169–172, http://dx.doi.org/10.1038/ngeo127.

Hurrell, J.W., Kushnir, Y., Ottersen, G., Visbeck, M., 2003. An Overview of the North Atlantic Oscillation. Geophys. Monog. Ser. 134, AGU, http://dx.doi.org/10.1029/134GM01.

Kalnay, E., Kanamitsu, M., Kistler, R., Collins, W., Deaven, D., Gandin, L., Joseph, D., 1996. The NCEP/NCAR 40-year reanalysis project. Bull. Am. Meteorol. Soc. 77 (3), 437–472, http://dx.doi.org/10.1175/1520-0477(1996) 077<0437:TNYRP>2.0.CO;2.

Levermann, A., Griesel, A., Hofmann, M., Montoya, M., Rahmstorf, S., 2005. Dynamic sea level changes following changes in the thermohaline circulation. Clim. Dynam. 24 (4), 347–354, http://dx.doi.org/10.1007/s00382-004-0505-y.

Lopez-parages, J., Villamayor, J., Gomaeai, I., Losada, T., Martinrey, M., Mohino, E., Polo, I., Rodriguez-Fonseca, B., Suarezi, R., 2013. Nonstationary interannual teleconnections modulated by multidecadal variability. Física de la Tierra 25, 11–39, http://dx.doi.org/10.5209/rev_FITE.2013.v25.43433.

Marcos, M., Chust, G., Jordá, G., Caballero, A., 2012. Effect of sea level extremes on the western Basque coast during the 21st century. Clim. Res. 51 (3), 237–248, http://dx.doi.org/10.3354/cr01069.

Martin-Rey, M., Polo, I., Rodriguez-Fonseca, B., Kucharski, F., 2012. Changes in the interannual variability of the tropical Pacific as a response to an equatorial Atlantic forcing. Sci. Mar. 76 (S1), 105–116, http://dx.doi.org/10.3989/scimar.03610.19A.

Masina, M., Lamberti, A., 2013. A nonstationary analysis for the Northern Adriatic extreme sea levels. J. Geophys. Res. 118, 3999–4016, http://dx.doi.org/10.1002/jgrc.20313.

Masina, M., Lamberti, A., Archetti, R., 2015. Coastal flooding: a copula based approach for estimating the joint probability of water levels and waves. Coast. Eng. 97, 37–52, http://dx.doi.org/10.1016/j.coastaleng.2014.12.010.

Massei, N., Dieppois, B., Hannah, D.M., Lavers, D.A., Fossa, M., Laignel, B., Debret, M., 2017. Multi time-scale hydroclimate dynamics of a regional watershed and links to large-scale atmospheric circulation: Application to the Seine river catchment, France. J. Hydrol. 546, 262–275, http://dx.doi.org/10.1016/j.jhydrol.2017.01.008.

Massei, N., Fournier, M., 2012. Assessing the expression of large-scale climatic fluctuations in the hydrological variability of daily Seine river flow (France) between 1950 and 2008 using Hilbert-Huang Transform. J. Hydrol. 448–449, 119–128, http://dx.doi.org/10.1016/j.jhydrol.2012.04.052.

Menendez, M., Woodworth, P.L., 2010. Changes in extreme high water levels based on a quasi-global tide-gauge data set. J. Geophys. Res. 115, C10011, http://dx.doi.org/10.1029/2009JC005997.

Minguez, R., Tomas, A., Mendez, F.J., Medina, R., 2012. Mixed extreme wave climate model for reanalysis databases. Stoch. Environ. Res. Risk. Assess. 27, 757–768, http://dx.doi.org/10.1007/s00477-012-0604-y.

Mitchell, J.M., Dzerdzeevskii Jr., Flohn, B., Hofmeyr, H., Lamb, W.L., Rao, H.H., Wallén, C.C., 1966. Climatic change: Technical Note No. 79, report of a working group of the Commission for Climatology. WMO No. 195 TP 100. World Meteorological Organization, Geneva, Switzerland, 81 pp.

Mitchell, M., Hershner, C., Herman, J., Schatt, D., Eggington, E., Stiles, S., 2013. Recurrent flooding study for Tidewater Virginia, Report SJR 76, 2012. Virginia Instit. Marine Sci., Gloucester Point, VA, 141 pp.

Nicholls, R., Brown, S., Hanson, S., Hinkel, J., 2010. Economics of coastal zone adaptation to climate change, Discussion Paper 10. World Bank, Washington, DC.

Polo, I., Rodriguez-Fonseca, B., Losada, T., Garcia-Serrano, J., 2008. Tropical Atlantic variability modes (1979–2002). Part I: Time evolving SST modes related to West African rainfall. J. Clim. 21, 6457–6475, http://dx.doi.org/10.1175/2008JCLI2607.1.

Pugh, D.J., 1987. Tides, Surges and Mean Sea-Level: A Handbook for Engineers and Scientists. John Wiley, Chichester, 472 pp.

Rodriguez-Fonseca, B., Polo, I., Garcia-Serrano, J., Losada, T., Mohino, E., Mechosos, C.R., Kucharski, F., 2009. Are Atlantic Niños enhancing Pacific ENSO events in recent decades? Geophys. Res. Lett. 36, L20705, http://dx.doi.org/10.1029/2009GL040048.

Ruigar, H., Golian, S., 2015. Prediction of precipitation in Golestan dam watershed using climate signals. Theor. Appl. Climatol. 123 (3–4), 671–682, http://dx.doi.org/10.1007/s00704-015-1377-2.

Sallenger, A.H., Doran, K.S., Howd, P., 2012. Hotspot of accelerated sea-level rise on the Atlantic coast of North America. Nat. Clim. Change 2, 884–888, http://dx.doi.org/10.1038/NCILMATE1597.

Shaw, A.G.P., Tsimplis, M.N., 2010. The 18.6 yr nodal modulation in the tides of Southern European Coasts. Cont. Shelf Res. 30 (2), 138–151, http://dx.doi.org/10.1016/j.csr.2009.10.006.

Stive, M.J.F., Aarninkhof, S.G.J., Hamm, L., Hanson, H., Larson, M., Wijnberg, K.M., Nicholls, R.J., Capobianco, M., 2002. Variability of shore and shoreline evolution. Coast. Eng. 47 (2), 211–235, http://dx.doi.org/10.1016/S0378-3839(02)00126-6.

Sweet, W., Zervas, C., Gill, S., 2009. Elevated east coast sea level anomaly: June-July 2009, NOAA Tech. Rep. No. NOS CO-OPS 051. NOAA NOS, Silver Spring, MD, 40 pp.

Tsimplis, M.N., Woodworth, P.L., 1994. The global distribution of the seasonal sea level cycle calculated from coastal tide gauge data. J. Geophys. Res. 99 (C8), 16031–16039.

Turki, I., Laignel, B., Chevalier, L., Costa, S., Massei, N., 2015. Coastal sea level changes in the southeastern side of the English channel: potentialities for future SWOT applicability. IEEE J. Sel. Top. Appl. Earth Obs. Remote Sens. 8 (4), 1564–1569, http://dx.doi.org/10.1109/JSTARS.2015.2419693.

Wood, F., 2001. Tidal dynamics. Volume 1: theory and analysis of tidal forces. J. Coast. Res. 259–326, https://www.jstor.org/stable/25736216.

Woodworth, P.L., Blackman, D.L., 2004. Evidence for systematic changes in extreme high waters since the mid-1970s. J. Clim. 17 (6), 1190–1197, http://dx.doi.org/10.1175/1520-0477(1996) 077<0437:TNYRP>2.0.CO;2.

Yang, Y., 2017. A signal theoretic approach for envelope analysis of real-valued signals. IEEE Access 5, 5623–5630, http://dx.doi.org/10.1109/ACCESS.2017.2688467.

Yin, J., Schlesinger, M.E., Stouffer, R.J., 2009. Model projections of rapid sea-level rise on the northeast coast of the United States. Nat. Geosci. 2, 262–266, http://dx.doi.org/10.1038/NGEO462.

Oceanologia (2019) 61, 331—340

Available online at www.sciencedirect.com

ScienceDirect

journal homepage: www.journals.elsevier.com/oceanologia/

ORIGINAL RESEARCH ARTICLE

Impact of a dipole on the phytoplankton community in a semi-enclosed basin of the southern Gulf of California, Mexico

Elizabeth Durán-Campos [a,1,*], María Adela Monreal-Gómez [b], David Alberto Salas de León [b], Erik Coria-Monter [c]

[a] *DGAPA Postdoctoral Fellowship, Institute of Marine Sciences and Limnology (ICML), National Autonomous University of Mexico (UNAM), Mexico City, Mexico*
[b] *Ecology and Aquatic Biodiversity Academic Unit, Institute of Marine Sciences and Limnology (ICML), National Autonomous University of Mexico (UNAM), Mexico City, Mexico*
[c] *Cátedras CONACYT, Institute of Marine Sciences and Limnology (ICML), National Autonomous University of Mexico (UNAM), Mexico City,Mexico*

Received 24 August 2018; accepted 22 January 2019
Available online 2 February 2019

KEYWORDS
Dipole;
Oceanic thermohaline front;
Phytoplankton;
Chlorophyll-*a*;
Gulf of California;
Bay of La Paz

Summary The present study assesses the impact of a dipole on the abundance and distribution of phytoplankton groups as well as the chlorophyll-*a* concentration in the Bay of La Paz, Gulf of California, Mexico. Based on *in situ* observations obtained in a multidisciplinary research cruise during the summer of 2008, a mesoscale dipole (cyclone-anticyclone) was observed; the cyclone had ~25 km diameter and tangential speed of ~45 cm s^{-1}, while the anticyclone had ~15 km diameter and tangential speed of ~40 cm s^{-1}. Strong gradients in conservative temperature and density were observed between both structures, suggesting the presence of an oceanic thermohaline front. Differences in phytoplankton distribution showed minimum abundance of diatoms in the southern bay and close to Roca Partida Island, and maximum in the periphery in the northern cold core. The maximum abundance of dinoflagellates and silicoflagellates occurred at the frontal zone. The chlorophyll-*a* concentration was high in the region associated with the frontal zone.

* Corresponding author at: Mazatlán Academic Unit, Institute of Marine Sciences and Limnology, National Autonomous University of Mexico (UNAM), Av. Joel Montes Camarena s/n, 82000 Mazatlán, Sinaloa, Mexico. Tel.: +52 (669) 985 2845; fax: +52 (669) 982 6133 6133 (Present address).
E-mail address: eduran@cmarl.unam.mx (E. Durán-Campos).
[1] Address: DGAPA Postdoctoral Fellowship, Institute of Marine Sciences and Limnology (ICML), National Autonomous University of Mexico (UNAM), Av. Universidad 3000, Col. Copilco, Del. Coyoacán, 04510 Mexico City, Mexico.
Peer review under the responsibility of Institute of Oceanology of the Polish Academy of Sciences.

ELSEVIER Production and hosting by Elsevier

https://doi.org/10.1016/j.oceano.2019.01.004

Although mesoscale eddies are ubiquitous processes in the Bay of La Paz, this study represents the first observational report of the impacts of a dipole on the phytoplankton structure and chlorophyll-*a* in the region. The observations presented here indicate the existence of a strong association between the mesoscale processes and the phytoplankton community in the study area. This study highlights the value of efforts to improve projections of physical forcing and its influence on the planktonic ecosystem.

1. Introduction

Phytoplankton are the primary source of the marine food chain, which contributes to the major fishery resources around the world and play a pivotal role in the marine ecosystem due to their contribution in mitigating climate change and global warming, by reducing global CO_2 levels (Vajravelu et al., 2017). Numerous studies highlight the fact that the phytoplankton community structure, composition, and distribution are determined by several physicochemical variables, as well as hydrodynamic processes such as mesoscale eddies (McGillicuddy, 2016). Mesoscale eddies (with radius scales of 10—100 km) are responsible for a major portion of ocean circulation energy (Gaube et al., 2013; Liu et al., 2013). Three types of ocean eddies are described: cyclonic, mode-water and anticyclonic. Cyclonic and mode-water eddies contribute significantly to the transport of nutrients affecting both the horizontal and vertical distribution of phytoplankton community (McGillicuddy et al., 2007) while the anticyclonic are related to a reduction of primary productivity by the fact that they induce convergent movements, sinking surface waters below the euphotic zone (McGillicuddy, 2016; McGillicuddy and Robinson, 1997).

To date, it is increasingly common to find reports in the scientific literature on the role of mesoscale eddies on the phytoplankton community in different domains. In the Sea of Japan, the timing and initiation mechanisms of the spring phytoplankton blooms is associated with the presence of mesoscale anticyclonic and cyclonic eddies (Maúre et al., 2017). The phytoplankton community in the Western South China Sea is highly influenced by the presence of a cyclonic eddy owing to the doming isopycnal within the eddy supplied nutrients gently into the upper mixing layer, and there is a remarkable enhancement in phytoplankton biomass at the surface layer (Wang et al., 2016). Eddies originating in the eastern South Indian Ocean are unique in that anticyclones, usually associated with reduction of primary productivity, contain elevated levels of chlorophyll, enhanced primary production and phytoplankton communities generally associated with nutrient-replete environments (Gaube et al., 2013).

Despite the fact that extensive observations of individual structures (cyclonic or anticyclonic) have appeared in the literature, dipole structures, consisting of two with opposite signs of vertical component of relative vorticity, are less frequent. Some studies showed that the vertical distribution of phytoplankton, in terms of community and physiology, in a dipole consisting of one warm-core and one cold-core formed off Western Australia varied between both; the warm-core eddy had a vertically dispersed photoautotrophic community dominated by large diatoms and coccolithophorids, while the cold-core had a shallower and more consistent mixed-layer depth with a deep chlorophyll maximum well-developed throughout the field (Thompson et al., 2007). In the North Pacific, an elevated chlorophyll-*a* and particle concentrations have been reported in the frontal region within an anticyclone-cyclone dipole, which is consistent with the mesoscale and submesoscale physical processes; the horizontal stirring in the region appears to have caused surface convergence within the mesoscale frontal zone, which in turn increased concentrations of buoyant particles (Guidi et al., 2012).

Mesoscale eddies are ubiquitous processes in the southern Gulf of California (GC) and in the Bay of La Paz (BoP). In the BoP, they are frequently generated in the deepest region and have been well described, mainly regarding the cyclonic structure. These studies have included the genesis and characteristics (Monreal-Gómez et al., 2001), the effects in nutrient, chlorophyll-*a* and phytoplankton distribution (Coria-Monter et al., 2014) as well as the zooplankton assemblages (Durán-Campos et al., 2015). Recent research indicated that the presence of a cyclonic circulation inside the bay induces a nutrient Ekman pumping with vertical velocities of $\sim$0.4 m d^{-1} rising up the nutricline. The fertilization of the euphotic zone is stimulating the phytoplankton to grow, resulting then in higher levels of chlorophyll-*a* within the center (Coria-Monter et al., 2017).

Although the effect of the cyclone inside the BoP is relatively well documented, the way in which anticyclonic eddies affect the phytoplankton structure remains uncertain. More uncertain is the dynamics of a dipole structure (cyclone-anticyclone) and its effect on the phytoplankton distribution as well as the chlorophyll-*a* concentration. Additionally, the effects of eddies on the biological communities and biogeochemical cycles have been mostly studied in open ocean environments and far less in semi-enclosed areas such as bays.

The aim of this study was to assess the impacts of a dipole structure on the phytoplankton abundance, distribution, and composition in the BoP during the summer of 2008. We hypothesize changes in the hydrographic/thermal structure of the water column due to the presence of the dipole structure with opposite rotation movement, resulting in differences in the phytoplankton community as well as in the chlorophyll-*a* concentration.

2. Material and methods

2.1. Study area

The BoP is the largest basin within the GC and is one of the most important ecological ecosystems, due to it is representing a place for refuge and growth of different organisms (Pardo et al., 2013). It is located in the southwestern portion of the GC, approximately 200 km from the connection with the Pacific Ocean (Fig. 1a); the bay connects with the GC through two openings: Boca Grande to the northeast (wide and deep) and the San Lorenzo Channel in the south (narrow and shallow); the bay has a maximum depth of 420 m in the Alfonso Basin. An important feature is the presence of a bathymetric sill along the Boca Grande, which partially isolates the BoP from the GC (Molina-Cruz et al., 2002). The wind in the region presents seasonal changes with northwest winds during the winter and southeast winds during the summer (Monreal-Gómez et al., 2001), however westerly winds were reported during the late spring of 2004 (Coria-Monter et al., 2017).

2.2. Sampling

High-resolution hydrographic records, fluorescence measurements and water samples for phytoplankton cell count were obtained during the oceanographic cruise "DIPAL-II" carried out on board the R/V "El Puma" of the National Autonomous University of Mexico (UNAM) from September 3 to 9, 2008 along a grid of stations covering both the bay as well as its connection with the GC at Boca Grande to the northeast (Fig. 1b).

A conductivity-temperature-depth probe (CTD) Sea Bird 19 plus was used to record conductivity, temperature, and pressure at 56 stations (Fig. 1b). The CTD casts extended almost to the bottom (~2 m above the seafloor) while the ship maintained its position on station, with accuracy not worse than 200 m. The temperature and conductivity accuracy resolution of the equipment was 0.005°C and 0.0005 S/m, respectively, and it was lowered at a rate of 1 m/s, acquiring data at 24 Hz. Chlorophyll fluorescence measurements were made using a WET Labs fluorometer sensor (range 0.00–125 mg m^{-3}) on the CTD/Rosette system, calibrated by the manufacturer prior to the cruise.

A General Oceanics rosette equipped with 10 L Niskin bottles was used to take surface water for phytoplankton count cells at 49 stations (Fig. 1b). Aliquots of 500 mL were preserved with Lugol solution in glass bottles. Samples were kept in the dark until cell counting, following the recommendations of Edler and Elbrächter (2010).

2.3. Data reduction

The CTD measurements were initially processed by the standard package from the manufacturer (SBE Data Processing V.7.26.7) and averaged to 1 dbar, and then conservative temperature (Θ, °C), absolute salinity (S_A, g kg^{-1}) and density (σ_t, kg m^{-3}) values were calculated from *in situ* temperature and practical salinity according to the Thermodynamic Equation of Seawater-2010 (IOC et al., 2010). The geostrophic velocities were calculated by standard geostrophic analysis, using CTD data to calculate the specific volume anomalies, in order to estimate the dynamic height (ΔD) at each oceanographic station relative to the bottom, then these were differentiated between pairs of stations, to obtain the relative velocity by mean the practical form of the geostrophic equation $\left(v_1 - v_2 = \frac{10}{Lf}[\Delta D_B - \Delta D_A]\right)$, which represents the difference between the geostrophic current at level p_1 from that at level p_2 averaged between the stations *A* and *B*, which are separated by a distance *L*, and *f* represents the Coriolis parameter (Pond and Pickard, 1983) and then compared with the distribution of the hydrographic parameters.

The phytoplankton biomass, expressed as chlorophyll-*a* concentration [mg m^{-3}], was estimated indirectly using the manufacturer's nominal conversion factor from the *in situ* fluorescence, and then was vertically integrated from 0 to 50 m depth.

Eight-day composite satellite images of chlorophyll-*a* and sea surface temperature from the Moderate Resolution Imaging Spectroradiometer (MODIS) sensors on board the satellite Aqua for the period when the research cruise took place (September 05 to 12, 2008) were used to compare with the *in situ* measurements. The images, with a spatial resolution of 3.5 km (Local Area Cover (LAC)), were processed using SeaDAS, version 7.4, with standard algorithms. These algorithms return the near-surface concentration of CHLA (in mg m^{-3}), calculated using an empirical relationship derived from *in situ* measurements of CHLA and remote sensing reflectance in the blue-to-green region of the visible spectrum; the algorithm employs the standard OC3/OC4 (OCx) band ratio algorithm merged with the color index (CI) of Hu et al. (2012).

2.4. Laboratory analyses

The phytoplankton cell count was assessed by the Utermöhl method, with 100 mL chamber sedimentation for 48 h following the protocols and recommendation by Edler and Elbrächter (2010). A Zeiss Axiovert 25A inverted microscope was used to count and identify the organisms by group (diatoms, dinoflagellates, and silicoflagellates) following Tomas (1997).

3. Results

3.1. Hydrography and geostrophic circulation

The surface conservative temperature distribution (contour interval 0.1°C) showed the presence of a cold core located at the central portion of the bay, reaching values of 29.4°C, whereas the distribution over the Boca Grande showed higher values (>30.3°C). Moreover, the isolines shown temperature gradients at the connection between the bay and the gulf, the temperature gradient was ~0.01°C/km (Fig. 2a). The density surface distribution (σ_t, contour interval of 0.1 kg m^{-3}) showed the presence of a high-density core at the central portion, in coincidence with the cold core, and low-density values over the Boca Grande region (Fig. 2b). The eight-day composite sea surface temperature satellite image (Fig. 2c), except in the southern BoP, matched well with the *in situ* measurements of conservative temperature, showing a relatively low temperature coincident with the *in situ*

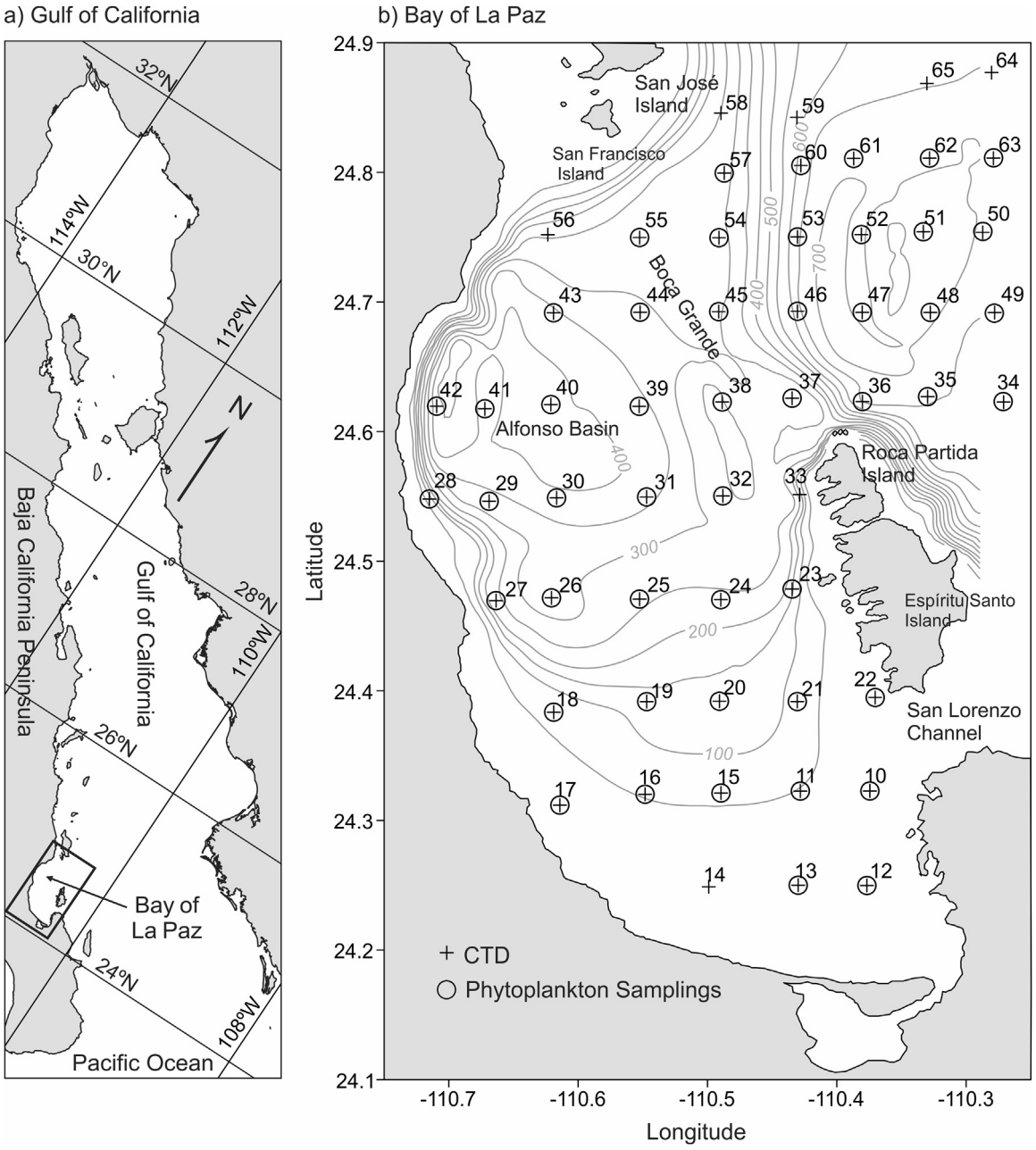

Figure 1 Location of: (a) Gulf of California and (b) Bay of La Paz and sampling stations. '+' represents CTD stations, 'O' represents phytoplankton samplings. Bathymetry (thin gray line) is shown in m.

measurements, and the highest temperature (~31.5°C) outside the bay. In addition, the image showed a relatively high temperature close to the Roca Partida Island, outside the bay. The geostrophic circulation was dominated by the presence of a dipole structure (cyclone-anticyclone). The cyclone was located at 24.5°N, 110.6°W, had ~25 km diameter and tangential speed of ~45 cm s^{-1}, while the anticyclone was located at 24.7°N, 110.4°W, with ~15 km diameter and tangential speed of ~40 cm s^{-1} extending out of the bay, reaching the Boca Grande region (Fig. 2d). According to Simpson and Lynn (1990), the classical hydrodynamic dipole (vortex pair) consists of two eddies of equal and opposite strength whose centers are separated by a distance small enough that the two structures interact, consistent with our observations.

3.2. Phytoplankton

The abundance of phytoplankton (diatoms, dinoflagellates, and silicoflagellates) analyzed in this study showed interesting variations. The diatom abundance ranged from 70 to 2800 cells L^{-1}, the dinoflagellates from 550 to 5060 cells L^{-1} while the maximum abundance of silicoflagellates was 50 cells L^{-1}. Dinoflagellates represented 64% of all organisms and diatoms 35%, while silicoflagellates represented only 1%.

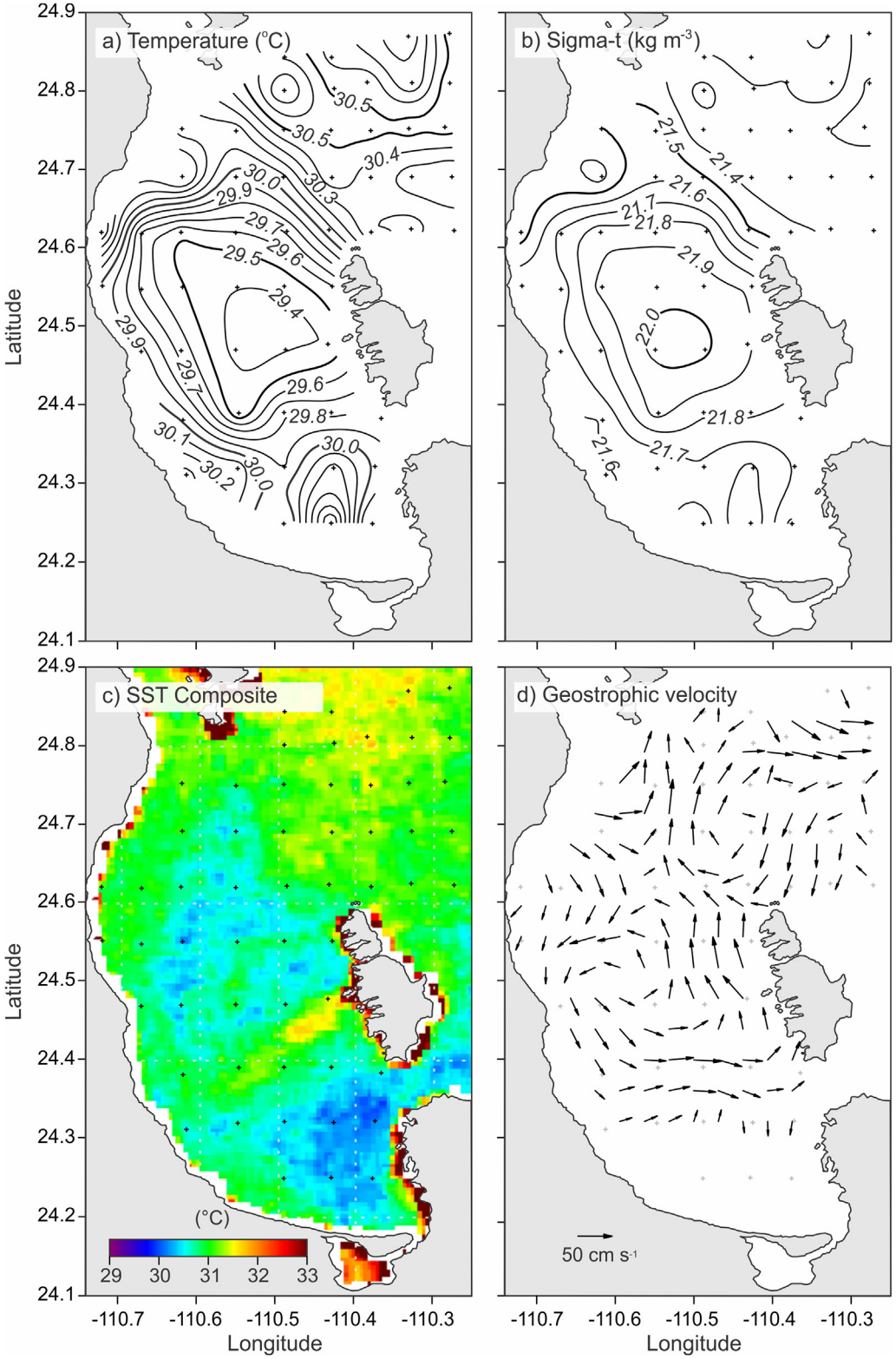

Figure 2 Surface horizontal distribution of: (a) conservative temperature [°C] (contour interval 0.1°C), (b) density [σ_t: kg m^{-3}] (contour interval 0.1 kg m^{-3}), (c) eight-day composite sea surface temperature satellite image (MODIS-AQUA) and (d) geostrophic circulation [cm s^{-1}].

Differences in their horizontal distributions were clearly observed along the dipole structure field. In order to visualize their distribution pattern, the same scale was used to compare the abundance of diatoms (Fig. 3a), dinoflagellates (Fig. 3b), and silicoflagellates (Fig. 3c). On the other hand, using different scales in order to easily visualize their patterns, the lower abundance of diatoms (~70 cells L^{-1}) was found on the southern bay and close to Roca Partida Island,

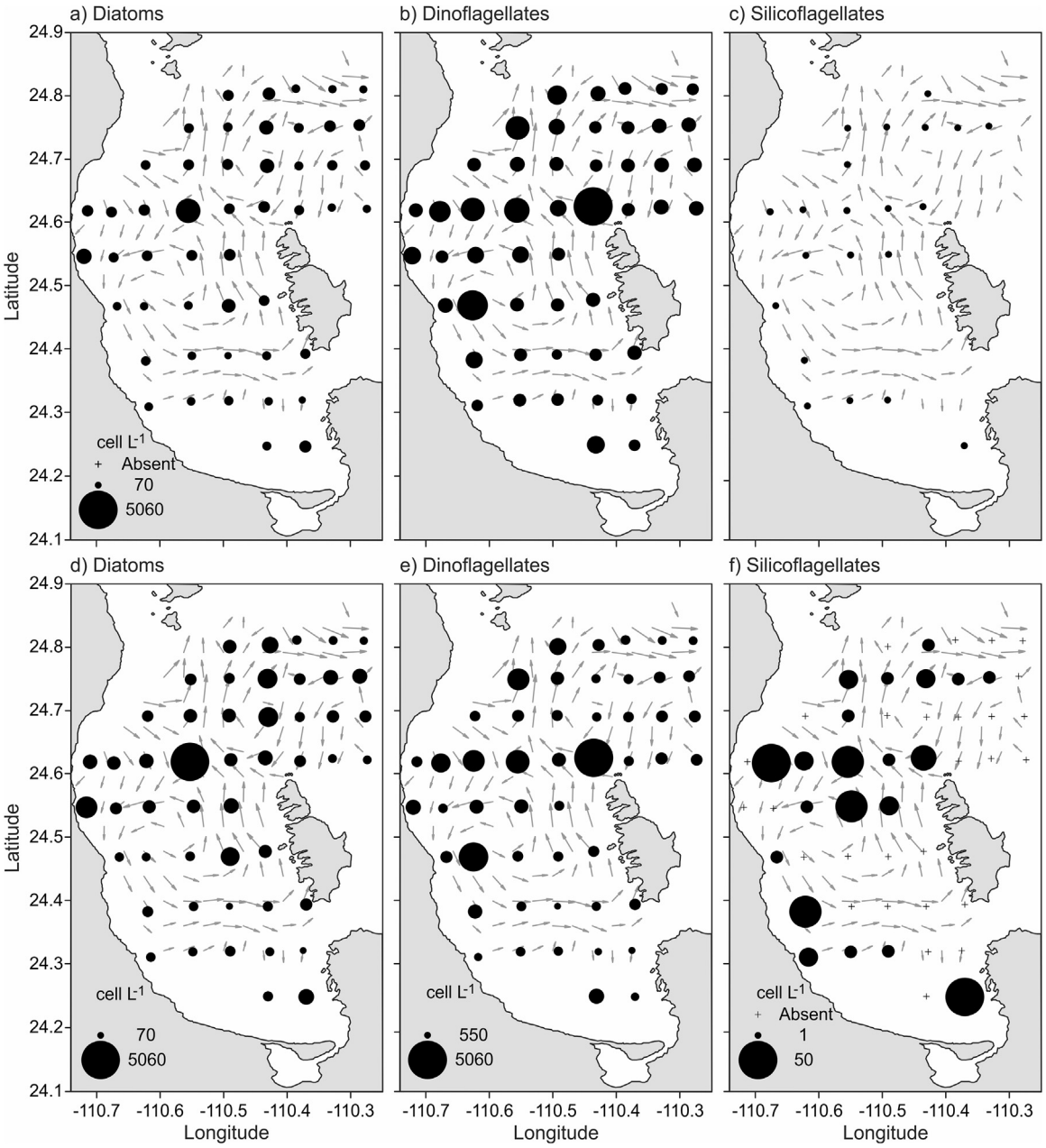

Figure 3 Horizontal distribution of phytoplankton [cells L^{-1}] at the surface: (a) diatoms, (b) dinoflagellates and (c) silicoflagellates, with same scales to compare the abundance between three groups, and (d) diatoms, (e) dinoflagellates, (f) silicoflagellates, using different scales in order to easily visualize their patterns.

while the maximum abundance occurred in the periphery in the northern cold core (Fig. 3d). The dinoflagellates distribution was found in three cores with different abundances along the bay; the first one located on the southwest portion near the coast, which is coincident with the core of the cyclone observed with an abundance of ~3200 cells L^{-1}; a second core located at the central BoP with an abundance of 2400 cells L^{-1} and a third core with the highest values located near Roca Partida Island on the Boca Grande with an abundance of 5060 cells L^{-1}, associated to the thermohaline front. Considering the abundance of the last two cores, the highest concentration of dinoflagellates was observed at the zone along the transect crossing the bay on latitude 24.6°N (Fig. 3e). The silicoflagellates distribution was similar to that of dinoflagellates, with highest abundance over the same transect and one core in the southwestern region close to the coast (Fig. 3f).

Although the organisms were not identified to species level, these results contributed to the knowledge of their ecology and contributed information on the patterns of distribution into a dipole system.

3.3. Chlorophyll-*a*

The surface chlorophyll-*a* concentration rose in a range from 0.02 to 0.18 mg m^{-3}. The maximum values inside the bay

were located over the southern region. The central zone of the bay showed concentrations (~0.1 mg m^{-3}) in a core close to the Roca Partida Island (Fig. 4a). The region outside the bay, in the GC, showed the lowest concentrations with ~0.02 mg m^{-3}. The eight-day composite satellite image for the period when the oceanographic cruise took place matched well with the *in situ* measurements (Fig. 4b) with maximum values located in the southern bay (~0.18 mg m^{-3})

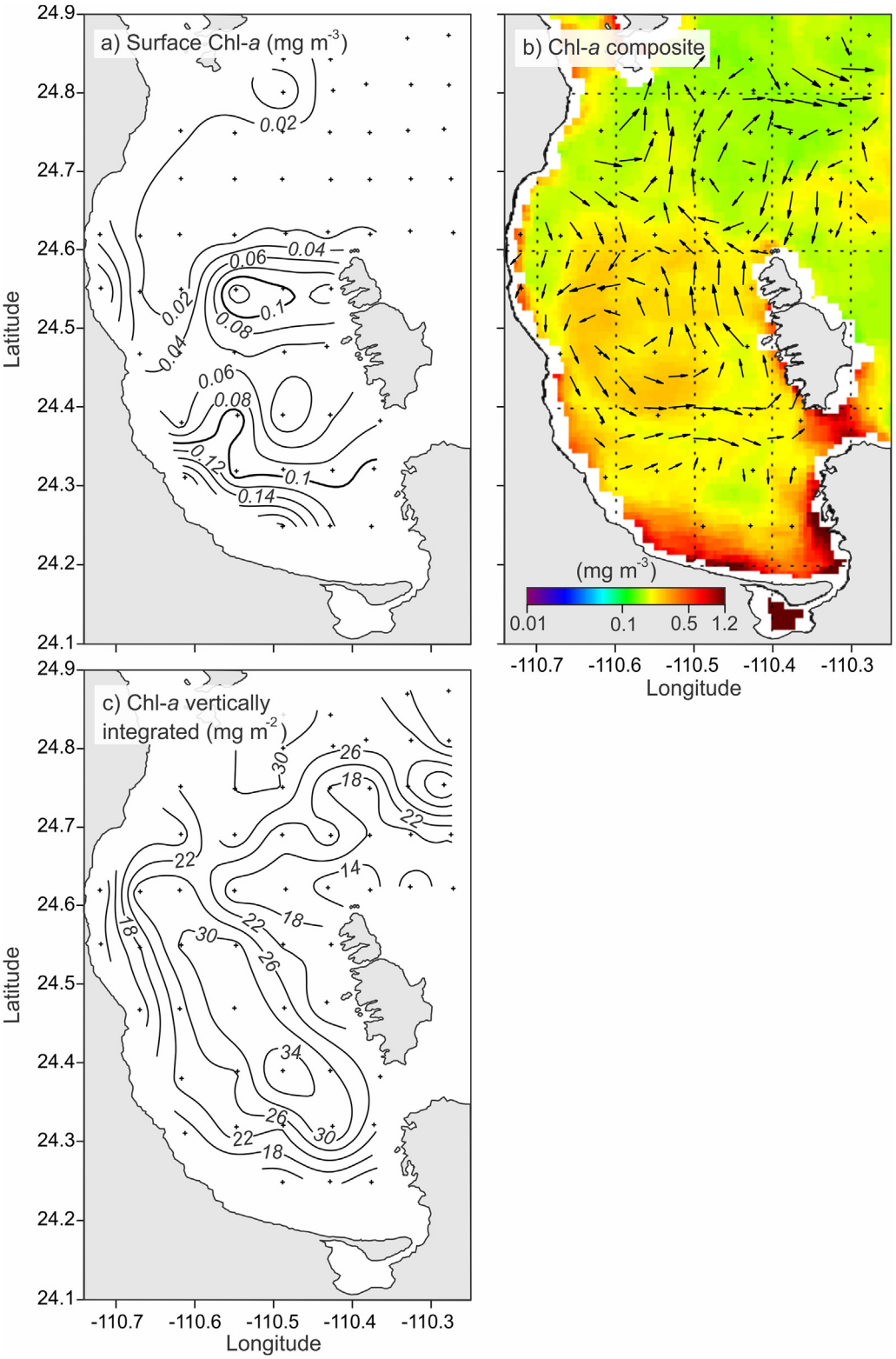

Figure 4 Surface horizontal distribution of chlorophyll-*a*: (a) *in situ* measurements [mg m^{-3}], (b) derived from eight-day composite satellite image [mg m^{-3}] (MODIS-AQUA) with geostrophic velocity field, and (c) horizontal distribution of chlorophyll-*a* vertically integrated from surface to 50 m depth [mg m^{-2}].

and relatively high concentrations in the central region (~0.10 mg m^{-3}), which coincided with phytoplankton cell counts. The vertically integrated values rose to a range of 10–34 mg m^{-2}; the maximum values occurred in a core in the southern region, with values between 30 and 34 mg m^{-2} and the pattern of distribution showed a tongue extended along the central part of the bay reaching the zone were the front is present, with values of 26 mg m^{-2} (Fig. 4c). The images also show a low-relative chlorophyll-*a* value (≈14 mg m^{-2}) in the region close to the Roca Partida Island, a region with high-temperature values.

4. Discussion

The generation of mesoscale eddies inside the GC and adjacent areas have received special attention in recent years. An important number of observational and numerical studies have contributed to elucidate their forcing mechanisms (Lavín et al., 2013; Salas de León et al., 2011). Particularly within the BoP, a quasi-permanent cyclonic circulation induced by the wind stress and by the interaction with the bottom topography and the currents between the GC and BoP has been well described (Coria-Monter et al., 2017; Monreal-Gómez et al., 2001). The information in the BoP described the presence of a single mesoscale cyclonic eddy; however, in this study, our observations showed a circulation pattern not previously reported for the region as the presence of a dipole structure consistent in a cyclone-anticyclone. In this regard, the polarity for each structure could be explained by the interaction of the currents between the BoP and the GC through the Boca Grande; if the entrance of the current to the bay is close to the Roca Partida or to the San José Island, the polarity may be cyclone or anticyclone, and once formed, this might originate another with a different rotation movement due to energy transfer, which could explain our results.

The presence of dipole structures (cyclone-anticyclone) can induce the generation of a front exerting a noticeable effect on chlorophyll-*a* levels and suspended particulate matter (Salas de León et al., 2004). A front could be represented as a linear zone that defines an axis of laterally convergent flow, below or above which vertical flows are induced and are regions of strong horizontal temperature and/or salinity contrast (Franks, 1992). Fronts not only promote fertilization by nutrients also may result in downward export of particles and organisms toward the adjacent areas, and account for the persistence of large animal populations at depth (Sournia, 1994). Erga et al. (2014) showed that a front in the Norwegian Sea is an area of higher production due to the vertical circulation bringing nutrients into the euphotic zone. In our particular case, the front was confirmed by the presence of strong gradients of both conservative temperature and density (Fig. 2a and b). Numerous studies have shown phytoplankton aggregations to be closely related to fronts in the ocean. That fronts are typically sites of enhanced phytoplankton biomass suggesting that there may be processes common to various types of fronts that support such aggregations (Franks, 1992). In the Catalan front (northwest Mediterranean), high chlorophyll-*a* concentrations and diatom dominance were observed during winter-spring, while a high abundance of coccolithophorids was observed to be offshore of the front (Estrada et al., 1999). Lehahn et al. (2007) showed that fronts in the Northeast Atlantic clearly separate regions of different chlorophyll-*a* concentration and produce chlorophyll filaments due to submesoscale vertical nutrient injection. Fronts occur over a wide range of scales and are ubiquitous throughout the ocean, being formed by a persistent wind stress curl or by spatially nonuniform surface fluxes of heat which in turn sustain the vertical advective transport of nutrients from the subsurface into the euphotic layer (Mahadevan, 2016). In the northeastern Arabian Sea, fronts are active biological spots owing to injection of subsurface nutrients into the surface layer where the plankton response depended on the age of the front as well as with the initial or background conditions under which a front forms (Sarma et al., 2018). Fronts are prominent structures that organize transport and dispersion of coastal waters in the Ibiza channel (Western Mediterranean), impacting physical and biological coupled processes at regional scales (Hernández-Carrasco et al., 2018).

Studies have shown that the presence of a mesoscale dipole structure has an important effect over the distribution of particulate organic matter and plays an important ecological role in enhancing pelagic production and transporting coastal production offshore (Kolasinski et al., 2012). High phytoplankton abundance and chlorophyll-*a* values have been associated with a thermal front induced in the boundary zone between a dipole in the south of the Gulf of Mexico (Aldeco-Ramírez et al., 2009). Abundances of phytoplankton are frequently higher near the edges of a dipole in the Gulf of Alaska compared to the center or outside waters (Batten and Crawford, 2005), demonstrating that enhanced primary production is capable of supporting higher trophic levels. These edge regions may, therefore, represent excellent forage areas for fish, birds and marine mammals. Indeed, larval fish are often associated with high standing stocks of chlorophyll *a*nd zooplankton found at the edges of eddies in the northwest of the Gulf of Alaska, suggesting that frontal regions may play important roles in the survival or growth of some species (Peterson et al., 2011).

Our observations evidenced that phytoplankton group distribution is closely related to the front formed between both cyclone-anticyclone structures considering the high abundance of the three phytoplankton groups analyzed and relatively high values of chlorophyll-*a* were found in that region. Additionally, a higher concentration of the phytoplankton groups was observed at the zone along the transect crossing the bay on latitude 24.6°N which can be associated with other processes and not only with the front.

High phytoplankton abundances at the surface and high concentrations of chlorophyll-*a* were observed in regions considered to be frontal zones between a dipole with high horizontal shear rates (Thompson et al., 2007).

Using two high-resolution ocean transects across a pair of mesoscale eddies (cyclone–anticyclone) in the North Pacific Ocean, Guidi et al. (2012) showed that horizontal turbulent stirring has a dominant control on the spatial distribution of some planktonic organisms around this feature, considering that the horizontal stirring associated with mesoscale eddies affects the distribution of plankton blooms and may even determine phytoplankton community structure and dominant groups by creating fluid dynamical niches within scales of a few kilometers; in this way, buoyant phytoplankton cells are advected into the frontal zone and accumulated in

regions of convergent flow, enhancing chlorophyll-*a* concentrations there.

The high biomass values commonly seen at fronts are often explained by a physiological response of the organisms to the frontal environment. However, some intuitive idea of the physiological response of the organisms to their new environment can be obtained by consideration of the physical processes affecting the organisms during swimming and accumulation (Franks, 1992).

Because they are not under the influence of the ambient vertical velocities, strong swimmers are very likely to create accumulation zones. Weak swimmers may not always create such zones, but their swimming behavior will alter the amount of time they spend in any given region of the flow (Persson et al., 2013). Due to the absence of turbulence measurements in the front during the time of our observations, we assume it to be high; under this scheme the tolerance to high turbulence by dinoflagellates, which is often accompanied by high swimming speeds, could explain the abundance of this group, which in consequence could serve as pelagic seed stock for subsequent plankton aggregations (Smayda, 2002). The ability of dinoflagellate species to tolerate the vertical velocities of frontal zones has suggested that fronts may serve as "pelagic seed banks" (Smayda, 2002). Although there are no nutrient measurements for the time of our observations, it is well known that in BoP, the presence of mesoscale cyclonic eddies modulate the pulses of fertilization to the euphotic zone due to an Ekman pumping (Coria-Monter et al., 2017), then a differential distribution of phytoplankton has been observed, with a predominance of diatoms in the periphery of the eddy due to a high concentration ($>10\ \mu M$) of soluble reactive Si (Coria-Monter et al., 2014). Under this scheme the surface layer divergence by eddies may be transporting the upwelled subsurface nutrient-rich water to the eddy field at a rate similar as it takes for the diatoms and silicoflagellates to flourish.

The stretching of the isolines in the frontal region between the cyclone-anticyclone has dynamical consequences, as it intensifies the existing lateral subsurface temperature and density gradient, as reported in mesoscale fronts created by a dipole in the North Pacific Ocean (Guidi et al., 2012).

5. Conclusions

The dipole and its front associated can be the dominant physical features influencing the horizontal distribution of phytoplankton in the BoP. To date, the information available in the area showed the presence of a quasi-permanent cyclonic eddy, which originates fertilization in the euphotic zone and a differential phytoplankton distribution, with a high abundance of dinoflagellates at its center and a high abundance of diatoms at the periphery. The results presented in this study showed the presence of a dipole structure (cyclone-anticyclone), which induced a frontal region between both structures, prompting a high accumulation of phytoplankton. Additionally, a high abundance of diatoms was observed close to the center of the anticyclonic pole. Many aspects of the influence of physical forcing on the phytoplankton community remain uncertain, then more detailed observations are required in order to enable the evaluation of many aspects of eddies, such as differences and variations in hydrographic properties, seed populations, and food-web dynamics.

Acknowledgments

Dirección General de Asuntos del Personal Académico (DGAPA-UNAM) sponsored E. Durán-Campos and Consejo Nacional de Ciencia y Tecnología (CONACyT) E. Coria-Monter during this study. The ship time of the research cruise DIPAL-II on board the R/V *El Puma* was funded by Universidad Nacional Autónoma de Mexico (UNAM). We would like to thank the participants of this research cruise. We appreciate the assistance of Jorge Castro in improving the figures, and F. Sergio Castillo-Sandoval for technical assistance in the laboratory analyses. We are grateful for the numerous helpful comments by two anonymous reviewers.

References

Aldeco-Ramírez, J., Monreal-Gómez, M.A., Signoret-Poillon, M., Salas de León, D.A., Hernández-Becerril, D.U., 2009. Occurrence of a subsurface anticyclonic eddy, fronts and *Trichodesmium* spp. over the Campeche Canyon region, Gulf of Mexico. Cienc. Mar. 35 (4), 333–344.

Batten, S.D., Crawford, W.R., 2005. The influence of coastal origin eddies on oceanic plankton distributions in the eastern Gulf of Alaska. Deep-Sea Res. Pt. II 52 (7–8), 991–1010, http://dx.doi.org/10.1016/j.dsr2.2005.02.009.

Coria-Monter, E., Monreal-Gómez, M.A., Salas de León, D.A., Aldeco-Ramírez, J., Merino-Ibarra, M., 2014. Differential distribution of diatoms and dinoflagellates in a cyclonic eddy confined in the Bay of La Paz, Gulf of California. J. Geophys. Res. 119, 6258–6268, http://dx.doi.org/10.1002/2014JC009916.

Coria-Monter, E., Monreal-Gómez, M.A., Salas de León, D.A., Merino-Ibarra, M., Durán-Campos, E., 2017. Wind driven nutrient and subsurface chlorophyll-*a* enhancement in the Bay of La Paz, Gulf of California. Estuar. Coast. Shelf Sci. 196, 290–300, http://dx.doi.org/10.1016/j.ecss.2017.07.010.

Durán-Campos, E., Salas de León, D.A., Monreal-Gómez, M.A., Aldeco-Ramírez, J., Coria-Monter, E., 2015. Differential zooplankton aggregation due to relative vorticity in a semi-enclosed bay. Estuar. Coast. Shelf Sci. 164, 10–18, http://dx.doi.org/10.1016/j.ecss.2015.06.030.

Edler, L., Elbrächter, M., 2010. The Utermohl method for quantitative phytoplankton analysis. In: Karlson, B., Cusack, C., Bresnan, E. (Eds.), Microscopic and Molecular Methods for Quantitative Phytoplankton Analysis. UNESCO, Paris, 13–21.

Erga, S.R., Ssebiyonga, N., Hamre, B., Frette, O., Hovland, E., Hancke, K., Drinkwater, K., Rey, F., 2014. Environmental control of phytoplankton distribution and photosynthetic performance at the Jan Mayen Front in Norwegian Sea. J. Mar. Syst. 130, 193–205, http://dx.doi.org/10.1016/j.jmarsys.2012.01.006.

Estrada, M., Varela, M., Salat, J., Cruzado, A., Arias, E., 1999. Spatio-temporal variability of the winter phytoplankton distribution across the Catalan and North Balearic fronts (NW Mediterranean). J. Plankton Res. 21 (1), 1–20, http://dx.doi.org/10.1093/plankt/21.1.1.

Franks, P.J.S., 1992. Sink or swim: accumulations of biomass at fronts. Mar. Ecol. Prog. Ser. 82, 1–12.

Gaube, P., Chelton, D.B., Strutton, P.G., Behrenfeld, M.J., 2013. Satellite observations of chlorophyll, phytoplankton, biomass and Ekman pumping in nonlinear mesoscale eddies. J. Geophys. Res. 118, 6349–6370, http://dx.doi.org/10.1002/2013JC009027.

Guidi, L., Calil, P.H.R., Duhamel, S., Björkman, K.M., Doney, S.C., Jackson, G.A., Li, B., Church, M.J., Tozzi, S., Kolber, Z.S., Richards, K.J., Fong, A.A., Letelier, R.M., Gorsky, G., Stemmann, L., Karl, D.M., 2012. Does eddy-eddy interaction control surface phytoplankton distribution and carbon export in the North Pacific Subtropical Gyre? J. Geophys. Res. 117 (G2), 12 pp., http://dx.doi.org/10.1029/2012JG001984 G02024.

Hernández-Carrasco, I., Orfila, A., Rossi, V., Garcon, V., 2018. Effect of small scale transport processes on phytoplankton distribution in coastal seas. Sci. Rep. 8, 8613, http://dx.doi.org/10.1038/s41598-018-26857-9.

Hu, C., Lee, Z., Franz, B., 2012. Chlorophyll-*a* algorithms for oligotrophic oceans: a novel approach based on three-band reflectance difference. J. Geophys. Res. 117, http://dx.doi.org/10.1029/2011JC007395 C01011, 25.

IOC, SCOR, IAPSO, 2010. The international thermodynamic equation of seawater-2010. Calculation and use of thermodynamic properties. Intergovernmental Oceanographic Commission, Manual and guides, No. 56. UNESCO, Paris, p. 196.

Kolasinski, J., Kaehler, S., Jaquemet, S., 2012. Distribution and sources of particulate organic matter in a mesoscale eddy dipole in the Mozambique Channel (south-western Indian Ocean): insight from C and N stable isotopes. J. Mar. Syst. 96—97, 122—131, http://dx.doi.org/10.1016/j.jmarsys.2012.02.015.

Lavín, M.F., Castro, R., Beier, E., Godínez, V.M., 2013. Mesoscale eddies in the southern Gulf of California during summer: characteristics and interaction with the wind stress. J. Geophys. Res. 118, 1367—1381, http://dx.doi.org/10.1002/jgrc.20132.

Lehahn, Y., d'Ovidio, F., Lévy, M., Heifetz, E., 2007. Stirring of the northeast Atlantic spring bloom: a Lagrangian analysis based on multisatellite data. J. Geophys. Res. 112 (C8), C08005, 15 pp., http://dx.doi.org/10.1029/2006JC003927.

Liu, F., Tang, S., Chen, C., 2013. Impact of nonlinear mesoscale eddy on phytoplankton distribution in the northern South China Sea. J. Mar. Syst. 123—124, 33—40, http://dx.doi.org/10.1016/j.jmarsys.2013.04.005.

Mahadevan, A., 2016. The impact of submesoscale physics on primary productivity of plankton. Annu. Rev. Mar. Sci. 8, 161—184, http://dx.doi.org/10.1146/annurev-marine-010814-015912.

Maúre, E.R., Ishizaka, J., Sukigara, C., Mino, Y., Aiki, H., Matsuno, T., Tomita, H., Goes, J.I., Gomes, H.R., 2017. Mesoscale eddies control the timing of spring phytoplankton blooms: a case study in the Japan Sea. Geophys. Res. Lett. 44 (21), 11115—11124, http://dx.doi.org/10.1002/2017GL074359.

McGillicuddy Jr., D.J., 2016. Mechanisms of physical—biological—biogeochemical interaction at the oceanic mesoscale. Annu. Rev. Mar. Sci. 8, 125—159, http://dx.doi.org/10.1146/annurev-marine-010814-015606.

McGillicuddy Jr., D.J., Anderson, L.A., Bates, N.R., Bibby, T., Buesseler, K.O., Carlson, C., Davis, C.S., Ewart, C., Falkowski, P., Goldthwait, S.A., Hansell, D.A., Jenkins, W.J., Johnson, R., Kosnyrev, V., Ledwell, J.R., Li, Q.P., Siegel, D.A., Steinberg, D. K., 2007. Eddy/wind interactions stimulate extraordinary mid-ocean plankton blooms. Science 316 (5827), 1021—1026, http://dx.doi.org/10.1126/science.1136256.

McGillicuddy Jr., D.J., Robinson, A.R., 1997. Eddy induced nutrient supply and new production in the Sargasso Sea. Deep-Sea Res. 44 (8), 1427—1450, http://dx.doi.org/10.1016/S0967-0637(97)00024-1.

Molina-Cruz, A., Pérez-Cruz, L., Monreal-Gómez, M.A., 2002. Laminated sediments in the Bay of La Paz, Gulf of California: a depositional cycle regulated by pluvial flux. Sedimentology 49, 1401—1410, http://dx.doi.org/10.1046/j.1365-3091.2002.00505.x.

Monreal-Gómez, M.A., Molina-Cruz, A., Salas de León, D.A., 2001. Water masses and cyclonic circulation in Bay of La Paz, Gulf of California, during June 1998. J. Mar. Syst. 30, 305—315, http://dx.doi.org/10.1016/S0924-7963(01)00064-1.

Pardo, M.A., Silverberg, N., Gendron, D., Beier, E., Palacios, D.M., 2013. Role of environmental seasonality in the turnover of cetacean community in the southwestern Gulf of California. Mar. Ecol. Prog. Ser. 487, 245—260, http://dx.doi.org/10.3354/meps10217.

Persson, A., Smith, B.C., Wikfors, G.H., Alix, J.H., 2013. Differences in swimming pattern between life cycle stages of the toxic dinoflagellate *Alexandrium fundyense*. Harmful Algae 21—22, 36—43, http://dx.doi.org/10.1016/j.hal.2012.11.005.

Peterson, T.D., Crawford, D.W., Harrison, P.J., 2011. Mixing and biological production at eddy margins in the eastern Gulf of Alaska. Deep-Sea Res. 58 (Pt I), 377—389, http://dx.doi.org/10.1016/j.dsr.2011.01.010.

Pond, S., Pickard, G.L., 1983. Introductory Dynamical Oceanography, 2nd ed. Pergamon Press, Oxford, 329 pp.

Salas de León, D.A., Carbajal, N., Monreal-Gómez, M.A., Gil-Zurita, A., 2011. Vorticity and mixing induced by the barotropic M2 tidal current and zooplankton biomass distribution in the Gulf of California. J. Sea Res. 66, 143—153, http://dx.doi.org/10.1016/j.seares.2011.05.011.

Salas de León, D.A., Monreal-Gómez, M.A., Signoret, M., Aldeco-Ramírez, J., 2004. Anticyclonic—cyclonic eddies and their impact on near-surface chlorophyll stocks and oxygen supersaturation over the Campeche Canyon, Gulf of Mexico. J. Geophys. Res. 109 (C5), C05012, 10 pp., http://dx.doi.org/10.1029/2002JC001614.

Sarma, V.V.S.S., Desai, D.V., Patil, J.S., Khandeparker, L., Aparna, S. G., Shankar, D., D'Souza, S., Dalabehera, H.B., Mukherjee, J., Sudharani, P., Anil, A.C., 2018. Ecosystem response in temperature fronts in the northeastern Arabian Sea. Prog. Oceanogr. 165, 317—331, http://dx.doi.org/10.1016/j.pocean.2018.02.004.

Simpson, J.J., Lynn, R.J., 1990. A mesoscale eddy dipole in the offshore California current. J. Geophys. Res. 95 (C8), 13009—13022, http://dx.doi.org/10.1029/JC095iC08p13009.

Smayda, T., 2002. Turbulence, water mass stratification and harmful algal blooms: an alternative view and frontal zones as "pelagic seed banks". Harmful Algae 1, 95—112, http://dx.doi.org/10.1016/S1568-9883(02)00010-0.

Sournia, A., 1994. Pelagic biogeography and fronts. Prog. Oceanogr. 34, 109—120, http://dx.doi.org/10.1016/0079-6611(94)90004-3.

Thompson, P.A., Pesant, S., Waite, A.M., 2007. Contrasting the vertical differences in the phytoplankton biology of a dipole pair of eddies in the south-eastern Indian Ocean. Deep-Sea Res. Pt. II 54, 1003—1028, http://dx.doi.org/10.1016/j.dsr2.2006.12.009.

Tomas, C.R., 1997. Identifying Marine Phytoplankton. New York Acad. Press, New York, 858 pp.

Vajravelu, M., Martin, Y., Ayyappan, S., Mayakrishnan, M., 2017. Seasonal influence of physic—chemical parameters on phytoplankton diversity, community structure and abundance at Parangipettai coastal waters, Bay of Bengal, south east coast of India. Oceanologia 60 (2), 114—127, http://dx.doi.org/10.1016/j.oceano.2017.08.003.

Wang, L., Huang, B., Chiang, K.P., Liu, X., Chen, B., Xie, Y., Xu, Y., Dai, M., 2016. Physical—biological coupling in the western South China Sea: the response of phytoplankton community to a mesoscale cyclonic eddy. PLOS ONE 11 (4), e0153735, http://dx.doi.org/10.1371/journal.pone.0153735.

Oceanologia (2019) 61, 341—349

Available online at www.sciencedirect.com

ScienceDirect

journal homepage: www.journals.elsevier.com/oceanologia/

ORIGINAL RESEARCH ARTICLE

Limited success of the non-indigenous bivalve clam *Rangia cuneata* in the Lithuanian coastal waters of the Baltic Sea and the Curonian Lagoon

Sabina Solovjova [a,b,*], **Aurelija Samuilovienė** [a], **Greta Srėbalienė** [a], **Dan Minchin** [a,c], **Sergej Olenin** [a]

[a] *Marine Research Institute, Klaipėda University, Klaipėda, Lithuania*
[b] *Department of Environmental Research, Environmental Protection Agency, Klaipėda, Lithuania*
[c] *Marine Organism Investigations, Ballina, Killaloe, Ireland*

Received 29 January 2018; accepted 29 January 2019
Available online 13 February 2019

KEYWORDS
Semitropical bivalve;
Coastal lagoon;
Exposed coast;
Winter conditions;
Ballast water;
Natural spread.

Summary The gulf wedge clam, common rangia *Rangia cuneata*, with a native origin in the Gulf of Mexico has spread to north European brackish and freshwaters. This semitropical species is able to survive in conditions of low winter temperatures in boreal environment of the Baltic Sea. Its expansion within lagoons and sheltered bays in the southern and eastern parts of the Baltic Sea appears to be with natural spread and its discontinuous distribution is likely to have been with shipping, either within ballast water or as settled stages transported with dredged material. In this account, we report on the occurrence of *R. cuneata* in Lithuanian waters. We compare habitats of the common rangia in the Curonian Lagoon and in the exposed coastal waters of the Baltic Sea. We notice high mortality of the species in the Lithuanian waters in comparison to the neighboring Vistula Lagoon. Based on finding of small specimens of *R. cuneata* attached to the spiked watermilfoil *Myriophyllum spicatum*, we indicate a risk of local spread with movements of fishing equipment and snagged plants on anchors or boat trailers removed from the water. We discuss the possibility of further spread of the common rangia to similar environments in the Baltic Sea and elsewhere in Europe.

* Corresponding author at: Marine Research Institute, Klaipėda University, Universiteto ave. 17, 92294, Klaipėda, Lithuania.
E-mail address: sabina.lt@gmail.com (S. Solovjova).
Peer review under the responsibility of Institute of Oceanology of the Polish Academy of Sciences.

ELSEVIER Production and hosting by Elsevier

https://doi.org/10.1016/j.oceano.2019.01.005

1. Introduction

The common rangia *Rangia cuneata* (G.B. Sowerby I, 1832) (Bivalvia, Mactridae), has a native origin within the Gulf of Mexico and extended its range northwards to the Chesapeake Bay by the 1960s and arrived to the lower reaches of the Hudson River (Carlton, 1992). It is spreading within north European brackish waters (AquaNIS, 2018; Verween et al., 2006; and references therein). It was first found, and well established, in Belgium during 2005 (Verween et al., 2006) and has since spread to estuaries in southern regions of the North Sea (Bock et al., 2015; Gittenberger et al., 2015; Kerckhof et al., 2018; Neckheim, 2013; Wiese et al., 2016) and has been found in freshwater in Britain (Willing, 2015).

It entered the south-eastern Baltic Sea about 2010, in the waterway leading to the port of Kaliningrad, Vistula Lagoon region in Russia (Ezhova, 2012; Rudinskaya and Gusev, 2012). In 2011 it was recorded in the Polish part of the Vistula Lagoon (Janas et al., 2014; Warzocha and Drgas, 2013; Warzocha et al., 2016). It was in 2013 when it was recorded at an early stage along Lithuanian coastal waters (Solovjova, 2014), and further to the north in Pärnu Bay, Gulf of Riga, Estonia (Möller and Kotta, 2017). In 2015 it appeared on the German Baltic coast (Wiese et al., 2016) and in a Swedish Baltic fjord in 2016 (Florin, 2017). In this account, we present data on the first record and spread of *R . cuneata* in Lithuanian waters. We compare habitats of the common rangia in the Curonian Lagoon and in the exposed coastal waters of the Baltic Sea, and discuss the possibility of its further spread to similar environments in the Baltic Sea and elsewhere in Europe.

2. Material and methods

2.1. Study area

The Baltic Sea area along the exposed coast of the Curonian Spit is mesohaline, with a stable salinity (Table 1). From June to September where the epilimnion extends down to 20—30 m (Olenin and Daunys, 2004). In winter, ice usually occurs along this shoreline, but does not extend offshore where wedge clam rangia is found. Coastal currents in the south-eastern Baltic are usually from south to north and on account of its exposure the seabed is well oxygenated (Olenin and Daunys, 2004) and is densely packed with fine sand at all stations with the exception of an admixture of mud near the Curonian Lagoon outlet.

The Curonian Lagoon is exposed to irregular inflows of marine water, causing abrupt changes in salinity within the Klaipėda Strait and extending up to 40 km within the lagoon, where otherwise the average annual salinity is 2.5 (Dailidienė and Davulienė, 2008). Due to the shallow depths, the lagoon rapidly heats up in spring and remains warmer during the summer than the surface water of the open sea (Gasiūnaitė et al., 2008). The lagoon has no seasonal thermocline and in winter there is ice-cover (Table 1) which in recent years occurs for fewer days on account of warmer winter conditions. Whereas the Klaipėda Strait is always ice-free. Localized anoxia events may take place during ice coverage and overnight during summer (Gasiūnaitė et al., 2008). The main sediments within the Lagoon are sand and silt where there are shell deposits. In the port area of the Klaipėda Strait bottom sediments are influenced by constant dredging and water flow from being at the lagoon entrance. When compared with the exposed coast, the lagoon is more eutrophic by having seasonal phytoplankton blooms and high accumulations of organic carbon in bottom sediments (Remeikaitė-Nikienė et al., 2016).

2.2. Morphological identification

R. cuneata can be confused with the Baltic clam *Limecola balthica* (Linnaeus, 1758) especially for specimens <10 mm shell length (Fig. 1). These two species can be distinguished based on the identification descriptions of the common rangia (Abbott and Morris, 2001; Janas et al., 2014; Leal, 2000; Verween et al., 2006): (a) a thicker and more convex shell; (b) the prominent and anteriorly curved umbo; (c) internal ligament of the left shell with chondrophore, typically with two fused cardinal teeth forming an 'inverted V'.

2.3. Molecular identification

For molecular identification DNA was extracted from a specimen, which was clearly identified by morphological features as *R. cuneata* (shell length 27 mm) using InnuPREP DNA Mini Kit (Analytik Jena AG, Germany) according to manufacturer's instructions. The identification was performed using a species-specific molecular marker developed by Ardura et al. (2015) for *R. cuneata*. For amplification of a 205 bp long fragment of the 16S rRNA gene the *R. cuneata*-specific forward primer RC-16Sar: 5′-AATTTCTTCTAATGATGTGAGG-3 (Ardura et al., 2015) and universal revers primer 16Sbr: 5′-CCGGTCTGAACTCAGATCACGT-3′ (Palumbi, 1996) were used.

Table 1 Environmental parameters at stations with living and vacant *Rangia cuneata* in 2013—2018.

Parameter	Exposed coast	Curonian Lagoon
Depth range [m]	13—17	0.3—11.2
Salinity [PSU]	6.40—7.48	0.18—7.27
Temperature [°C]	1.05—20.35	0.52—21.76
Duration of ice cover, days per year	None	30—64
Dissolved oxygen [mg L^{-1}]	4.44—13.28	4.70—14.64
Oxygen saturation [%]	40—119	48—126

Salinity, temperature, dissolved oxygen, and oxygen saturation are indicated for the near bottom layer. (Lithuanian Environmental Protection Agency (LEPA) monitoring data.)

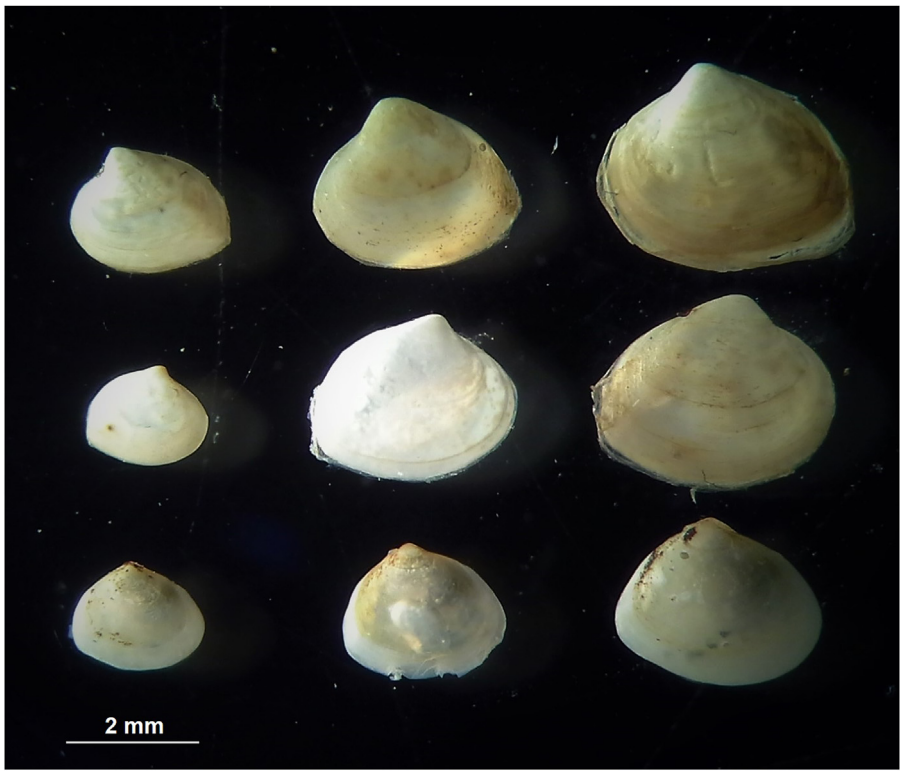

Figure 1 A view of small (<10 mm) shells of *Rangia cuneata* (two above rows) and *Limecola balthica* (row below) under dissecting microscope (Photo: S. Solovjova).

Amplification was carried out in six replicates of *R. cuneata* using InnuTaq DNA polymerase (Analytik Jenna AG, Germany) in 20 μl reactions containing 2 μl of DNA, 2.5 mM $MgCl_2$, 250 μM of each dNTP, 1.25 μg μl^{-1} BSA and 0.7 pmol of each primer. The PCR protocol consisted of a denaturation at 95°C for 3 min followed by 35 cycles at 95°C for 30 s, 54°C for 30 s, 72°C for 45 s followed by a final extension at 72°C for 5 min and a 4°C hold. PCR products were visualized on a 1.5% agarose gel stained by SybrSafe. To exclude the possibility of false positives, species-specific PCR was performed with three other bivalve mollusks species occurring within the sampling area: *L. balthica*, *Dreissena polymorpha* (Pallas, 1771) and *Mytilus* spp. Linnaeus, 1758. To exclude the possibility of PCR inhibition causing negative PCR results, a PCR with universal primers 16Sar and 16Sbr described by Palumbi (1996) was performed.

2.4. Sampling at monitoring stations

The annual benthic monitoring program, which began in 1980, involves 22 stations at depths of 13—117 m within the Lithuanian sector of the southeastern Baltic and 10 stations in the Curonian Lagoon (Fig. 2). Further samples, taken monthly from May to November were at selected stations in the Curonian Lagoon. Three of these are located in the dredged area of the Klaipėda Strait at depths 7—12 m and elsewhere in the Lithuanian part of the Lagoon at 2—5 m. The most recent survey was undertaken in September 2018.

A 71 kg Van Veen grab sampler with a sample area of 0.1 m^{-2} was used capable of penetrating sediments to 10—15 cm at the coastal stations and to *ca.* 10—20 cm within the Lagoon. Three to five samples were taken at each station, each separately sieved using a 0.5 mm mesh size. Retained material was fixed in a 4% formaldehyde solution and later examined using a stereomicroscope at 7.8× to 120×, according to the procedure of HELCOM (2014). In total, approximately 230 Van Veen grab samples were taken in the Lithuanian part of the Baltic Sea and 140 in the Curonian Lagoon were the common rangia was expected to occur. Samples were examined for live common rangia and also their vacant shells. All rangia were counted and measured for live wet weight (with shells, without water in the mantle cavity) using an analytical balance (0.0001 g). A digital caliper (0.01 mm) was used to measure the length of the living and vacant shells.

Salinity, temperature and oxygen concentration were measured at each station using a Multi Water Sampler.

2.5. Additional sampling

In the Curonian Lagoon additional samples were taken during 2015 close to the shoreline, at depths <0.8 m, using a standard Boettger hand net (sampler steel frame 25 × 25 cm; net sieve mesh size 0.5 mm) near Juodkrantė, Preila, Nida and in the Klaipėda strait (Fig. 2). A basket dredge (260 mm open diameter, 300 mm height, 180 mm bottom diameter, diagonal mesh size 5 mm; Minchin, 2014) was used in the Lagoon each month from May to September 2018 in areas where vacant shells and living specimens were obtained using grab sampler.

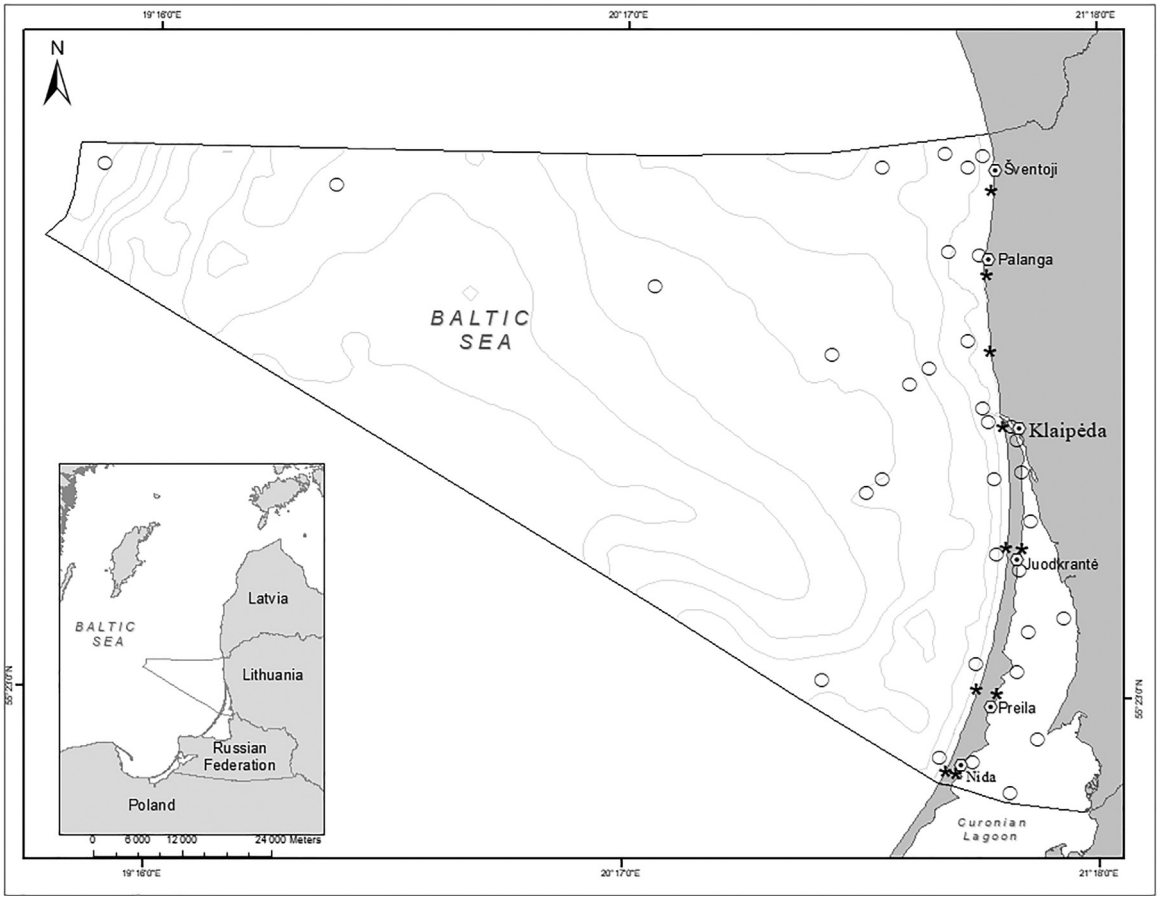

Figure 2 Map of the benthic monitoring stations (opened circles) in the Lithuanian part of the Baltic Sea and in the Curonian Lagoon. Places of littoral excursions and additional nearshore sampling shown by asterisks. A line designates the Lithuanian Exclusive Economic Zone; isobaths indicate 10 m depth intervals.

Shore surveys were undertaken in 2016—2018 for beached shells of *R. cuneata* on either side of the Curonian Spit and to the north of Klaipėda (Fig. 2). Observations were performed for more than 50 sampling occasions along 50 m belt transects between the water's edge to the highest accumulations of shore drift.

3. Results

3.1. Distribution and size structure

R. cuneata was first recognized in Lithuanian marine waters in May 2013, at two coastal stations west of the Curonian Spit. Here two small living individuals and vacant shells were found (Fig. 3, left). At the same time at the entrance to the Curonian Lagoon, only vacant shells were detected.

Living individuals were found only once at the coastal marine stations after 2013, whereas in the Klaipėda Strait they were detected in all years, except 2017 (Fig. 3, right). Generally, the number of living rangia detected remained low with a maximum of four individuals taken in a Van Veen sample in 2016. It is noteworthy that two living 4—5 mm specimens were found 20 km from the Lagoon entrance during September 2015. These were byssally attached to the spiked watermilfoil *Myriophyllum spicatum* L. at the depth 0.3—0.6 m. The detailed information on *R. cuneata* findings in the Lithuanian waters together with environmental data is presented in Table S1 in Appendix. Therewith, environmental conditions data one year before *R. cuneata* found are presented in Table S2 in Appendix.

The vacant shells did not increase over the following years at marine coastal stations, whereas in the Lagoon their numbers were gradually growing (Fig. 4). Also, the maximum size of the living mollusks and vacant shells in the Lagoon was four times greater than at exposed marine sites. Living individuals attained 27 mm shell length and weighing 5.4 g and vacant shell up to 37 mm (Fig. 5). Size distribution of the vacant shells in the Curonian Lagoon is shown in Fig. 6.

3.2. Shore surveys

During the initial period of observation (2016—2017) only shells of common mollusks were found: *L. balthica*, *Mya arenaria* Linnaeus, 1758 and *Cerastoderma glaucum* (Bruguière, 1789) at the seaside exposed sandy coast. Beached shells within the Lagoon consisted of the freshwater bivalves — *Anodonta cygnea* (Linnaeus, 1758), *Unio tumidus* Philipsson, 1788, *D. polymorpha* and gastropods — *Viviparus viviparus* (Linnaeus,

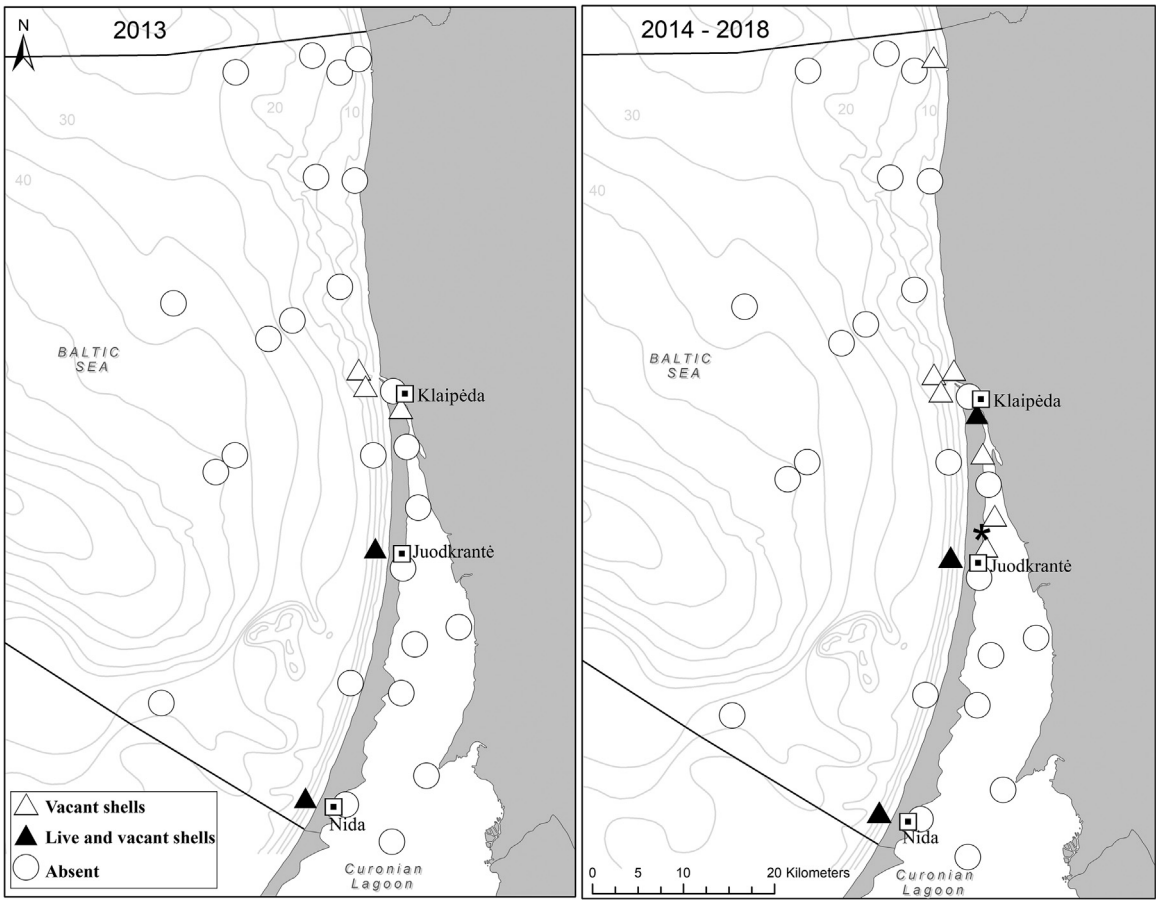

Figure 3 First records of *Rangia cuneata* in the Lithuanian waters in 2013 (left); findings of *R. cuneata* in 2014—2018 (right): ▲ findings of both live mollusks and vacant shells; △ only vacant shells, * live mollusks attached to the spiked watermilfoil *Myriophyllum spicatum*, ○ stations with no presence of *R. cuneata*.

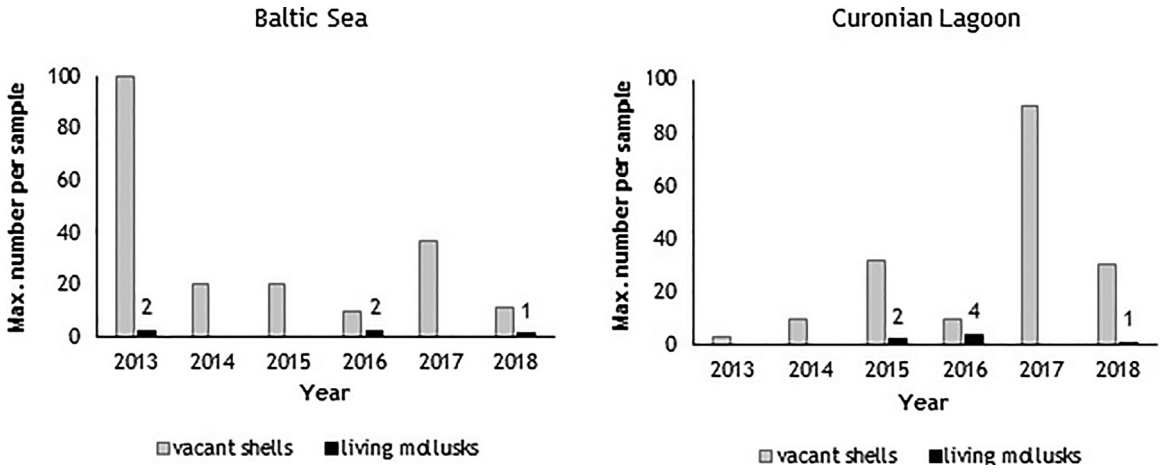

Figure 4 Dynamic of the maximum number of the vacant shells and living mollusks in grab samples at the monitoring stations at the southeastern Baltic and in the Curonian Lagoon. The number of living mollusks found is indicated.

1758), *Radix auricularia* (Linnaeus, 1758) and *Planorbarius corneus* (Linnaeus, 1758). For the first time, one beached shell of *R. cuneata* was found in 2018 April (shell length 27 mm) on the seashore to the north of Klaipėda (Fig. 3). In October, after storm events, 15 vacant shells (shells length 26—35 mm) were found. Remarkably, they were found in a debris, most probably transported by currents from the Curonian Lagoon as they contained remains of freshwater organisms (*A. cygnea*, *U. tumidus*, *V. viviparus*, canes, reeds, *etc.*) not occurring in the marine area.

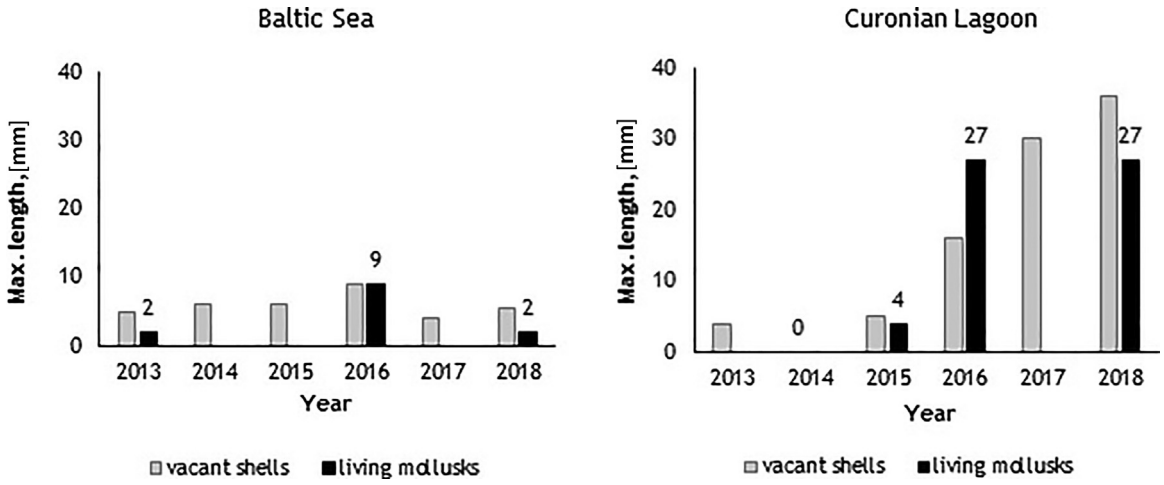

Figure 5 Dynamic of the maximum shell length, mm of *Rangia cuneata* in the southeastern Baltic and in the Curonian Lagoon. Numbers indicate the maximum size of living mollusks found in the particular year.

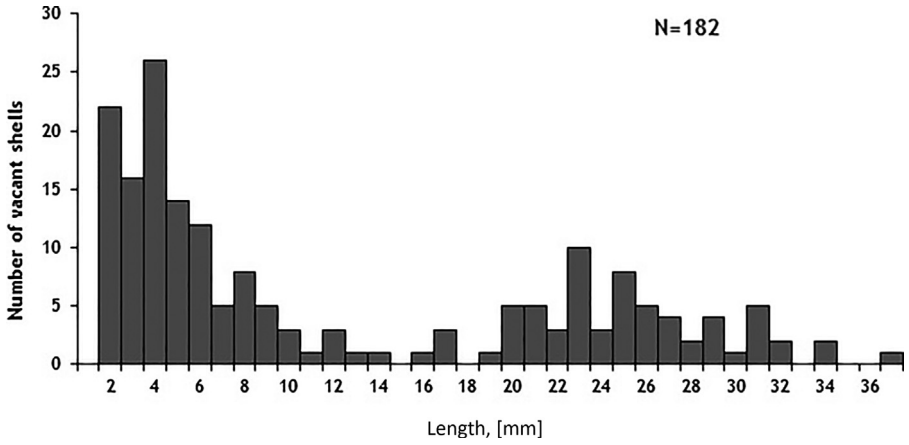

Figure 6 Length-frequency distribution of *Rangia cuneata* collected in the Klaipėda Strait, Curonian Lagoon in May—September 2018.

3.3. Molecular species identification

Universal 16S rRNA gene-targeted primers yielded positive PCR amplifications in all samples — the amplicons were approximately 500 bp long that is the expected size (Fig. 7b). Amplification using *R. cuneata*-specific primers was detected only when DNA from *R. cuneata* specimen was used as a template. Only one PCR product of the expected size (approximately 200 bp) was obtained with no additional bands (Fig. 7a). Amplification using DNA extracted from other bivalve mollusks did not get any result.

4. Discussion

4.1. Living conditions and status of the common rangia population in the Lithuanian waters

The high number of small vacant shells in the initial period and slow growth of the common rangia in the marine coastal area (Figs. 4 and 5) indicates that conditions here generally are less suitable than in the Curonian Lagoon. This may be due to higher hydrodynamic action at the exposed marine coast, hard-packed sediments, less organics and reduced food resources than in the Curonian Lagoon, where the bottom sediments are softer and richer with organic material (Remeikaitė-Nikienė et al., 2016). Temporal anoxia, which may occur during the ice coverage and in summer at night in the Lagoon (Gasiūnaitė et al., 2008) is an unlikely limiting factor for common rangia as adult specimens have the ability to live anaerobically for up to 2 weeks (Risk Assessment, 2017). However, even in the Curonian Lagoon, the abundance of the common rangia remains low (only seven live specimens found during five years since the first detection) than compared to the neighbouring Vistula Lagoon (max. abundance up to 4040 ind. m^{-2}; Rudinskaya and Gusev, 2012) and coastal waters of the Gulf of Gdańsk (540 ind. m^{-2}; Janas et al., 2014). At the same time the number of vacant shells on sites is attaining a hundred per sample.

According to Rudinskaya and Gusev (2012) the rangia yearlings in the Vistula Lagoon can reach 14 mm in size, therefore finding of numerous vacant shells (<10 mm) in

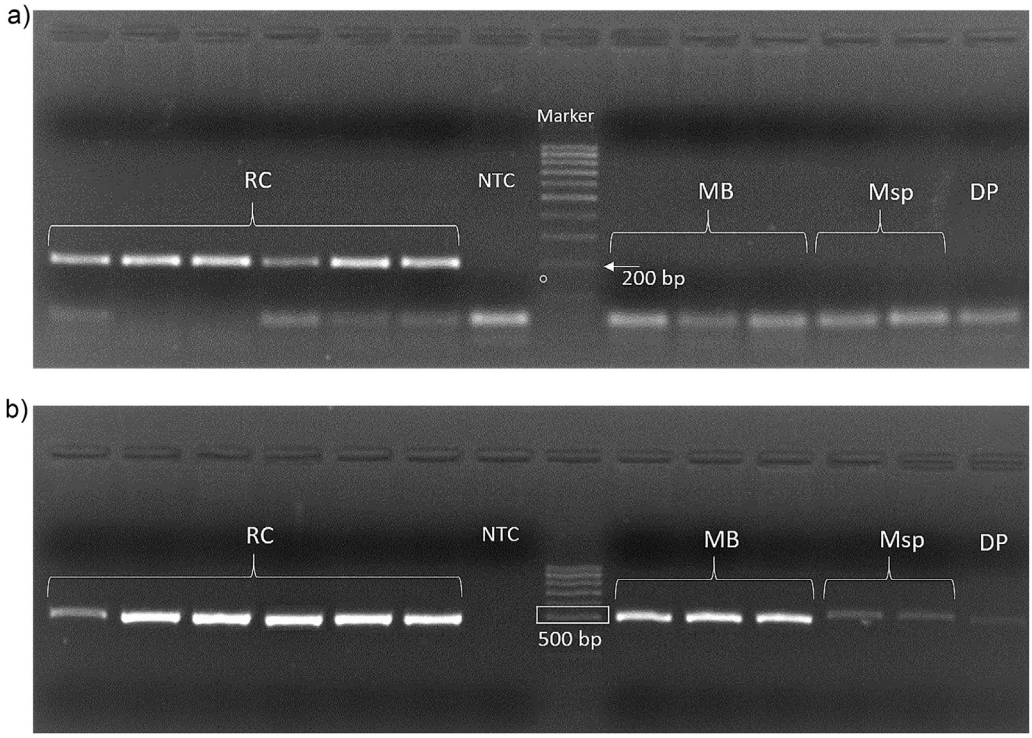

Figure 7 (a) Agarose gel of PCR products obtained with *Rangia cuneata*-specific primers. RC: *Rangia cuneata*, MB: *Limecola balthica*, Msp: *Mytilus* spp., DP: *Dreissena polymorpha*, NTC: non-template control, Marker: DNA size marker (100 bp DNA ladder). (b) Agarose gel of PCR products obtained with universal primers (Palumbi, 1996). RC: *Rangia cuneata*, MB: *Limecola balthica*, Msp: *Mytilus* spp., DP: *Dreissena polymorpha*, NTC: non-template control, Marker: DNA size marker (100 bp DNA ladder).

our samples implies high mortality of the juvenile *R. cuneata*. Interestingly, in the same samples where numerous vacant shells of *R. cuneata* were found, the number of vacant shells of common local species, such as *L. balthica*, *C. glaucum*, *D. polymorpha* and unionids never exceeded a few per sample. Kornijów et al. (2018) experimentally established that non-predatory mass mortality of the common rangia in the Vistula Lagoon occurs in spring, when water temperature begins to exceed approximately 10°C and not during or immediately after the end of winter at lower temperature. It is not clear what is causing high mortality of the common rangia in the Curonian Lagoon, where seasonal temperature variation and the salinity range are similar to the Vistula Lagoon (Chubarenko and Margoński, 2008).

In US populations, gametogenesis of *R. cuneata* is triggered by a spring rise in temperature to at least 10°C and can take place over at least a 7-month period if conditions remain suitable (Risk Assessment, 2017). Another source indicates that gametogenesis initiates at the water temperature above 15°C (Cain, 1975, cit. by Verween et al., 2006) and with salinities above 0 or below 15 (Hopkins, 1970, cit. by Verween et al., 2006). It is important, that the key trigger to *R. cuneata* spawning is an abrupt salinity change from either a higher or lower salinity to a range between 3 and 10 (Risk Assessment, 2017), which is the case in the Curonian Lagoon (Dailidienė and Davulienė, 2008; Gasiūnaitė et al., 2008).

The size structure of the vacant shells of *R. cuneata* in the Curonian Lagoon indicates presence of at least two cohorts: the yearlings (<14 mm) and the adult specimens, which age may be 2–4 years, according to Rudinskaya and Gusev (2012). Thus, it is likely that the population in the Curonian Lagoon has established itself and will continue to increase, while in the exposed marine coastal area, where no shells greater than 9 mm were found, the population status of *R. cuneata* (established/not established) remains unclear.

4.2. Possible vectors of introduction and further dispersal

The distribution pattern of the Atlantic rangia in northern Europe supposes involvement of shipping vectors in its spread, such as ballast water or sediments transported by dredgers. In European waters *R. cuneata* was found in limnic-to-mesohaline conditions with salinity 0.0 to 10.3, and in a wide range of temperatures, from 0 to 25°C (Bock et al., 2015; Janas et al., 2014; Möller and Kotta, 2017; Rudinskaya and Gusev, 2012; Verween et al., 2006; Wiese et al., 2016; and the present study).

Based on the distribution pattern of *R. cuneata* along the Curonian Spit and small size of shells found in 2013 we suspect that planktonic larvae were brought by currents from the region of the Vistula Lagoon and/or Gulf of Gdańsk during 2012. In these southern regions the populations are well established and occur at high densities (Ezhova, 2012; Janas et al., 2014; Rudinskaya and Gusev, 2012; Warzocha and Drgas, 2013; Warzocha et al., 2016).

The arrival of *R. cuneata* in Lithuania due to a possible natural spread differs to its arrival to the Estonian and Swedish coasts (Florin, 2017; Möller and Kotta, 2017). These two localities form the most northern known populations

within the Baltic Sea. Both are found in areas adjacent to ports, and possible means of introduction are beyond what might be expected with the natural drift of rangia larvae but most likely by ballast water or with craft involved in the dredging port channels. We are aware of dredging activities having taken place to the ports of Kaliningrad, Pärnu but also at Klaipėda. Further human-mediated spread with fishing equipment and snagged weed on retrieved anchors is possible, because, as found in this study, small individual can attach to macrophytes. In a separate study, small clams (<1 mm) were observed attached to a hydroid colony (Hoese, 1973, cit. by LaSalle and de la Cruz, 1985).

Möller and Kotta (2017) assumed, that some predicted climate change scenarios might allow this species to flourish in the northern Baltic Sea. From here, it may spread elsewhere by both natural and anthropogenic means. We suggest coastal lagoons and estuarine areas will be more suitable for such colonization due to the greater levels of eutrophication and higher water temperatures than in the open sea. We predict that there will be further expansions within estuarine areas of western and southern Europe and possibly the Black and Caspian Sea regions. Populations may already exist in some areas where to date they have not been revealed.

In this study, beached rangia were not found for some five years after its first known occurrence, which was established from the monitoring samples and based on identification of small specimens requiring a dissecting microscope. The small shells that will have occurred on exposed marine coasts would be unlikely to be detected in shore surveys. In most of other cases (Bock et al., 2015; Janas et al., 2014; Rudinskaya and Gusev, 2012; Verween et al., 2006; Willing, 2015), the first detection of the new mollusk occurred during a routine benthic monitoring or specialized monitoring program aimed at detection of non-indigenous species.

5. Conclusion

The semi-tropical non-indigenous clam *R. cuneata* continues its spread within the boreal environment of the Baltic Sea. Both human-mediated vectors (ballast water or dredged material) and natural spread by coastal currents appear to be involved in the process. Coastal bays and lagoons seem most suitable for colonization, probably due to higher levels of eutrophication and availability of food resources, and higher summer water temperatures than in the open sea. Further spread of *R. cuneata* to similar environments in Europe and perhaps in the Black and Caspian Seas is possible, either from the Baltic or from the North Sea or perhaps the Americas.

Acknowledgements

The authors are grateful to the Environmental Research Department, Environmental Protection Agency, Lithuania (LEPA) for providing environmental monitoring data used in this study. This work was supported by the Doctorate Study programme in Ecology and Environmental Sciences, Klaipėda University, Klaipėda, Lithuania(for S.S. and G.S.) and the project COMPLETE "Completing management options in the Baltic Sea Region to reduce risk of invasive species introduction by shipping", INTERREG Baltic Sea Region (for A.S., G.S., D.M. and S.O.).

Appendix A. Supplementary data

Supplementary data associated with this article can be found, in the online version, at doi:10.1016/j.oceano.2019.01.005.

References

Abbott, R.T., Morris, P.A., 2001. A Field Guide to Shells: Atlantic and Gulf Coasts and the West Indies, fourth ed. Houghton Mifflin, Boston, 350 pp.

AquaNIS, 2018. Editorial Board. Information System on Aquatic Non-indigenous and Cryptogenic Species. World Wide Web Electronic Publication www.corpi.ku.lt/databases/aquanis. Version 2.36+ (accessed 12.01.18).

Ardura, A., Zaiko, A., Martinez, J.L., Samuliovienė, A., Semenova, A., Garcia-Vazquez, E., 2015. eDNA and specific primers for early detection of invasive species — a case study on the bivalve *Rangia cuneata*, currently spreading in Europe. Mar. Environ. Res. 112 (B), 48—55, http://dx.doi.org/10.1016/j.marenvres.2015.09.013.

Bock, G., Lieberum, C., Schütt, R., Wiese, V., 2015. Erstfund der Brackwassermuschel *Rangia cuneata* in Deutschland (Bivalvia: Mactridae). Schr. Malakozool. 28, 13—16, https://www.researchgate.net/publication/295912832.

Carlton, J.T., 1992. Introduced marine and estuarine mollusks of North America: an end-of-the-20th-century perspective. J. Shellfish Res. 11 (2), 489—505.

Chubarenko, B., Margoński, P., 2008. The Vistula Lagoon. In: Schiewer, U. (Ed.), Ecology of Baltic Coastal Waters. Ecological Studies. Springer, Berlin, Heidelberg, 167—195.

Dailidienė, I., Davulienė, L., 2008. Salinity trend and variation in the Baltic Sea near the Lithuanian coast and in the Curonian Lagoon in 1984—2005. J. Mar. Syst. 74, 20—29.

Ezhova, E.E., 2012. New alien species in the Baltic Sea — the clam *Rangia cuneata* (Bivalvia: Mactridae). Mar. Ecol. J. 11 (1), 29—32, (in Russian).

Florin, A.B., 2017. *Rangia cuneata* introduction to Sweden/Baltic Sea. In: AquaNIS Editorial Board (Eds.), Information System on Aquatic Non-indigenous and Cryptogenic Species. World Wide Web Electronic Publication www.corpi.ku.lt/databases/aquanis. Version 2.36+ (accessed 28.12.17).

Gasiūnaitė, Z.R., Daunys, D., Olenin, S., Razinkovas A., 2008. The Curonian Lagoon. In: Schiewer, U. (Ed.), Ecology of Baltic Coastal Waters. Ecological Studies. Springer, Berlin, Heidelberg, 197—215.

Gittenberger, A., Rensing, M., Dekker, R., Niemantsverdriet, P., Schrieken, N., 2015. Native and Non-native Species of the Dutch Wadden Sea in 2014. Report Nr. GiMaRIS 2015_08, 111 pp.

HELCOM, 2014. Manual for the Marine Monitoring in the COMBINE Programme of HELCOM. Soft Bottom Macrozoobenthos. Annex C-8. 277—287.

Hoese, H.D., 1973. Abundance of the low salinity clam, *Rangia cuneata*, in southwestern Louisiana. Proc. Natl. Shellfish. Assoc. 63, 99—106.

Janas, U., Kendzierska, H., Dąbrowska, A.H., Dziubińska, A., 2014. Non-indigenous bivalve — the Atlantic rangia *Rangia cuneata* — in the Wisła Śmiała River (coastal waters of the Gulf of Gdańsk, the southern Baltic Sea). Oceanol. Hydrobiol. Stud. 43 (4), 427—430, http://dx.doi.org/10.2478/s13545-014-0158-3.

Kerckhof, F., Devleeschouwer, M., Hamers, N., 2018. De Amerikaanse brakwaterstrandschelp *Rangia cuneata* (G.B. Sowerby, 1832) aangetroffen in Frankrijk. De Strandvlo 37, 141—145.

Kornijów, R., Pawlikowski, K., Drgas, A., Rolbiecki, L., Rychter, A., 2018. Mortality of post-settlement clams *Rangia cuneata* (Mactridae, Bivalvia) at an early stage of invasion in the Vistula Lagoon (South Baltic) due to biotic and abiotic factors. Hydrobiologia 811, 207—219, http://dx.doi.org/10.1007/s10750-017-3489-4.

LaSalle, M.W., de la Cruz, A.A., 1985. Species profiles: life histories and environmental requirements of coastal fishes and invertebrates (Gulf of Mexico): common rangia. US Fish. Wild. Serv. Biol. Rep. 82 (11.31). US Army Corps of Engineers, TR EL-82-4, 16 pp.

Leal, J.H., 2000. Bivalves. In: Carpenter, K.E. (Ed.), The Living Marine Resources of the Western Central Atlantic. FAO Identification Guide for Fishery Purposes (1) 25—98.

Minchin, D., 2014. The distribution of the Asian clam *Corbicula fluminea* and its potential to spread in Ireland. Manag. Biol. Invasions 5, 165—177.

Möller, T., Kotta, J., 2017. *Rangia cuneata* (G.B. Sowerby I, 1831) continues its invasion in the Baltic Sea: the first record in Pärnu Bay, Estonia. Bioinvasions Rec. 6 (2), 167—172, http://dx.doi.org/10.3391/bir.2017.6.2.13.

Neckheim, C.M., 2013. Verspreding van de Brackwaterstrandschelp *Rangia cuneata* (Sowerby 1831) in Nederland. Spirula 391, 37—38.

Olenin, S., Daunys, D., 2004. Coastal typology based on benthic biotope and community data: the Lithuanian case study. In: Schernewski, G., Wielgat, M. (Eds.), Baltic Sea Typology, Coast-line Reports 4. The Coastal Union, Leiden, 65—83.

Palumbi, S.R., 1996. Nucleic acids II: the polymerase chain reaction. In: Hillis, D.M., Moritz, C., Mable, B.K. (Eds.), Molecular Systematics. Sinauer and Associates Inc., Sunderland, MA, 205—247.

Remeikaitė-Nikienė, N., Lujanienė, G., Malejevas, V., Barisevičiūtė, R., Žilius, M., Garnaga-Budrė, G., Stankevičius, A., 2016. Distribution and sources of organic matter in sediments of the south-eastern Baltic Sea. J. Mar. Syst. 157, 75—81, http://dx.doi.org/10.1016/j.jmarsys.2015.12.011.

Risk Assessment, 2017. Gulf Wedge Clam (*Rangia cuneata*). Rapid Risk Assessment Summary Sheet. World Wide Web electronic publication http://www.nonnativespecies.org/search.cfm (accessed 24.11.18).

Rudinskaya, L.V., Gusev, A.A., 2012. Invasion of the North American wedge clam *Rangia cuneata* (G.B. Sowerby I, 1831) (Bivalvia: Mactridae) in the Vistula Lagoon of the Baltic Sea. Russ. J. Biol. Invasions 3 (3), 220—229, http://dx.doi.org/10.1134/S2075111712030071 (in Russian).

Solovjova, S., 2014. *Rangia cuneata* introduction to Lithuania/Baltic Sea. In: AquaNIS. Editorial Board, 2017. Information System on Aquatic Non-INDIGENOUS and Cryptogenic Species. World Wide Web Electronic Publication www.corpi.ku.lt/databases/aquanis. Version 2.36+ (accessed 12.01.18).

Verween, A., Kerckhof, F., Vincx, M., Degraer, S., 2006. First European record of the invasive brackish water clam *Rangia cuneata* (G.B. Sowerby I, 1831) (Mollusca: Bivalvia). Aquat. Invasions 1 (4), 198—203.

Warzocha, J., Drgas, A., 2013. The alien gulf wedge clam (*Rangia cuneata* G.B. Sowerby I, 1831) (Mollusca: Bivalvia: Mactridae) in the Polish part of the Vistula Lagoon (SE. Baltic). Folia Malacol. 21, 291—292, http://dx.doi.org/10.12657/folmal.021.030.

Warzocha, J., Szymanek, L., Witalis, B., Wodzinowski, T., 2016. The first report on the establishment and spread of the alien clam *Rangia cuneata* (Mactridae) in the Polish part of the Vistula Lagoon (southern Baltic). Oceanologia 58 (1), 54—58, http://dx.doi.org/10.1016/j.oceano.2015.10.001.

Wiese, L., Niehus, O., Faass, B., Wiese, V., 2016. Ein weiteres Vorkommen von *Rangia cuneata* in Deutschland (Bivalvia: Mactridae). Schr. Malakozool. 29, 53—60, Cismar.

Willing, M.J., 2015. Two invasive bivalves, *Rangia cuneata* (B. Sowerby I, 1831) and *Mytilopsis leucophaeata* (Conrad, 1831), living in freshwater in Lincolnshire, Eastern England. J. Conchol. 42 (2), 189—192.

Oceanologia (2019) 61, 350—367

Available online at www.sciencedirect.com

ScienceDirect

journal homepage: www.journals.elsevier.com/oceanologia/

ORIGINAL RESEARCH ARTICLE

Laboratory study of suspended sediment dynamics over a mildly sloping sandy seabed

Barbara Stachurska *, **Ryszard Staroszczyk**

Institute of Hydro-Engineering, Polish Academy of Sciences, Gdańsk, Poland

Received 9 July 2018; accepted 29 January 2019
Available online 21 February 2019

KEYWORDS
Sediment dynamics;
Sloping seabed;
Bed ripples;
Wave bottom boundary layer;
Particle image velocimetry

Summary This paper presents the results of laboratory measurements of suspended sediment movement induced by regular non-linear water waves propagating over a mildly sloping sandy seabed covered with ripples. The measurements conducted in a water flume were carried out by applying the technique of particle image velocimetry (PIV). The aim of those experiments was to investigate near-bed velocities of sediment particles under controlled surface wave conditions. In particular, horizontal and vertical profiles of sand grain velocities were measured, and some comparisons between the measured and theoretically-predicted quantities were carried out. A number of selected wave cases were examined, for which the Ursell number ranged from 18 to 39, and the sediment grain mobility numbers varied between 12 and 26. For these flow conditions, the near-bed layer of intense sediment grain movements had a thickness of about 2—3 ripple heights. The maximum horizontal sediment velocities measured over ripple crests were about twice as large as those over ripple troughs. Vertical sediment velocities above ripple crests and troughs were similar, amounting to about 1/4 to 1/3 of horizontal velocities over ripple crests. The detailed quantitative results obtained in the flume can help validate other experimental techniques and can be useful in testing numerical models for simulating surface wave-induced sediment dynamics.

1. Introduction

When deep water waves approach a seashore, they enter a shoaling region (see Fig. 1), in which they undergo a significant transformation that gives rise to a complex oscillatory motion of water particles and generates water currents near the seabed. As surface waves enter a region of gradually decreasing water depth, their height and steepness grow,

* Corresponding authors at: Institute of Hydro-Engineering, Polish Academy of Sciences, Gdańsk, Poland.
E-mail address: b.stachurska@ibwpan.gda.pl (B. Stachurska).
Peer review under the responsibility of Institute of Oceanology of the Polish Academy of Sciences.

ELSEVIER Production and hosting by Elsevier

https://doi.org/10.1016/j.oceano.2019.01.006

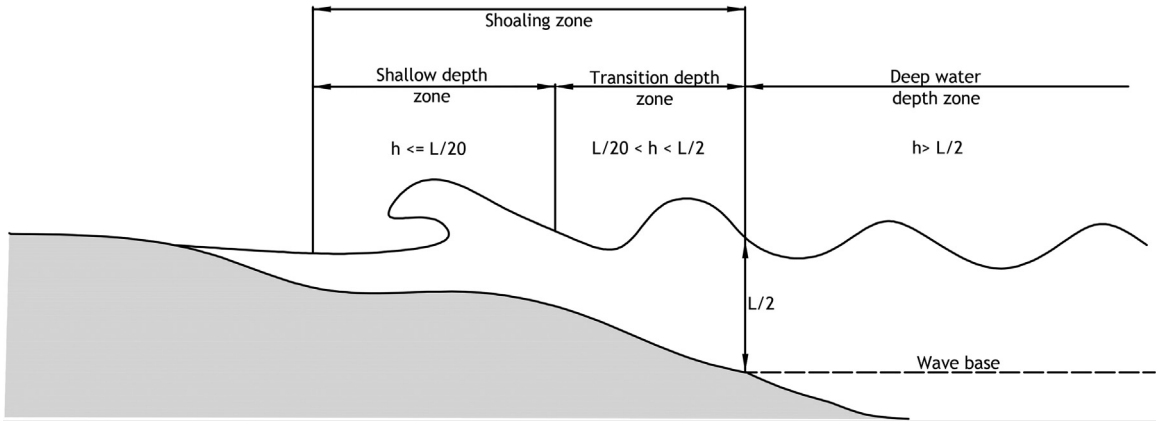

Figure 1 Schematic diagram of a coastal zone profile (*h* denotes water height, and *L* denotes deep-water wavelength).

resulting in increasing orbital velocities of water particles across the water column. The increasing water velocities near a sandy seabed increase shear stresses exerted by oscillating water on sediment grains, which intensifies all dynamic processes occurring in a near-bed layer of turbulent flow, such as the formation, evolution and migration of bed ripples, the entraining of sand grains into suspension, and onshore/offshore transport of sediment along the bed. Such complex phenomena have been investigated, both empirically and theoretically, for decades (Alsina et al., 2012; Bagnold, 1946; Doering and Baryla, 2002; Grant and Madsen, 1982; Inman and Bowen, 1962; Sato et al., 1984), but it seems that, despite the vast literature, the fundamental mechanisms underlying the motion of sediment particles over the seabed are not yet fully understood. The development of modern experimental techniques offers new opportunities for observation and measurement of fundamental mechanisms occurring on small spatial scales near the seabed. One such modern technique is particle image velocimetry (PIV).

The PIV technique is based on a digital analysis of images of tracer particles seeded in water and observed within a thin sheet of fluid lit by laser light (Willert and Gharib, 1991). Originally, this technique was intended for use in one-phase fluid flows, and has been successfully used in many problems of hydrodynamics and related disciplines. Its application to two-phase fluid flows, and such is the flow of sediment particles suspended in water, can still be regarded as a novel approach. One of the first attempts to use the PIV method in experiments involving the motion of sandy sediments induced by water waves was due to Ahmed and Sato (2001). Van der Werf et al. (2007) applied this experimental method for the detailed investigation of water vortex generation above seabed ripples and their effect on the ejection of sand grains into the water column. Yang et al. (2011) developed an approach that makes it possible to simultaneously determine the velocity fields of water and sediment particles by using fluorescent seed particles. Further, Umeyama (2012) applied the PIV technique to measure particle trajectories due to surface waves propagating in water of finite depth. More recently, Stachurska and Staroszczyk (2016) used the PIV method to investigate the motion of sediment particles in the vicinity of a rippled bed for surface wave-generated flows in water of constant depth.

This paper is a continuation and extension of research reported in the latter paper (Stachurska and Staroszczyk, 2016). Thus, wave-generated flows in water of slightly varying depth are now investigated, that is, the region denoted in Fig. 1 as the 'transition zone' is considered. For this purpose, sediment motion generated by non-linear (Stokes) waves propagating over a bed inclined at a constant angle of 2% with a system of well-developed ripples was analyzed experimentally in a water flume. The objective of the laboratory PIV measurements was to investigate in detail the dynamics of sediment particles under controlled surface wave conditions. The main point of interest was to determine the velocities of sand particles near a rippled bed. In particular, the vertical profiles of horizontal and vertical sediment velocities over ripple crests and ripple troughs were measured, and the variation of sediment velocities in the horizontal direction along the bed ripples was investigated. Moreover, a number of parameters characterizing sediment dynamics were determined, including the grain mobility number, the Shields parameter and the thickness of the turbulent near-bed layer, commonly referred to as the wave bottom boundary layer (WBBL). Some of the results from the flume measurements were compared with theoretical estimations based on analytical formulae available in the literature.

The experimental results obtained in the laboratory and described in this study give insights into the complex mechanisms taking place in the immediate vicinity of sandy ripples in water-induced flows. The quantitative results can be used to validate other experimental techniques (especially those to be applied on larger scales in the field), and they can also be useful in testing numerical models developed to simulate sediment behaviour in surface wave-induced flows.

The paper is organized as follows. Section 2 provides some basic theoretical background and introduces some parameters used throughout the paper. Section 3 describes the experimental setup and the methodology of measurements and data post-processing. Section 4 presents detailed results obtained during the laboratory work, including the vertical and horizontal profiles of sediment particle velocities. Section 5 is devoted to the comparisons of the measured data with theoretical estimations, and Section 6 presents the most important conclusions from the laboratory experiments.

2. Theoretical framework

Before the presentation and discussion of experimental results obtained in the flume, some basic theoretical framework is given below.

2.1. Description of surface waves

The laboratory experiments were carried out for surface waves with parameters (the wave length and height) corresponding to those of finite-amplitude non-linear waves propagating in shallow water. Hence, it was assumed that waves generated in the flume during the experiments can be approximated by the second-order Stokes theory (Fenton, 1990). Accordingly, in a rectangular coordinate system Oxz with the horizontal x-axis assumed along the wave propagation direction and the vertical z-axis pointing upwards and its origin assumed at the still water surface, the water particle horizontal and vertical velocity components u and v respectively, for waves travelling over a horizontal bottom, are given by:

$$u = \frac{HgT}{2L}\frac{\cosh\left(\frac{2\pi(z+h)}{L}\right)}{\cosh\left(\frac{2\pi h}{L}\right)}\cos\left(\frac{2\pi x}{L}-\frac{2\pi t}{T}\right) + \frac{3}{4}\left(\frac{\pi H}{L}\right)^2 c\frac{\cosh\left(\frac{4\pi(z+h)}{L}\right)}{\sinh^4\left(\frac{2\pi h}{L}\right)}\cos\left(\frac{4\pi x}{L}-\frac{4\pi t}{T}\right), \quad (1)$$

$$v = \frac{HgT}{2L}\frac{\sinh\left(\frac{2\pi(z+h)}{L}\right)}{\sinh\left(\frac{2\pi h}{L}\right)}\sin\left(\frac{2\pi x}{L}-\frac{2\pi t}{T}\right) + \frac{3}{4}\left(\frac{\pi H}{L}\right)^2 c\frac{\sinh\left(\frac{4\pi(z+h)}{L}\right)}{\sinh^4\left(\frac{2\pi h}{L}\right)}\sin\left(\frac{4\pi x}{L}-\frac{4\pi t}{T}\right). \quad (2)$$

In the above equations, L denotes the surface wave length, H is the wave height, t is time, T is the wave period, h is the still water depth, c is the wave phase velocity (celerity) and g stands for the gravitational acceleration. The derived quantities, ω and k, representing the angular frequency and the wave number, are also used in the theoretical description. These are defined by the formulae:

$$\omega = \frac{2\pi}{T}, \quad k = \frac{2\pi}{L}, \quad c = \frac{\omega}{k}. \quad (3)$$

The quantities ω, k and h are related through the dispersion relation:

$$\omega^2 = gk\tanh kh. \quad (4)$$

In order to determine whether, for given wave parameters, we deal with Stokes or cnoidal wave regimes, an Ursell number (Ursell, 1953) defined by the formula

$$U_r = \frac{H}{h_s}\left(\frac{L_s}{h_s}\right)^2 \quad (5)$$

was calculated, where L_s and h_s denote, respectively, the wave length and water depth at a given location over the sloping bed. It was found that for the waves generated in the flume during our experiments, the Ursell number ranged between the values of around 18 and 39, see Table 1 in Section 3. According to Fenton (1990) and Hedges (1995), the latter range corresponds indeed to the Stokes wave regime (the cnoidal wave theory is applicable for $U_r \geq 40$).

To characterize the water flow regime near the bed, the Reynolds number defined by the relation

$$Re = \frac{u_0^2}{\omega\nu} \quad (6)$$

was calculated, where u_0 is the amplitude of the horizontal velocity of water near the bed, and ν is the kinematic viscosity of water (equal to 10^{-6} m^2 s^{-1}). The values of the Reynolds number calculated for our laboratory conditions are listed further in Table 1 in the next section. They range, approximately, between 0.9×10^4 and 2.1×10^4, which indicates that the flow near the flume bed was turbulent, and the laboratory conditions were close to those encountered in the field, for which the Reynolds numbers commonly have the values of order 10^5 (Nielsen, 1992).

2.2. Relations describing sediment dynamics

One of the key parameters in mechanics of sediment transport is the so-called Shields parameter θ which describes the ratio of the water flow-generated shear force acting on a sediment particle resting on the bed to its own weight in water. The value of this parameter allows us to estimate, in an approximate manner, the sediment movement regime in the vicinity of a rough bed. In the literature, the Shields parameter is commonly defined on the assumption that the bed grain roughness equals $2.5d_{50}$ (where d_{50} denotes the median grain diameter). In this case, the Shields parameter, denoted then as $\theta_{2.5}$, is given by the following relation (Nielsen, 1992):

$$\theta_{2.5} = \frac{\frac{1}{2}f_{2.5}(A\omega)^2}{(s-1)gd_{50}}. \quad (7)$$

Table 1 Parameters of surface waves investigated in the experiments. *Notations*: h and h_s are deep and shallow water depths, respectively, H is the wave height, T is the wave period, L and L_s are wave lengths in deep and shallow water, respectively, U_r are Ursell numbers, Re are Reynolds numbers, and ψ are mobility numbers.

Case	h [m]	h_s [m]	H [m]	T [s]	L [m]	L_s [m]	U_r	Re	ψ
A	0.35	0.185	0.08	1.0	1.4	1.2	17.6	8.6×10^3	12.7
B			0.10	1.0			22.0	1.5×10^4	21.6
C			0.11	1.0			24.2	1.8×10^4	26.2
G			0.06	1.4	2.3	1.8	29.5	1.1×10^4	11.6
H			0.08	1.4			39.4	2.1×10^4	24.6

The parameter $f_{2.5}$ entering the above equation denotes the grain roughness friction factor and is determined by the following formula (Nielsen, 1992):

$$f_{2.5} = \exp\left[5.213\left(\frac{2.5d_{50}}{A}\right)^{0.194} - 5.977\right]. \tag{8}$$

In Eqs. (7) and (8), A is the orbital displacement amplitude of the fluid immediately above the bed boundary layer and s is the ratio of the densities of the sediment grain and water ($s = 2.65$ for quartz sand).

Based on the observations, it is usually assumed that grains at the bed start to move at $\theta_{2.5} \sim 0.05$, sand ripples develop and remain stable at $\theta_{2.5} \sim 0.2 \div 0.3$, and at $\theta_{2.5} \sim 0.8 \div 1.0$ all bedforms are destroyed and a mass sediment movement occurs (Nielsen, 1992; Ostrowski, 2004). As will be shown in Section 5, the values of the Shields parameter $\theta_{2.5}$ for flow conditions investigated in the flume experiments varied from about 0.1 to about 0.3, that is, within the range at which sandy ripples develop at the bed and remain stable.

An alternative dimensionless parameter that is often used for measuring forces exerted by water waves on sediment particles is the mobility number, ψ, defined by

$$\psi = \frac{(A\omega)^2}{(s-1)gd_{50}}. \tag{9}$$

By comparing Eqs. (7) and (9) it can be noted that the two dimensionless quantities, $\theta_{2.5}$ and ψ, are related by the simple formula

$$\theta_{2.5} = \frac{1}{2} f_{2.5}\psi. \tag{10}$$

The roughness of the sandy bed, even if there are no ripples thereon, considerably affects the oscillatory flow of water in the water column close to the bed. This is caused by the development of a turbulent boundary layer, which, if due to the propagation of surface waves, is often referred to as the wave bottom boundary layer (WBBL). There are a number of approximate analytic formulae proposed in the literature (e.g. Fredsoe, 1984; Fredsoe and Deigaard, 1992; Grant and Madsen, 1979) for the estimation of the WBBL thickness in terms of parameters defining a surface wave and the properties of the rough bed. In this work, for a bed which is covered by a system of ripples (i.e. is not flat), we apply an approach due to Nielsen (1992), by which the WBBL thickness, δ, is given by:

$$\delta = \frac{1}{2}\frac{u}{\omega} f_w, \tag{11}$$

where u is the horizontal velocity of water at the top of the boundary layer (the so-called free-stream velocity), and f_w denotes a quantity known as the wave friction factor. To calculate the latter quantity, the value of the Shields parameter defined above by Eqs. (7) and (8) is used. Accordingly, at first the hydraulic roughness of the rippled bed, r, is estimated by applying the formula (Nielsen, 1992):

$$r = \frac{8\eta_r^2}{\lambda_r} + 170d_{50}\sqrt{\theta_{2.5} - 0.05}, \tag{12}$$

in which η_r and λ_r denote the characteristic ripple height and length, respectively. Assuming that the bed is hydraulically rough (implying turbulent flow in the boundary layer), the wave friction parameter f_w is defined in terms of the roughness parameter r by the equation:

$$f_w = \exp\left[5.5\left(\frac{r\omega}{u}\right)^{0.2} - 6.3\right]. \tag{13}$$

Given the value of f_w calculated from relation (13), the boundary layer thickness δ can be estimated from Eq. (11). The values of δ predicted by the theory for the surface waves investigated in this work will be compared with those observed in the flume experiments in Section 5.2.

In order to evaluate from Eq. (12) the bed roughness r, the bed ripple length and height are needed. For regular waves, the ripple length is calculated from the following formula (Nielsen, 1981):

$$\frac{\lambda_r}{A} = 2.2 - 0.345\psi^{0.34}, \tag{14}$$

which is valid for the mobility number range $2 < \psi < 230$. The characteristic ripple height, in turn, is given by the relation

$$\frac{\eta_r}{A} = \max\{0.275 - 0.022\psi^{0.5}, 0\}. \tag{15}$$

Alternatively, the ripple height can be determined in terms of the Shields parameter $\theta_{2.5}$ by applying the formula

$$\frac{\eta_r}{\lambda_r} = 0.182 - 0.24\theta_{2.5}^{1.5}. \tag{16}$$

Since the laboratory experiments presented in this work focus on the measurement of suspended sediment particle velocities, it is of interest to evaluate the settling velocity of a single particle descending in fluid in rest (this velocity is determined from the condition that the fluid drag force acting on the particle balances the gravity force). From among a number of formulae which are available in the literature, we chose an empirical one proposed by Onoszko (1965):

$$v_s = 9.45(s-1)^{0.8} d_{50}, \tag{17}$$

in which v_s is in units [m s^{-1}] and d_{50} in [m]. The above-defined settling velocity can be treated as a characteristic scale for the vertical sediment particle velocities measured in the flume experiments.

3. Experimental setup and data processing

The experiments were carried out in a wave flume belonging to the Institute of Hydro-Engineering of the Polish Academy of Sciences in Gdańsk, Poland. The facility is 64 m long, 0.6 m wide and 1.4 m deep. Water waves are generated in the flume by a programmable piston-type wave maker. The experiments described in this work were carried out for the still water depth $h = 0.35$ m. For the purpose of the experiments, an inclined bottom section with a slope of 2% and a length of 20.0 m was inserted into the flume (see Fig. 2). The inclined bottom started at a distance of 21.25 m from the wave generator. Natural sand, taken from a beach at a village of Sobieszewo (part of the Gdańsk agglomeration), was used in the experiments. The median diameter of sand grains, determined by sieve analysis, was $d_{50} = 0.257$ mm. The sand was placed in a tray (cuvette), which was mounted on the sloping bottom at a depth of about

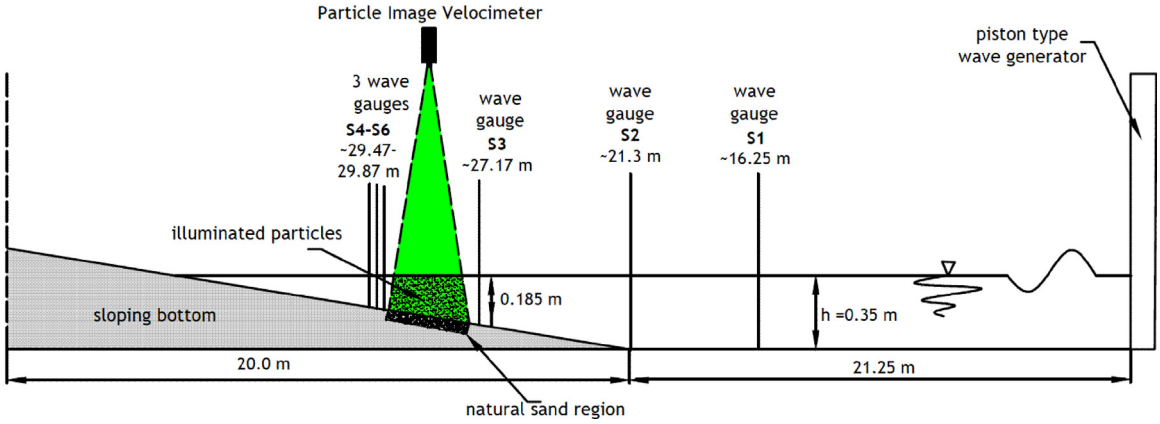

Figure 2 Experimental setup.

0.185 m, that is, at approximately 1/2 of the still water level measured relative to the flat horizontal section of the flume bottom. This particular location of the sand tray was chosen to ensure full transformation (steepening and shortening) of waves coming from the constant-depth section of the flume, with wave parameters selected in such a way that near-breaking wave conditions occurred for the highest waves considered in the experiments.

A PIV laser beamer was mounted over the middle part of the sand tray, and a high-definition video camera was placed in front of the glazed vertical sidewall of the flume to record laser light-illuminated sediment particles (see Fig. 3). The PIV system used in the experiments was supplied by LaVision. The sampling frequency (at which pairs of PIV images were recorded) was 15 Hz, with an inter-frame separation time in each pair of frames ranging from 400 to 2000 μs. Successive images of sediment particle distributions were recorded by a high-speed CCD camera Imager Pro HS 500 with a sensor spatial resolution of 1280 px × 1024 px at 520 fps (frames per second). The size of the measurement window was approximately 20 cm × 17 cm. The PIV images were post-processed by the PIVlab1.4 software for MATLAB (Thielicke and Stamhuis, 2014), which uses cross-correlation to calculate vector fields between two successive frames. Spurious spikes (outliers) in velocity distributions were detected by the so-called local median filter method (based on a window of 3 × 3 grid points). Typically, the PIV technique requires seeding (small tracer particles suspended in a fluid), but it turned out in the course of the experiments that the fine sand particles reflected the laser light sufficiently well, so artificial seeding was not necessary.

Prior to the PIV measurements, water waves were generated in the flume for approximately 30 min, so that sand ripples developed on the bed and reached a state of equilibrium for given surface wave conditions, with ripple crests aligned in parallel to form a very regular pattern. The

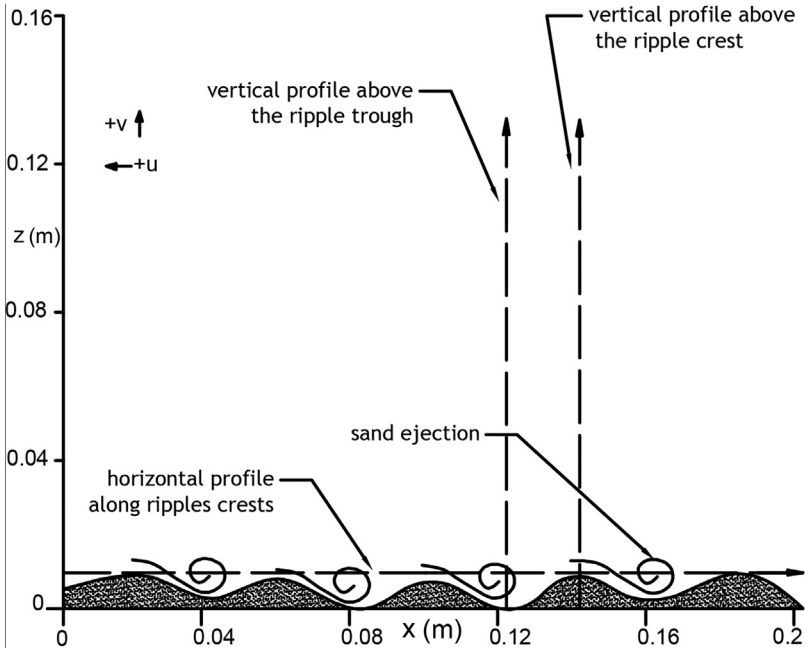

Figure 3 Vertical and horizontal profiles.

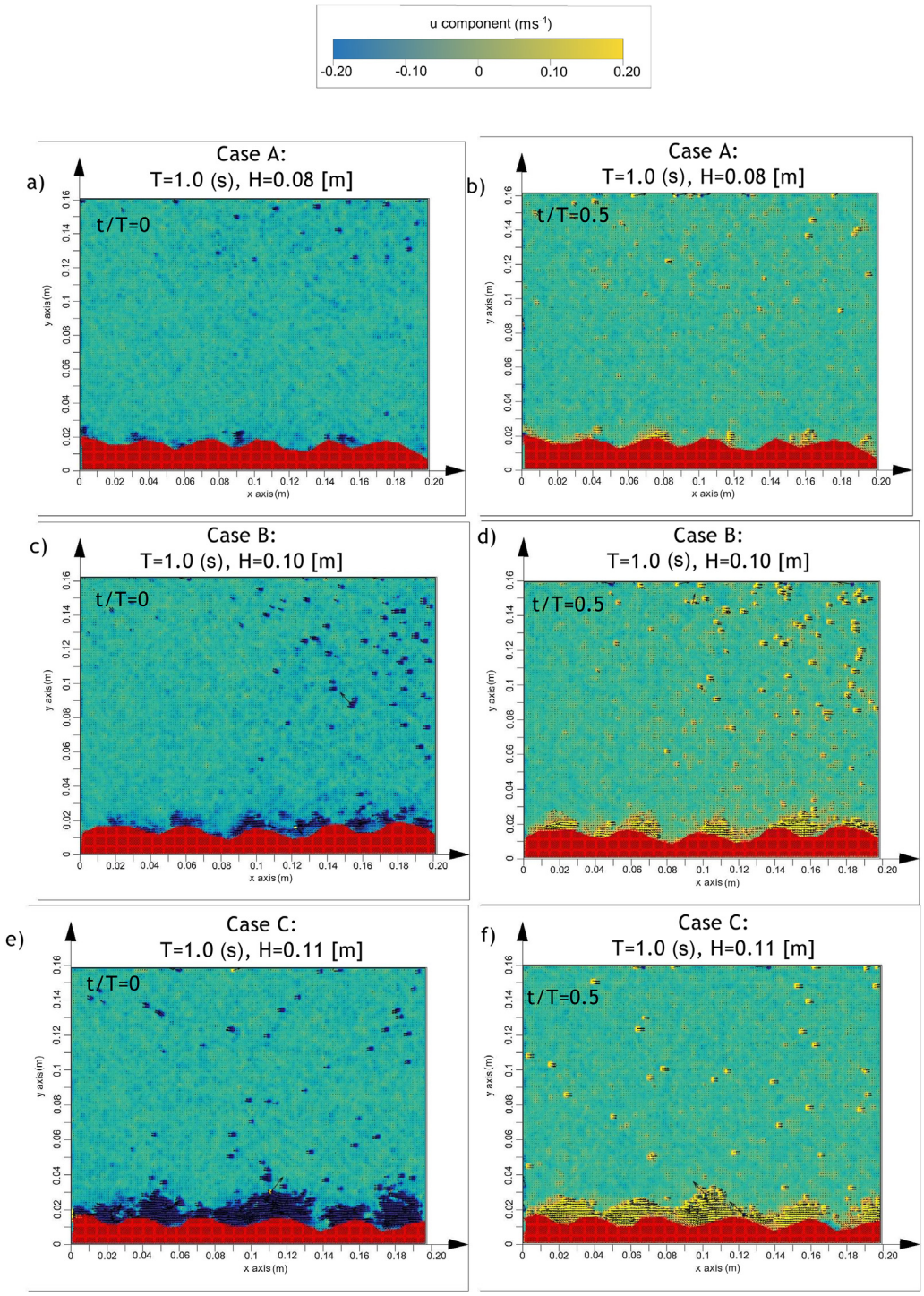

Figure 4 Instantaneous horizontal sediment velocity fields over a rippled bed for three cases of the wave height H and the wave period T = 1.0 s.

geometry of the ripples (their length and height) was measured along the lateral glass walls manually with a ruler, so the measurements were accurate to within 1 mm.

In order to record changes in the water free surface elevation, a system of six wave gauges (denoted as S1 to S6 in Fig. 2) was used. The gauges were placed near the middle of the horizontal bottom, at the beginning of the slope and directly behind the sand tray, as indicated in Fig. 2. The analysis of data recorded by these gauges showed that the distortion and damping of surface waves caused by the presence of the lateral walls of the channel were negligibly small, so the flow could be regarded as two-dimensional.

Before the proper experiments started, a series of preliminary test runs with various combinations of surface wave parameters was conducted to identify those cases in which

systems of well-developed and stable (i.e. not migrating) bed ripples were formed, no-breaking of waves took place, and no excessive vibrations of the inclined bed (which cause errors in measurements) occurred. Five of the cases tried in the preliminary tests were selected for detailed examination. These cases included waves of two different periods T, one corresponding to a medium-length wave and the other to a long wave. The maximum heights H of these two waves chosen for experiments were the largest for which the waves did not break (those higher by 1 cm broke over the sloping section of the bed). The three remaining wave cases, with smaller wave heights, were used for comparisons. The five cases selected for presentation, thereafter labelled A, B, C, G and H, are defined in Table 1 in terms of wave period T, wavelength L and wave height H. In the table, also the values of the Ursell number U_r defined by Eq. (5), the wave Reynolds number Re defined by (6), and the mobility number ψ given by relation (9) are listed for reference in the table.

4. Experimental results

In this section, the results of the laboratory tests in the flume are presented, with the five cases of surface waves investigated experimentally defined in Table 1. In the experiments, the focus was on measuring the velocities of sand particles suspended in water near the rippled bed. The results obtained in the flume are illustrated by means of velocity profiles, showing the variation of both components of the sediment grain velocity vector along an either vertical or horizontal direction. The profiles used for illustration are defined in Fig. 3. One of the two vertical profiles is located over a ripple crest, and the other is loced over a ripple trough, with the zero z-coordinates in both profiles assumed at the ripple trough level. The horizontal profile is located along a line parallel to the bed and passing through the top of the highest ripple in the PIV image window (which covered about five ripple lengths). The zero coordinate of this profile

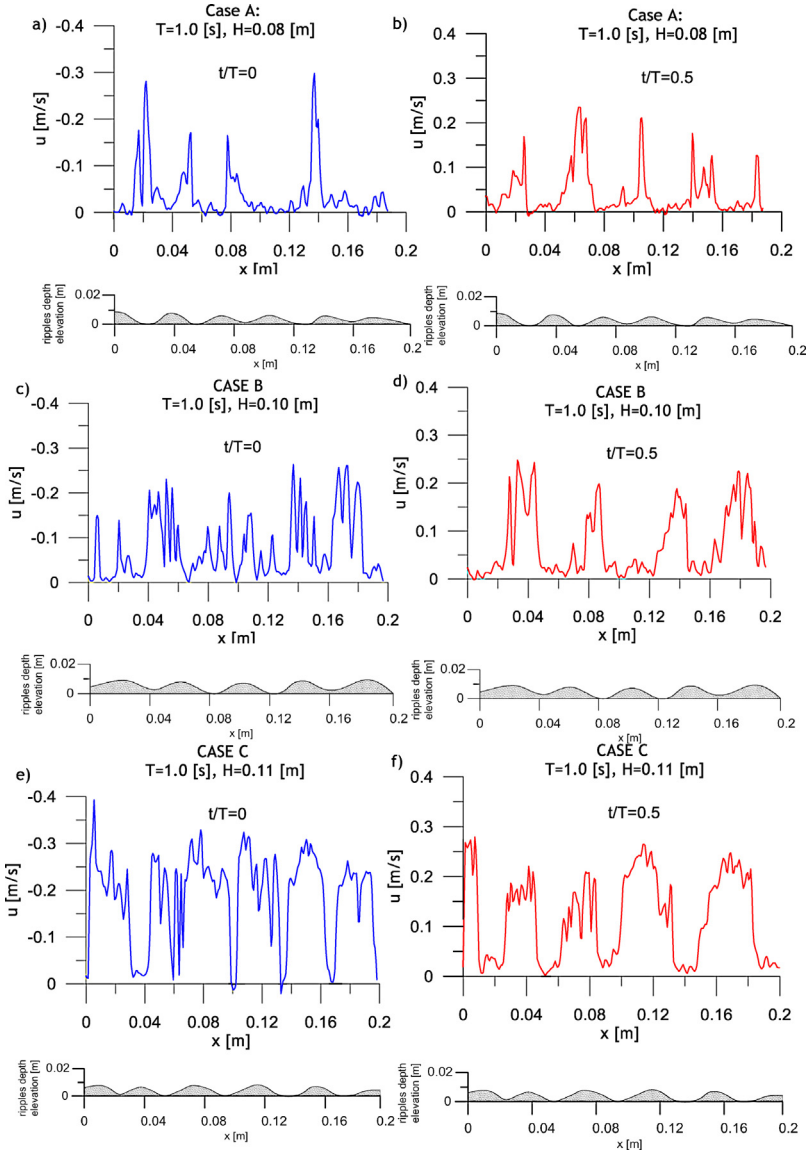

Figure 5 Instantaneous horizontal velocities of sediment grains along the horizontal profile over the bed ripples for three values of the wave height H and the wave period $T = 1.0$ s, at wave phases $t/T = 0$ (wave trough) and $t/T = 0.5$ (wave crest).

was assumed at the left side of the window, as shown in the figure.

The results of PIV measurements are presented separately for the waves of a period T = 1.0 s (cases A, B and C defined in Table 1) and the longer waves of a period T = 1.4 s (cases G and H).

4.1. Sediment velocities due to surface waves of the period T = 1.0 s

The PIV images of the instantaneous horizontal velocities of sediment particles for the three cases A, B and C are shown in Fig. 4. The images on the left correspond to the instant of a wave trough passage (t/T = 0) over the middle of the measurement window, while the images on the right illustrate the velocities at the passage of a surface wave crest (t/T = 0.5) over the same point.

The following figures illustrate sediment velocity profiles measured by the PIV technique. Fig. 5 shows plots of horizontal sediment velocities along the horizontal profile for three different values of the wave height H. Under each plot, there is the corresponding profile of bed ripples that developed under given wave conditions. The characteristics of the ripples are provided in Section 5.2. It is seen that despite the scatter in the data, the measured velocities reflect well the phenomenon of increased sediment velocities above ripple crests compared to those above ripple troughs. The case of H = 0.08 m, illustrated in Fig. 5a and b, shows that instantaneous sand particle velocities varied between -0.29 m s^{-1} during surface trough transition to 0.25 m s^{-1} during the wave crest transition. The corresponding velocities for the case H = 0.10 m were about $\pm$0.26 m s^{-1} (see Fig. 5c and d), whereas for the highest wave H = 0.11 m the measured velocities ranged from about -0.40 to 0.28 m s^{-1} (Fig. 5e and f), depending on the surface wave phase.

Fig. 6 presents the vertical distributions of instantaneous horizontal sediment velocities measured along a profile located on a ripple crest (see Fig. 3) for the three wave heights considered. It can be seen that similar, quasi-symmetric sediment velocity patterns occur in all three cases, with velocity magnitudes $|u_s|$ in the near-bed turbulent layer of much larger than those in the water column above. The magnitudes of near-bed sediment velocities, at both wave trough (t/T = 0 blue lines) and wave crest ($t/T = 0.5$, red lines) passages, increase with the wave height, as expected, though this increase, with the wave height H, can be considered as moderate. For instance, for the wave height $H = 0.08$ m (Fig. 6a), the measured sediment velocities vary between $u_s = -0.21$ m s^{-1} and u_s = +0.22 m s^{-1}, for $H = 0.10$ m (Fig. 6b) they vary between the values of about $\pm$0.25 m s^{-1}, and finally, for $H = 0.11$ m (Fig. 6c), they vary between $u_s = -0.32$ m s^{-1} and u_s = +0.27 m s^{-1}. One can expect some asymmetry in near-bottom sediment velocities (differences between the velocity magnitudes at wave trough and crest passages) that increase with the wave height, and this effect is indeed observed in Fig. 6c for the highest wave $H = 0.11$ m. The asymmetry results from the fact that, for steep non-linear waves propagating in shallow water, the wave trough passage lasts longer than the crest passage phase, so there is more time for sediment particles to catch up with water during its oscillatory flow. This explains why the most intense movement of sediment occurs during the passage of wave troughs. It is also seen in the plots that the thickness of the near-bed layer of intense sediment movement is significantly affected by the wave height H, increasing by a factor of about three between the smallest and highest waves illustrated in the figure.

Corresponding to Fig. 5 are the plots in Fig. 7, showing variations in vertical sediment velocities along the horizontal profile over the bed ripple crests. The case of $H = 0.08$ m, illustrated in Fig. 7a and b, shows that sand particle velocities varied from 0.04 m s^{-1} to -0.03 m s^{-1} during a surface trough passage and from 0.08 m s^{-1} to -0.03 m s^{-1} during a wave crest passage. The analogous velocities for the case $H = 0.10$ m changed from about 0.05 m s^{-1} to -0.04 m s^{-1} during a wave trough passage (see Fig. 7c), and from 0.07 m s^{-1} to -0.03 m s^{-1} during a crest passage (Fig. 7d).

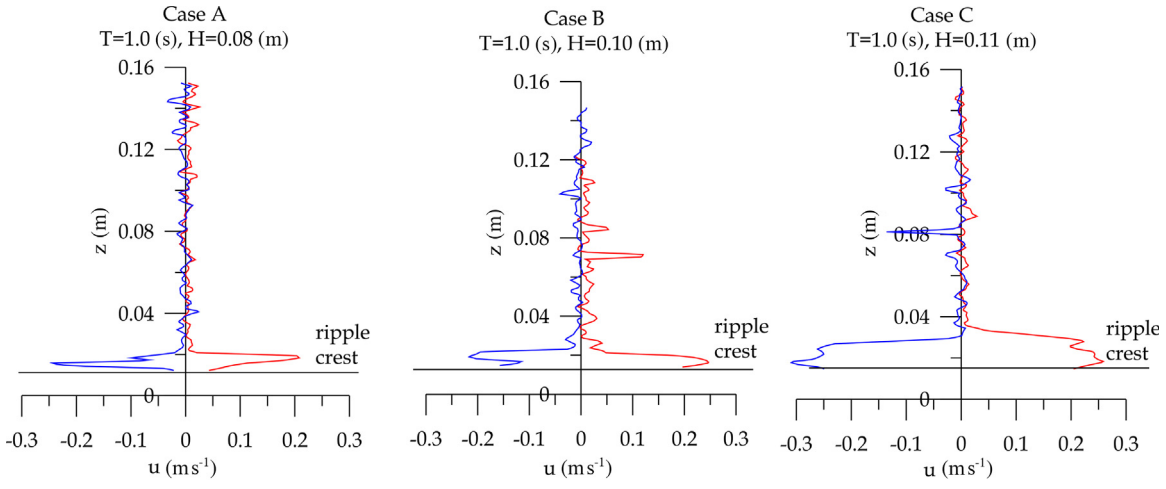

Figure 6 Instantaneous horizontal velocities of sediment grains along the vertical profile over a ripple crest for three values of the wave height H and the wave period $T = 1.0$ s, at wave phases $t/T = 0$ (wave trough passage, blue lines) and $t/T = 0.5$ (wave crest passage, red lines). (For interpretation of the references to color in this figure legend, the reader is referred to the web version of this article.)

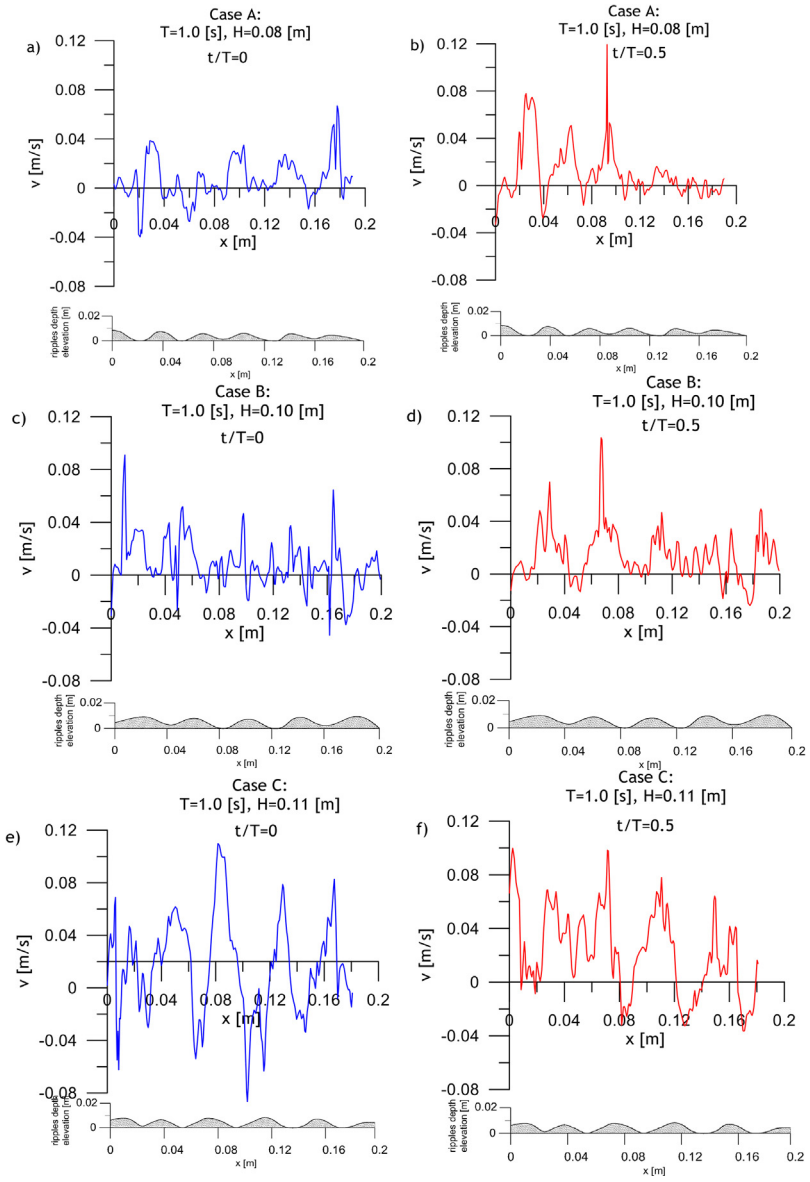

Figure 7 Instantaneous vertical velocities of sediment grains along the horizontal profile over the bed ripples for three values of the wave height H and the wave period $T = 1.0$ s, at wave phases $t/T = 0$ (wave trough) and $t/T = 0.5$ (wave crest).

For the highest wave $H = 0.11$ m, the measured horizontal velocities ranged from about 0.10 m s^{-1} to -0.08 m s^{-1} during a wave trough passage (Fig. 7e), and from 0.09 m s^{-1} to -0.04 m s^{-1} during a crest passage (Fig. 7f).

The plots in Fig. 8 illustrate the distributions of instantaneous vertical sediment velocities measured along a vertical profile located over a ripple crest (see Fig. 3) for the three wave heights considered. By comparing the plots in Figs. 6 and 8, it can be noted that the magnitudes of vertical velocities of sediment grains in the wave bottom boundary layer are about 1/3 of their horizontal counterparts. It can be observed again (see Fig. 6) that the wave height considerably affects the thickness of the near-bed turbulent layer of intense sediment movement, increasing it by a factor of about three between the smallest and the highest waves. Some asymmetry in the near-bed velocities can also be noticed, especially apparent for the highest wave illustrated in Fig. 8c.

The plots in Figs. 6 and 8 illustrate sediment velocity distributions along a vertical profile located over the top of a ripple crest. The six plots in Fig. 9 display corresponding velocity distributions for a profile located over a bed ripple trough (see Fig. 3). The upper row of plots shows horizontal components for the three wave height cases, and the lower row shows the vertical components of the velocity vector. Comparing Figs. 6 and 9, one can note that the measured magnitudes of the horizontal velocities of sediment grains immediately over ripple troughs are smaller than those over ripple crests and the relative velocity reduction decreases with the turbulent boundary layer thickness. Hence, for the

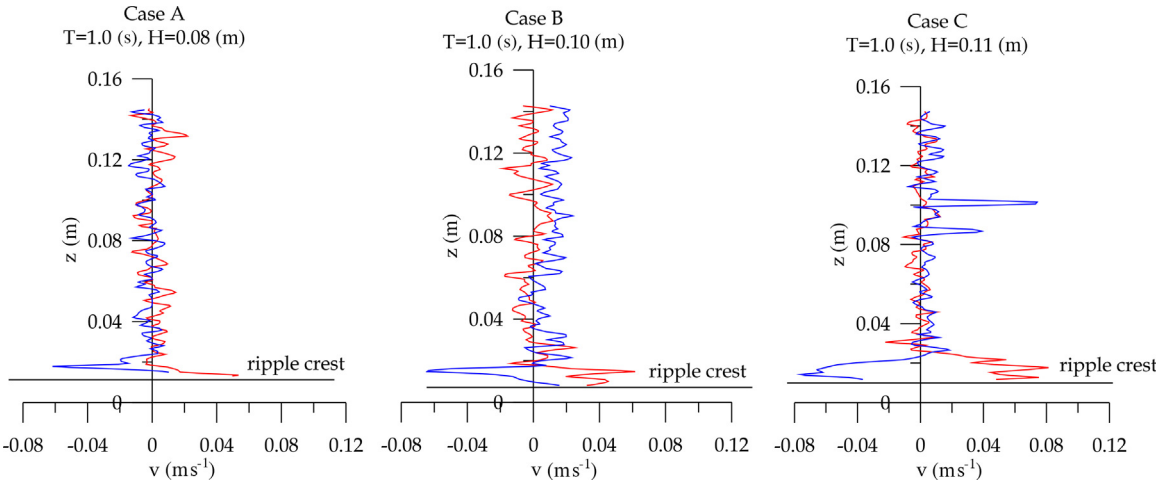

Figure 8 Instantaneous vertical velocities of sediment grains along a vertical profile over a ripple crest for three values of the wave height H and the wave period $T = 1.0$ s, at wave phases $t/T = 0$ (wave trough transition, blue lines) and $t/T = 0.5$ (wave crest transition, red lines). (For interpretation of the references to color in this figure legend, the reader is referred to the web version of this article.)

thinner layer (case A), the velocities over the ripple trough are approximately half of those over the crest, whereas for the thicker layer (case C) the near-bed horizontal velocities are reduced by about 30%. A different pattern is observed for the vertical velocities (see Fig. 8), since the magnitudes of near-bed sediment velocities over ripple crests and troughs are similar, irrespective of the wave height (and hence of the bottom boundary layer thickness).

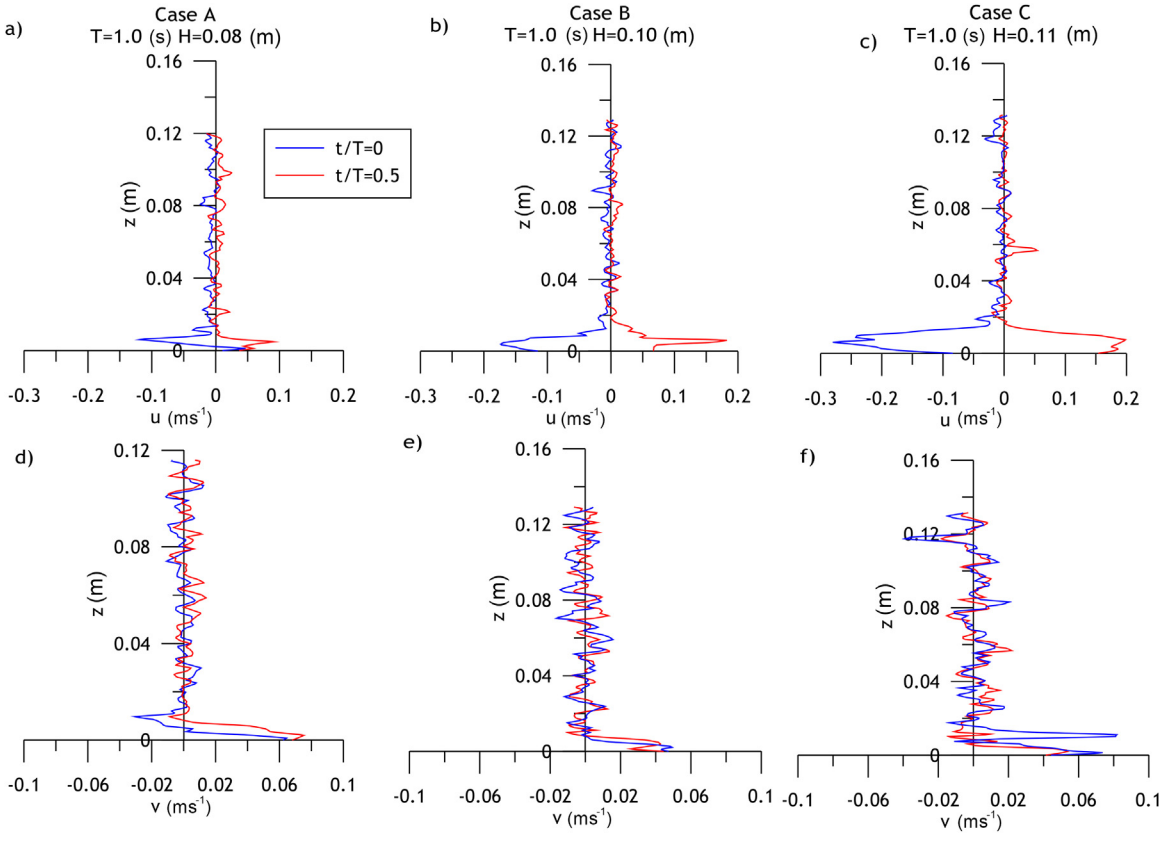

Figure 9 Instantaneous horizontal (plots a–c) and vertical (d–f) sediment velocities along a vertical profile over a ripple trough for three values of the wave height H and the wave period $T = 1.0$ s, at wave phases $t/T = 0$ (wave trough transition, blue lines) and $t/T = 0.5$ (wave crest transition, red lines). (For interpretation of the references to color in this figure legend, the reader is referred to the web version of this article.)

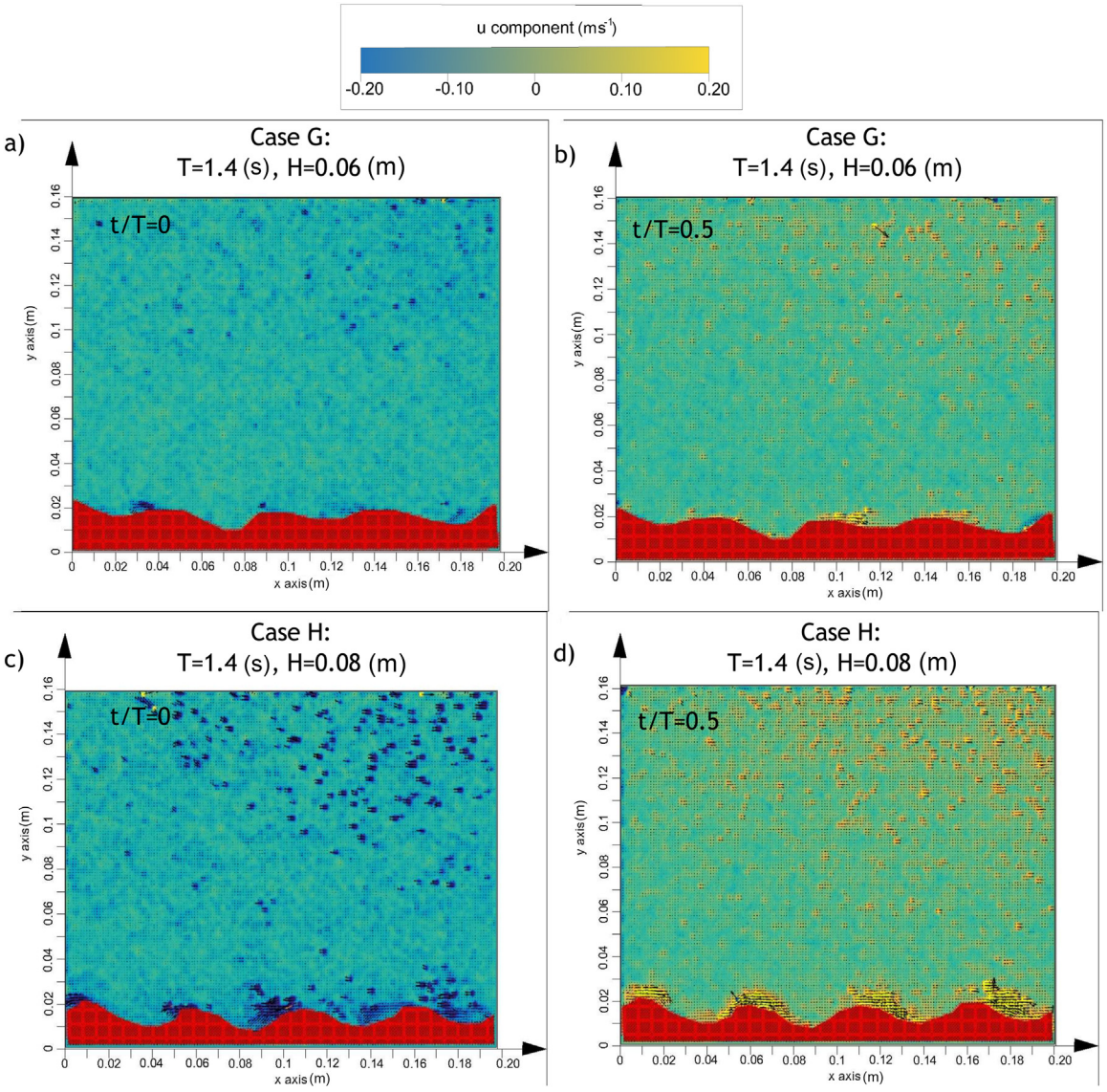

Figure 10 Instantaneous horizontal sediment velocity fields over a rippled bed for two cases of the wave height H and the wave period $T = 1.4$ s.

4.2. Sediment velocities due to surface waves of the period T = 1.4 s

Now we proceed to the results obtained for longer, more nonlinear, waves of the wave period $T = 1.4$ s. Two cases denoted by G and H and defined in Table 1, with the wave height H equal to either 0.06 or 0.08 m, respectively, were investigated in the flume. PIV images showing instantaneous horizontal velocity fields in the vicinity of a rippled bed for the two wave heights are displayed in Fig. 10. The images on the left correspond to the instant of a surface wave trough passage ($t/T = 0$) over the plotted area, while the analogous images on the right show velocities during the passage of a wave crest ($t/T = 0.5$).

The plots in the following figures illustrate sediment velocity profiles in the near-bed region determined for the two wave height cases. Fig. 11 presents horizontal velocity distributions along the horizontal profile over the ripples crests. The case of the smaller wave height ($H = 0.06$ m) is illustrated in Fig. 11a and b, showing that horizontal sediment velocities range from $u_s = -0.09$ m s^{-1} at the wave trough transition to about +0.11 m s^{-1} at a wave crest passage. The corresponding values of sediment velocities for the higher wave ($H = 0.08$ m) range from about -0.20 m s^{-1} at the wave trough transition to about +0.18 m s^{-1} at the wave crest transition, as is seen in Fig. 11c and d.

The plots in Fig. 12 illustrate the distributions of instantaneous horizontal sediment velocities along the vertical profile extending over a ripple crest (see Fig. 3). Fig. 12a shows velocities determined for the wave of the height $H = 0.06$ m. It is seen, for this particular data set, that the maximum near-bed sediment velocity magnitudes during a wave crest passage ($t/T = 0.5$, red lines) are equal to about 0.13 m s^{-1}, and those at the wave trough transition ($t/T = 0$, blue lines) are slightly larger and equal to about 0.15 m s^{-1}. Fig. 12b displays horizontal velocity profiles for the larger

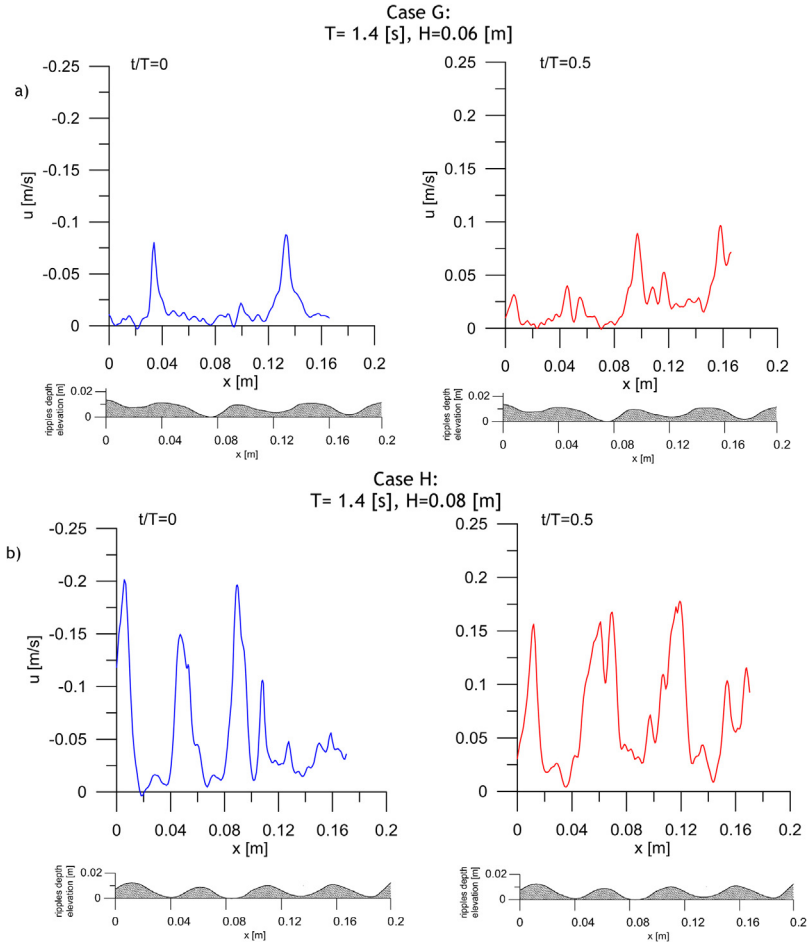

Figure 11 Instantaneous horizontal velocities of sediment grains along the horizontal profile over the bed ripples for two values of the wave height H and the wave period $T = 1.4\,\mathrm{s}$, at wave phases $t/T = 0$ (wave trough) and $t/T = 0.5$ (wave crest).

wave height $H = 0.08\,\mathrm{m}$. In this case, the near-bed sediment velocity magnitudes are equal to about $0.18\,\mathrm{m\,s^{-1}}$ at the wave crest transition, and $0.17\,\mathrm{m\,s^{-1}}$ at a wave trough passage. Again, it is observed (cf. Fig. 6) that the increase in the surface wave height significantly affects the thickness of the near-bed layer of intense sediment movement.

Fig. 13 displays variations in the vertical sediment velocity along the horizontal near-bed profile. Plots 13a and b, illus-

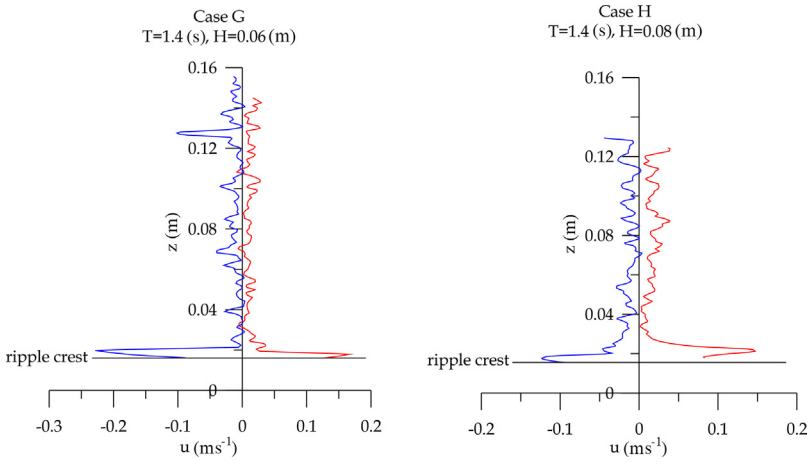

Figure 12 Instantaneous horizontal velocities of sediment grains along the vertical profile over a ripple crest for two values of the wave height H and the wave period $T = 1.4\,\mathrm{s}$, at wave phases $t/T = 0$ (wave trough transition, blue lines) and $t/T = 0.5$ (wave crest transition, red lines). (For interpretation of the references to color in this figure legend, the reader is referred to the web version of this article.)

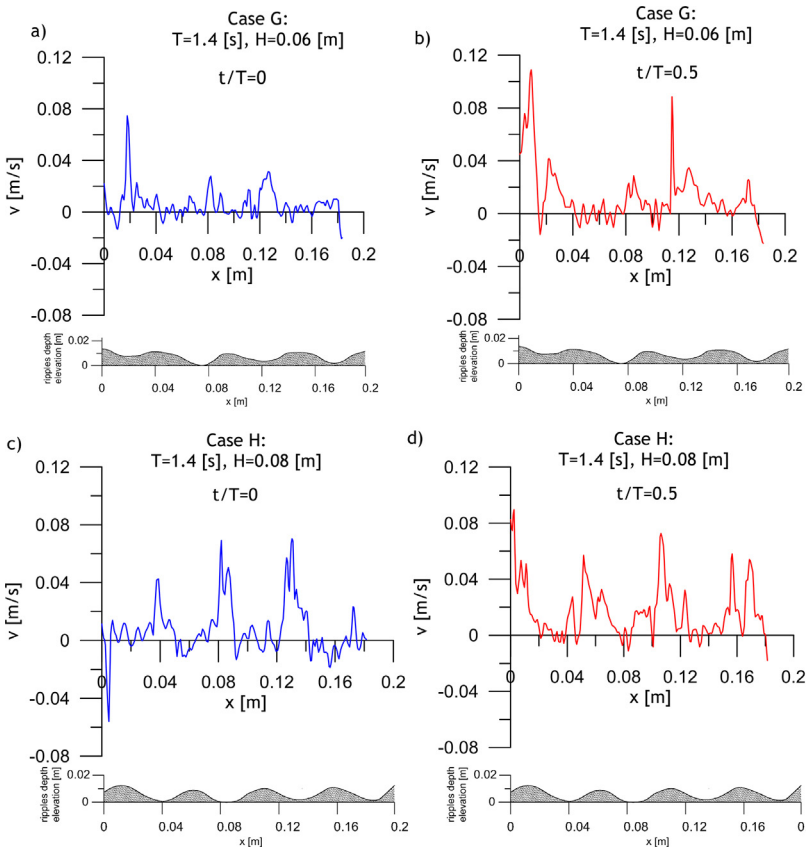

Figure 13 Instantaneous vertical velocities of sediment grains along the horizontal profile over the bed ripples for two values of the wave height H and the wave period $T = 1.4$ s, at wave phases $t/T = 0$ (wave trough) and $t/T = 0.5$ (wave crest).

trating the case of the smaller wave height $H = 0.06$ m, show velocities changing between 0.06 m s^{-1} and -0.03 m s^{-1} at the wave trough passage, and between 0.08 m s^{-1} and -0.03 m s^{-1} at the wave crest passage. The analogous values for the higher wave ($H = 0.08$ m), illustrated in Fig. 13c and d, range from about 0.07 m s^{-1} to -0.04 m s^{-1} at a wave trough passage, and from 0.08 m s^{-1} to -0.03 m s^{-1} at a wave crest passage.

Fig. 14 illustrates the distributions of sediment vertical velocities along the vertical profile extending over a ripple

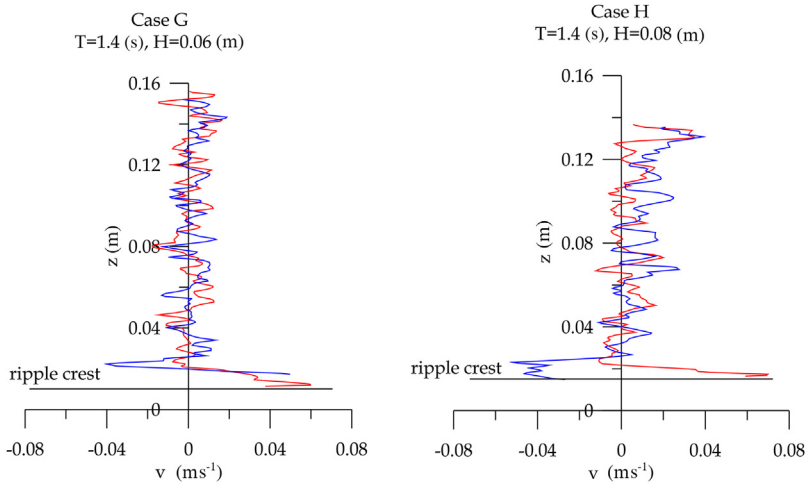

Figure 14 Instantaneous vertical velocities of sediment grains along the vertical profile over a ripple crest for two values of the wave height H and the wave period $T = 1.4$ s, at wave phases $t/T = 0$ (wave trough transition, blue lines) and $t/T = 0.5$ (wave crest transition, red lines). (For interpretation of the references to color in this figure legend, the reader is referred to the web version of this article.)

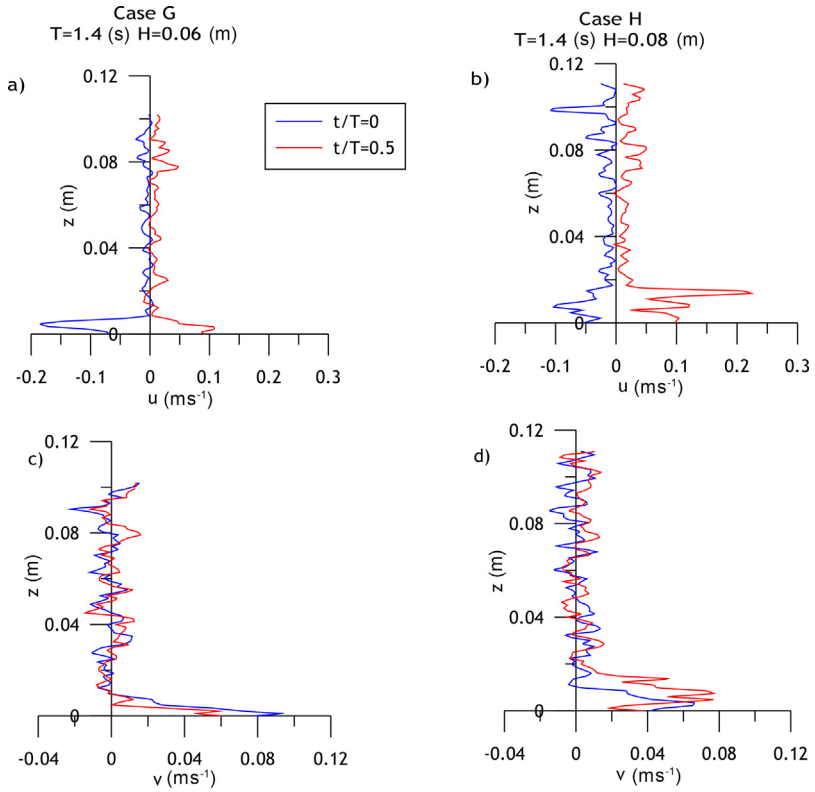

Figure 15 Instantaneous horizontal (plots a, b) and vertical (plots c, d) sediment velocities along the vertical profile over a ripple trough for three values of the wave height H and the wave period $T = 1.4$ s, at wave phases $t/T = 0$ (wave trough transition, blue lines) and $t/T = 0.5$ (wave crest transition, red lines). (For interpretation of the references to color in this figure legend, the reader is referred to the web version of this article.)

crest for the two wave heights. Comparing the plots for both cases with the corresponding plots in Fig. 12, one can note that the magnitudes of vertical sediment velocities in the near-bed turbulent layer are equal to about 1/3 of their horizontal counterparts.

Finally, Fig. 15 illustrates sediment velocity variation along the vertical profile located over a ripple trough. The two plots 15a and b show the distributions of horizontal velocities, and the corresponding plots 15c and d display vertical velocities.

5. Comparisons of experimental and analytical results

It is clearly seen in Figs. 5–9 and 11–15 that the spatial distributions of instantaneous sediment grain velocities are highly variable, reflecting complex physical mechanisms governing the movement of sediment grains in highly turbulent water flow in near-bed regions. First of all, the complexity of the phenomenon is due to the presence of vortices which cyclically appear and disappear near the slopes of bed ripples during successive phases of the oscillatory motion of water induced by surface waves, as described in detail by Van der Werf et al. (2007). In addition, the dynamic interactions of sediment grains with the bed (the mechanism of grain saltation), along with the interactions between grains suspended in water, all contribute to random fluctuations in sediment particle movements near the bed.

In this section, the empirical results from the flume are compared with results that can be obtained by applying analytical formulae presented in Section 2, describing velocity fields generated by surface waves of the Stokes type, the characteristics of the wave boundary layer, and the parameters (length and height) of bed ripples. Since the PIV technique fails to measure water particle velocities in the presence of sand grains suspended in water (because the latter are detected by this technique), water particle velocities are calculated analytically and then compared, in Section 5.1, with sediment grain velocities measured in the laboratory. In Section 5.2, the results from the flume experiments are compared with those known from the literature on sediment dynamics. Thus, the characteristics of the measured bedforms are compared with those predicted by the theory for given surface wave parameters, forces acting on sediment grains at the bed (expressed in terms of the Shields parameter) are evaluated, and the thicknesses of the wave-induced oscillating turbulent boundary layer (WBBL) are calculated and compared with those determined experimentally.

5.1. Sediment particle velocities versus water particle velocities

To compare the instantaneous velocities of sediment particles with those of water in the near-bed region, theoretical relations (1) and (2) describing second-order Stokes waves

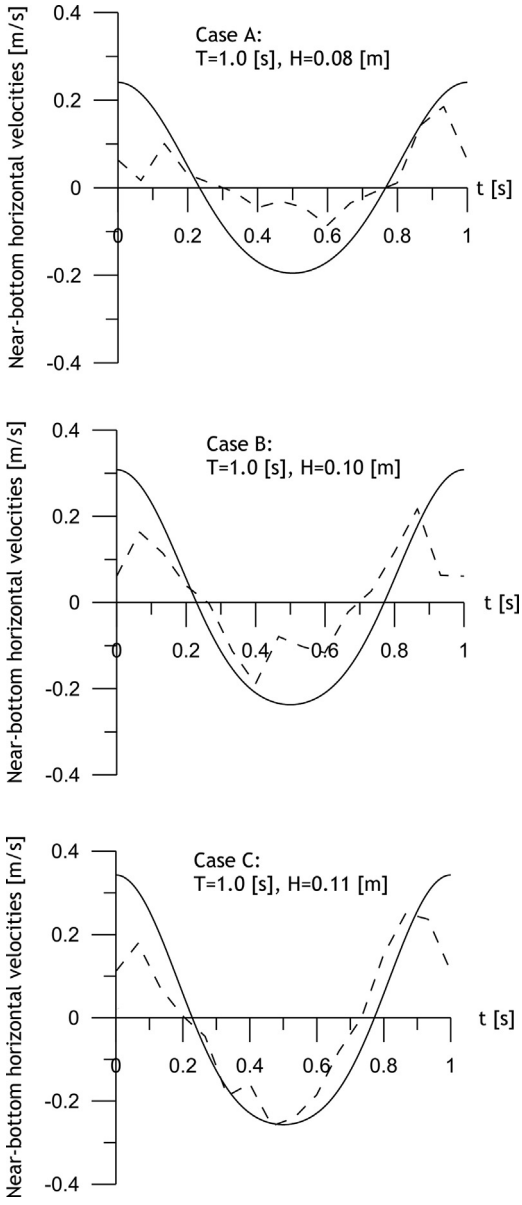

Figure 16 Variations in near-bed horizontal velocities of sediment particles (dashed lines) and water particles (solid lines) during one period of a surface wave for cases A, B and C ($T = 1.0$ s).

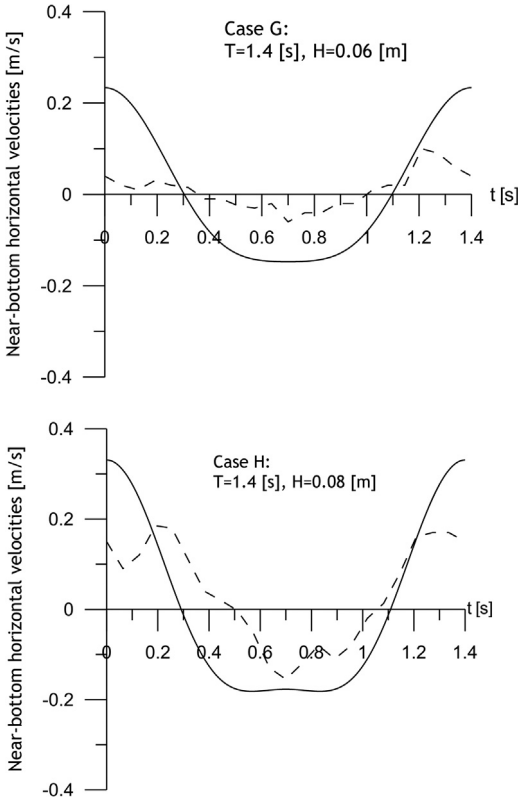

Figure 17 Variations in near-bed horizontal velocities of sediment particles (dashed lines) and water particles (solid lines) during one period of a surface wave for cases G and H ($T = 1.4$ s).

are employed. The plots in Figs. 16 and 17 display variations in the horizontal velocities of sediment and water particles at a point near a ripple crest point during the time of one wave period T. The plotted quantities for the sediment represent mean values calculated for a series of ten consecutive wave periods. Sediment velocities are plotted in the figures with an interval of 1/15 s, which is related to the frequency of 15 Hz at which successive images were recorded by the PIV system used in the experiments. This corresponds to only 16 time-points in the plots for the waves of the period $T = 1.0$ s, and 22 points for the waves with $T = 1.4$ s. The three cases (A, B and C) of waves with the period $T = 1.0$ s are illustrated in Fig. 16, with the solid lines showing water velocities, and the dashed lines representing sediment velocities. The corresponding plots for the longer waves, represented by cases G and H (of the period $T = 1.4$ s), are displayed in Fig. 17. In all the plots in Figs. 16 and 17, the instant $t = 0$ represents the time of a wave crest passage over a given point. It can be noted in the plots that the higher the wave height H, the higher the ratio of the horizontal velocity of sand grains to water velocity, u_s/u_w. For smaller wave heights (cases A and G), the ratios u_s/u_w, on average, do not exceed the values of about 0.3. On the other hand, for the higher and more non-linear waves, with the wave crests becoming shorter and the troughs becoming longer, the ratios u_s/u_w significantly increase during the wave trough passage. This is seen in the plots for cases C and H, representing the steepest waves investigated in the experiments, for which the above velocity ratios are, on average, as large as about 0.8 and more. This property is due to the fact that, for steep waves in shallow water, the trough passage phase lasts longer than the crest passage phase, so that there is more time for sediment particles to catch up with water during the trough phase of the oscillatory wave motion. This, in a way, also explains why the most intense changes in the sandy bedforms occur during the passage of wave troughs.

Fig. 18 illustrates time-variations in the vertical velocities of near-bed sediment particles versus wave-induced vertical water velocities defined by Eq. (2). Unlike the plots in Figs. 16 and 17, which show horizontal velocities at a point located on a ripple crest (at which vertical water velocities given by

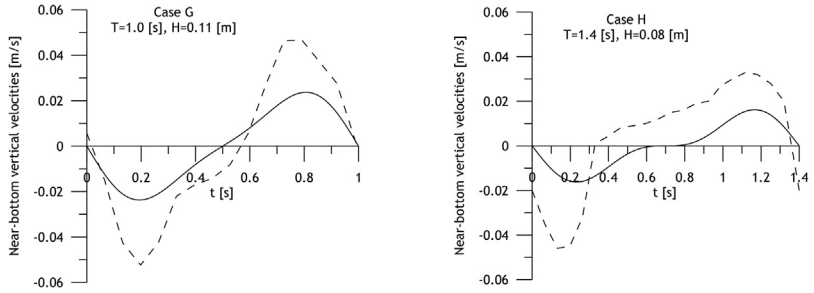

Figure 18 Variations in near-bed vertical velocities of sediment particles (dashed lines) and water particles (solid lines) during one period of a surface wave for cases C ($T = 1.0$ s, $H = 0.11$ m) and H ($T = 1.4$ s, $H = 0.08$ m).

Eq. (2) are zero), the plots in Fig. 18 show vertical velocities at a point directly above the middle of a ripple trough, at the ripple crest height. These plots illustrate cases C and H, representing the highest waves with the period 1.0 s and 1.4 s, respectively. It follows from the plots (see also Figs. 16c and 17b) that the maximum vertical velocities v_s of sediment particles at that point are about 20–25% of the maximum horizontal sediment velocities u_s at the neighbouring crest points. Unlike the maximum horizontal sediment velocities, which are equal to a fraction of the maximum water velocities, the maximum vertical sediment velocities considerably exceed the corresponding wave-induced water velocities. This effect, caused by the ejection of sand grains from the bed by ripple vortices, is particularly well pronounced for the longer wave represented by case H, which corresponds to the most non-linear wave analyzed in the experiments, see the Ursell and Reynolds number values listed in Table 1. It may be of interest to compare the maximum vertical velocities of sand grains, equal to about 0.05 m s^{-1}, with the grain settling velocity. It turns out that the latter, calculated from Eq. (17) in Section 2, is equal to 0.036 m s^{-1} for the sand grain diameter $d_{50} = 0.257$ mm.

The magnitudes of near-bed sediment grain and water velocities for the five wave cases investigated in the flume are compared in Table 2. For sediment, the numbers in the table represent time-averaged velocities calculated as means of extreme (both positive and negative) quantities over ten subsequent wave periods. The columns labelled u_s and u_w list the horizontal velocity magnitudes of sediment and water, respectively, at a wave crest passage, whereas those labelled $-u_s$ and $-u_w$ give the corresponding magnitudes at a wave trough passage over a given near-bed spatial point.

Finally, the plots in Fig. 19 show the dependence of the maximum near-bed sediment particle velocities on the value of the Shields parameter $\theta_{2.5}$ for the five wave cases investigated in the flume experiments.

5.2. Bed forms and wave bottom boundary layer thickness

In all surface wave cases investigated in the laboratory experiments described in this work, well-developed systems of regular bed ripples formed and remained stable in time. The characteristic geometric parameters of the ripples (their lengths λ_r and heights η_r) measured in the flume for the five cases considered are listed in Table 3. Given are the mean values and standard deviations (appearing after the signs $\pm$). The measured quantities, indicated by the suffix 'exp', are compared with corresponding quantities obtained from analytical formulae: (14) for λ_r and (15) for η_r, indicated by the suffix 'the'. In addition, the table also contains the values of the Shields parameter $\theta_{2.5}$ calculated from Eqs. (7) and (8). The last two columns in the table give the empirically and theoretically estimated depths δ of the wave bottom boundary layer, see Eqs. (11)–(13).

It is seen in the table that the empirically measured geometric parameters of the bed ripples are, in general, in good agreement with those predicted by the theory. In particular, the analytically determined ripple heights η_r fall within the range of values observed in the flume, except for case A, in which a small discrepancy (0.1 cm) has occurred. Regarding the ripple lengths λ_r, the agreement between empirically and theoretically evaluated values is seen for cases A, B and G, whereas for the most non-linear waves represented by cases C and H the observed ripple lengths are smaller than those given by the analytical formula.

As can be seen in Table 3, the values of the Shields parameter $\theta_{2.5}$ in our experiments varied between

Table 2 Magnitudes of near-bottom horizontal velocities of sediment and water particles for five surface wave cases considered.

Case	H [m]	T [s]	Water particles				Sediment particles			
			u_w [m s^{-1}]	$-u_w$ [m s^{-1}]	v_w [m s^{-1}]	$-v_w$ [m s^{-1}]	u_s [m s^{-1}]	$-u_s$ [m s^{-1}]	v_s [m s^{-1}]	$-v_s$ [m s^{-1}]
A	0.08	1.0	0.23	0.19	0.02	0.01	0.17	0.20	0.06	0.07
B	0.10	1.0	0.30	0.24	0.03	0.025	0.23	0.25	0.08	0.07
C	0.11	1.0	0.33	0.26	0.03	0.03	0.3	0.35	0.08	0.10
G	0.06	1.4	0.22	0.15	0.02	0.01	0.10	0.12	0.03	0.04
H	0.08	1.4	0.32	0.18	0.04	0.02	0.18	0.18	0.03	0.05

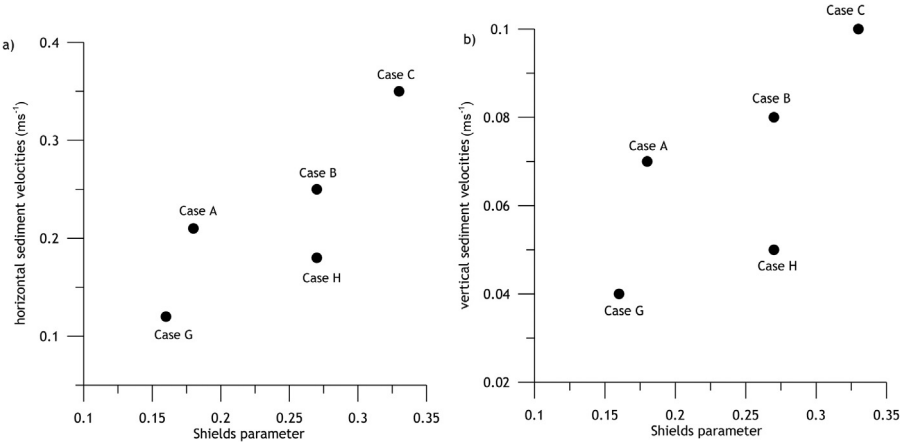

Figure 19 Maximum horizontal (a) and vertical (b) sediment near-bed velocities as functions of the Shields parameter $\theta_{2.5}$ for the five surface wave cases analyzed in the laboratory experiments.

Table 3 The values of the bed ripple length (λ_r), height (η_r), Shields parameter ($\theta_{2.5}$) and the thickness (δ) of the wave bottom boundary layer determined experimentally and theoretically for five surface wave cases considered.

Case	H [m]	T [s]	λ_r^{exp} [cm]	λ_r^{the} [cm]	η_r^{exp} [cm]	η_r^{the} [cm]	$\theta_{2.5}$ [–]	δ^{exp} [cm]	δ^{the} [cm]
A	0.08	1.0	3.5 ± 0.4	3.5	0.9 ± 0.1	0.71	0.18	1.5	2.31
B	0.10	1.0	4.1 ± 0.2	4.2	0.8 ± 0.1	0.80	0.27	3	3.58
C	0.11	1.0	3.7 ± 0.3	4.5	0.8 ± 0.1	0.81	0.33	4	4.01
G	0.06	1.4	5.4 ± 0.5	5.1	1.0 ± 0.2	0.92	0.16	2.5	3.12
H	0.08	1.4	5.1 ± 0.2	6.2	1.1 ± 0.1	1.02	0.27	4	4.92

0.16 and 0.33, which confirms that the range of $0.1 \leq \theta_{2.5} \leq 0.3$, approximately, corresponds to a stable system of bed forms, as was observed during the experiments.

With regard to the values of the wave bottom boundary layer thicknesses δ observed in the laboratory for the five wave cases investigated, they are in reasonable agreement with the corresponding values determined analytically.

6. Conclusions

The paper presents the results of laboratory measurements of surface wave-induced sediment movement over a mildly inclined rippled seabed carried out in a flume. The flow conditions investigated in the experiments corresponded to non-linear waves of the Stokes type with the Ursell number ranging from about 18 to about 39 for wave parameters selected for the measurements. For the fine sand used in the experiments, with the median diameter d_{50} = 0.257 mm, grain mobility numbers varied between 12 and 26. The near-bed water velocities generated by surface waves propagating in the flume resulted in the formation of a stable system of ripples with heights between approximately 0.7 and 1.2 cm and Shields parameter values between 0.18 and 0.33.

For the above-described flow conditions, the near-bed layer of intense sediment grain movements had a thickness of about 2–3 ripple heights above ripple crests, depending on the surface wave height. The maximum magnitudes of horizontal sediment velocities measured over ripple crests were about twice as large as those over ripple troughs. The maximum vertical sediment velocities measured above ripple crests and troughs were similar, amounting to approximately 1/4 to 1/3 of horizontal velocities over ripple crests.

It was found out during the laboratory experiments that sand grain velocities were successfully measured by the PIV method in a region extending a few centimetres over the bed, where the sediment concentration is the highest, and no seeding, which is commonly used in PIV measurements, was necessary. Above this layer, with decreasing concentration of sediment particles in water, the PIV system failed to distinguish sediment grains from water particles. For this reason, i.e. the inability of the PIV equipment to uniquely determine water particle velocities, water particle velocities were evaluated by analytical formulae in order to compare them with measured sediment grain velocities. Such comparisons showed that near-bed grain horizontal velocities were 1/3 to 1/2 of the corresponding water velocities, whereas maximum sediment grain vertical velocities exceeded those of water.

As mentioned in Introduction, the subject of this paper is very close to that considered in an earlier paper by Stachurska and Staroszczyk (2016), in which wave-induced flow over a horizontal sandy bed was analyzed in a flume. Horizontal velocity profiles in the two flow configurations were compared, but no clear qualitative differences were found between the flows over the horizontal bed and the bed inclined at 2%, bearing in mind the scatter in the measured data.

The laboratory measurements carried out in the flume produced detailed data sets containing the velocities of sediment grains above the rippled bed recorded for a series

of wave-induced oscillatory flows. These data sets can be used to test numerical models for simulating suspended sediment dynamics. One such model is being currently developed by the authors of this work.

Acknowledgements

Financial support for this research was provided by the National Science Centre (NCN), Poland, under contract no. UMO-2013/11/B/ST8/03818. The authors thank Dr Marek Szmytkiewicz, Associate Professor at the Institute of Hydro-Engineering of the Polish Academy of Sciences in Gdańsk, for his constructive comments which greatly helped to improve an early version of this paper. We are also grateful to two anonymous reviewers for their valuable comments on this manuscript.

References

Ahmed, A.S.M., Sato, S., 2001. Investigation of bottom boundary layer dynamics of movable bed by using enhanced PIV technique. Coast. Eng. 43 (4), 239–258, http://dx.doi.org/10.1142/S0578563401000360.

Alsina, J.M., Caceres, I., Brocchini, M., Baldock, T.E., 2012. An experimental study on sediment transport and bed evolution under different swash zone morphological conditions. Coast. Eng. 68, 31–43, http://dx.doi.org/10.1016/j.coastaleng.2012.04.008.

Bagnold, R.A., 1946. Motion of waves in shallow water, interaction between waves and sand bottoms. Philos. Trans. R. Soc. Lond. A187, 1–15, http://dx.doi.org/10.1098/rspa.1946.0062.

Doering, J.C., Baryla, A.J., 2002. An investigation of the velocity field under regular and irregular waves over a sand beach. Coast. Eng. 44, 275–300, http://dx.doi.org/10.15142/T3ZP4F.

Fenton, J.D., 1990. Nonlinear wave theories. Sea 9 (1), 3–25.

Fredsoe, J., 1984. Turbulent boundary layer in wave-current motion. J. Hydraul. Res. 110 (8), 1103–1120, http://dx.doi.org/10.1061/(ASCE)0733-9429(1984)110:8(1103).

Fredsoe, J., Deigaard, R., 1992. Mechanics of Coastal Sediment Transport. World Scientific Publ., Singapore, 392 pp., http://dx.doi.org/10.1142/1546.

Grant, W.D., Madsen, O.S., 1979. Combined wave and current interaction with a rough bottom. J. Geophys. Res 84, 1797–1808, http://dx.doi.org/10.102/JC084iC04p01797.

Grant, W.D., Madsen, O.S., 1982. Movable bed roughness in unsteady oscillatory flow. J. Geophys. Res. 87, 469–481, http://dx.doi.org/10.1029/JC087iC01p00469.

Hedges, T.S., 1995. Regions of validity of analytical wave theories. Proc. Inst. Civ. Eng. Water Marit. Energy 112, 111–114, http://dx.doi.org/10.1680/iwtme.1995.27656.

Inman, D., Bowen, A.J., 1962. Flume experiments of sand transport by waves and currents. Coast. Eng. Proc. 8, 137–150, http://dx.doi.org/10.1016/0378-3839(79)90019-X.

Nielsen, P., 1981. Dynamics and geometry of wave generated ripples. J. Geophys. Res. 86 (C7), 6467–6472, http://dx.doi.org/10.1029/JC086iC07p06467.

Nielsen, P., 1992. Coastal Bottom Boundary Layers and Sediment Transport. Advanced Series on Ocean Eng. World Scientific Publishing, Singapore, 340 pp., http://dx.doi.org/10.1142/1269.

Onoszko, J., 1965. Dynamics of a Sandy Seashore Profile Under the Action of Water Waves Normal to the Shoreline: Experimental Investigations. (Ph.D. thesis). Inst. Hydro-Eng. PAS, Gdańsk, Poland, (in Polish).

Ostrowski, R., 2004. Morphodynamics of a Multi-bar Coastal Zone. Instit. Hydro-Engineering PAS, Gdańsk, Poland, http://dx.doi.org/10.1515/heem-2016-0017.

Sato, S., Mimura, N., Watanabe, A., 1984. Oscillatory Boundary Layer Flow Over Rippled Beds. In: Proc. 19th Conf. Coast. Eng., Houston, 2293–2309, http://dx.doi.org/10.1061/9780872624382.155.

Stachurska, B., Staroszczyk, R., 2016. An investigation of the velocity field over rippled sand bottom. In: Proc. 6th IAHR IJREWHS, Lubeck, Germany, 122–131, http://dx.doi.org/10.15142/T3ZP4F.

Thielicke, W., Stamhuis, E.J., 2014. PIVlab – towards user-friendly, affordable and accurate digital Particle Image Velocimetry in MATLAB. J. Open Res. Software, http://dx.doi.org/10.5334/jors.bl.

Umeyama, T., 2012. Eulerian–Lagrangian analysis for particle velocities and trajectories in a pure wave motion using particle image velocimetry. Phil. Trans. R. Soc. A 370, 1687–1702, http://dx.doi.org/10.1098/rsta.2011.0450.

Ursell, F., 1953. The long-wave paradox in the theory of gravity waves. Math. Proc. Camb. Philos. Soc. 49 (4), 685–694, http://dx.doi.org/10.1017/S0305004100028887.

Van der Werf, J.J., Doucette, J.S., O'Donoghue, T., Ribberink, J.S., 2007. Detailed measurements of velocities and suspended sand concentrations over full-scale ripples in regular oscillatory flow. J. Geophys. Res. 112, F02012, http://dx.doi.org/10.1029/2006JF000614.

Willert, C.E., Gharib, M., 1991. Digital particle image velocimetry. Orig. Exp. Fluids 10, 181–193, http://dx.doi.org/10.1007/BF00190388.

Yang, B., Wang, Y., Liu, J., 2011. PIV measurements of two-phase velocity fields in aeolian sediment transport using fluorescent tracer particles. Measurement 44, 708–716, http://dx.doi.org/10.1016/j.measurement.2011.01.007.

Oceanologia (2019) 61, 368–383

Available online at www.sciencedirect.com

ScienceDirect

journal homepage: www.journals.elsevier.com/oceanologia/

ORIGINAL RESEARCH ARTICLE

Short-term variation of zooplankton community in Cintra Bay (Northwest Africa)

Amina Berraho*, **Hinde Abdelouahab, Tarik Baibai, Said Charib, Jamila Larissi, Aziz Agouzouk, Ahmed Makaoui**

National Institute of Fisheries Research, Casablanca, Morocco

Received 19 October 2018; accepted 14 February 2019
Available online 27 February 2019

KEYWORDS
Cintra Bay;
Zooplankton;
Copepods;
Diversity indices;
Environmental parameters

Summary This is the first study that describes the spatial-temporal distributions of the zooplankton community and potential control factors in Cintra Bay. Zooplankton were sampled using a bongo net, 150 μm mesh size, during two surveys, in autumn 2015 and spring 2016, extending from the coast to the open sea. Fourteen zooplankton groups were identified, where copepods represented 49.1% and 92.5% of the total abundance in autumn 2015 and spring 2016, respectively. Tintinnids accounted for 39.7% and 4.7%, respectively. The total zooplankton abundance was higher in autumn (55 992 ind m^{-3}) than in spring (2123 ind m^{-3}). Nineteen species of copepods, belonging to 14 families, were identified. *Euterpina acutifrons* and *Oithona nana* were the most common and abundant species. The Acartiids were represented by three species (*Acartia clausi*, *A. tonsa* and *A. bifilosa*) in autumn and one species in spring (*A. clausi*). The copepods diversity was significantly different between the two seasons showing high values at the entrance and the center of the bay in autumn 2015 and in the southern half of the bay in spring 2016. The copepod structure was characterized by 13 species at different degrees of contribution in autumn 2015. In spring 2016, only four species qualified as indicator species although their contribution was not significant. Given its large opening

* Corresponding authors at: Département d'Océanographie, Institut National de Recherche Halieutique, Boulevard Sidi Abderrahmane, 2 Aï Diab, 20240, Casablanca. Tel.: +212522397385; fax: +212522397388.
E-mail addresses: aminaberraho@gmail.com (A. Berraho), hind.abdelouahab@gmail.com (H. Abdelouahab), baibaitarik@gmail.com (T. Baibai), saidcharib@gmail.com (S. Charib), larissijamila@gmail.com (J. Larissi), oceanosaad@gmail.com (A. Agouzouk), oceanomakaoui@gmail.com (A. Makaoui).
Peer review under the responsibility of Institute of Oceanology of the Polish Academy of Sciences.

Production and hosting by Elsevier

https://doi.org/10.1016/j.oceano.2019.02.001

on the ocean, Cintra Bay benefits largely from the conditions of the oceanic environment, particularly the upwelling. This situation is likely to have an impact on the spatiotemporal variability of the composition and distribution of zooplankton, especially the copepods.

1. Introduction

In Northwest Africa, the Moroccan coastal zone includes several lagoons, estuaries and bays that present a high potential for socio-economic development. Locate between Dakhla Bay and Cape Barbas, Cintra Bay is currently one of three geographical areas identified in the Oued Eddahab region (Dakhla Bay, Cintra Bay and the area between them) that would benefit from a large regional aquaculture development program. Cintra Bay is part of the marine ecosystem, influenced by the cold Canary Current and trade winds that generate a quasi-permanent upwelling. In addition to the upwelling effect, this region is influenced by the contribution of the South Atlantic Central Waters (SACW), characterized by low salinities and high nutrient content (Makaoui et al., 2005). This makes the area one of the richest fishing grounds in the world, mainly for small pelagics, and Cintra Bay serves as a spawning ground for several species (Ettahiri et al., 2012).

The first investigations of the coastal ecosystem of Cintra Bay, which began in 2015, described the marine circulation in the bay (Hilmi et al., 2017) and its hydro-sedimentary characteristics (Makaoui et al., 2017). No studies on plankton biodiversity (phytoplankton and zooplankton) were done. These two biological components play a key role in the trophic web and any change in their abundance or structure leads to significant disturbances in the ecosystem structure and functioning (Keister et al., 2012; Paturej and Kruk, 2011). Indeed, because of its strong integration to the environment and its quick response to environmental changes, zooplankton is currently a tool for monitoring the quality of aquatic environments, especially in coastal areas (Abdul et al., 2016; Davies, 2009; Etilé et al., 2015; Jose et al., 2015; Wokoma, 2016). The composition, abundance, and distribution of zooplankton species in any particular aquatic habitat usually provide information on the prevailing physical and chemical conditions in that habitat (Jakhar, 2013); hence, they are of great ecological importance (Abdul et al., 2016; Jose et al., 2015). Several studies have shown that the structure and abundance of zooplankton were closely correlated with the trophic state of the coastal ecosystems, known for their high environmental parameter variability (Kudari and Kanamadi, 2008; Paturej, 2006; Paturej and Kruk, 2011; Pinto-Coelho et al., 2005; Uriarte and Villate, 2005; Wang et al., 2007).

The main aim of the present work is to investigate the zooplankton community structure of Cintra Bay, which will allow for the establishment of the first taxonomic list of zooplankton groups with emphasis on the copepods. Hence, in this study, a description of the spatio-temporal variations of the composition, distribution and abundance of zooplankton groups and copepods species in relation to studied environmental parameters will be discussed.

2. Material and methods

2.1. Study site and sampling network

Having the form of a half-moon oriented NE-SW, Cintra Bay is wide open to the ocean (18 km) and its periphery consists of a very large sandy beach, which contains many dunes of low height, limited by Punta de las Raimas to the north and Punta Negra to the south. Its coastline is sparsely populated, thus leaving the wild areas mainly undisturbed. Mainly governed by wind and semidiurnal tides, the intensity of the currents outside the bay are generally strong (mainly >0.5 m s^{-1}). Inside the bay, their intensity is less pronounced (<0.3 m s^{-1}) and generally oriented toward the south of the bay due to the influence of the trade winds (NE) (Hilmi et al., 2017) (Fig. 1). Due to this circulation pattern and the depth of the bay, increasing from the coast ($\approx$5 m) to the open sea ($\approx$13 m) (Makaoui et al., 2017), the influence of open ocean waters is more pronounced at the entrance of the northern part of the bay.

Two oceanographic surveys were conducted in Cintra Bay in autumn 2015 (11—15 October) and spring 2016 (8—11 May) and sampling was carried out in 13 stations covering the entire bay (Fig. 2).

2.2. Sampling and sample processing

Zooplankton was sampled using a plankton net (30 cm aperture, 2.5 m total length and 150 μm mesh size) equipped with a flow meter for calculating the volume of the filtered water. The net was towed horizontally at high tide and samples were preserved in 5% formaldehyde-seawater solution, previously buffered with $CaCO_3$.

In the laboratory, zooplankton samples were fractionated using a Motoda box-splitter (Motoda, 1959) where the number of fractions is related to the sample consistency. This operation allows better identification and enumeration of specimens under a stereo microscope. Taxonomic identification of copepods was performed to the species or genus level, but only to the groups for other zooplankton specimens, given their low abundance. Zooplankton and copepod abundances were expressed as individuals per cubic meter [ind m^{-3}].

Surface environmental parameters were collected at the same time as zooplankton sampling. Temperature (T), salinity (Sal) and dissolved oxygen (O_2) were measured in situ with a multi-parameter probe (Hanna, HI9828 Multiparameter Water Quality Meter). At each station, water samples were collected with Niskin bottles. A volume of 500 ml of sampling water was filtered on GF/F filters for the determination of surface chlorophyll-*a* (Chl-*a*) concentration using a fluorimeter (Turner Designs 10 AU) and 30—50 ml of filtered water were used to determine surface nutrients, nitrates

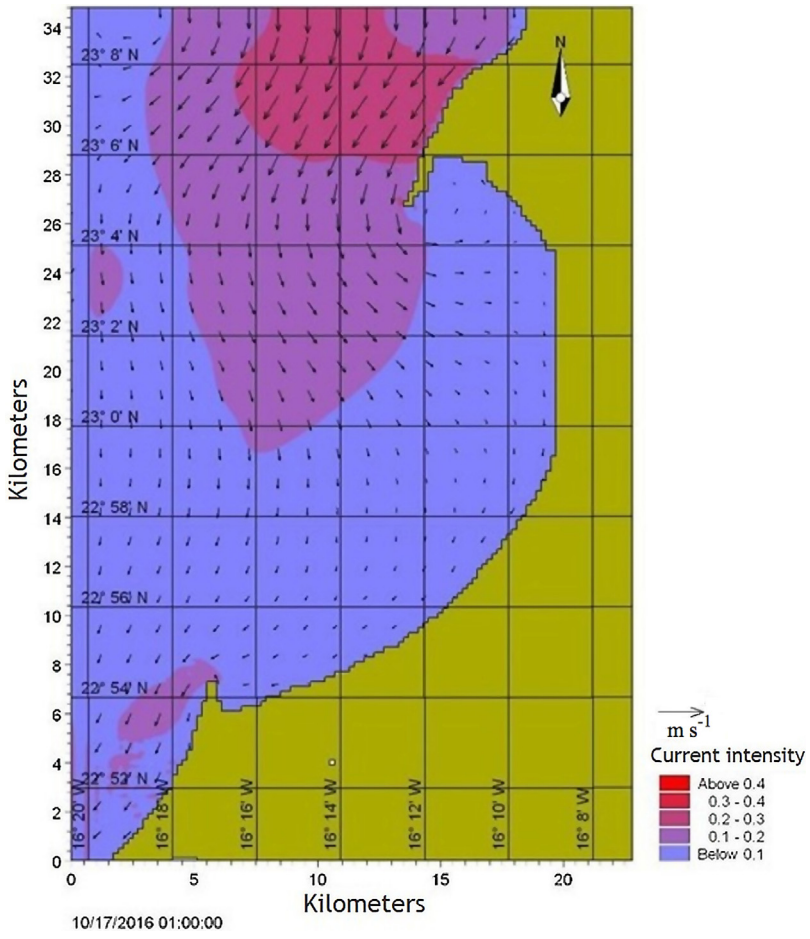

Figure 1 Circulation and current intensity in Cintra Bay during high tide (Hilmi et al., 2017).

(NO_3), nitrites (NO_2), phosphates (PO_4) and silicates (SiO_2) using an Auto Analyzer (AA3 AxEFlow).

2.3. Data analysis

Species diversity of copepods was assessed with the Shannon–Wiener diversity index (H') (Shannon and Wiener, 1949) according to the following formula:

$$H' = -\sum_{i=1}^{S} p_i \log_2 p_i,$$

where S is the total number of copepods species recorded in the sample (species richness) and p_i is the relative frequency of the species i.

Indicator species analysis (Dufrêne and Legendre, 1997) was conducted to identify potential indicator species of copepod for particular environmental conditions in each period. Indicator Value (*IndVal*) for each species i in the group j were computed using the following equation:

$$\mathrm{IndVal}_{ij} = RA_{ij} \times RF_{ij} \times 100.$$

RA_{ij} and RF_{ij} are respectively the relative abundance and the relative occurrence for species i in group j (period in our study). A threshold $IndVal \geq 25\%$ and $p < 0.05$ were used as a cutoff for the indicator species (Dufrêne and Legendre, 1997).

The proportion of samples in which the species is recorded determines the frequency of occurrence of a given species.

The relationships between environmental variables and the abundance of both zooplankton groups and copepod species were determined using a Canonical Correspondence Analysis (CCA). The data matrix was composed of abundances transformed into $\log(x + 1)$ and the environmental parameters (T, Sal, NO_3, NO_2, PO_4, SiO_2, O_2 and Chl-*a*) of the surface layer. The results were presented as a biplot, in which the biological variables and environmental variables were represented together. The correlations between biological and environmental variables were tested using the Spearman correlation test.

Additionally, a one-way analysis of variance (ANOVA) and a multivariate analysis of variance (MANOVA) were used to determine whether there were significant differences in zooplankton/copepod abundances and in environmental variables between different periods in the study area.

All statistical analyses were performed using R (R Development Core Team 2013), except CCA that was produced using XLSTAT (statistical analysis software version 2018).

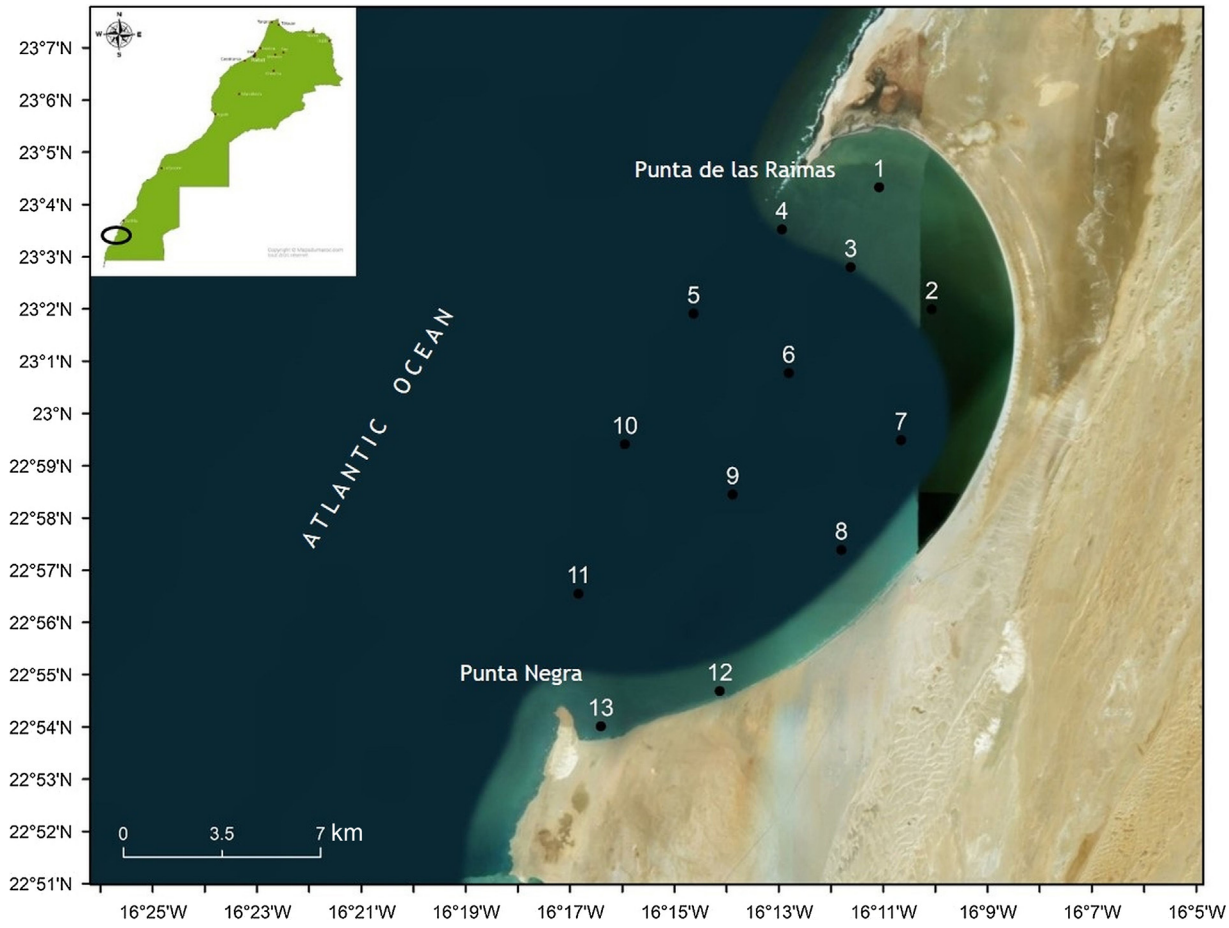

Figure 2 Location of the Cintra Bay (top left) and position of the stations sampled in 2015 and 2016.

3. Results

3.1. Environmental parameters

The average surface temperature recorded in autumn 2015 was relatively high (21.8 ± 1°C) compared to spring 2016 (20.1 ± 1°C). During both seasons, the lowest temperatures were recorded in the middle of the bay and at the entrance. In autumn 2015, these low temperatures were spatially limited to the open part of the bay; while in spring 2016, the cooler offshore waters invaded almost the entire bay with the exception of the northern part and some southern areas where the temperature was over 21°C (Fig. 3a). The seasonal variation of surface temperature was highly significant (MANOVA, $p < 0.001$) (Table 1).

Similarly, the seasonal variation of surface salinity was significant with high levels observed in autumn 2015 (average: 36.81 ± 0.41 psu) compared to spring 2016 (average: 36.52 ± 0.09 psu). Spatially, the distribution of salinity in autumn was characterized by an area of high values recorded in the northern part whereas low salinities were observed particularly at the entrance of the bay (stations 5 and 6). In the rest of the bay, salinities were mid-range (Fig. 3b).

The concentrations of surface nutrients (nitrates, nitrites, phosphates and silicates) did not show significant variations between the two sampling periods (Table 1), with the exception of phosphates. The concentrations of phosphates were significantly higher in autumn 2015 than in spring 2016 (MANOVA, $p < 0.05$). The averages were 0.59 ± 0.39 and 0.28 ± 0.13 μM, respectively.

In autumn 2015, nitrates, nitrites and phosphates (Fig. 3c–e) showed similar distributions in the bay with low concentrations in the central part and near Punta Negra, in the southern part. High concentrations were essentially distributed at the entrance of the bay (starting at station 10) and in the northern part of the bay. The spatial distribution of silicates was slightly different, showing low concentrations limited to the central area, while the rest of the bay was rich in silicates (Fig. 3f).

Non-significant differences in dissolved oxygen content were observed between the two seasons (MANOVA, $p > 0.05$) whose averages in autumn 2015 and spring 2016 were 6.58 ± 0.91 and 5.94 ± 0.53 mg l^{-1}, respectively. The spatial distributions were similar, characterized by well-oxygenated waters in the center of the bay and the least oxygenated waters at the entrance, near Punta de las Raimas (Fig. 3g).

The surface chlorophyll-*a* concentrations showed a highly significant variation between the two seasons (Table 1). In autumn 2015, the bay waters were very rich in phytoplankton; chlorophyll-*a* concentrations were ranging from 1 to 2.72 μg l^{-1} while in spring 2016 the concentrations did not

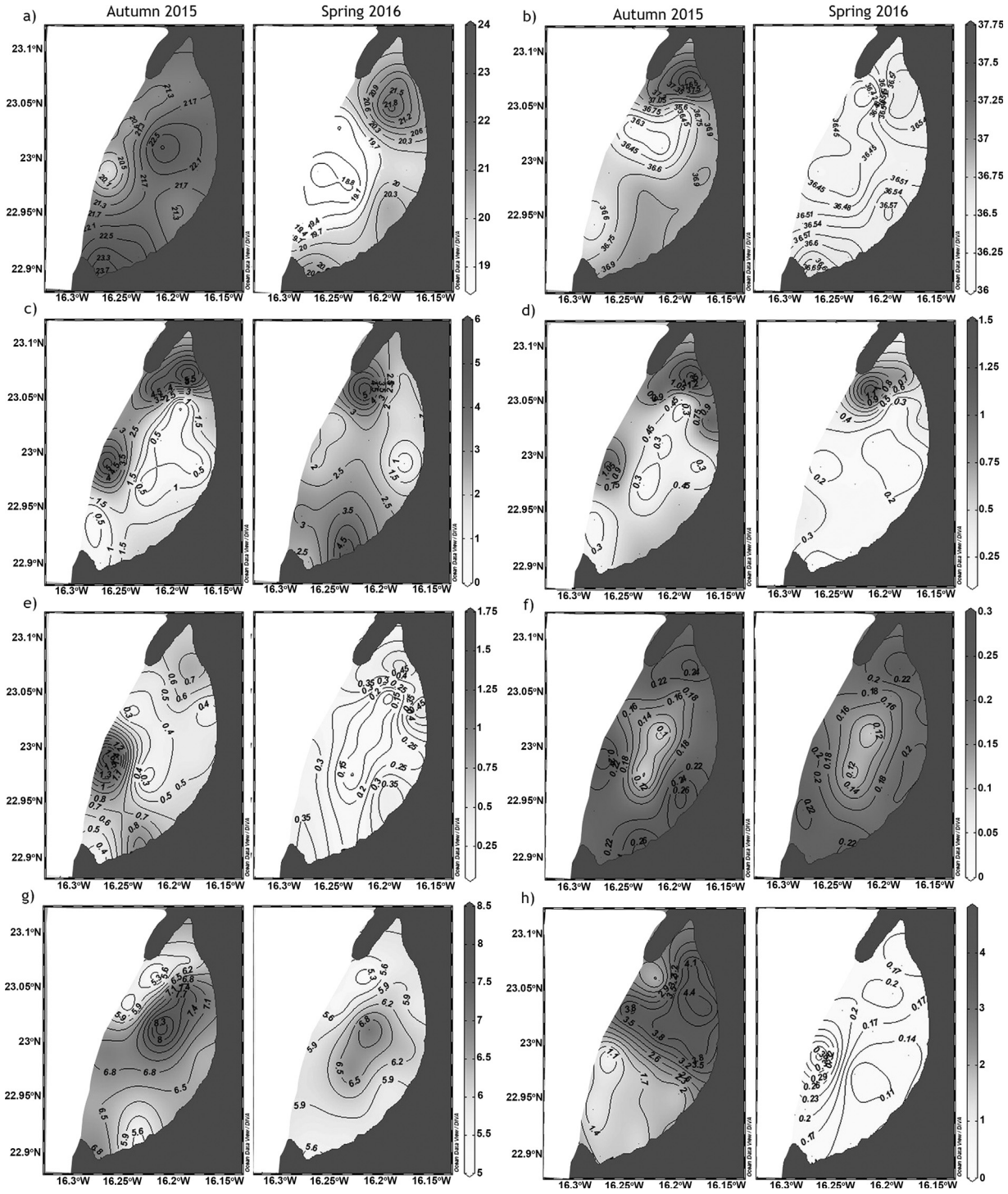

Figure 3 Spatial distribution of the surface temperature [°C] (a), salinity [psu] (b), nitrates [μM] (c), nitrites [μM] (d), phosphates [μM] (e), silicates [μM] (f), dissolved oxygen [mg l^{-1}] (g) and chlorophyll-*a* [μg l^{-1}] (h) in autumn 2015 and spring 2016.

exceed 0.39 μg l^{-1}. According to the spatial distribution of chlorophyll-*a* in autumn 2015, the bay was subdivided into a northern part, rich in chlorophyll-*a*, and a southern part where the lowest chlorophyll-*a* values were recorded.

In spring 2016, concentrations of chlorophyll-*a* increased following an inshore-offshore gradient across the bay (Fig. 3h).

3.2. Zooplankton community structure and distribution

A total of 14 groups of zooplankton were found during the two study periods where 11 groups were identified in autumn 2015 and 10 in spring 2016 (Table 2). Copepods dominated

Table 1 Average, minimum–maximum and standard deviation (Std) values of the surface environmental parameters in Cintra Bay, and MANOVA test between periods.

Parameters	2015		2016		*p*
	Average (min–max)	Std	Average (min–max)	Std	
Temperature [°C]	21.8 (19.7–23.7)	1.0	20.1 (18.6–21.8)	1.0	***
Salinity [psu]	36.8 (36.2–37.7)	0.4	36.5 (36.4–36.7)	0.1	*
Nitrate [μM]	2.0 (0.14–6)	2.1	2.6 (0.67–5.45)	1.3	ns
Nitrite [μM]	0.6 (0.18–1.40)	0.4	0.3 (0.10–1.19)	0.3	ns
Phosphate [μM]	0.6 (0.28–1.69)	0.4	0.30 (0.10–0.47)	0.1	*
Silicate [μM]	0.2 (0.1–0.27)	0.1	0.20 (0.10–0.24)	0.04	ns
Dissolved oxygen [mg l^{-1}]	6.6 (5.25–8.5)	1.0	5.9 (5.17–7.11)	0.5	ns
Chlorophyll-*a* [μg l^{-1}]	2.7 (0.85–4.57)	1.4	0.2 (0.10–0.39)	0.1	***

* Significance level: $p < 0.05$.
*** Significance level: $p < 0.001$.
ns – $p \geq 0.05$ indicates not significant.

Table 2 Zooplankton groups abundance (Ab) (mean ± standard deviation) [ind m^{-3}] and frequency of occurrence (Occ) [%] in Cintra Bay, in autumn 2015 and spring 2016.

Taxa	2015		2016	
	Ab	Occ	Ab	Occ
Annelid larvae	15.1 ± 58	46.2	0.012 ± 0.04	7.7
Appendicular	44.6 ± 63	53.8	0.048 ± 0.7	7.7
Chaetognaths	15.2 ± 32	38.5	0.012 ± 0.4	7.7
Cirriped larvae			2.62 ± 5	38.5
Cladocerans	17.1 ± 34	53.8	1.19 ± 2	53.8
Copepods	2292.6 ± 1857	100	151.1 ± 243	84.6
Decapod larvae		38.5		
Fish (eggs/larvae)	39.6 ± 68	61.5	0.03 ± 0.1	15.4
Foraminifera			0.10 ± 0.3	15.4
Mollusk veligers	159.8 ± 319	69.2	1 ± 1.14	30.8
Mysidacea	0.20 ± 1	7.7		
Ostracods	0.84 ± 1	30.8		
Radiolarians	104.7 ± 251	23.1		
Tintinnids	1612.5 ± 2060	100	7.6 ± 14	38.5

zooplankton abundance in both surveys, representing 49.1% in the autumn and 92.5% in the spring. The tintinnids were the second most abundant group with 39.7% of total abundance in autumn 2015 and only 4.7% in spring 2016.

Overall, the other groups were not abundant (<1%) and mainly represented by mollusk veligers, radiolarians, appendicular and fish in 2016, and mainly of cirriped larvae in 2015 (Fig. 4). In autumn 2015, fish eggs were collected in relatively high abundance (516 eggs m^{-3}), indicating that Cintra Bay was a favorable area for fish spawning in this period.

The total zooplankton abundance was higher in autumn 2015 (55 992 ind m^{-3}) than in spring 2016 (2123 ind m^{-3}) and the difference was highly significant ($p < 0.001$).

The spatial distribution of copepods abundance in autumn 2015 did not show any clear distribution pattern. The abundances recorded in most stations were high and exceeded 1000 ind m^{-3}. The highest value was observed at station 5 (5948 ind m^{-3}), where the offshore water masses enter the bay, while the lowest abundance (79 ind m^{-3}) was recorded

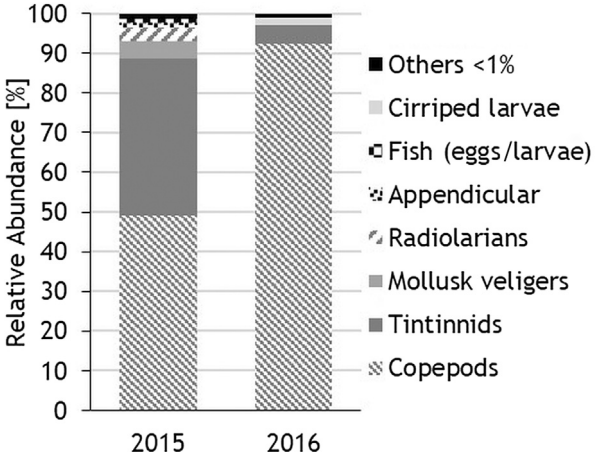

Figure 4 Relative abundance of zooplankton groups identified in Cintra Bay in autumn 2015 and spring 2016.

near the coast at station 8 (Fig. 5a). Spring 2016 was marked by a quasi-absence of zooplankton, and therefore of copepods, in the extreme northern part of the bay (stations 1, 2, 3 and 4) where only one specimen was recorded at each station 2 and 4. Generally low in this season (maximum: 859 ind m^{-3}), the abundance of copepods was higher in the transect located at the Bay opening than along the central and coastal transects.

Tintinnids showed a highly significant difference in abundance between the two periods ($p < 0.01$). Indeed, the total abundance was very high in autumn 2015 (20 963 ind m^{-3}) with a wide spatial distribution throughout the bay. The maximum abundance was recorded at station 11 (6906 ind m^{-3}) and the minimum, as it was the case for copepods, at station 8 (27 ind m^{-3}). In spring 2016, the spatial distribution of tintinnids was limited to a few stations whose maximum abundance (47 ind m^{-3}) was recorded in station 5 and the minimum (6 ind m^{-3}) in station 8 (Fig. 5b).

The larval stages of copepods, particularly the nauplii, were relatively abundant and accounted for 19 and 29.5% of the total copepods respectively in autumn 2015 and spring 2016. The copepodite stage only represented 1 and 2.3%, respectively. A total of 19 species of adult copepods, belonging to 14 families, were identified in Cintra Bay with 15 species found in autumn 2015 and 12 in spring 2016 (Table 3).

In autumn 2015 the copepod community was dominated by *Euterpina acutifrons* (39.3% of total adult copepods), distributed throughout the bay (100% occurrence) with a total abundance of 9836 ind m^{-3}. The Acartiidae family was represented by three species (*Acartia clausi*, *A. tonsa* and *A. bifilosa*) occupying the second position (34% of total adult copepods) with a total abundance of 8392 ind m^{-3}. *Paracalanus parvus*, *Oithona nana* and *Clausocalanus arcuicornis* were also abundant and widely distributed.

In spring 2016, the most abundant species of copepods were *O. nana* and *E. acutifrons*, with 54.4 and 27.7%, respectively and were distributed throughout the bay except in the northern part where copepods were almost absent. The only species of Acartiidae identified (*A. clausi*), displayed a wide distribution despite its low abundance (99 ind m^{-3}), that accounted for 7.4% of total adult copepods.

Specimens of the genus *Tigriopus* were present in low numbers (total abundance 11.3 ind m^{-3} in autumn 2015 and 0.63 ind m^{-3} in spring 2016) and were located mainly in the northern part of the bay. Species of this genus had not been previously reported on the Moroccan coast.

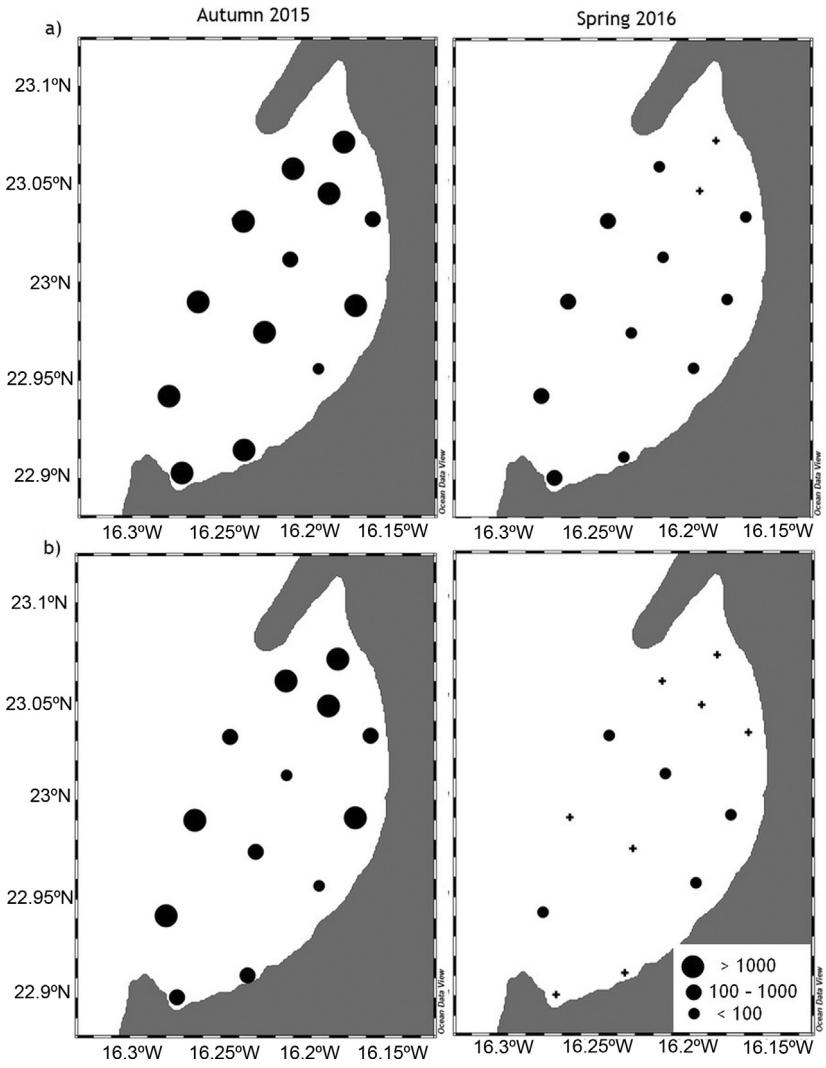

Figure 5 Spatial distribution of total copepods (a) and tintinnids (b) abundances [ind m^{-3}].

Table 3 Species abundance of adult copepods (Ab) (mean ± standard deviation) [ind m^{-3}] and frequency of occurrence (Occ) [%] in Cintra Bay in autumn 2015 and spring 2016.

Families	Species	Code	2015		2016	
			Ab	Occ	Ab	Occ
Acartiidae	*Acartia bifilosa* (Giesbrecht, 1881)	Aca bif	35.6 ± 56	46.2		
	Acartia clausi Giesbrecht, 1889	Aca cla	393.7 ± 697	92.3	7.63 ± 12	69.2
	Acartia tonsa Dana, 1848	Aca ton	216 ± 282	92.3		
Calanidae	*Calanus helgolandicus* (Claus, 1863)	Cal hel	3.3 ± 8	15.4		
	Nanocalanus minor (Claus, 1863)	Nan min	2 ± 7	7.7		
Calocalanidae	*Calocalanus styliremis* Giesbrecht, 1888	Calo sty	2.2 ± 6	15.4		
Centropagidae	*Centropages typicus* Krøyer, 1849	Cen typ	3.01 ± 4	7.7	0.38 ± 1	7.7
Clausocalanidae	*Clausocalanus arcuicornis* (Dana, 1849)	Cla arc	100.9 ± 174	61.5	0.24 ± 1	7.7
Corycaeidae	*Ditrichocorycaeus anglicus* (Lubbock, 1857)	Dit ang	0.08 ± 031	76.9		
Eucalanidae	*Eucalanus elongatus* (Dana, 1848)	Euc elo			3.19 ± 11	15.4
Tachydiidae	*Euterpina acutifrons* (Dana, 1847)	Eut acu	756.6 ± 822	100	28.5 ± 41	84.6
Ectinosamatidae	*Microsetella rosea* (Dana, 1847)	Mic ros			0.14 ± 0.43	69.2
Oithonidae	*Oithona similis* (Claus, 1863)	Oit sim			0.19 ± 1	7.7
	Oithona nana Giesbrecht, 1891	Oit nan	122.3 ± 93	100	56 ± 116	15.4
Oncaeidae	*Oncaea venusta* Philippi, 1843	Onc ven	1.75 ± 6	7.7	1.54 ± 5	46.2
Paracalanidae	*Paracalanus parvus* (Claus, 1863)	Par par	206 ± 376	92.3	5.03 ± 14	15.4
Temoridae	*Temora longicornis* (Muller, 1792)	Tem lon	0.24 ± 1	7.7		
	Temora stylifera (Dana, 1849)	Tem sty			0.048 ± 0.17	7.7
Harpacticidae	*Tigriopus* sp.	Tri sp.	0.86 ± 2	15.4	0.048 ± 0.17	7.7

Copepod diversity indices differ significantly between the two seasons ($p < 0.05$ for H' and $p < 0.01$ for S). In autumn 2015, H' varied between 0.71 and 2.75 with high copepods diversity at the stations located at the opening and the center of the bay. Species richness was also high in the center of the bay. In the northern and southern parts of the bay, both H' and S were low.

In spring 2016, the copepod community was more diversified in the southern part of the bay where values of H' were greater than 1 (maximum 2.90). In the northern part, only the stations close to the entrance of offshore waters (stations 5 and 6) showed a high diversity (Fig. 6).

According to the indicator species analysis (*IndVal*) (Table 4), different copepod assemblages characterized seasons. In autumn 2015, among the 13 species of copepods that characterized this period, seven contributed significantly to this assemblage (*IndVal* $\geq 25\%$ and $p < 0.05$). In contrast, only four species have been associated with the spring season but their contribution were not significant.

The results of the CCA, revealed a significant correlation between zooplankton groups and the environment (Monte Carlo Permutation Test; $p = 0.001$) for the first two axes ($F1 = 0.868$ and $F2 = 0.835$). The cumulative percent of variance for these two axes was 67.6%. Temperature was strongly and positively correlated with the $F1$ axis ($r = +0.739$) and chlorophyll-*a* with the $F2$ axis ($r = +0.707$). Salinity contributed the least in the ordination of zooplankton groups.

The projection of zooplankton groups into the factorial biplot $F1 \times F2$ showed a few distinct groups linked to extreme values of the environmental parameters. For instance, radiolarians, positively correlated with temperature (Spearman's $r = 0.24$, $p = 0.01$) were collected only in autumn 2015, mainly in the southern area at higher temperatures. On the contrary, cirriped larvae found in spring 2016 were significantly correlated with low values of temperature, nitrites and chlorophyll-*a* (Spearman's $r = 0.26$, $p = 0.008$; $r = 0.18$, $p = 0.03$ and $r = 0.20$, $p < 0.0001$, respectively). Although the foraminifera form a distinct group, they did not show any significant correlation with environmental parameters, probably due to their low abundance and their presence limited to the spring 2016 (Fig. 7).

Copepods and tintinnids, the two dominant groups of zooplankton, were strongly correlated with chlorophyll-*a* (Spearman's $r = 0.51$ and $r = 0.56$, $p < 0.0001$), and moderately with temperature and phosphates (Spearman's $r = 0.25$, $p = 0.01$ and $r = 0.21$, $p = 0.02$, respectively).

The CCA carried out only with copepod species and environmental factors showed a strong significant correlation (Monte Carlo Permutation Test; $p = 0.001$) for first two axes (0.934 and 0.835, respectively, for $F1$ and $F2$) that explained 63.6% of the variance. Chlorophyll-*a*, temperature and dissolved oxygen contributed negatively to $F1$ axis with medium coefficients of correlation ($r = -0.667$, $r = -0.542$ and $r = -0.407$ respectively) in addition to silicates on the opposite side ($r = +0.479$). Salinity was the most positively correlated factor with the $F2$ axis ($r = +0.576$) in addition to temperature and phosphates ($r = +0.423$ and $r = +0.409$, respectively).

The $F1 \times F2$ biplot indicated that some copepod species, identified in either season, and showing a limited distribution along the bay, form distinct groups. On the positive side of the $F1$ axis, *Oithona similis*, *Eucalanus elongatus* and *Temora stylifera*, found only in spring 2016 and located in the

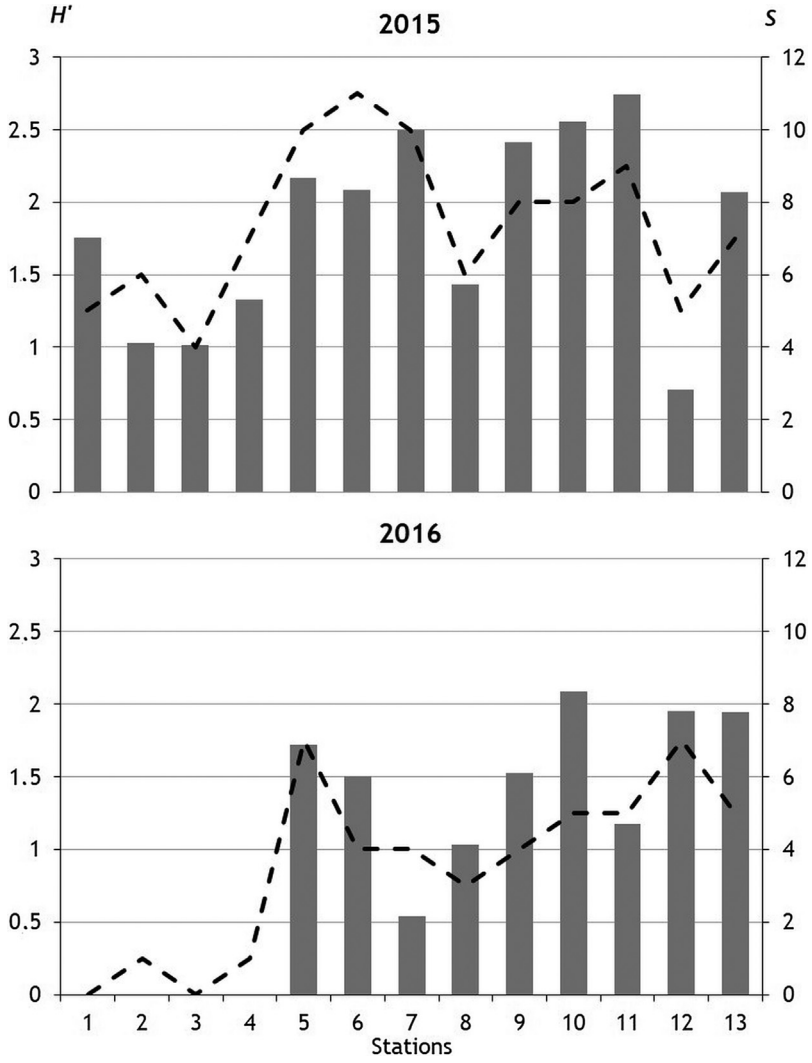

Figure 6 Spatial and temporal variations of Shannon-Wiener index (*H'*) (histograms) and species richness (*S*) (lines) in Cintra Bay during the two survey periods.

extreme southern part of the bay, showed no significant correlation with the environmental parameters. On the opposite side of the axis, the species *Calanus helgolandicus* and *Calocalanus styliremis*, found only in autumn 2015 and located mainly at stations 5 and 6, at the entrance of the bay, were correlated with salinity and silicates (Spearman's $r = 2.22$, $p = 0.02$ and $r = 0.16$, $p = 0.04$, respectively, for both species). Moreover, *Ditrichocorycaeus anglicus*, positioned on the same side of the axis, and *Oncaea venusta* in the middle, showed no correlation with environmental parameters, probably due to their low abundances (Fig. 8).

Despite its limited spatial distribution, *Tigriopus* sp., showed a significant correlation with nitrates (Spearman's $r = 0.19$, $p = 0.03$) and seemed to present a wide tolerance for variations in other parameters. The three species of Acartiidae have differential behavior with respect to some of the environmental parameters considered. Indeed, chlorophyll-*a* and temperature were the two factors that were significantly involved in distribution and abundance of *A. tonsa* (Spearman's $r = 0.57$, $p < 0.0001$ and $r = 0.35$, $p = 0.002$, respectively), dissolved oxygen and nitrates for *A. bifilosa* (Spearman's $r = 0.16$, $p = 0.04$ and $r = 0.15$, $p = 0.04$, respectively) and only chlorophyll-*a* for *A. clausi* (Spearman's $r = 0.18$, $p = 0.03$).

4. Discussion

Cintra Bay has a great potential for the development of aquaculture, given its geographical positioning in a part of Northwest Africa (21—26°N) that is characterized by a permanent upwelling, generating a high productivity and a high abundance of fishery resources. Given its orientation along the NW-SW axis, and its communication with the Atlantic Ocean through its wide opening, the environmental parameters in the Cintra Bay denote the influence of the offshore environment, which is more pronounced at the entrance and in the center of the bay. Indeed, the entrance and the central part of the bay were invaded by waters coming from the open ocean and therefore were cooler, less salty and rich in nutrients. Near to the coast, the shallow depth and the absence of freshwater input resulted in high values for

Table 4 Copepod indicator species for each period based on indicator values (IndVal ≥25%) and their significant contribution ($p < 0.05$).

Period	Species	*IndVal*	*p*
2015	*Euterpina acutifrons*	98.1	***
	Acartia tonsa	96.1	***
	Acartia clausi	95.1	**
	Paracalanus parvus	95.1	**
	Clausocalanus arcuicornis	87.6	***
	Centropage typicus	73.7	**
	Acartia bifilosa	67.9	*
	Calanus helgolandicus	39.2	ns
	Calocalanus styliremis	39.2	ns
	Tigriopus sp.	38.2	ns
	Ditrichocorycaeus anglicus	27.7	ns
	Nanocalanus minor	27.7	ns
	Temora longicornis	27.7	ns
2016	*Eucalanus elongatus*	39.2	ns
	Microsetella rosea	39.2	ns
	Oithona similis	27.7	ns
	Temora stylifera	27.7	ns

* Signif. code: $p < 0.05$.
** Signif. code: $p < 0.01$.
*** Signif. code: $p < 0.001$.
ns — $p \geq 0.05$ indicates not significant.

temperature and salinity and low values for nutrients. The high variability in environmental parameters between the two study periods, particularly temperature, chlorophyll-*a* concentration and phosphates, is related to the intensity of the upwelling in the adjacent marine environment (21—26°N). This upwelling has a low seasonality, a maximum intensity in autumn and a pronounced interannual variability (Benazzouz et al., 2014, 2015; Cropper et al., 2014).

As a confluence of inland and marine waters, the paralic systems are among the most fluctuating and productive ecosystems in the world (Etilé et al., 2015). These paralic systems are subject to internal and irregular variations, due to intrinsic characteristics (shallowness, continuous dissolved and particulate matter input) and external energy generating internal dynamics, which modulate their biocenosis (Brugnano et al., 2011; Etilé et al., 2009). Several studies have been conducted in a multitude of coastal ecosystems and have demonstrated the strong correlation between habitat conditions of these ecosystems and the abundance and structure of zooplankton communities (Abdul et al., 2016; Anton-Pardo and Armengol, 2012; Badsi et al., 2010; Dube et al., 2010; Etilé et al., 2009; Gao et al., 2008; Gozdziejewska and Karpowicz, 2013; Gutkowska et al., 2018; Joyce et al., 2005; Paturej and Kruk, 2011; Paturej and Gutkowska, 2015; Paturej et al., 2017; Zakaria et al., 2007).

Except for copepods and tintinnids, the autumn season was characterized by relatively high abundances of different zooplankton groups in Cintra Bay, particularly radiolarians, appendicular, cirriped larvae and early life stages of fish. In autumn 2015, exclusively fish eggs represented the latter group; while in spring 2016, fish eggs and larvae were almost absent. According to a simulation model and in situ observations of ichthyoplankton along 32—21°N region, high coastal retention rates were obtained from Cape Bojador to Cape Blanc (26—21°N), which includes Cintra Bay, especially in autumn and winter (Berraho, 2007; Brochier et al., 2008). This region is known for its great richness in fish resources, mainly the sardine whose main spawning takes place in autumn. Furthermore, the concave configuration of the Cintra Bay and its wide opening to the sea promote retention of coastal waters and consequently planktonic organisms whose

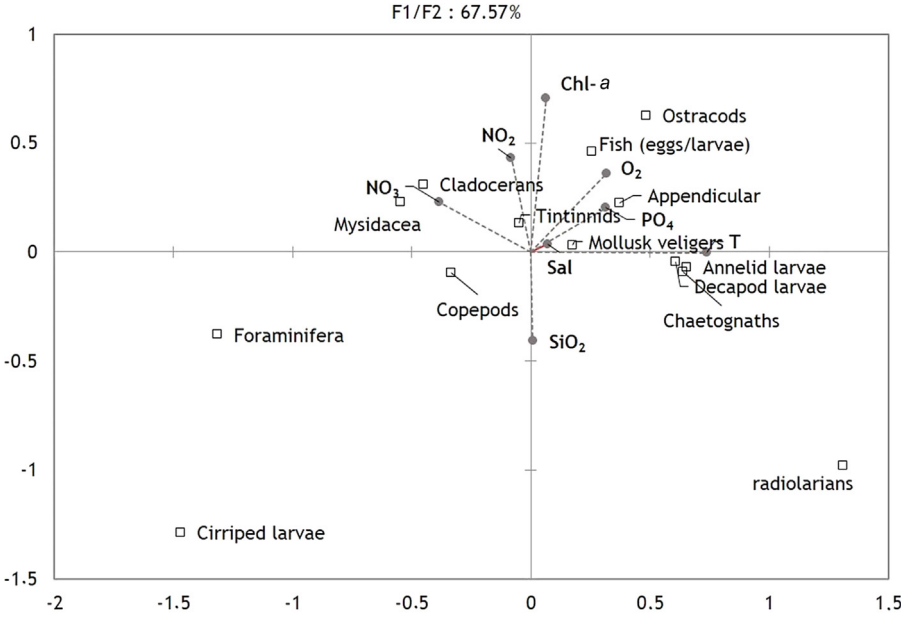

Figure 7 Canonical Correspondence Analysis (CCA) ordination plot for zooplankton groups and environmental variables of the surface layer (T: temperature; Sal: salinity; NO_3: nitrates, NO_2: nitrites; PO_4: phosphates; SiO_2: silicates; O_2: dissolved oxygen; Chl-*a*: chlorophyll-*a*).

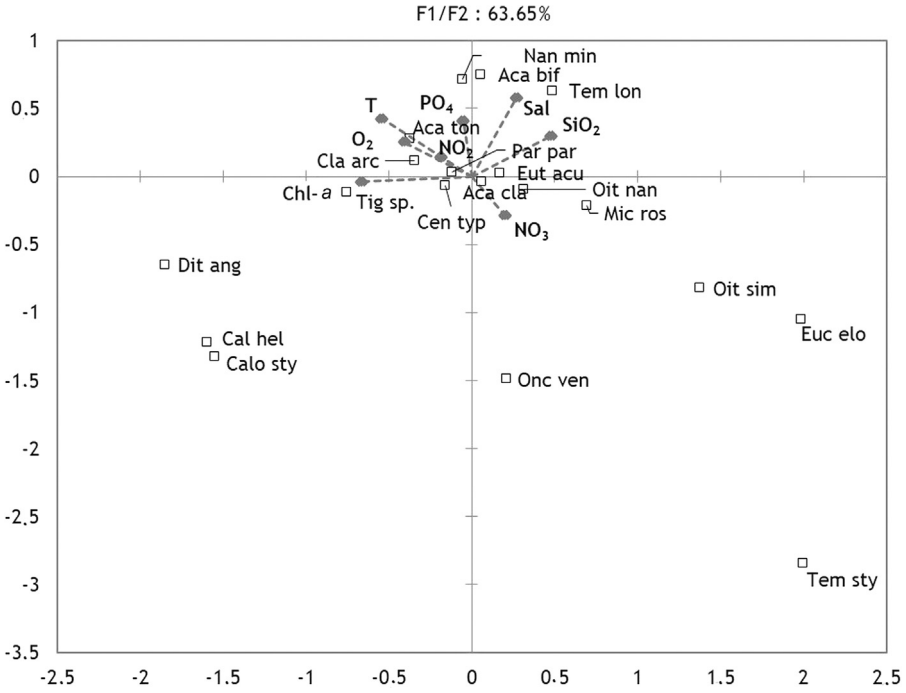

Figure 8 Canonical Correspondence Analysis (CCA) ordination plot for copepod species and environmental variables of the surface layer (T: temperature; Sal: salinity; NO_3: nitrates, NO_2: nitrites; PO_4: phosphates; SiO_2: silicates; O_2: dissolved oxygen; Chl-*a*: chlorophyll-*a*). Code for copepod species in Table 3.

abundance and diversity are related to the seasonal variability of environmental conditions and species life cycles.

If copepods are the key component of mesozooplankton, tintinnids are the key for microzooplankton. Tintinnids play a crucial role in transferring elements and energy from low trophic levels (pico- and nano-phytoplankton) to high one such as copepods and fish larvae (Crawford et al., 1997; Dolan, 2010; Stoecker, 2013) and they are considered to be bio-indicators for some environmental factors (El-Damhougy et al., 2017). According to Chaudhary et al. (2016), they display the most common global biogeographic pattern found among marine species, illustrated by the bimodal diversity gradient, wherein species richness increases from high to low latitudes with a slight dip near the equator. In Cintra Bay, tintinnids had a strong presence in autumn 2015, compared to the spring 2016. This seasonal variation could be attributed to the seasonality of upwelling, which generates a high nutrient and phytoplankton richness in the coastal zone in autumn. Indeed, the presence of tintinnids was strongly correlated with chlorophyll-*a*, temperature and phosphates. Recent studies revealed that chlorophyll-*a* and nutrients were the potential significant factors influencing the tintinnid abundance and distribution in coastal zones (Dash et al., 2017; Rakshit et al., 2016; Wang et al., 2014). In addition, Dolan et al. (2002) conclude that tintinnid diversity, both morphological and taxonomic, is more closely linked to phytoplankton diversity in terms of cell sizes, than competitive interactions or predation.

The copepod group was dominant in Cintra Bay, and showed a strong seasonal variability of abundance with a relatively high presence of larval stages (nauplii) particularly in spring. Taking into account the mesh size of the used net (150 μm), these larval proportions are probably underestimated but still indicate seasonal variability. According to Makabe et al. (2012), no significant underestimation of copepod abundance was found using the 100 μm mesh, except for copepod nauplii that should be quantified using a finer mesh size, such as 60 μm (Nichols and Thompson, 1991). However, despite the use of a mesh size 44 μm, Emir Akbulut and Tavşanoğlu (2018) found no seasonality for nauplii but did find a seasonality for different life stages of copepod in relation to the variation of temperature and salinity. Several authors have highlighted the influence of local hydrographic factors and their seasonal and interannual variability in coastal zooplankton dynamics, including copepods in the Mediterranean Sea (Berline et al., 2012; Beşiktepe et al., 2015; Fernandez de Puelles et al., 2003; Gaudy and Champalbert, 1998; Krsinic et al., 2007; Molinero et al., 2008; Siokou-Frangou, 1996; Uysal and Shmeleva, 2012). In upwelling systems, the life cycle of copepods is multigenerational (up to 10 generations or more each year) depending upon water temperature, food concentration and length of the upwelling season (Peterson, 1998). Different strategies (diapause, resting phase, diel vertical migration) can be adopted by the species according to each upwelling system such as the case of *Calanoides carinatus* in the southern Benguela ecosystem where upwelling is not restricted to the main upwelling season (6-8 month), but it also takes place occasionally during winter (Verheye et al., 1991). In the permanent upwelling along the African region 19–24°N, the SeaWiFS data analysis showed a high primary production throughout the year with a minimum and a maximum production detected, respectively, in December and in April–May (Demarcq and Somoue, 2015; Lathuilière et al., 2008).

This situation can lead to a seasonality of the different life stages of the copepods including the nauplius stage. In Oualidia lagoon (Moroccan Atlantic coast), the nauplii was prevalent in the system throughout the whole year with a large seasonal variation characterized by very low densities in winter (Ouldessaib et al., 1998).

The structure of the copepod community along the Cintra Bay was dominated by neritic marine species, characterized by high spatial and seasonal variability of their abundances. In autumn 2015, *E. acutifrons* and three species of Acartiidae (*A. clausi*, *A. tonsa* and *A. bifilosa*) accounted for the majority of adult copepods while in spring 2016, *O. nana* largely dominated the copepod community. In the spring, *A. clausi* species was the only representative of Acartiidae with low abundance but with a wide spatial distribution in both seasons. Generally, marine forms of copepod communities, whose structure depends on the environmental characteristics of each site and the sampling period, dominated in different areas along the Moroccan Atlantic coast (Aittalborjt et al., 2016; Badsi et al., 2010; Ouldessaib et al., 1998; Youssara et al., 2004). The coexistence of several congeneric species of *Acartia* is particularly linked to variations in temperature and salinity (Brugnano et al., 2011; Conover, 1956; Gutkowska et al., 2018; Herman et al., 1968; Paturej and Kruk, 2011; Paturej and Gutkowska et al., 2015; Peck et al., 2015; Sage and Herman, 1972). Along the northwestern African coast, *A. clausi* is reported as a common species in marine and coastal areas cohabiting with other congeners (Ait-Talborjet et al., 2016;Berraho et al., 2016; Boucher, 1982; El Khalki and Moncef, 2007; Ndour et al., 2018; Ouldessaib et al., 1998; Salah, 2013; Somoue et al., 2005; Youssara et al., 2004; Zaafa et al., 2012). Furthermore, *A. tonsa* was mentioned only recently (in 1990s) in the marine environment, between Cape Bojador and Cape Blanc (26—21°N) (Somoue et al., 2005; Zizah et al., 2012) and currently in Dakhla Bay (24°N) (Berraho et al., 2018). However, *A. bifilosa* was not previously listed in copepod community studies on the Moroccan coast, although its presence is mentioned in this region by Razouls et al. (2005—2018). According to Ruiz et al. (1997), the occurrence of invasive species of zooplankton is increasing at an alarming rate in marine and estuarine systems and it is often associated with ship ballast waters or release by aquaculture, fisheries or pet industries. It is the case of *A. tonsa*, which appeared in Europe in the first half of the 20th century and progressively colonized European seas and estuaries. The species was possibly introduced from the northern Atlantic coast of America (Chaalali et al., 2013; David et al., 2007). Similarly, recent studies have reported the presence of this species in brackish Nigerian waters (southern West Africa) (Nkwoji et al., 2010; Wokoma, 2016), probably due to the same cause. In contrast, since its description by Giesbrecht (1881) from samples collected at Kiel (Germany), *A. bifilosa* has been reported as an autochthonous species from temperate and North Atlantic, characteristic of brackish and estuarine systems (Hirst and Castro-Longoria, 1998). There is no monitoring of planktonic communities in coastal areas of northwest Africa, and therefore it impossible to state the origin and date the appearance of some species. This is the case of Cintra Bay, where this first inventory of copepod species allowed the identification of a species of the genus *Tigriopus*, not previously mentioned in the Northwest African region. This genus is reported to be highly speciose and generally restricted to high intertidal and supralittoral rock pools worldwide that are naturally fragmented with low connectivity among populations (Altermatt et al., 2012; Davenport et al., 1997). The northern tip of the bay is a flood-prone peninsula extending for 2 miles to the southwest and ending in sandy rocks and a natural reef. It protects the entire northern extremity of the bay, characterized by shallower depths (less than 5 m) and low marine hydrodynamic (Hilmi et al., 2017; Makaoui et al., 2017). All these characteristics are probably favorable for the population development of *Tigriopus* sp., which must be confirmed by further studies.

Cintra Bay is largely open to the Atlantic Ocean, which provides abiotic and biotic characteristics largely influenced by the upwelling and the general circulation of the offshore water masses, which explains the high spatial and temporal variability of temperature and chlorophyll-*a*. This also implies a variability in the structure and abundance of zooplankton, illustrated particularly by the high variability of copepod diversity indices (H' and S) which showed a clear separation between the open part and the coastal part of the Bay. In addition, the CCA results highlighted the significant role of temperature and chlorophyll-*a* in structuring zooplankton communities and particularly the dominant groups: copepods and tintinnids. Generally, the main spatial and seasonal gradients of zooplankton were associated with temperature and food availability (Benítez-Díaz Mirón et al., 2014; Tackx et al., 2004; Terbiyik Kurt and Polat, 2015). This is the case of radiolarians, located mainly in the southern part of Cintra Bay, at high water temperatures, and cirriped larvae, significantly correlated with low water temperatures. The involvement of other environmental factors in structuring the zooplankton community and abundance is related to the margin variation of each parameter, the taxon tolerance margins and the taxonomic scale considered. In Cintra Bay, salinity contributed the least to the ordination of zooplankton but was a strong contributing factor for some copepod species with other factors. However, salinity has been found to be a major structuring factor in the composition and distribution of zooplankton taxa in coastal areas subjected to the freshwater input and/or anthropogenic activities (Benítez-Díaz Mirón et al., 2014; Brucet et al., 2009; Etilé et al., 2009; Montoya-Maya and Strydom, 2009; Nkwoji et al., 2010; Prado et al., 2017). This is likely to increase further in light of global-warming (Brucet et al., 2010). The salinity range recorded during both study periods in Cintra Bay (36.2—37.7 psu) indicated a high influence of open ocean waters and relatively low variability and hence, exerted a negligible effect in structuring zooplankton.

According to the indicator species analysis, the copepod structure was characterized by a wide diversity in autumn, with *E. acutifrons*, *P. parvus*, *C. arcuicornis*, *C. typicus* and the three species of Acartiidae (*A. clausi*, *A. tonsa* and *A. bifilosa*) contributing significantly to this structure. The CCA analysis showed a wide tolerance of these species to the environmental parameters with a highly significant correlation with chlorophyll-*a*. However, the three species of Acartiidae had a differential behavior with respect to some environmental parameters. *A. clausi* is a perennial species with a succession of peak abundances, whose amplitude varies during an annual cycle (Ouldessaib et al., 1998; Youssara et al., 2004). This

succession is linked to food availability that could act as a limiting factor and determine the duration of each or any stage and hence affect the total generation length (Christou and Verriopoulos, 1993). *Acartia tonsa* and *A. bifilosa* were reported as a summer-autumn species in Mediterranean lagoons and many North European estuaries (Brugnano et al., 2011; David et al., 2007; Uriarte and Villate, 2005). They are able to produce resting eggs under unfavorable conditions (Castro-Longoria, 2003; Katajisto, 2003; Peck et al., 2015).

The indicator species analysis highlighted the species poorly represented and only recorded in the spring (*E. elongatus*, *M. rosea*, *O. similis* and *T. stylifera*), showing no significant correlation with environmental parameters. These four species, whose abundance is widely fluctuating, have been reported in both offshore and coastal waters of the Atlantic coast of Morocco. *T. stylifera* and *O. similis* are the most commonly encountered throughout the year, with high abundances in spring and autumn-winter, respectively, whereas the presence of *E. elongatus* and *M. rosea* is generally sporadic (Ouldessaib et al., 1998; Somoue et al., 2005; Youssara et al., 2004; Zizah et al., 2012). The succession of species displays different spatial and/or seasonal patterns, suggesting differences in their ecological traits (Beşiktepe et al., 2015; Siokou-Frangou et al., 2010).

In conclusion, this study showed that the structure and abundance of zooplankton taxa in Cintra Bay is closely related to the environmental conditions that were mainly driven by the bay configuration and the regional hydrodynamics, particularly the upwelling, which was more intense in autumn. This coastal ecosystem could host different activities (aquaculture, industry, tourism, etc.), the implementation of which requires knowledge of the abiotic and biotic components and their spatio-temporal variations. In addition, Cintra Bay is part of a large marine area considered to be a spawning ground for fish species, particularly sardine, which is the dominant species of the Moroccan pelagic fishery. Thus, this study is a first step toward better knowledge of the planktonic biodiversity in this region.

Acknowledgements

This work was carried out in the context of the oceanographic program of the Moroccan coastal sites undertaken by the National Institute of Fisheries Research. The authors thank all team members who participated in the surveys, particularly the staff of the Regional INRH Centre of Dakhla. The authors would also like to thank the editor and the reviewers for their useful comments and N. Valerio for the linguistic revision.

References

Abdul, W.O., Adekoya, E.O., Ademolu, K.O., Omoniyi, I.T., Odulate, D.O., Akindokun, T.E., Olajide, A.E., 2016. The effects of environmental parameters on zooplankton assemblages in tropical coastal estuary, South-west, Nigeria. Egypt. J. Aquat. Res. 42 (3), 281—287, http://dx.doi.org/10.1016/j.ejar.2016.05.005.

Ait-talborjt, E., Hafidi, N., El ouizgani, H., 2016. Study of plankton communities in the Imessouane Bay. Int. J. Sci. 30 (5), 204—214.

Altermatt, F., Bieger, A., Morgan, S.G., 2012. Habitat characteristics and metapopulation dynamics of the copepod *Tigriopus californicus*. Mar. Ecol. Prog. Ser. 468, 85—93, http://dx.doi.org/10.3354/meps09994.

Anton-Pardo, M., Armengol, X., 2012. Effects of salinity and water temporality on zooplankton community in coastal Mediterranean ponds. Estuar. Coast. Shelf Sci. 114, 93—99.

Badsi, H., Ali, H.O., Loudiki, M., Hafa, M.E., Chakli, R., Aamiri, A., 2010. Ecological factors affecting the distribution of zooplankton community in the Massa Lagoon (Southern Morocco). Afr. J. Environ. Sci. Technol. 4 (11), 751—762.

Benazzouz, A., Demarcq, H., González-Nuevo, G., 2015. Changes and trends of the upwelling intensity in the Canary Current Large Marine Ecosystem. In: Valdés, L., Déniz-González, I. (Eds.), Oceanographic and Biological Features in the Canary Current Large Marine Ecosystem. IOC-UNESCO, IOC Technical Series 115, Paris, 321—330.

Benazzouz, A., Mordane, S., Orbi, A., Chagdali, M., Hilmi, K., Atillah, A., Pelegrí, J.L., Demarcq, H., 2014. An improved coastal upwelling index from sea surface temperature using satellite-based approach — the case of the Canary Current upwelling system. Cont. Shelf Res. 81, 38—54, http://dx.doi.org/10.1016/j.csr.2014.03.012.

Benítez-Díaz Mirón, M.I., Castellanos-Páez, M.E., Garza-Mouriño, G., Ferrara-Guerrero, M.J., Pagano, M., 2014. Spatiotemporal variations of zooplankton community in a shallow tropical brackish lagoon (Sontecomapan, Veracruz, Mexico). Zool. Stud. 53 (59), 1—18.

Berline, L., Siokou-Frangou, I., Marasovic´, O., Fernández de Puelles, M.L., Mazzocchi, M.G., Assimakopoulou, G., Zervoudaki, S., Fonda Umani, S., Conversi, A., Garcia-Comas, C., Ibanez, F., Gasparini, S., Stemmann, L., Gorsky, G., 2012. Intercomparison of six Mediterranean zooplankton time series. Prog. Oceanogr. 97, 76—91.

Berraho, A., 2007. Relations spatialisées entre milieu et ichtyoplancton des petits pélagiques de la côte Atlantique Marocaine (Zones central et sud). (Ph.D. thesis). Mohammed V Univ., Rabat, Morocco, 161 pp.

Berraho, A., Abdelouahab, H., Charib, S., Essarraj, S., Larissi, J., Abdellaoui, B., Christou, E.D., 2016. Copepod community along the Mediterranean coast of Morocco (Southwestern Alboran Sea) during spring. Medit. Mar. Sci. 17 (3), 661—665, http://dx.doi.org/10.12681/mms.1733.

Berraho, A., Abdelouahab, H., Larissi, J., Baibai, T., Charib, S., Idrissi, M., Belbchir, Y., Ettahiri, O., Hilmi, K., 2018. Biodiversity and spatio-temporal variability of copepods community in Dakhla Bay (southern Moroccan coast). Reg. Stud. Mar. Sci.(in press), http://dx.doi.org/10.1016/j.rsma.2018.10.005.

Beşiktepe, Ş., Tang, K.W., Mantha, G., 2015. Seasonal variations of abundance and live/dead compositions of copepods in Mersin Bay, northeastern Levantine Sea (eastern Mediterranean). Turk. J. Zool. 39, 494—506, http://dx.doi.org/10.3906/zoo-1405-23.

Boucher, J., 1982. Peuplement de copépodes des upwellings côtiers nord-ouest africains. I. Composition faunistique et structure démographique. Oceanol. Acta 5 (1), 49—62.

Brochier, T., Ramzi, A., Lett, C., Machu, E., Berraho, A., Fréon, P., Hernandéz-Leon, S., 2008. Modelling sardine and anchovy ichthyoplankton transport in the Canary Current System. J. Plankton Res. 30 (10), 1133—1146.

Brucet, S., Boix, D., Gascón, S., Sala, J., Quintana, X.D., Badosa, A., Søndergaard, M., Lauridsen, T.L., Jeppesen, E., 2009. Species richness of crustacean zooplankton and trophic structure of brackish lagoons in contrasting climate zones: north temperate Denmark and Mediterranean Catalonia (Spain). Ecography 32, 692—702, http://dx.doi.org/10.1111/j.1600-0587.2009.05823.x.

Brucet, S., Boix, D., Quintana, X.D., Jensen, E., Nathansen, L.W., Trochine, C., Meerhoff, M., Gascón, S., Jeppesena, E., 2010. Factors influencing zooplankton size structure at contrasting temperatures in coastal shallow lakes: implications for effects of climate change. Limnol. Oceanogr. 55 (4), 1697—1711, http://dx.doi.org/10.4319/lo.2010.55.4.1697.

Brugnano, C., D'Adamo, R., Fabbrocini, A., Granata, A., Zagami, G., 2011. Zooplankton responses to hydrological and trophic variability in a Mediterranean coastal ecosystem (Lesina Lagoon, South Adriatic Sea). Chem. Ecol. 27 (5), 461—480, http://dx.doi.org/10.1080/02757540.2011.579962.

Castro-Longoria, E., 2003. Egg production and hatching success of four *Acartia* species under different temperature and salinity regimes. J. Crust. Biol. 23 (2), 289—299.

Chaalali, A., Beaugrand, G., Raybaud, V., Goberville, E., David, V., Boët, P., Sautour, B., 2013. Climatic facilitation of the colonization of an estuary by *Acartia tonsa*. PLOS ONE 8, e74531, http://dx.doi.org/10.1371/journal.pone.0074531 1—11.

Chaudhary, C., Saeedi, H., Costello, M.J., 2016. Bimodality of latitudinal gradients in marine species richness. Trends Ecol. Evol. 31 (9), 670—676, http://dx.doi.org/10.1016/j.tree.2016.06.001.

Christou, E.D., Verriopoulos, G.C., 1993. Analysis of the biological cycle of *Acartia clausi* (Copepoda) in a meso-oligotrophic coastal area of the eastern Mediterranean Sea using time-series analysis. Mar. Biol. 115, 643—651.

Conover, R.J., 1956. Biology of *Acartia clausi* and *A. tonsa*. Bull. Bingham Oceanogr. Collect. 15, 156—233.

Crawford, D.W., Purdie, D.A., Lockwood, A.P.M., Weissman, P., 1997. Recurrent red-tides in the Southampton water estuary caused by the phototrophic ciliate *mesodinium rubrum*. Estuar. Coast. Shelf Sci. 45, 799—812.

Cropper, T.E., Hanna, E., Bigg, G.R., 2014. Spatial and temporal seasonal trends in coastal upwelling off Northwest Africa, 1981—2012. Deep-Sea Res. Pt. I 86, 94—111, http://dx.doi.org/10.1016/j.dsr.2014.01.007.

Dash, S., Behera, R.K., Mohapatra, P.K., Sarangi, R.K., Raut, D., Pati, A., Patnaik, L., 2017. Species composition of microzooplankton Tintinnid from the coastal waters of Digha, Bay of Bengal. Environ. Monit. Assess. 189 (6), 258, http://dx.doi.org/10.1007/s10661-017-5961-z.

Davenport, J., Barnett, P.R.O., McAllen, J.R., 1997. Environmental tolerances of three species of the Harpacticoid copepod genus *Tigriopus*. J. Mar. Biol. Assoc. U. K. 77, 3—16.

David, V., Sautour, B., Chardy, P., 2007. Successful colonization of the calanoid copepod *Acartia tonsa* in the oligo-mesohaline area of the Gironde estuary (SW France) — natural or anthropogenic forcing? Estuar. Coast. Shelf Sci. 71 (3—4), 429—442, http://dx.doi.org/10.1016/j.ecss.2006.08.018.

Davies, O.A., 2009. Spatio-temporal distribution, abundance and species composition of zooplankton of Woji-okpoka Creek, Port Harcourt, Nigeria. Res. J. Appl. Sci. Eng. Technol. 1 (2), 14—34.

Demarcq, H., Somoue, L., 2015. Phytoplankton and primary productivity off Northwest Africa. In: Valdés, L., Déniz-González, I. (Eds.), Oceanographic and Biological Features in the Canary Current Large Marine Ecosystem. IOC-UNESCO, IOC Technical Series 115, Paris, 161—174.

Dolan, J.R., 2010. Morphology and ecology in tintinnid ciliates of the marine plankton: correlates of lorica dimensions. Acta Protozool. 49, 235—344.

Dolan, J.R., Claustre, H., Carlotti, F., Plounevez, S., Moutin, T., 2002. Microzooplankton diversity: relationships of tintinnid ciliates with resources, competitors and predators from the Atlantic Coast of Morocco to the Eastern Mediterranean. Deep-Sea Res. Pt. I 49, 1217—1232.

Dube, A., Jayaraman, G., Rani, R., 2010. Modelling the effects of variable salinity on the temporal distribution of plankton in shallow coastal lagoons. J. Hydro. Environ. Res. 4 (3), 199—209, http://dx.doi.org/10.1016/j.jher.2010.03.003.

Dufrêne, M., Legendre, P., 1997. Species assemblages and indicator species: the need for a flexible asymmetrical approach. Ecol. Monogr. 67, 345—366.

El-Damhougy, K.A., El-Sayed, A.A., Aboul Ezz, S.M., Abu Husein, M. S., 2017. Tintinnida (Ciliophora) as bio-indicator for certain pollutants at al-max area, Alexandria. Egypt. Int. J. Fish. Aquat. Stud. 5 (3), 297—305.

El Khalki, A., Moncef, M., 2007. Etude du peuplement de copépodes de l'estuaire de l'Oum er Rbia (côte Atlantique du Maroc): effets des marées et des lâchers de barrages. Leban. Sci. J. 8 (1), 3—18.

Emir Akbulut, N., Tavşanoğlu, Ü.N., 2018. Impacts of environmental factors on zooplankton taxonomic diversity in coastal lagoons in Turkey. Turk. J. Zool. 42, 68—78, http://dx.doi.org/10.3906/zoo-1704-37.

Etilé, R.N., Kouassi, M.A., Aka, M.N., Pagano, M., N'douba, V., Kouassi, N.J., 2009. Spatio-temporal variations of the zooplankton abundance and composition in a West African tropical coastal lagoon (Grand-Lahou, Côte d'Ivoire). Hydrobiologia 624 (1), 171—189, http://dx.doi.org/10.1007/s10750-008-9691-7.

Etilé, R.N., Kouassi, M.A., Pagano, M., Yao, S.S., Aka, M.N., N'douba, V., 2015. Diel variation of zooplankton community composition, abundance and biomass in a West African tropical coastal Lagoon (Grand-Lahou, Côte d'Ivoire). Int. J. Agric. Innov. Res. 3 (5), 2319-2473.

Ettahiri, O., Berraho, A., Houssa, R., Ramzi, A., Somoue, L., Zizah, S., Machu, E., 2012. Characteristics of the spawning habitats of sardine, *Sardina pilchardus*, off the Moroccan Atlantic coast (21°N—26°N). FAO, Pêch. Aquac. 18, 157—186.

Fernandez de Puelles, M.L.F., Gras, D., Hernandez-Leon, S., 2003. Annual cycle of zooplankton biomass, abundance and species composition in the neritic area of the Balearic Sea, Western Mediterranean. Mar. Ecol. 24, 123—139.

Gao, Q., Xu, Z., Zhuang, P., 2008. The relation between distribution of zooplankton and salinity in the Changjiang Estuary. Chin. J. Oceanol. Limnol. 26 (2), 178—185, http://dx.doi.org/10.1007/s00343-008-0178-1.

Gaudy, R., Champalbert, G., 1998. Space and time variations in zooplankton distribution south of Marseilles. Oceanol. Acta 21, 793—802.

Giesbrecht, W., 1881. Vorlaufige Mitteilung aus einer Arbeit liber die freilebenden Copepoden des Kieler Hafens. Zool. Anz. 4, 254—258.

Gozdziejewska, A., Karpowicz, M., 2013. Dynamics of zooplankton structure in three small water bodies on the area of an agritourism farm. Teka. Kom. Ochr. Kszt. Środ. Przyr. — OL PAN 10, 102—114.

Gutkowska, A., Paturej, E., Koszalka, J., 2018. Does the location of coastal brackish waters determine diversity and abundance of zooplankton assemblages? Turk. J. Zool. 42, 230—244, http://dx.doi.org/10.3906/zoo-1705-22.

Herman, S.S., Mihursky, J.A., Mc Erlan, A.J., 1968. Zooplankton and environmental characteristics of the Patuxent River estuary 1963—1965. Chesap. Sci. 9 (2), 67—82.

Hilmi, K., Makaoui, A., Ettahiri, O., Idrissi, M., Abdellaoui, B., Agouzouk, A., Baibai, T., Ait Chattou, M., Bessa, I., Bouksim, H., 2017. Circulation Marine de la baie de Cintra (Sud du Maroc) par Modèle Hydrodynamique 2D. Eur. Sci. J. 13 (12), 175—194, http://dx.doi.org/10.19044/esj.2017.v13n12p175.

Hirst, A.G., Castro-Longoria, E., 1998. *Acartia bifilosa* (Copepoda: Calanoida): a clarification of the species and its varieties inermis and intermedia. J. Plankton Res. 20 (6), 1119—1130.

Jakhar, P., 2013. Role of phytoplankton and zooplankton as health indicators of aquatic ecosystem (a review). Int. J. Innov. Res. Stud. 2 (12), 490—500.

Jose, E.C., Furio, E.F., Borja, V.M., Gatdula, N.C., Santos, M.D., 2015. Zooplankton composition, abundance and its relationship with physico-chemical parameters in Manila Bay. Oceanography 3 (1), 1—6, http://dx.doi.org/10.4172/2332-2632.1000136.

Joyce, C.B., Vina-Herbon, C., Metcalfe, D.J., 2005. Biotic variation in coastal water bodies in Sussex, England: implications for saline lagoons. Estuar. Coast. Shelf Sci. 65, 633—644.

Katajisto, T., 2003. Development of *Acartia bifilosa* (Copepoda: Calanoida) eggs in the northern Baltic Sea with special reference to dormancy. J. Plankton Res. 25, 357—364.

Keister, J.E., Bonnet, D., Chiba, S., Johnson, C.L., Mackas, D.L., Escribano, R., 2012. Zooplankton population connections, community dynamics, and climate variability. ICES J. Mar. Sci. 69, 347—350.

Krsinic, F., Bojanic, D., Precali, R., Kraus, R., 2007. Quantitative variability of the copepod assemblages in the northern Adriatic Sea from 1993 to 1997. Estuar. Coast. Shelf Sci. 74 (3), 528—538, http://dx.doi.org/10.1016/j.ecss.2007.05.036.

Kudari, V.A., Kanamadi, R.D., 2008. Impact of changed trophic status on the zooplankton composition in six water bodies of Dharwad district, Karnataka state (South India). Environ. Monit. Assess. 144 (1-3), 301—313, http://dx.doi.org/10.1007/s10661-007-9993-7.

Lathuilière, C., Echevin, V., Lévy, M., 2008. Seasonal and intraseasonal surface chlorophyll-*a* variability along the northwest African coast. J. Geophys. Res. 113 (C05007), 1—12, http://dx.doi.org/10.1029/2007JC004433.

Makabe, R., Tanimura, A., Fukuchi, M., 2012. Comparison of mesh size effects on mesozooplankton collection efficiency in the Southern Ocean. J. Plankton Res. 34 (5), 432—436, http://dx.doi.org/10.1093/plankt/fbs014.

Makaoui, A., Agouzouk, A., Baibai, T., Idrissi, M., Larissi, J., Bessa, I., Obad, S., Ettahiri, O., Ait Chattou, M., Hilmi, K., 2017. Caractéristiques hydro sédimentaires de la baie de Cintra (sud-Maroc). Int. J. Adv. Res. 5 (7), 2055—2068, http://dx.doi.org/10.21474/IJAR01/4942.

Makaoui, A., Orbi, A., Hilmi, K., Zizah, S., Larissi, J., Talbi, M., 2005. L'upwelling de la côte Atlantique du Maroc entre 1994 et 1998. C. R. Geosci. 337, 1518—1524.

Molinero, J.C., Ibanez, F., Souissi, S., Buecher, E., Dallot, S., Nival, P., 2008. Climate control on the long-term anomalous changes of zooplankton communities in the Northwestern Mediterranean. Global Change Biol 14 (1), 11—26, http://dx.doi.org/10.1111/j.1365-2486.2007.01469.x.

Montoya-Maya, P.H., Strydom, N.A., 2009. Zooplankton composition, abundance and distribution in selected south and west coast estuaries in South Africa. Afr. J. Aquat. Sci. 34 (2), 147—157, http://dx.doi.org/10.2989/AJAS.2009.34.2.5.892.

Motoda, S., 1959. Devices of Simple Plankton Apparatus. Memoirs, vol. 7. Faculty of Fisheries, Hokkaido Univ, 73—94.

Ndour, I., Berraho, A., Fall, M., Ettahiri, O., Sambe, B., 2018. Composition, distribution and abundance of zooplankton and ichthyoplankton along the Senegal-Guinea maritime zone (West Africa). Egypt. J. Aquat. Res. 44 (2), 109—124, http://dx.doi.org/10.1016/j.ejar.2018.04.001.

Nichols, J.H., Thompson, A.B., 1991. Mesh selection of copepodite and nauplius stages of four calanoid copepod species. J. Plankton Res. 13, 661—671.

Nkwoji, J.A., Onyema, I.C., Igbo, J.K., 2010. Wet season spatial occurrence of phytoplankton and zooplankton in Lagos lagoon, Nigeria. Sci. World J. 5 (2), 7—14.

Ouldessaib, E.T., El Khalki, M., Moncef, M., 1998. Etude qualitative et quantitative du peuplement de Copépodes de la lagune de Oualidia (côte atlantique du Maroc). Mar. Life 8 (1—2), 35—43.

Paturej, E., 2006. Assessment of the trophic state of the coastal lake Gardno based on community structure and zooplankton-related indices. Electron. J. Pol. Agric. Univ. Ser. Biol. 9 (2).

Paturej, E., Gutkowska, A., 2015. The effect of salinity levels on the structure of zooplankton communities. Arch. Biol. Sci. 67 (2), 483—492, http://dx.doi.org/10.2298/ABS140910012P.

Paturej, E., Gutkowska, A., Koszalka, J., Bowszys, M., 2017. Effect of physicochemical parameters on zooplankton in the brackish, coastal Vistula Lagoon. Oceanologia 59 (1), 49—56, http://dx.doi.org/10.1016/j.oceano.2016.08.001.

Paturej, E., Kruk, M., 2011. The impact of environmental factors on zooplankton communities in the Vistula Lagoon. Oceanol. Hydrobiol. Stud. 40 (2), 37—48, http://dx.doi.org/10.2478/s13545-011-0015-6.

Peck, N., Peters, J., Diekmann, R., Laakmann, S., Renz, J., 2015. Interactive effects of temperature and salinity on population dynamics of the calanoid copepod *Acartia tonsa*. J. Plankton Res. 37 (1), 197—210, http://dx.doi.org/10.1093/plankt/fbu093.

Peterson, W., 1998. Life cycle strategies of copepods in coastal upwelling zones. J. Mar. Syst. 15, 313—326.

Pinto-Coelho, R.M., Giani, A., Morais Jr., C.A., Carvalho Jr., E.R., Bezerra-neto, J.F., 2005. The nutritional status of zooplankton in a tropical reservoir: effects of food quality and community structure. Braz. J. Biol. 65 (2), 313—324.

Prado, P., Caiola, N., Ibáñez, C., 2017. Water management alters phytoplankton and zooplankton communities in Ebro delta coastal lagoons. Limnetica 36 (1), 113—126, http://dx.doi.org/10.23818/limn.36.09.

Rakshit, D., Sarkar, S.K., Satpathy, K.K., Ganesh, P.S., Godhantaraman, N., Biswas, J.K., 2016. Diversity and distribution of microzooplankton tintinnid (Ciliata: Protozoa) in the core region of Indian Sundarban WETLAND. Clean — Soil Air Water 44 (10), 1278—1286, http://dx.doi.org/10.1002/clen.201500781.

Razouls, C., de Bovée, F., Kouwenberg, J., Desreumaux, N., 2005—2018. Diversity and Geographic Distribution of Marine Planktonic Copepods. Sorbonne Univ., CNRS, http://copepodes.obs-banyuls.fr/en.

Ruiz, G.M., Carlton, J.T., Grosholz, E.D., Hines, A.H., 1997. Global invasions of marine and estuarine habitats by non-indigenous species: mechanisms, extent, and consequences. Am. Zool. 37, 621—632.

Sage, L.E., Herman, S.S., 1972. Zooplankton of the Sandy Hook Bay area. N. J. Chesap. Sci. 13 (1), 29—39.

Salah, S., 2013. Structure spatio-temporelle du zooplancton dans les deux filaments d'upwelling Cap Ghir et Cap Juby. Effet de la dynamique des filaments sur la dispersion des copépodes. (Ph.D. thesis). Hassan II Univ., Casablanca, Morocco, 277 pp.

Shannon, C., Wiener, E., 1949. The Mathematical Theory of Communications. Urbana Illinois Press, 117 pp.

Siokou-Frangou, I., 1996. Zooplankton annual cycle in a Mediterranean coastal area. J. Plankton Res. 18, 203—223.

Siokou-Frangou, I., Christaki, U., Mazzocchi, M.G., Montresor, M., Ribera d'Alcalá, M., Vaqué, D., Zingone, A., 2010. Plankton in the open Mediterranean Sea: a review. Biogeosciences 7, 1543—1586, http://dx.doi.org/10.5194/bg-7-1543-2010.

Somoue, L., Elkhiati, N., Ramdani, M., Lam, T., 2005. Abundance and structure of copepod communities along the Atlantic coast of southern Morocco. Acta Adriat. 46 (1), 63—76.

Stoecker, D.K., 2013. Predators of tintinnids. In: Dolan, J.R., Montagnes, D.J.S., Agatha, S., Coats, W.D., Stoecker, D.K. (Eds.), The Biology and Ecology of Tintinnid Ciliates: Models for Marine Plankton. Wiley-Blackwell, West Sussex, 122—144.

Tackx, M.L.M., De Pauw, N., Mieghem, R.V., Azénar, F., Hannouti, A., Damme, S.V., Fiers, F., Daro, N., Meire, P., 2004. J. Plankton Res. 26 (2), 133—141, http://dx.doi.org/10.1093/plankt/fbh016.

Terbiyik Kurt, T., Polat, S., 2015. Zooplankton abundance, biomass, and size structure in the coastal waters of the northeastern Mediterranean Sea. Turk. J. Zool. 39, 378—387, http://dx.doi.org/10.3906/zoo-1311-14.

Uriarte, I., Villate, F., 2005. Differences in the abundance and distribution of copepods in two estuaries of the Basque coast (Bay of Biscay) in relation to pollution. J. Plankton Res. 27 (9), 863—874, http://dx.doi.org/10.1093/plankt/fbi059.

Uysal, Z., Shmeleva, A.A., 2012. Species composition, abundance and biomass of Copepoda in plankton of Northern Levantine Basin (Eastern Mediterranean). Crustaceana 85, 909—935.

Verheye, H.M., Hutchings, L., Peterson, W.T., 1991. Life history and population maintenance strategies of *Calanoides carinatus* (Copepoda: Calanoida) in the southern Benguela ecosystem. Afr. J. Mar. Sci. 11 (1), 179—191, http://dx.doi.org/10.2989/025776191784287600.

Wang, S., Xie, P., Wu, S., Wu, A., 2007. Crustacean zooplankton distribution patterns and their biomass as related to trophic indicators of 29 shallow subtropical lakes. Limnologica 37 (3), 242—249, http://dx.doi.org/10.1016/j.limno.2007.02.002.

Wang, Y., Zhang, W., Lin, Y., Zheng, L., Cao, W., Yang, J., 2014. Spatial and seasonal variations of large tintinnid ciliates in Shenhu Bay of China. Oceanol. Hydrobiol. Stud. 43 (3), 292—302, http://dx.doi.org/10.2478/s13545-014-0144-9.

Wokoma, O.A.F., 2016. Zooplankton species composition and abundance in the brackish water axis of Sombreiro River, Niger Delta. Appl. Sci. Rep. 15 (1), 31—34.

Youssara, F., Gaudy, R., Moukrim, A., Moncef, M., 2004. Variations spatio-temporelles du mésozooplancton de la région d'Agadir (Maroc) entre mai 1999 et décembre 2000. Mar. Life 14 (1—2), 3—18.

Zaafa, A., Ettahiri, O., Elkhiati, N., Blahen, M., Berraho, A., Somoue, L., Elghrib, H., 2012. Variability of spatial and temporal distribution of marine zooplankton communities in relation with environmental parameters in Tangier and M'Diq (Gibraltar strait) regions. J. Mater. Environ. Sci. 3 (2), 262—269.

Zakaria, H.Y., Radwan, A.A., Said, M.A., 2007. Influence of salinity variations on zooplankton community in El-Mex bay, Alexandria, Egypt. Egypt. J. Aquat. Res. 33 (2), 52—67.

Zizah, S., Ettahiri, O., Salah, S., Yahyaoui, A., Ramdani, M., 2012. Evolution spatio-temporelle des abondances zooplanctoniques au large de la côte atlantique marocaine entre Cap Boujdour (26°30′N) et Cap Blanc (21°N). Bull. Inst. Sci. Sect. Sci. Vie 34 (2), 79—94.

Oceanologia (2019) 61, 384—394

Available online at www.sciencedirect.com

ScienceDirect

journal homepage: www.journals.elsevier.com/oceanologia/

ORIGINAL RESEARCH ARTICLE

Bedload transport in the Vistula River mouth derived from dune migration rates, southern Baltic Sea

Aliaksandr Lisimenka [a,b,*], **Adam Kubicki** [c]

[a] *Maritime Institute in Gdańsk, Gdańsk, Poland*
[b] *Institute of Oceanology, Polish Academy of Sciences, Sopot, Poland*
[c] *GEO Ingenieurservice Nord-West, Wilhelmshaven, Germany*

Received 3 December 2018; accepted 27 February 2019
Available online 15 March 2019

KEYWORDS
Sand dune migration;
Bedload transport;
Vistula River mouth

Summary In this paper, bedload sediment transport to the Baltic Sea in the main Vistula River mouth (Przekop Wisły) is estimated. For the first time in this area, investigations were performed based on the non-invasive measurement techniques with the using of hydroacoustic tools. Repeated bathymetric surveys were carried out using a multibeam echosounder for the period with hydrological conditions close to that of the long-term mean annual water discharge. Quantification of the bedload transport, as a main factor for the subaqueous Vistula delta development, involved applying the bedform tracking technique, and estimating the dune celerity by analysing the cross-correlation functions of bed elevation profiles (BEPs). The BEPs were obtained along two transects of 500 m in length situated in two different morphological parts of the river mouth — in the "shallow" and in the "deep" sites located upstream and downstream of the submerged sandbar, respectively. Contrarily to previous observations, the bedload transport was found to take place constantly. Moreover, a significant difference in a character of dune migration between the two sites of the investigated area was determined. The "shallow" dunes migrate 7 times faster (0.022 m/h) than the "deep" ones (0.003 m/h). Estimation of the daily bedload transport towards the Baltic Sea revealed values about 40.9 t/day and 8.4 t/day for "shallow" and "deep" sites, respectively. This result can probably indicate that a significant portion of sediments (ca. 80%) transported by the river during average hydrological conditions is deposited temporarily on the submerged sandbar, causing its growth.

* Corresponding author at: Maritime Institute in Gdańsk, Dlugi Targ 41/42, 80-830, Gdańsk, Poland. Tel.: (+48 58) 301-16-41; fax: (+48 58) 301-35-13.
E-mail address: sasha@im.gda.pl (A. Lisimenka).
Peer review under the responsibility of Institute of Oceanology of the Polish Academy of Sciences.

https://doi.org/10.1016/j.oceano.2019.02.003

1. Introduction

The phenomenon of sediment transport is one of the key processes taking place in marine and fluvial environments. Knowledge and understanding of sediment transport processes are particularly needed for water resource management to ensure the safety of navigation, to support hydrotechnical planning, and to minimise the risk of flooding.

In general, the total sediment load is divided into three components — bedload, suspended load and dissolved load (Bravard and Petit, 2009). The phenomenon of bedload transport is defined as the movement of sediment particles caused by their rolling, sliding and saltation along the bed in almost continuous contact with it, and is dominated by flow-induced drag forces, and by gravity forces acting on the particles (Van Rijn, 1993). It provides the major process linkage between the hydraulic and material conditions that govern river-channel morphology (Gomez, 2006). Although it is widely considered that bedload transport constitutes a relatively small percentage of the overall sediment transport budget — about 5% to 20% (Knighton, 1998), it forces the appearance and migration of bedforms on the bottom surface, and it plays a major role in controlling the bed morphology as well as the water body geometry as a whole. Similarly, Babiński (2005) pointed out that the suspended load is several times greater than the bedload transport with values commonly falling within the bounds 85–99% for suspended load, and 1–15% for bedload. He summarised that the proportion between suspended load and bedload depends on various factors such as the transport power of the river, the hydrological regime, the geological structure of the river basin, and human activity such as agriculture, industry, building construction, and river regulation.

Due to the diversity of the bedload transport mechanisms, there is no perfect method for quantification of fluvial bedload. The most commonly used are the bedload samplers, these, however, tend to interfere hydraulically with the neighbourhood of the sampling station, thus affecting the sampling results (Childers, 1999). Non-invasive methods, on the other hand, are based on bathymetry data-sets obtained by using hydroacoustic or optical methods. Having charted large river sections, a comparison of subsequent bathymetric surveys can be made. Through cut-fill volumetric calculations, one can assess the net export from the investigated sections, which is considered equal to the bedload transport (Hickin, 1995). Whenever bedforms are present on the seabed, and the identification of individual bedforms is possible in repetitive bathymetric data, one can also trace migration rates of subaqueous dunes (e.g. Kostaschuk et al., 1989).

First published data on bedload contribution into the total sediment transport at the Middle and the Lower Vistula were obtained with bedload samplers (Brański and Skibiński, 1968). Based on the author's estimation, in the case of hydrological conditions close to the mean annual water discharge ($Q_{Tczew} \approx 1000$ m^3/s), bedload transport constitutes up to about 30% of the total sediment transport (at the Tczew cross-section profile, see Fig. 1 for location). Later, based on measurements of sediment granulometry performed downstream of Tczew, and with calculations using different empirical equations, Manthey and Gilewski (1980) found that the annual bedload transport to the Baltic Sea amounted to 523,000 m^3 on average (during the 1965 hydrological year, with the mean annual water discharge $Q_{Tczew} = 1055$ m^3/s). Moreover, the author's assessment of bedload contribution into the total sediment transport

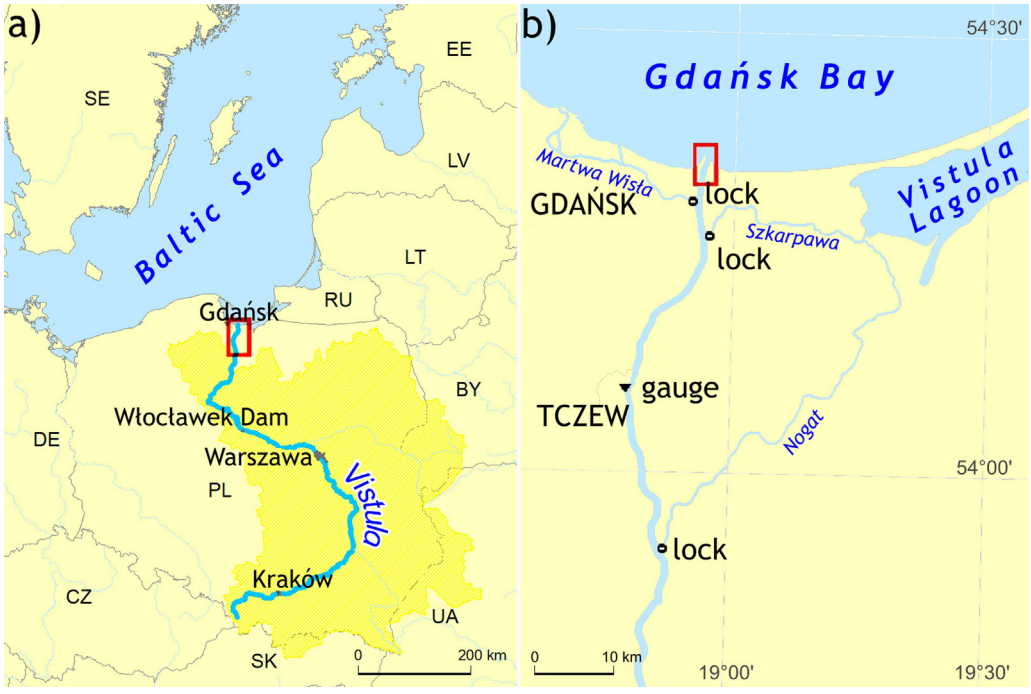

Figure 1 Location of the area of interest "Przekop Wisły" including (a) the Vistula River basin (in dark yellow), and (b) other Vistula arms closed by locks. (For interpretation of the references to color in this figure legend, the reader is referred to the web version of this article.)

revealed values ranging from 35.8% up to 49.2% (41% on average), with a clear trend of decrease downstream of the river. Recent studies were focused on better estimates of suspended sediment transport, finding evidently more important suspension transport share, which accounted for forming the Vistula prodelta (Damrat et al., 2013; Szymczak and Galińska, 2013; Zajączkowski et al., 2010).

This paper presents the results of investigations aimed at estimating the bedload transport in the main Vistula River mouth (Przekop Wisły). Based on data-sets obtained by repeated bathymetric surveys, the quantification of the bedload was performed by applying the bedform tracking technique and the estimation of the dune migration rate based on the data-set obtained by repeated bathymetric surveys. Unlike previous studies, in which bedload transport was not traceable on the river sections located several kilometres upstream of the investigated area, it was found that dunes migrate constantly all the way towards the river mouth even at low hydrological conditions. Moreover, the distinct character of sand dune migration at two different morphological parts of the Vistula outlet stretch was revealed.

2. Material and methods

2.1. Geographical setting

A bathymetric survey was performed in the main mouth of the Vistula River "Przekop Wisły" located in Polish coastal waters (Fig. 1). The Vistula (Wisła) is the largest river of the southern Baltic Sea and the most important source of sediments in the area. The total length of the river is 1047 km and its basin measures 194,000 km^2 (Fig. 1a, in dark yellow). The Vistula plays a dominant role with regards to the quantity of discharged fresh water flowing into the Gulf of Gdańsk. According to Majewski (2013), the average multiyear water outflow amounts to 33.3 km^3, supplying about 7% of fresh water to the Baltic Sea.

Due to the existence of locks controlling the water levels in the old channels of the Vistula (Nogat, Szkarpawa and Martwa Wisła, Fig. 1b), about 95% of the total Vistula water outflows into the Baltic Sea through this channel. The closest gauging station is located in Tczew 31.2 km upstream of the Vistula channel mouth (Fig. 1b). This gauge represents 99.92% of the Vistula catchment area (Augustowski, 1982). Based on operational data obtained from this gauging section (IMGW-PIB, 2017), the long-term (1921–2016) mean annual water discharge reaches 1026 m^3/s. The average daily water discharge, however, varies from 238 m^3/s in dry seasons up to the 9530 m^3/s during the flood in 1924.

The main river mouth "Przekop Wisły" is a cross-cut artificial channel with a total length of about 7 km, 400 m width, and temporarily up to 10 m water depth. Since the opening of the channel in 1895 (Makowski, 1995; Szymański, 1897a,b), the Vistula waters has brought hundreds of millions of tonnes of sediments into the Gulf of Gdańsk, creating a new river-mouth alluvial fan (Graniczny et al., 2004). Based on the morphodynamic model resulting from the bathymetric plans of the contemporary Vistula mouth area over the period of 1894–2000, Franz et al. (2005) and later Koszka-Maroń (2016) estimated that the volume of the sediment accumulated in the fan was more than about 133 million m^3. According to Pruszak et al. (2005), the Vistula carries 0.6–1.5 million m^3 of sediments annually, of which about 0.5 million m^3 deposits in the subaqueous delta, thus expanding the delta front. This was confirmed by investigations performed recently by Wróblewski et al. (2015). As reported by Pruszak and Szmytkiewicz (2015), river sediment accumulation was subjected mostly to significant reduction over the years. However, the river sediment accumulation had been reducing since the early years following the channel opening, from 2.4 mln m^3/year during the first twenty-five years to ca 0.2 mln m^3/year in recent years.

It should be noted that the character of the hydrology, and consequently the sediment transport in the Lower Vistula was significantly changed in October 1970, when the Włocławek Dam was completed (264 km upstream of the investigated area, Fig. 1a). From the hydrological point of view, the reservoir minimally reduced the volume of high water in the Vistula below the dam, but reduced very low water levels as well (Babiński and Habel, 2013). The authors estimated that the Włocławek Dam trapped the entire bedload carried from the upper river, and caught 42% of the suspended load, but also caused permanent erosion of the bed below the dam.

The most recent outcomes of granulometric analysis of grab samples collected in the area of interest revealed that the sediment particles were relatively even-sized, with coarse and/or medium-grained sands, quite well-sorted, with moderately negative skewness and a leptokurtic distribution (Rudowski et al., 2017). The authors could also establish that deposition of sediments was progressing, especially in its estuarial section, which impacted significantly on the river channel patency.

The most distinctive morphological feature of the "Przekop Wisły" bottom relief is a submerged sandbar which is situated along the western bank and elongated towards the middle of the river valley. It forms the last sediment deposit before the sediment sinks in the Vistula prodelta. Both the upstream and downstream neighbourhood of the sandbar are covered by complex patterns of subaqueous dunes that were investigated recently by Lisimenka and Kubicki (2017).

2.2. Hydrological regime of lower Vistula

The time-series of the Vistula River discharge values (Fig. 2) collected at the Tczew gauge in the period of the experiment from March and April 2015 revealed that, in general, the observed discharge values were relatively close to the long-term mean annual water outflow with some short-term events characterised by increased flow between 1100 and 1400 m^3/s and connected mainly with spring snowmelt and atmospheric precipitations.

In addition, an analysis of the meteorological conditions during the measurement campaign was performed. Based on the wind speed and wind direction data obtained from the numerical weather forecast model "High Resolution Limited Area Model" (HIRLAM; Cats and Wolters, 1996) for the point located in the Gulf of Gdańsk 2 km away to NE from the Vistula mouth, no storm surges and thus no backwaters phenomena were observed during the period of the survey (Fig. 3). During the surges caused by northerly winds, marine waters can penetrate the Vistula River valley along several kilometres (Pruszak and Szmytkiewicz, 2015).

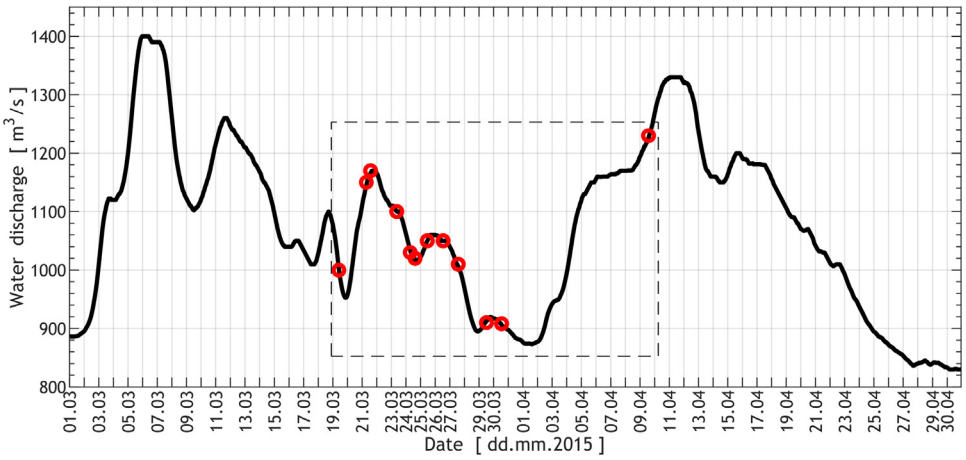

Figure 2 Hourly water discharges Q [m^3/s] (black curve) of the Vistula River at the Tczew gauge in the period between 01.03.2015 and 30.04.2015 (data source: operational data of the IMGW-PIB). Particular moments of time in a period between 19.03.2015 and 09.04.2015 when the repeated bathymetry measurements were performed are marked with red circles. (For interpretation of the references to color in this figure legend, the reader is referred to the web version of this article.)

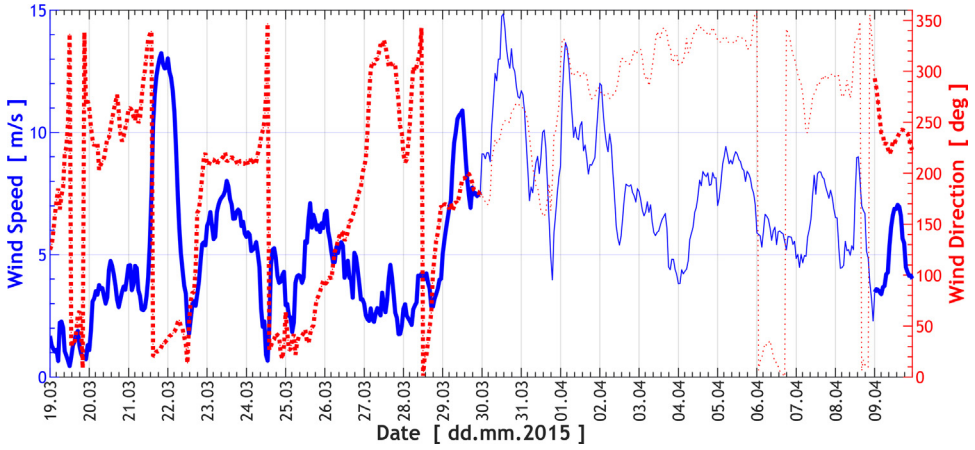

Figure 3 Time series of the wind speed (blue solid curve) and the wind direction (red dotted curve) obtained from the HIRLAM model in the period between 19.03.2015 and 09.04.2015. Period of time with a break in the measurements caused by unfavourable wind conditions in the area are marked by thin curves. (For interpretation of the references to color in this figure legend, the reader is referred to the web version of this article.)

2.3. *In-situ* measurements

The measurement campaign in the Vistula River mouth area was carried out in the period between 19th of March and 9th of April 2015. The bathymetry was mapped using the Reson SeaBat 7125 multibeam echosounder (MBES) operating at 400 kHz. The MBES provides 512 discrete sounding beams across the wide 128° swath with 1° along-track transmit beam width, and 0.5° across-track receive beam width. The sound velocity probe Reson SVP-70 was fixed to the MBES head, and the portable sound velocity profiler Reson SVP-15 was used to obtain the sound speed at the depth of the MBES draft, and through the water column, respectively. The positioning system DGPS RTK Trimble BX 982 together with the Ixsea Hydrins inertial navigation system were integrated with the MBES and SVPs using the QINSy data acquisition software package. The post-processing of the MBES raw data were performed in the QINSy Processing Manager according to the standard hydrographic procedures.

A series of bathymetric measurements were made along the central axis of the investigated river channel. Two profiles, the shallower upstream and the deeper downstream of the central sandbar, 500 m long each were chosen for the analysis (Fig. 4) to avoid a complicated flow pattern at the sandbar. Between the 19th of March and the 30th of March, the measurements were, in general, conducted one per day. The last measurement on 9th of April, however, was performed after ten days of the break caused by unfavourable wind conditions in the area. Thus, the database consisting of 12-bed elevation profiles at each of the sections was collected.

2.4. Calculation of dune migration rates

In the first step, one-dimensional bedform elevation profiles were analysed using the approach of Van der Mark and Blom (2007), who were able to perform bedform tracking by determination of crest and trough positions of individual

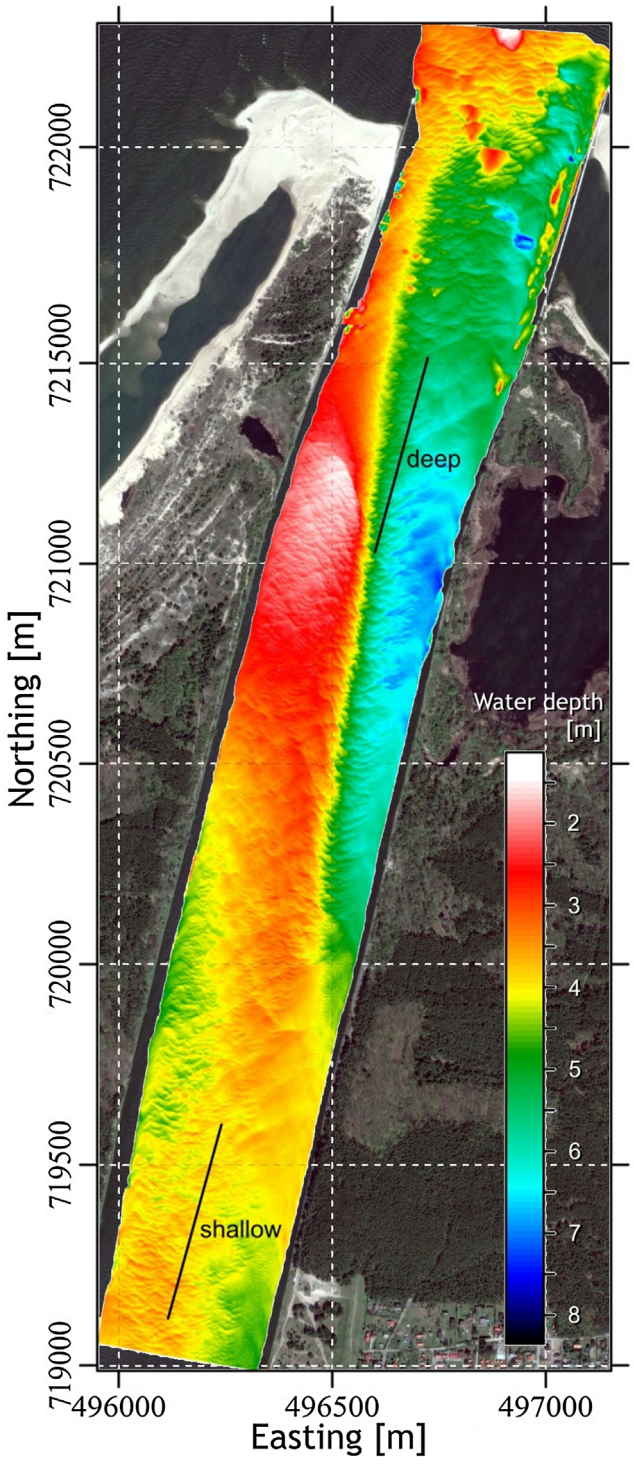

Figure 4 Bathymetry map of the Vistula River mouth (state in April 2015) with two segments of 500 m length ("shallow" and "deep") located close to the channel axis, along which the experiment was accomplished. The background consists on an aerial photo of the area from May 2017. Coordinates in Polish national geodetic coordinate system PUWG1992.

bedforms based on the zero-crossing technique (Figs. 5 and 6). Subsequently, histograms of bedform height (defined as the vertical distance between a crest and its downstream trough) and bedform length (defined as the horizontal distance between two subsequent crests) were obtained (Figs. 7 and 8). In addition, mean and median values of the appropriate dunes geometrical dimensions were derived from the statistics.

In the next step, the cross-covariance functions (using the Matlab® *xcov* function) between the initial depth data function and the subsequent ones were calculated. By definition, cross-covariance measures the similarity between two discrete-time sequences – the first one and shifted (lagged) copies of the second one as a function of the lag m. In the general case, the cross-covariance sequence c_{xy} of two jointly stationary random processes of length N, is the cross-correlation of mean-removed sequences (e.g. Orfanidis, 2007; Stoica and Moses, 2005):

$$c_{xy}(m) = E\{(x_{n+m}-\mu_x)(x_n-\mu_y)^*\}, \quad (1)$$

where μ_x and μ_y are the mean values of the two stationary random processes, the asterisk (*) denotes complex conjugation, and E is the expectation operator. In the case of real data series, Eq. (1) can also be represented in the more detailed form (Eq. (2)):

$$c_{xy}(m) = \sum_{n=0}^{N-m-1}\left(x_{n+m}-\frac{1}{N}\sum_{i=0}^{N-1}x_i\right)\left(y_n-\frac{1}{N}\sum_{i=0}^{N-1}y_i\right). \quad (2)$$

Taking into account the moments of time in which depth data were collected, the mean velocity (celerity) of dunes migration can be estimated by determining the space lag of the cross-covariance function maximum (the maximum correlation corresponds to the approximate distance the bedforms have translated).

Finally, assuming suitability of the approximation of the bedload transport for ripples and dunes formulated and proposed by Simons et al. (1965), the volume rate of bedload for idealised triangular bedforms was calculated based on Eq. (3):

$$q_b = (1-p)V_s\frac{\eta}{2}, \quad (3)$$

where q_b is the volumetric bedload transport rate per unit width [$m^2/s = (m^3/s)/m$], p the porosity of the sand bed (typically ranges from 0.26 to 0.43 in the case of coarse sand – Geotechdata.info, 2013), V_s is the mean velocity (celerity) of dunes in the direction of the flow, and η the mean dune height. Eq. (3) is widely used in literature (e.g., Aberle et al., 2012; Dinehart, 2002; Holmes, 2010; Van den Berg, 1987; Venditti et al., 2016; Villard and Church, 2003). As Simons et al. (1965) mentioned, the equation is more suited for a dune-bed configuration than for ripples and gives more reliable results for coarse bed material due to the fact that the dunes of coarse sand are more frequently near-triangular in shape than are the dunes comprised of fine material. Values of bedload q_b were subsequently converted from volume to weight by multiplying Eq. (3) by the sediment mineral density $\rho = 2650\ kg/m^3$.

3. Results

The analysis of bed elevation profiles revealed the presence of small to large sand dunes (as in Ashley, 1990) with geometrical dimensions ranges up to $\eta = 0.71$ m in height and up to $\lambda = 35.4$ m in length. Comparison of bed elevation profiles

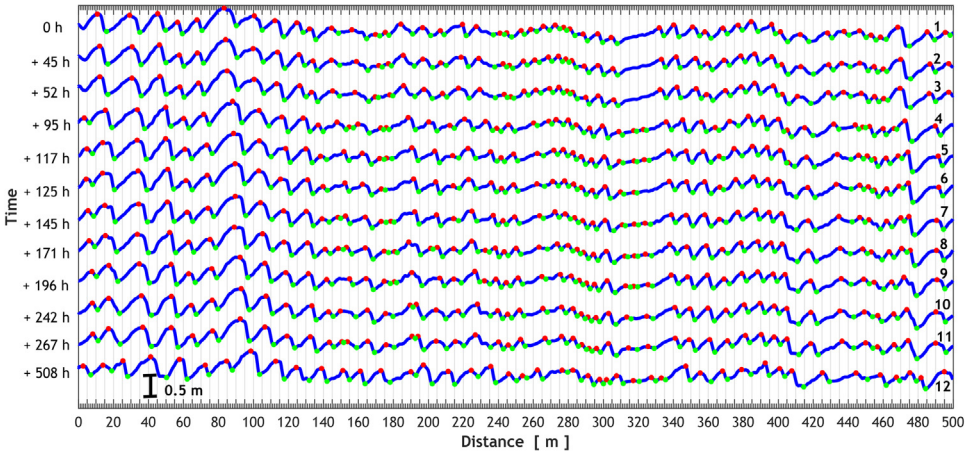

Figure 5 Depth elevation profiles along the "shallow" segment of 500 m length for all successive days of echosounding. The respective time steps are in hours relative to the initial survey. Location of crests and troughs are depicted with red and green points, respectively. The height of the black vertical scale is 0.5 m. (For interpretation of the references to color in this figure legend, the reader is referred to the web version of this article.)

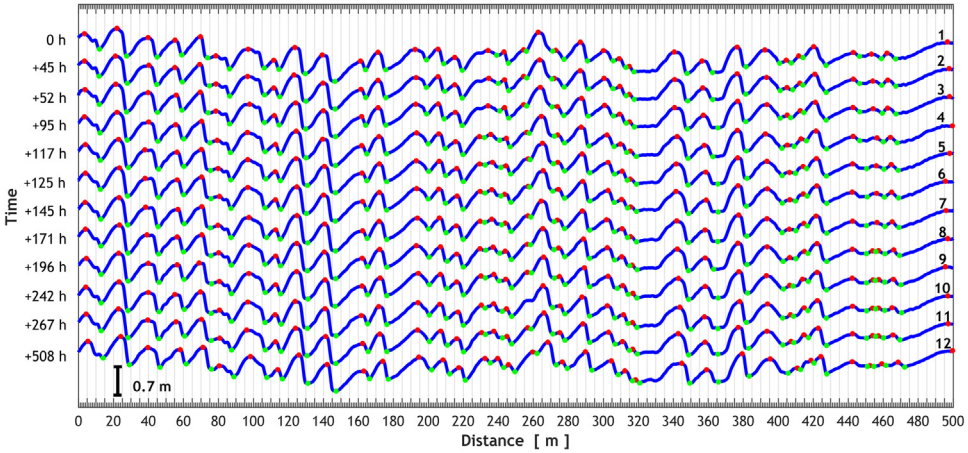

Figure 6 Depth elevation profiles along with "deep" segment of 500 m length for all successive days of echosounding. The appropriate time steps are in hours relative to the initial survey. Location of crests and troughs are depicted with red and green points, respectively. The height of the black vertical scale is 0.7 m. (For interpretation of the references to color in this figure legend, the reader is referred to the web version of this article.)

along two longitudinal segments (Fig. 4) indicated a distinct character of subaqueous bedforms — with dunes, in general, smaller in height and shorter in length at the "shallow" part of the investigated area (upstream of the submerged sandbar).

The number of individual dunes observed at the "shallow" segment (Fig. 5) reduced slightly in time from 48 at the beginning of the experiment (profile 1) to 44 bedforms 508 h later (profile 12). The mean and median values of dune heights η and lengths λ were derived from the statistics. Changes of these parameters revealed that both of them increased in time — from η_{mean} = 0.20 m, η_{median} = 0.18 m and λ_{mean} = 10.3 m, λ_{median} = 9.9 m to η_{mean} = 0.24 m, η_{median} = 0.22 m and λ_{mean} = 11.2 m, λ_{median} = 11.4 m in what can be interpreted as the amalgamation (merging) of a few small bedforms.

In turn, almost the same number of bedforms (34–36 individual dunes) was observed at the "deep" area (Fig. 6). Contrastingly to the "shallow" case, the mean values of dune heights and lengths remained almost without any changes — from η_{mean} = 0.33 m, η_{median} = 0.32 m and λ_{mean} = 14.5 m, λ_{median} = 13.6 m to η_{mean} = 0.32 m, η_{median} = 0.31 m and λ_{mean} = 13.7 m, λ_{median} = 13.9 m in the beginning (profile 1) and in the end (profile 12) of the experiment, respectively.

The most suitable probability density functions (with the smallest error estimated based on Eq. (1) in Van der Mark et al., 2008) were fitted to the appropriate distributions of the geometric variables (Figs. 7 and 8). Thus, it was found that the Gamma, Normal and Weibull distributions (blue, red and black curves respectively) yield the best approximation for bedform height and wavelength. It is in reliable agreement with the results of Van der Mark et al. (2008) as well as with the outcomes presented in Lisimenka and Kubicki (2017).

Calculation of the cross-covariance functions (Eq. (2)) for particular pairs of the bed elevation profiles (between the

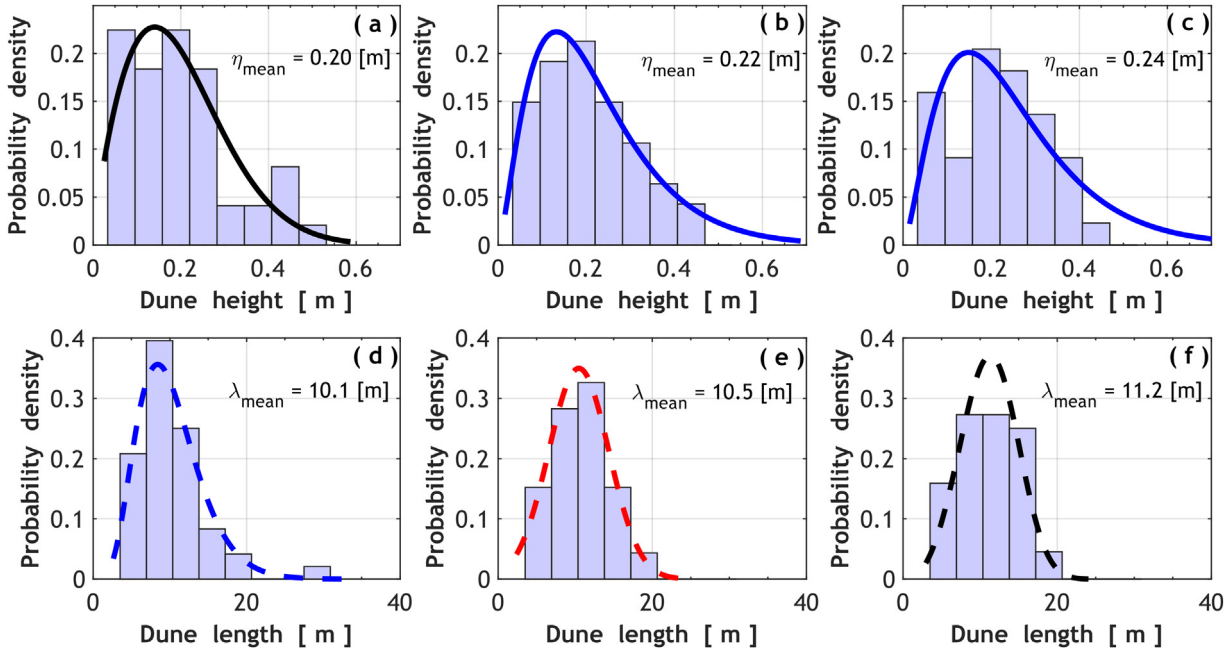

Figure 7 Histograms of dune height and length obtained, based on the measurements performed along the "shallow" segment at different moments of time – at 0 h (a, d), +267 h (b, e) and +508 h (c, f). The most suitable probability density functions are depicted by solid and dashed curves for dune height and length, respectively (blue – Gamma, red – Normal, black – Weibull). (For interpretation of the references to color in this figure legend, the reader is referred to the web version of this article.)

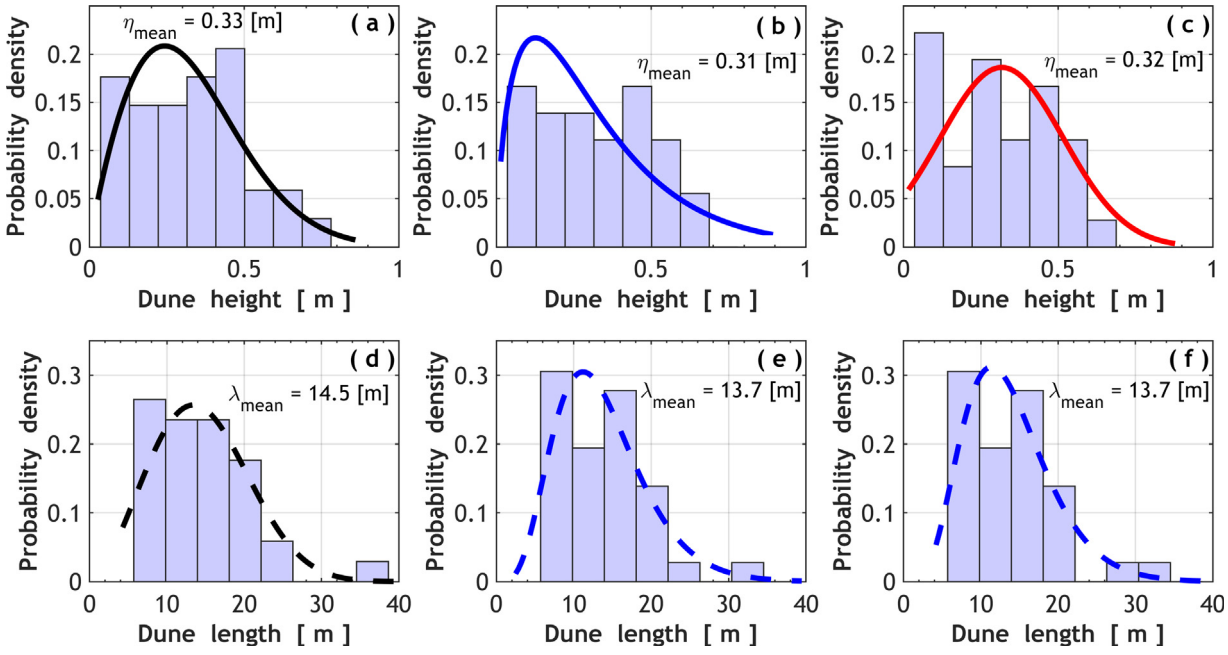

Figure 8 Histograms of dune height and length obtained, based on the measurements performed along the "deep" segment at different moments of time – at 0 h (a, d), +267 h (b, e) and +508 h (c, f). The most suitable probability density functions are depicted by solid and dashed curves for dune height and length, respectively (blue – Gamma, red – Normal, black – Weibull). (For interpretation of the references to color in this figure legend, the reader is referred to the web version of this article.)

initial one and the subsequently measured profiles) revealed distinct character of dunes migration at two different morphological parts of the river mouth. Progressive increasing of the spatial lag of the cross-covariance function maximums has got evidently "faster" character at the "shallow" segment in comparison with the "deep" one (Fig. 9). This can be explained by the difference in kinematics of the small-scale bedforms in comparison with the large ones (e.g. Bridge,

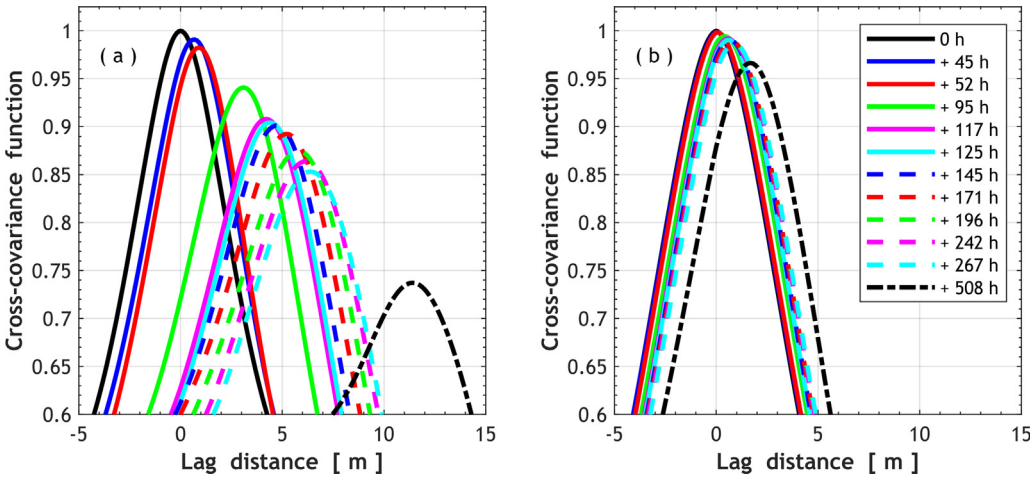

Figure 9 Cross-covariance functions (zoomed) calculated based on Eq. (2) for particular pairs of the bed elevation profiles (relative to the initial one) at the "shallow" (a) and the "deep" (b) segments.

2003). In addition, lag distance changes between successive time steps showed that dune migration rates were not constant in time (Table 1).

Overall downstream displacement of the "shallow" and "deep" ensembles of dunes (as a whole) for the entire period of the experiment (508 h) amounted to 11.4 m and 1.7 m, respectively. It means that, in general, dunes observed at the "shallow" area migrated 7 times faster in average than the "deep" dunes, with mean dune celerity equal to 0.022 m/h and 0.003 m/h, respectively.

Taking into account the average migration rates for the entire experiment together with mean dune heights (Table 1), as well as assuming that the porosity of the coarse sand bed equals to $p = 0.35$, an estimation of the volumetric bedload transport rate was calculated (Eq. (3)). The calculation revealed values of $q_{b\_shallow} = 4.25 \cdot 10^{-7}$ m^2/s and $q_{b\_deep} = 8.7 \cdot 10^{-8}$ m^2/s for the shallow and deep sections, respectively. Based on the assumption that the effective river channel width at the area of interest is about 420 m and the density of sand $\rho = 2650$ kg/m^3, it can be roughly estimated that the daily bedload transport amounts to 40.9 t/day and 8.4 t/day for the "shallow" and "deep" sections, respectively.

4. Discussion

In this study, estimation of bedload transport of Vistula River mouth into the Baltic Sea was approached over two dune fields. The calculation was done in the "shallow" part upstream from the submerged sandbar and in the "deep"

Table 1 Mean statistics in bedform geometry and migration of the "shallow" and "deep" ensembles of dunes for particular time steps.

#	Date/time of survey	Time step, Δt_i [h]	"shallow"/"deep"									
			Mean dune height, η_{mean} [m]		Mean dune length, λ_{mean} [m]		Mean dune steepness, $\eta_{mean}/\lambda_{mean}$		Distance travelled, Δx_i [m]		Mean dune celerity, $V_i = \Delta x_i/\Delta t_i$ [m/h]	
1	19 March 10:00	0	0.20	0.33	10.3	14.5	0.019	0.023	–	–	–	–
2	21 March 07:00	45	0.20	0.32	10.3	14.5	0.019	0.022	0.7	0.05	0.016	0.001
3	21 March 14:00	7	0.20	0.33	10.3	14.5	0.019	0.023	0.2	n/a	0.029	n/a
4	23 March 09:00	43	0.20	0.32	9.7	14.2	0.020	0.022	2.2	0.35	0.05	0.008
5	24 March 07:00	22	0.20	0.31	9.9	14.1	0.020	0.022	1.1	0.2	0.05	0.009
6	24 March 15:00	8	0.21	0.32	10.6	14.0	0.020	0.023	0.2	0.05	0.025	0.006
7	25 March 11:00	20	0.20	0.32	10.1	14.1	0.020	0.023	0.3	0.05	0.015	0.003
8	26 March 13:00	26	0.20	0.31	9.7	13.7	0.020	0.023	0.5	0.05	0.019	0.002
9	27 March 14:00	25	0.21	0.31	10.3	13.6	0.020	0.023	0.6	0.05	0.024	0.002
10	29 March 12:00	46	0.22	0.32	10.7	14.1	0.020	0.023	0.4	0.05	0.009	0.001
11	30 March 13:00	25	0.22	0.31	10.5	13.7	0.021	0.023	0.2	0.05	0.008	0.002
12	9 April 14:00	241	0.24	0.32	11.2	13.7	0.021	0.023	5.0	0.8	0.021	0.003
Total		*508*	*0.21*	*0.32*	*10.3*	*14.1*	*0.020*	*0.023*	*11.4*	*1.7*	*0.022*	*0.003*

part downstream from it (Fig. 4). Obtained values differ by a factor of 5 with much more bedload being transported upstream from the sandbar. This result may suggest that the sandbar intercepts ca. 78% of bedload coming from the upper part of the river during the average discharge of the river. The accumulated sediment is thus trapped at the sandbar, which supported findings of previous research (Wróblewski et al., 2015). The authors, using a cut-fill method, showed that the sandbar grew by nearly 1 m in height between 2009 and 2014. Further studies are needed to compare the accumulated volume with our calculations. It is however, unlikely that the entire bedload stays at the sandbar. Tarnowski (1995), using hydraulic models as well as analysis of bathymetric changes observed in the Vistula fan in the period between 1983 and 1990, speculated that bedload transport decays as a function of river discharge. Manthey and Gilewski (1980) observed that in the case of low water discharge of about 800–1100 m^3/s (similar to hydrological conditions during our measurement campaign), the bedload transport was not traceable at the river section located about 7–10 km upstream of the investigated area. In turn, Tarnowski (1995) postulated that, in the case of a river water discharge of about $Q \approx 1250\ m^3/s$, no bedload transport was observed about 3 km upstream of the area of interest.

Our results however, suggest constant dune migration all the way towards the river mouth even at average (low) hydrological conditions. Tarnowski (1995) estimated in his study that the riverbed material was mobilised only during river discharge larger than $Q \approx 3000\ m^3/s$. Although there is not enough data to support this claim, it is likely that accelerated currents during increased water discharge initiate erosional processes in the Vistula River mouth. We can therefore theorise that the sandbar is only temporarily intercepting riverine bedload, and that during more energetic conditions it is being eroded, and sediments are carried away towards the subaqueous river delta.

In such a case, the result obtained at the "shallow" section could be treated as the total quantity of bedload material reaching the outlet stretch from upstream parts of the river, whereas the outcome obtained at the "deep" section could be acknowledged as the bedload transport actually delivered to the subaqueous Vistula delta during the hydrological conditions of the experiment. The two aforementioned results should not be therefore averaged, but instead considered separately.

The application of high-resolution bathymetry gave a great overview of the river mouth relief. The investigated sections of the riverbed were chosen carefully, but due to the lack of riverine current speed data one is not certain which dune field is representative for the investigated hydrological conditions. High discrepancy of results for the studied "shallow" and "deep" sections proves that the applied method of bedload calculation is very sensitive to several factors of which the educated selection of tested dune field seems to be of highest importance.

Knowing that the experiment covered merely 21 days, and only during hydrological conditions close to the long-term mean annual water discharge, it is little justified that the annual bedload transport to the Baltic Sea would be calculated. However, by doing so, the results can be compared with previous studies on the bedload transport in the Vistula River mouth and delta. If extrapolated uniformly to the annual basis, our results reveal that the estimated volume of the annual bedload transport is of about 5900 m^3/year (at the "shallow" section of the investigated area). In turn, based on the data from the years 1895–1953 presented in Słomianko (1956), the mean annual bedload transport can be estimated at 24,100 m^3/year. This was however, the period before even the Włocławek Dam was constructed. Contrastingly, other investigators (Manthey and Gilewski, 1980) predicted the bedload transport at about ~500,000 m^3/year, which is at least two orders more in comparison to the values obtained in our study. It is worth to note that their estimation was based on empirical equations applied for the Tczew cross-section (31.2 km upstream of the investigated area). Moreover, the authors conducted their calculations for the 1965 hydrological year, during which long-lasting intensive discharges (significantly higher than the mean annual water outflow) together with the flood wave up to $Q = 4520\ m^3/s$ were observed (confirmed based on data shared courtesy of IMGW-PIB). Manthey and Gilewski (1980) established also that, in spite of increased bedload caused by high water discharges, the Vistula River transports significantly more sediments in suspend during the spring. The authors estimated that the ratio of bedload to suspended load is the smallest (about 30%) at the beginning (March–April) of the spring season. Therefore, such a significant difference in bedload can be explained mainly by lack of energetic events during our experiment. Increased river discharge due to spring meltwaters and autumn rainfalls was not included in our approach, what probably resulted in underestimated volumes obtained in this study.

The great importance of sediment material transported by the river as a bedload was underlined by many investigators. Granulometry analysis of sediments forming of the Vistula alluvial fan (Wypych, 1968 as cited in Tarnowska and Zeidler, 1980) as well as its lithofacies model (Koszka-Maroń, 2016) show that the bedload transport powered by the riverine processes is the main source of sediments participating in the subaqueous delta development. Coarse and medium-grained sands, which are the main components of the bedload material supplied by the river into the sea (Rudowski et al., 2017), are deposited mainly on the alluvial fan. In turn, finer sediments are washed out by wave-bottom interaction and transported far away by wave currents.

Although, the accumulation processes in the alluvial fan are subjected primarily to the hydrological conditions in the river, the shape of the fan and its offshore edges is dependent also on the amplitude/directional characteristics of the wave-current field in the area. Due to the shield of a significant part of the Gulf of Gdańsk caused by the Hel Peninsula, the surface waves with the longest fetch from the east and north-east directions have the most powerful influence on the rebuilding of the fan. In general, the wind circulations induce the relatively low speed currents in the coastal area of the Gulf of Gdańsk (Pruszak and Szmytkiewicz, 2015) and so, wave currents generated by breaking waves have a crucial impact on hydrodynamics and in consequence on the bathymetry changes at the Vistula River mouth area, as well as influence on the longshore sediment transport processes. Results of numerical modelling obtained by Ostrowski et al. (2009) showed that the storm wave conditions should be lasted at least several hours in order to observe measur-

able erosion of the seabed. Such events, in principle, are caused by strong winds from the north and are very infrequent in the area of the Vistula River fan.

Besides, independently of the character of sediment transport in the river, there are two equivalent streams of longshore sediment transport in the coastal region enclosing the area of investigation. One of them flows from west to east, and the other one in the opposite direction, and are observed at the western and the eastern sides of the Vistula fan respectively. Based on a one-dimensional wave model, Pruszak and Skaja (2014) estimated that these streams are of about 20,000 m^3/year. However, in our opinion, this estimation is rather discussable (overestimated) at least in the case of the west-east stream, due to lack of significant sediment sources at the western part of the Gulf of Gdańsk which could supply this longshore stream. Nevertheless, it can be stated that the quantitative role of both these "sea" streams in sediment transport processes is essentially weaker in comparison with the amount of the sediments supplied by the Vistula River.

It is important to note that the influence of the storm surges in the Gulf of Gdańsk, or wave currents on the total balance of sediment transport in the area remains still unknown. It is common however, that the storm surge pushes marine waters into the Vistula River mouth (backwater phenomena). Such energetic events are likely to trigger erosion of the marine deltaic sediments, and part of these can be easily re-suspended and carried back into the investigated river mouth. There has been however, no safe method developed which would allow for the analysis of the marine influence on riverine sediment transport during storm surges. On the contrary, the period of storm surge has been avoided in our study in order to present undisturbed data obtained during the average riverine discharge period.

5. Conclusions

For the first time, based on the non-invasive hydroacoustic method, bedload sediment transport to the Baltic Sea has been estimated in the main Vistula River mouth (Przekop Wisły).

During a 21-day observation conducted in hydrological conditions close to that of the long-term mean annual water discharge, the bedload transport was found to take place constantly. The analysis of dune migration rates revealed the distinct character of sand dune migration at two different morphological parts of the Vistula outlet stretch. It has been found that the smaller in size dunes (mean dune height η_{mean} = 0.21 m and dune length λ_{mean} = 10.3 m) located upstream from the submerged sandbar that forms the last depositional barrier before the mouth, migrate 7 times faster than the larger ones (η_{mean} = 0.32 m and λ_{mean} = 14.1 m) located downstream from it. Average migration rates for the entire experiment revealed values of 0.022 m/h and 0.003 m/h and daily bedload sediment transport values of about 40.9 t/day and 8.4 t/day were obtained for "shallow" (upstream) and "deep" (downstream) sites, respectively. Such difference was attributed to sediment trapping by the submerged sandbar during the hydrological conditions of the experiment.

The presented method proved to be successful for estimation of the bedload transport but the approach should be repeated during high water discharges of the Vistula River to deliver better approximation of sediment volume to the subaqueous Vistula delta in the Baltic Sea.

Acknowledgements

The authors are grateful to the National Centre for Research and Development (Poland) for funding this work by grant VISTULA No. PBS1/A2/3/2012. We wish to thank our colleagues from the Department of Operational Oceanography of the Maritime Institute in Gdańsk for their help in preparing and carrying out the bathymetric survey. The authors also thank Dr. Maciej Kałas from the Maritime Institute in Gdańsk for his help in analysing the hydrological data. The authors would like to express their gratitude to both reviewers and the journal editors for their constructive criticism and valuable comments.

References

Aberle, J., Stephen, E., Coleman, S.E., Nikora, V.I., 2012. Bed load transport by bed form migration. Acta Geophys. 60 (6), 1720—1743, http://dx.doi.org/10.2478/s11600-012-0076-y.

Ashley, G.M., 1990. Classification of large-scale subaqueous bedforms: a new look at an old problem. J. Sediment. Res. 60, 160—172, http://dx.doi.org/10.2110/jsr.60.160.

Augustowski, B. (Ed.), 1982. Dolina Dolnej Wisły. ([The valley of the lower Vistula]).Ossolineum, Wroclaw, 454 pp. (in Polish, English summaries).

Babiński, Z., 2005. The relationship between suspended and bed load transport in river channels. In: Proc. 7th IAHS Sci. Assembly. Foz do Iguaçu, Brazil, April 2005, 182—188, IAHS Publ. 291.

Babiński, Z., Habel, M., 2013. Hydromorphological conditions of the lower Vistula in the development of navigation and hydropower. Acta Energetica 2 (15), 83—90, http://dx.doi.org/10.12736/issn.2300-3022.2013206.

Brański, J., Skibiński, J., 1968. Udział rumowiska wleczonego w ogólnej masie rumowiska rzecznego transportowanego w korycie środkowej i dolnej Wisły. Wiad. Służby Hydrolog. Meteorolog. 3—4, 13—23.

Bravard, J.P., Petit, F., 2009. Geomorphology of streams and rivers. In: Encyclopedia of Inland Waters. Elsevier, 387—395.

Bridge, J.S., 2003. Rivers and Floodplains: Forms, Processes, and Sedimentary Record. Blackwell Sci., Malden, MA, 504 pp.

Cats, G., Wolters, L., 1996. The Hirlam project. IEEE Comput. Sci. Eng. 3 (4), 4—7.

Childers, D., 1999. Field comparison of six-pressure-difference bedload samplers in high energy flow. Water-Resources Investigations Report 92-4068. U.S. Geological Survey, Vancouver, Washington, 71 pp.

Damrat, M., Zaborska, A., Zajączkowski, M., 2013. Sedimentation from suspension and sediment accumulation rate in the River Vistula prodelta, Gulf of Gdańsk (Baltic Sea). Oceanologia 55 (4), 937—950, http://dx.doi.org/10.5697/oc.55-4.937.

Dinehart, R.L., 2002. Bedform movement recorded by sequential single-beam surveys in tidal rivers. J. Hydrol. 258, 25—39, http://dx.doi.org/10.1016/S0022-1694(01)00558-3.

Franz, M., Kozakiewicz, A., Naguszewski, A., Piwowarska, M., Ostrowski, R., Skaja, M., Szmytkiewicz, M., 2005. Evolution of Vistula cross-cut in view of historical bathymetry data. Inż. Morska Geotech. 26 (5), 383—391, (in Polish).

Geotechdata.info, 2013. Soil porosity, http://www.geotechdata.info/parameter/soil-porosity.html (updated 18 November 2013).

Gomez, B., 2006. The potential rate of bed-load transport. Proc. Natl. Acad. Sci. U.S.A. 103 (46), 17170—17173, http://dx.doi.org/10.1073/pnas.0608487103.

Graniczny, M., Janicki, T., Kowalski, Z., Koszka-Maroń, D., Jegliński, W., Uścinowicz, Sz., Zachowicz, J., 2004. Recent development of the Vistula River outlet. Polish Geolog. Inst. Spec. Papers 11, 103—108.

Hickin, E.J. (Ed.), 1995. River Geomorphology. Wiley, Chichester, 255 pp.

Holmes Jr., R.R., 2010. Measurement of bedload transport in sand-bed rivers: a look at two indirect sampling method. U.S. Geolog. Surv. Sci. Inv. 236—252, Rep. no. 2010-5091.

IMGW-PIB, 2017. www.pogodynka.pl. Online hydrological and meteorological database of the Institute of Meteorology and Water Management — National Research Institute, Warsaw; Instytut Meteorologii i Gospodarki Wodnej — Państwowy Instytut Badawczy, Warszawa (accessed on 31 December 2017).

Knighton, D., 1998. Fluvial Forms and Processes: A New Perspective. Hodder Arnold Publ., Routledge, London, New York, 383 pp.

Kostaschuk, R.A., Church, M.A., Luternauer, J.L., 1989. Bedforms, bed material, and bedload transport in a salt-wedge estuary: Fraser River, British Columbia. Can. J. Earth Sci. 26 (7), 1440—1452, http://dx.doi.org/10.1139/e89-122.

Koszka-Maroń, D., 2016. Lithofacies model of the Vistula river-mouth fan as a record of the interaction of marine and terrestial environments. Prz. Geolog. 64, 315—327, (in Polish).

Lisimenka, A., Kubicki, A., 2017. Estimation of dimensions and orientation of multiple riverine dune generations using spectral moments. Geo-Mar. Lett. 37 (1), 59—74, http://dx.doi.org/10.1007/s00367-016-0475-1.

Majewski, W., 2013. Sustainable development of the Lower Vistula. Meteorol. Hydrol. Water Manage. 1 (1), 33—37, http://dx.doi.org/10.26491/mhwm/21814.

Makowski, J., 1995. Setna rocznica wykonania Przekopu Wisły 1885—1995. IBW PAN, Gdańsk, 100 pp.

Manthey, T., Gilewski, J., 1980. Określenie natężenia transportu rumowiska w postaci unoszonej i wleczonej w ujściowym odcinku rzeki Wisły. Stud. Mat. Oceanograf. 30, 179—214.

Orfanidis, S.J., 2007. Optimum Signal Processing: An Introduction. Rutgers Univ. Press, New Brunswick, NJ, USA, 391 pp.

Ostrowski, R., Kapiński, J., Piotrowska, D., Pruszak, Z., Robakiewicz, M., Różyński, G., Schönhofer, J., Skaja, M., Szmytkiewicz, M., Szmytkiewicz, P., 2009. Badania modelowe ujścia Wisły do Zatoki Gdańskiej. IBW PAN, 19 pp.

Pruszak, Z., Skaja, M., 2014. Problemy dynamiki i ochrony brzegu morskiego. IBW PAN, Gdańsk, 184 pp.

Pruszak, Z., Szmytkiewicz, M., 2015. Delta Wisły: ogólne mechanizmy tworzenia się delt i estuariów rzecznych. IBW PAN, 127 pp.

Pruszak, Z., van Ninh, P., Szmytkiewicz, M., Manh Hung, N., Ostrowski, R., 2005. Hydrology and morphology of two river mouth regions (temperate Vistula Delta and subtropical Red River Delta). Oceanologia 47 (3), 365—385.

Rudowski, S., Edut, J., Wróblewski, R., Dworniczak, J., Lisimenka, A., Jereczek-Korzeniewska, K., Galer-Tatarowicz, K., 2017. Granulometry of bottom sediments of the Przekop Wisły canal. Bull. Maritime Inst. Gdańsk 32 (1), 14—20, http://dx.doi.org/10.5604/12307424.1224050.

Simons, D.B., Richardson, E.V., Nordin Jr., C.F., 1965. Bedload equation for ripples and dunes. U.S. Geolog. Surv. Prof. Paper 462-H 9 pp.

Słomianko, P., 1956. Studium zapiaszczania ujścia Wisły pod Świbnem. Prace Inst. Morskiego 95, 85—103.

Stoica, P., Moses, R., 2005. Spectral Analysis of Signals. Prentice Hall, Upper Saddle River, New Jersey, 452 pp.

Szymański, E., 1897a. The regulation of the Vistula River mouth. Tech. Rev. 17, 270—274, (in Polish).

Szymański, E., 1897b. The regulation of the Vistula River mouth (continuation). Tech. Rev. 18, 285—289, (in Polish).

Szymczak, E., Galińska, D., 2013. Sedimentation of suspensions in the Vistula River mouth. Oceanol. Hydrobiol. Stud. 42 (2), 195—201, http://dx.doi.org/10.2478/s13545-013-0075-x.

Tarnowska, M., Zeidler, R.B., 1980. Ruch wody i osadów dennych w rejonie stożka ujściowego Wisły. Stud. Mat. Oceanograf. 30, 215—261.

Tarnowski, A., 1995. Zmiany stożka ujściowego Wisły w świetle pomiarów w naturze i badań na modelu hydraulicznym. IBW PAN, Gdańsk, 23 pp.

Van den Berg, J.H., 1987. Bedform migration and bed-load transport in some rivers and tidal environments. Sedimentology 34, 681—698, http://dx.doi.org/10.1111/j.1365-3091.1987.tb00794.x.

Van der Mark, C.F., Blom, A., 2007. A new and widely applicable tool for determining the geometric properties of bedforms, Civil Eng. & Man. Res. Reports 2007R-003/WEM-002, No. 1568-4652. Water Eng. & Manage., Enschede, 57 pp.

Van der Mark, C.F., Blom, A., Hulscher, S.J.M.H., 2008. Quantification of variability in bedform geometry. J. Geophys. Res. 113, F03020, http://dx.doi.org/10.1029/2007JF000940.

Van Rijn, L.C., 1993. Principles of Sediment Transport in Rivers, Estuaries and Coastal Seas. Aqua Publ., Amsterdam, The Netherlands, 687 pp.

Venditti, J.G., Lin, C.-Y.M., Kazemi, M., 2016. Variability in bedform morphology and kinematics with transport stage. Sedimentology 63, 1017—1040, http://dx.doi.org/10.1111/sed.12247.

Villard, P.V., Church, M., 2003. Dunes and associated sand transport in a tidally influenced sand-bed channel: Fraser River, British Columbia. Can. J. Earth Sci. 40, 115—130, http://dx.doi.org/10.1139/E02-102.

Wróblewski, R., Rudowski, S., Gajewski, L., Sitkiewicz, P., Szefler, K., Kałas, M., Koszałka, J., 2015. Changes of the Vistula River External Delta in the period of 2009—2014. Bull. Maritime Inst. Gdańsk 30 (1), 16—22, http://dx.doi.org/10.5604/12307424.1158154.

Wypych, K., 1968. Osady denne strefy przybrzeżnej rejonu Martwej Wisły (typescript). PIHM Oddział Morski, Gdynia.

Zajączkowski, M., Darecki, M., Szczuciński, W., 2010. Report on the development of the Vistula River plume in the coastal waters of the Gulf of Gdańsk during the May 2010 flood. Oceanologia 52 (2), 311—317, http://dx.doi.org/10.5697/oc.52-2.311.

Oceanologia (2019) 61, 395—399

Available online at www.sciencedirect.com

ScienceDirect

journal homepage: www.journals.elsevier.com/oceanologia/

SHORT COMMUNICATION

First new record of two diatoms (*Caloneis africana* (Giffen) Stidolph and *Luticola nivalis* (Ehrenberg) D. G. Mann) from South West Coast of India (Cochin backwaters)

Geo Joseph *, **Mannancheril Sebastian Francis**

Sacred Heart College, Mahatma Gandhi University, Kerala, India

Received 23 October 2018; accepted 14 December 2018
Available online 28 December 2018

KEYWORDS
South West Coast of India;
Diatoms;
Caloneis africana;
Luticola nivalis

Summary The main objective of this paper is to report two diatoms (*Caloneis africana* (Giffen) Stidolph and *Luticola nivalis* (Ehrenberg) D. G. Mann) from Cochin backwaters, which prove to be a new finding from Indian waters. Surface water samples were collected monthly from twelve stations covering the ecosystem from May 2015 to April 2016. The analysis of physicochemical parameters and the preparation of permanent slides of diatoms were performed based on standard procedures. Descriptions, world distribution and photographs of the two diatoms are included in this paper. These two new species further enrich the diatom floristic diversity of Cochin backwaters in India.

Diatoms are the most species-rich group of algae. The number of diatoms has been estimated to include approximately 100,000 species over 1000 genera. Diatoms are widely used in ecological monitoring and paleoecological reconstruction (Mann, 1999). The net primary production from diatoms is more than that of all the worlds' tropical rainforests (Field et al., 1998). Diatoms produce 20—25% of global oxygen (Smol and Stoermer, 2010). In an aquatic ecosystem, they represent

* Corresponding author at: Sacred Heart College, Mahatma Gandhi University, Kerala, India.
E-mail address: geojoseph7777@gmail.com (G. Joseph).
Peer review under the responsibility of Institute of Oceanology of the Polish Academy of Sciences.

Production and hosting by Elsevier

https://doi.org/10.1016/j.oceano.2018.12.002

the overall ecological conditions and reflect the pollution status of the system (Dakshini and Soni, 1982). The habitats of diatoms at the regional and global scale are changing due to natural and anthropogenic activities. Therefore, scientific understanding of the ecological conditions of diatoms is important in order to use them as bioindicators.

Diatoms from tropics are least documented. Approximately 7000 diatom taxa in freshwater, brackish, marine environment and fossils have been reported from the Indian subcontinent (Kale and Karthick, 2015). The scientific study of diatoms in India was reported long back in 1845 on diatoms of Calcutta (Ehrenberg, 1845). Skvortzow (1935) reported 56 forms of diatoms from Calcutta and Biswas (1936) reported common diatoms of the Loktak Lake, Manipur, Assam. Venkataraman (1939) reported 98 diatoms from south India. The diatom floristic diversity of Indian waters was enriched by many Indian diatom taxonomists (Das and Santra, 1982; Desikachary and Devi, 1986; Desikachary et al., 1987; Gandhi, 1959a,b, 1961, 1962, 1967; Gonzalves and Gandhi, 1952; Karthick et al., 2011; Karthick and Kociolek, 2011; Menon, 1945; Roy, 1954; Sarode and Kamat, 1979; Subrahmanyan, 1946). The present study sheds light on the occurrence of two new diatom taxa from Cochin backwaters.

Cochin backwater ecosystem is situated on the southwest coast of India. It is approximately 320 km^2 in the area of Vembanad lake and surrounding islands with six rivers flowing to the backwater. The tidal intrusion from the Arabian Sea and the annual freshwater discharge (20,000 $\times$ 10^6 m^3) from six rivers maintain the dynamism of the system (Srinivas et al., 2003). The climate of Cochin backwater is typical of tropical features with monsoon yielding 60–65% of total rainfall (Menon et al., 2000). The samples were collected from the Cochin backwater ecosystem, running parallel (9°48′ and 10°9′N and 76°10′ and 76°19′E) to the south-west coast of India (Fig. 1). The depth of the ecosystem varies from 2 to 7 m, but the ship channel regions are dredged and maintained at 10–13 m (Qasim, 2003). The backwater system got two permanent connections to the Arabian Sea, one at the Cochin bar mouth (450 m) and the other at Azhikode (100 m) (Sankaranarayanan and Qasim, 1969).

Surface water samples were collected monthly from twelve stations covering the ecosystem from May 2015 to April 2016. The surface water temperature was recorded using 0–50°C precision thermometer and pH by eco tester PH1. The surface water samples were collected in 500 ml Tarsons narrow mouth bottles (Code: 583140) and nutrients (nitrate, nitrite, phosphate and silicate) were analysed within 6 h from collection, based on a standard protocol, using UV 1800 Shimadzu spectrophotometer (APHA, 2005). The collected diatom samples were incubated overnight to settle after adding the fixative ethyl alcohol (98%). Concentrated diatom samples were cleared by hot HCl and $KMnO_4$ method (Taylor et al., 2007) and permanent slides were prepared by Naphrax mounting medium. The samples were observed under Leitz BIOMED research microscope and digital photographs were taken with Nikon Cool pix 4500 camera attached with 100X objectives. The measurements were taken using ocular and stage micrometry. The diatoms were identified according to Krammer and Lange-Bertalot (1986) and Witkowski et al. (2000), based on the classification of Cox (2015).

The paper presents the description, world distribution and ecology of the two diatoms from Cochin backwaters in India. Physico-chemical parameters of the sampling site are given in Table 1.

Order: Naviculales
Family: Pinnulariaceae
Genus: Caloneis
Species: ***Caloneis africana* (Giffen) Stidolph** (Fig. 2A)
Basionym: *Caloneis brevis* f. *africana* M. H. Giffen
Reference: Witkowski et al. (2000) (p. 152, Figs. 1 and 2)
Dimensions: Valve length: 36–108 μm, Valve breadth: 20–24.5 μm, Stria density: 11–12/10 μm.
Diagnosis: Valves elliptic with broadly rounded or with obtusely rounded apices. Raphe straight, external central endings expanded, distant apical endings sickle-shaped, curved on one side, axial area at apices narrow, broadening towards the middle, central area weakly separated, large and usually circular. Transapical striae radiate throughout the valves.
Distribution: Marine water species widespread in the Northern sea tidal flat (Brockmann, 1950), Southern hemisphere (Giffen, 1967), White Sea (Witkowski et al., 2000), New Zealand (Harper et al., 2012), Korea (Joh, 2012) and Australia (John, 2016).
Distribution in India: New Record
Order: Naviculales
Family: Diadesmidiaceae
Genus: Luticola
Species: ***Luticola nivalis* (Ehrenberg) D. G. Mann** (Fig. 2B)
Basionym: *Navicula nivalis* Ehrenberg 1854
Reference: Krammer and Lange-Bertalot (1986) (Fig. 61, 17–20).
Dimensions: Valve length: 12–14 μm, Valve breadth: 5–13 μm, Stria density: 17–20 (24)/10 μm.
Diagnosis: Shells linear, in smaller specimens linear-elliptic, with ± pronounced triangular edges. Raphe branches thread-fencing with weakly one-sided bent central pores. Axial artery moderately narrow, linear or slightly lanceolate to the middle, central artery forming a transverse band extending to almost the edges with a punctiform isolated stigma on the side remote from the central pores.
Distribution: Marine and freshwater species recorded from Germany (Reichardt, 1984), Australia (Day et al., 1995), Romania (Caraus, 2002), Germany (Mauch and Schmedtje, 2003), United States of America (Kociolek, 2005), Czech Republic (Hasler et al., 2007), China (Liu, 2008) and Israel (Barinova et al., 2010).
Distribution in India: New Record

Round et al. (1990) considered the genera Caloneis and Pinnularia as synonyms and eliminated the genus Caloneis from his book. Cox (2015) placed Caloneis under Pinnulariaceae. The present study agrees with the discussions of Mann (2001) regarding the genus level identification difficulties of Caloneis and Pinnularia. The identification of *C. africana* (Giffen) Stidolph in this study was completely based on Witkowski et al. (2000). Moreover, the characteristics exhibited by the present specimen is not matching with any of the Pinnularia species reported in the literature, and at the same

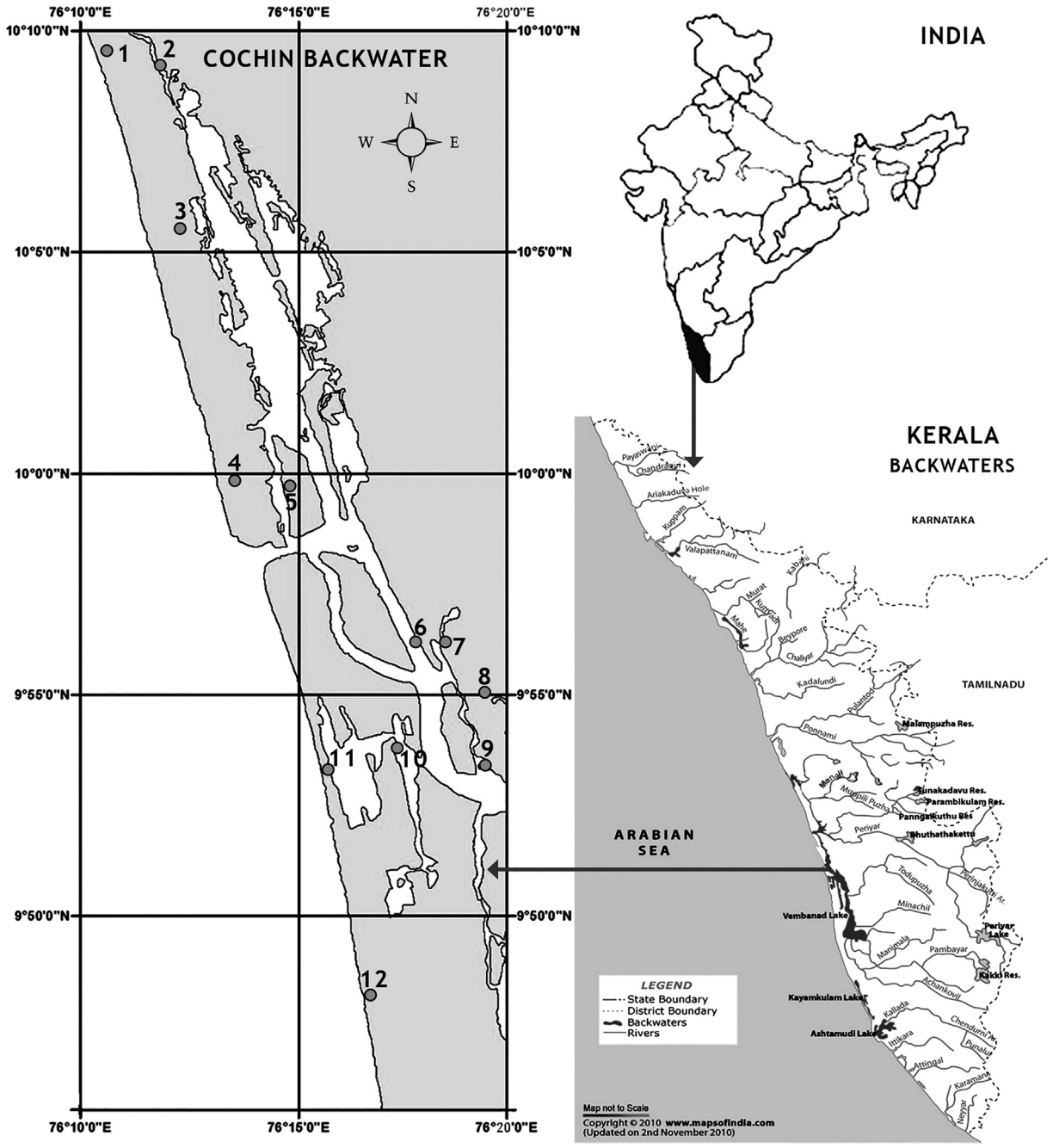

Figure 1 Map of the station in the South West Coast of India (Cochin backwaters) where *Caloneis africana* and *Luticola nivalis* have been recorded.

time it perfectly matches with the *C. africana* (Giffen) Stidolph. Hence future research works on gene sequence data of Caloneis species will provide substantial evidence for proper identification and classification of the taxa. Even though several studies have been carried on diatom flora of Cochin backwaters (Aneeshkumar and Sujatha, 2012; Dayala et al., 2014; Gopinathan, 1975; Gopinathan et al., 1984; Jyothibabu et al., 2015; Kumar et al., 2014; Madhu et al., 2010, 2017; Sanilkumar et al., 2009; Selvaraj et al., 2003), the two diatoms reported in this paper from Cochin backwaters are new to Indian diatom flora.

The new record of diatoms reported from the Cochin estuary will act as a bioindicator of the ecosystem and it will implicate the importance of continuous assessment of diatom diversity in India, for exploring new taxa and new records. The floristic study of diatoms at the regional scale will provide information regarding the endemism in diatoms. To understand the distribution of two diatoms presently reported, detailed and systematic studies are required in different aquatic ecosystems that will further enrich the biodiversity list of diatoms in India.

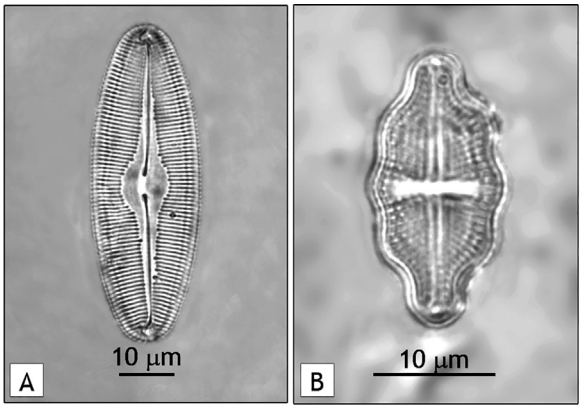

Figure 2 Light microscopy images of diatom species; (A) *Caloneis africana* (Giffen) Stidolph; (B) *Luticola nivalis* (Ehrenberg) D. G. Mann.

Table 1 Water quality parameters at the sampling sites.

	Caloneis africana	*Luticola nivalis*
Locality	Chellanam, Site XII	Pattanam, Site II
Month/year	(76°16′38.6″E and 9°48′14.4″N) 09/2015	(76°11′50.4″E and 10°9′19.7″N) 09/2015
Temperature (°C)	30	30
pH	8.9	7.2
Salinity (ppt)	6	4.8
Nitrate (μmol L^{-1})	0.58	0.76
Nitrite (μmol L^{-1})	2.13	0.27
Phosphate (μmol L^{-1})	0.57	0.86
Silicate (μmol L^{-1})	1.53	4.55

Acknowledgements

The study was supported by Kerala State Biodiversity Board, Kerala, India. The authors are thankful to the Principal and Head, Department of Botany, Sacred Heart College, Thevara, Cochin for providing necessary facilities to carry out the work.

References

Aneeshkumar, N., Sujatha, C.H., 2012. Biomarker pigment signatures in Cochin back water system — a tropical estuary south west coast of India. Estuar. Coast. Shelf Sci. 99, 182—190, http://dx.doi.org/10.1016/j.ecss.2011.12.029.

APHA, 2005. Standard Methods for the Examination of Water and Waste-water, 21st edn. Am. Public Health Assoc., Washington, DC, 2671 pp.

Barinova, S.S., Yeuda, G., Nevo, E., 2010. Comparative analysis of algal communities in the rivers of northern and southern Israel as bearing on ecological consequences of climate change. J. Arid Environ. 74 (7), 765—776.

Biswas, K., 1936. Common diatoms of the Loktak Lake, Manipur, Assam. J. R. Asiat. Soc. Bengal. 2 (2), 171—175.

Brockmann, C.H., 1950. Die Watt-Diatomeen der Schleswig-holsteinischen Westküste. Abh. Senkenb. Naturf. Ges. 478, 1—26.

Caraus, I., 2002. The algae of Romania. Studii si Cercetari, Universitatea Bacau. Studii si Cercetari, Univ. Bacau, 694 pp.

Cox, E.J., 2015. Syllabus of Plant Families. Adolf Engler's Syllabus der Pflanzenfamilien. Pt. 2/1 Photoautotrophic eukaryotic algae Glaucocystophyta, Cryptophyta, Dinophyta/Dinozoa, Heterokontophyta/Ochrophyta, Chlorarachniophyta/Cercozoa, Euglenophyta/Euglenozoa, Chloro, 13th edn. Borntraeger Sci. Publishers, Berlin, 64—113.

Dakshini, K.M.M., Soni, J.K., 1982. Diatom distribution and status of organic pollution in sewage drains. Hydrobiologia 87 (3), 205—209, http://dx.doi.org/10.1007/BF00007229.

Das, P.R., Santra, S.C., 1982. Diatoms of Senchal lake, Darjeeling, West Bengal, Phykos, 21, 99 pp.

Day, S.A., Wickham, R.P., Entwisle, T.J., Tyler, P.A., 1995. Bibliographic check-list of non-marine algae in Australia. Flora Aust. Suppl. Ser. 4 (i—vii, 276).

Dayala, V.T., Salas, P.M., Sujatha, C.H., 2014. Spatial and seasonal variations of phytoplankton species and their relationship to physicochemical variables in the Cochin estuarine waters, Southwest coast of India. Indian J. Geo Mar. Sci. 43 (6), 943—956.

Desikachary, T.V., Devi, R.K.A., 1986. Marine Fossil Diatoms from India and Indian Ocean region. Atlas of Diatoms. Fascle. I. Madras Science Foundation, Madras, 77 pp.

Desikachary, T.V., Gowthaman, S., Latha, Y., 1987. Diatom Flora of Some Sediments from the Indian Ocean Region, Atlas of Diatoms. Fasc. II. Madras Sci. Foundation, Madras, 221 pp.

Ehrenberg, C.G., 1845. Diatoms from Calcutta (as given by SKVORTZOW, 1935. Diatoms from Calcutta) India. J. Philos. Sci. 58, 179—192.

Field, C.B., Behrenfeld, M.J., Randerson, J.T., Falkowski, P., 1998. Primary production of the biosphere: integrating terrestrial and oceanic components. Science 281 (5374), 237—240.

Gandhi, H.P., 1959a. Freshwater diatom flora of the Panhalgarh Hillfort in the Kolhapur district. Hydrobiol. Int. J. Aquat. Sci. 14 (2), 93—129, http://dx.doi.org/10.1007/BF00042594.

Gandhi, H.P., 1959b. Notes on the Diatomaceae from Ahmedabad and its environs — II: On the Diatom flora of Fontain-reservoirs of the Victoria Garden. Hydrobiologia 14 (2), 130—146, http://dx.doi.org/10.1007/BF00042595.

Gandhi, H.P., 1961. Notes on the diatomaceae of Ahmedabad and its environs. Hydrobiologia 17 (3), 218—236.

Gandhi, H.P., 1962. Some fresh-water diatoms from Lonavla Hill-Station in the Bombay-State (Maharashtra). Hydrobiologia 20 (2), 128—154, http://dx.doi.org/10.1007/BF00046312.

Gandhi, H.P., 1967. Notes on the diatomaceae from Ahmedabad and its environs — VI. On some diatoms from fountain reservoir of Seth Sarabhai's garden. Hydrobiologia 30 (2), 248—272, http://dx.doi.org/10.1007/BF00034596.

Giffen, M.H., 1967. Contributions to the diatom flora of South Africa IV. The marine littoral diatoms of the Estuary of the Kowie River Port Alfred, Cape province. Nov. Hedwigia Beih 31, 289—312.

Gonzalves, E.A., Gandhi, H.P., 1952. A systematic account of the diatoms of Bombay and Salsette. Pt. I. J. Indian Bot. Soc. 31 (3), 117—151.

Gopinathan, C.P., 1975. Studies on the estuarine diatoms of India. Bull. Dep. Mar. Sci. 7 (4), 995—1004.

Gopinathan, C.P., Nair, P.V.R., Nair, A.K.K., 1984. Quantitative ecology of phytoplankton in the Cochin backwaters. Indian J. Fish. 31 (3), 325—336.

Harper, M.A., Cassie Cooper, V., Chang, F.H., Nelson, W.A., Broady, P.A., 2012. Phylum Ochrophyta: brown and golden-brown algae, diatoms, silicioflagellates, and kin. In: Gordon, D.P. (Ed.), New Zealand Inventory of Biodiversity. Vol. 3. Kingdoms Bacteria, Protozoa, Chromista, Plantae, Fungi, Canterbury Univ. Press, Christchurch, pp. 114—163.

Hasler, P., Handák, F., Handákova, A., 2007. Phytoplankton of the Morava and Dyje Rivers in spring and summer 2006. Fottea, Olomouc 7 (1), 49—68.

Joh, G., 2012. Algal Flora of Korea. Volume 3, Number 9. Chrysophyta: Bacillariophyceae: Pennales: Raphidineae: Naviculaceae. Freshwater Diatoms VII. National Institute of Biological Resources, Incheon, 1—6.

John, J., 2016. Diatoms from Stradbroke and Fraser Islands, Australia: Taxonomy and Biogeography. The Diatom Flora of Australia, Vol.1. Koeltz Botanical Books, Oberreifenberg, 377 pp.

Jyothibabu, R., Madhu, N.V., Martin, G.D., Aneesh, C., Sooria, P., Vineetha, G., 2015. Waning of plankton food web in the upstream region of the Cochin backwaters during the Southwest Monsoon. Indian J. Geo-Mar. Sci. 44 (8), 1145—1154.

Kale, A., Karthick, B., 2015. The diatoms: big significance of tiny glass houses. Resonance 20 (10), 919—930.

Karthick, B., Kociolek, J.P., 2011. Four new centric diatoms (Bacillariophyceae) from the Western Ghats, South India. Phytotaxa 22, 25—40, http://dx.doi.org/10.11646/phytotaxa.22.1.2.

Karthick, B., Kociolek, J.P., Mahesh, M.K., Ramachandra, T.V., 2011. The diatom genus Gomphonema Ehrenberg in India: Checklist and description of three new species. Nov. Hedwigia 93 (1—2), 211—236, http://dx.doi.org/10.1127/0029-5035/2011/0093-0211.

Kociolek, J.P., 2005. A checklist and preliminary bibliography of the Recent, freshwater diatoms of inland environments of the continental United States. Proc. Calif. Acad. Sci. Fourth Ser. 56 (27), 395—525.

Krammer, K., Lange-Bertalot, H., 1986. Bacillariophyceae. 1. Teil: Naviculaceae. Gustav Fischer Verlag, Stuttgart, New York, 876 pp.

Kumar, M.R., Vishnu, S.R., Sudhanandh, V.S., Faisal, A.K., Shibu, R., Vimexen, V., Ajmal, K., Aneesh, K.S., Antony, S., Krishnan, A.K., 2014. Proliferation of dinoflagellates in Kochi estuary, Kerala. J. Environ. Biol. 35 (3), 877—882.

Liu, R., 2008. Checklist of Biota of Chinese Seas. Science Press, Academia Sinica, Beijing, 1267 pp., (in Chinese).

Madhu, N.V., Balachandran, K.K., Martin, G.D., Jyothibabu, R., Thottathil, S.D., Nair, M., Joseph, T., Kusum, K.K., 2010. Short-term variability of water quality and its implications on phytoplankton production in a tropical estuary (Cochin backwaters-India). Environ. Monit. Assess. 170, 287—300, http://dx.doi.org/10.1007/s10661-009-1232-y.

Madhu, N.V., Martin, G.D., Haridevi, C.K., Nair, M., Balachandran, K. K., Ullas, N., 2017. Differential environmental responses of tropical phytoplankton community in the southwest coast of India. Reg. Stud. Mar. Sci. 16, 21—35, http://dx.doi.org/10.1016/j.rsma.2017.07.004.

Mann, D.G., 2001. A discussion of Caloneis and related genera. Diatom 17, 29—36.

Mann, D.G., 1999. The species concept in diatoms. Phycologia 38 (6), 437—495, http://dx.doi.org/10.2216/i0031-8884-38-6-437.1.

Mauch, E., Schmedtje, S., 2003. Taxaliste der Gewässerorganismen Deutschlands zur Kodierung biologischer Befunde. Informationsberichte des Bayerischen Landsamtes für Wasserwirtschaft Heft. Bayerisches Landesamt für Wasserwirtschaf, München, 388 pp.

Menon, M.A.S., 1945. Observations on the seasonal distribution of the plankton of the Trivandrum coast. Proc. Indian Acad. Sci.-Sect. B 22 (2), 31—62, http://dx.doi.org/10.1007/BF03049878.

Menon, N.N., Balchand, A.N., Menon, N.R., 2000. Hydrobiology of the Cochin backwater system — a review. Hydrobiologia 430, 149—183.

Qasim, S.Z., 2003. Indian Estuaries, 1st edn. Allied Publication PVT Ltd, Heriedia Marg, Ballard Estate, Mumbai, 420 pp.

Reichardt, E., 1984. Die Diatomeen der Altmühl (Beitrage¨ zur Diatomeenflora der Altmühl 2). Bibl. Diatomol. 6 (1), 169.

Round, F.E., Crawford, R.M., Mann, D.G., 1990. The Diatoms: Biology and Morphology of the Genera. Cambridge Univ. Press, Cambridge, 747 pp.

Roy, J.C., 1954. Periodicity of plankton diatoms of the Chilika lake for the years 1950—51. J. Bombay Nat. Hist. Soc. 52 (1), 112—123.

Sanilkumar, M.G., Saramma, A.V., Joseph, K.J., 2009. Vertical distribution of microphytobenthos in Cochin estuary. J. Mar. Biol. Assoc. India 51 (1), 61—68.

Sankaranarayanan, V.N., Qasim, S.Z., 1969. Nutrients of the Cochin Backwater in relation to environmental characteristics. Mar. Biol. 2 (3), 236—247, http://dx.doi.org/10.1007/BF00351146.

Sarode, P., Kamat, N.D., 1979. Diatoms of Marathwada, Maharashtra — I. Phykos 18 (1—2), 25—32.

Selvaraj, G.S.D., Thomas, V.J., Khambadkar, L.R., 2003. Seasonal variation of phytoplankton and productivity in the surf zone and backwater at Cochin. J. Mar. Biol. Assoc. India 45 (1), 9—19.

Skvortzow, B.W., 1935. Diatoms from Culcutta, India. Philipp. J. Sci. 58 (2), 179—192.

Smol, J.P., Stoermer, E.F., 2010. The Diatoms: Applications for the Environmental and Earth Sciences, 2nd edn. Cambridge Univ. Press, Cambridge, UK, 667 pp.

Srinivas, K., Revichandran, C., Thottam, T.J., Maheswaran, P.A., Mohamed Asharaf, T.T., Murukesh, N., 2003. Currents in the Cochin estuarine system (southwest coast of India) during March 2000. Indian J. Mar. Sci. 32 (2), 123—132.

Subrahmanyan, R., 1946. A systematic account of the marine plankton diatoms of the Madras coast. Proc. Indian Acad. Sci. 24 (4), 85—197.

Taylor, J.C., Harding, W.R., Archibald, C.G.M., 2007. A methods manual for the collection, preparation and analysis of diatom samples, Report to the Water Research Commission. Pretoria, South Africa, 49 pp.

Venkataraman, G., 1939. A Systematic account of some South Indian Diatoms. Proc. Indian Acad. Sci. Bangal. 10 (6), 293—369.

Witkowski, A., Lange-Bertalot, H., Metzeltin, D., 2000. Diatom Flora of Marine Coasts 1. A.R.G. Gantner Verlag K.G., Germany, 925 pp.